Universidade do Minho
Escola de Engenharia

Vera Luísa Carreira Faustino

Microfluidic system for cell separation and deformation assessment by using passive methods

Microfluidic system for cell separation and deformation assessment by using passive methods

Vera Luísa Carreira Faustino

October de 2022

Universidade do Minho
Escola de Engenharia

Vera Luísa Carreira Faustino

Microfluidic system for cell separation and deformation assessment by using passive methods

Doctoral Thesis in Biomedical Engineering

Work developed under supervision of
Professor Rui Alberto M. M. de Lima
Professor Graça Maria Henriques Minas

October 2022

DIREITOS DE AUTOR E CONDIÇÕES DE UTILIZAÇÃO DO TRABALHO POR TERCEIROS

Este é um trabalho académico que pode ser utilizado por terceiros desde que respeitadas as regras e boas práticas internacionalmente aceites, no que concerne aos direitos de autor e direitos conexos.

Assim, o presente trabalho pode ser utilizado nos termos previstos na licença abaixo indicada.

Caso o utilizador necessite de permissão para poder fazer um uso do trabalho em condições não previstas no licenciamento indicado, deverá contactar o autor, através do RepositóriUM da Universidade do Minho.

Licença concedida aos utilizadores deste trabalho

Acknowledgments

First, I would like to thanks to my advisors Professors Rui Lima and Graça Minas for their support, understanding, time, comprehension and above all, for the all the dedication to finish this work successfully.

I would like to thank all the people in the lab, that contributed directly or indirectly to this work. In particularly to Susana Catarino for brainstorming, for good ideas and also, for make pressure when it was need it, without a doubt that she contributes a lot to the development of this work.

I would like to thanks to all my friends, that spend so much time listening to me that I was finishing my thesis. A special thanks to Diana Pinho, for more than guiding and debating ideas, for being a Friend and a great emotional support in this long journey.

During this journey, I can't forget to thank my other half, my companion, boyfriend, Marcelo Pereira, that support me, always, in the worst and in the best moments.

Finally, I want to express my gratitude to my parents and my brother, for all the financial and emotional support and patience, that hold their anxiety, because this was a very long journey.

Statement of Integrity

I hereby declare having conducted this academic work with integrity. I confirm that I have not used plagiarism or any form of undue use of information or falsification of results along the process leading to its elaboration.

I further declare that I have fully acknowledged the Code of Ethical Conduct of the University of Minho.

Resumo

Os sistemas microfluídicos têm sido usados com sucesso em muitas aplicações biomédicas. As principais vantagens destes sistemas consistem na utilização de volumes de amostras reduzidos e com tempos de ensaios curtos. Além disso, os sistemas microfluídicos possibilitam a execução de várias tarefas em paralelo numa única plataforma microfluídica, como por exemplo a separação e medição da deformabilidade de células/partículas. Em dispositivos microfluídicos, existem dois métodos principais para separar células: métodos passivos, baseados em microestruturas e escoamentos laminares, e métodos ativos, baseados em campos de forças externos. Muitos estudos têm sido realizados com métodos passivos, pois estes não necessitam de forças externas. Nesta tese serão apresentadas diferentes geometrias passivas para um dispositivo microfluídico, constituído por vários filtros de fluxo cruzado e multiníveis com o intuito de separar células/partículas em função do seu tamanho. Outra característica importante é a implementação de microcanais hiperbólicos a montante das saídas por forma a criar um escoamento extensional homogéneo e consequentemente medir a deformabilidade das células de forma controlada. Após a separação e avaliação da deformação, a quantidade de glóbulos vermelhos será quantificada por um método de espectrofotometria. Os resultados indicam que várias geometrias mostraram uma boa taxa de separação, confirmada pelas medidas de camada livre de células e pela espectrofotometria. Verificou-se também que os sistemas microfluídicos testados são capazes de separar amostras patológicas de sangue, demostrando assim o seu potencial em realizar simultaneamente a separação e deformação de células patológicas, como por exemplo células provenientes de pacientes diagnosticados com malária e/ou diabetes.

Palavras-Chave

Deformação e separação de glóbulos vermelhos, espectrofotometria, filtros de fluxo cruzado, microdispositivos passivos e microfabricação

Abstract

Microfluidic systems have been successfully used at many biomedical applications. Their great advantages allow working with minimal sample volumes and with short assays times. Additionally, microfluidic systems allow parallel operations in a single microfluidic platform such as separation and measurement of single cell/particles deformability. In microfluidic devices, there are two main methods for cells separation: passive methods, based on microstructures and laminar flow, and active methods, based on external force fields. Many studies have been made using passive methods because they do not require external forces. In this thesis it will be presented different geometrical passive approaches for a microfluidic device, that will have crossflow filters and multilevel steps that will separate the cells/particles by their size. Another important feature is the implementation of hyperbolic microchannels upstream the outlets in order to create a homogeneous extensional flow and consequently to measure the cells deformability in a controlled way. After the separation and deformation assessment, the amount of RBCs will be quantified by a spectrophotometry method. The results indicate that several geometries have shown a good separation rate, confirmed by the cell free layer and spectrophotometry measurements. It was also verified that the tested microfluidic systems are able to separate pathological blood samples, showing its potential to perform simultaneously separation and deformation assessments of blood diseases, such as malaria and diabetes.

Key-words

Crossflow filters, microfabrication, passive microdevices, RBCs deformation and separation and spectrophotometry

Contents

List of Abbreviations

3D – three dimensional

CAD – computer-aided design

CFL – cell free layer

CNC – computer numerical controlled

COC – Cyclic Olefin Copolymer

DI – Deformation Index

DLD – Deterministic lateral displacement

DNA – deoxyribonucleic acid

Dx – Dextran 40

EDTA – Ethylenediaminetetraacetic

Hct – Hematrocrit

HDPE – High-density polyethylene

LDPE – Low-density polyethylene

LEDs – Light emitting diodes

MEMS – Microelectromechanical systems

PAP – Print and Peel methods

PCB – Printed Circuit Board

PDMS – Polydimethylsiloxane

PIV – particle image velocimeter

PMMA – Poly(methyl methacrylate)

PMMA - Polymethylmethacrylate

RBCs – Red Blood Cells

Re – Reynolds

Rpm – centrifuge rotor speed

SEM - Scanning electron microscope

SU-8 – Designation of epoxy-bored photoresist

TAS – Total analysis system

UV – Ultraviolet

WBCs – White Blood Cells

PS – polystyrene

arRBCs – rigid RBCs

DR – deformation ratio

IPA – isopropyl alcohol

List of Figures

List of Tables

Part I

Thesis purpose and state of the art

Chapter 1

Introduction

Blood is a complex multiphase fluid, largely studied by many researchers of different areas, including mechanics, electroacoustics and biology. The main components of blood are red blood cells (RBCs), white blood cells (WBCs), platelets and plasma. Blood is full of physiological and pathological information about the body that could give us information about various diseases, such as diabetes, cancer, cardiovascular disease and malaria (Chien et al. 1984; Baskurt and Meiselman 2003; Hou et al. 2010; Ishikawa et al. 2011; Tanaka et al. 2012). All the sampling and analysis of blood is traditionally made on clinical laboratories with expensive and not portable devices. It would be important find quickly and less expensive methods to analyse blood samples. Microfluidic devices are increasingly being developed for the diagnosis of major diseases, such as cancer, diabetes mellitus and cardiovascular disorders (Hou et al. 2010; Tanaka et al. 2012; Faustino et al. 2016). The first experimental *in vitro* studies of microcirculation were performed in glass capillaries (Chien et al. 1984) and the crescent interest in microcirculation have contributed to development of soft lithography (Whitesides 2006). Soft lithography consists in using photolithography methods to produce microfluidic devices of polydimethylsiloxane (PDMS). PDMS is widely used in microfluidic devices, due to its many advantageous properties, such as good optical transparency, biocompatibility, elasticity, easy replication of fine and complex geometries, permeability to gases, and low cost. Shevkoplyas et al. (2003) were the first to develop a PDMS-based microfluidic device to observe RBC deformation *in vitro*. The creation of biomimetic structures that reproduce the circulatory system could help us to understand the blood behaviour and could improve the tests, make them more accurate. There are two methods for fluid handling, i. e., mixing and separation, that are commonly used in microfluidic studies by means of passive and active methods. Passive methods consist in using several microstructures geometries and laminar flow inside microchannels. In the literature it can be found different kinds of microfluidic device used, not only to separate blood from the suspending plasma (Shevkoplyas et al. 2003;

Faivre et al. 2006; Sollier et al. 2010), but also to investigate clinical alterations of the blood cells deformability (Thadikkaran et al. 2005; Tanaka et al. 2012; Faustino et al. 2014b). The passive methods do not require external forces, which means less cost in microfabrication and in the optimization of the microchannels, since it is only necessary to improve geometries design according to the main goals of the microdevice, that will be explained in more detailed at the objectives and motivation part of this thesis. Follow by a summary of works done until now, that are related with the purpose of this thesis, starting with a review about low-cost fabrication, and a resume of passive separation methods, and a review about the deformation visualization of measurements of RBCs. This introduction chapter will be followed by the fabrication and microchannels design and after that the separation results and quantifications methods will be shown and discussed. At the end the conclusions and future works will be presented. In Chapter 12, in appendix, it is presented a work that complements the RBCs deformation section where the effect of nanoparticles in the physical structure of RBCs are investigated.

1.1 Objectives and motivation

Nowadays, the importance of easy, low-cost and rapid detection of diseases have become a milestone. The prevention and early detection of illnesses could improve the long life of people, and at same time save money on expensive treatments. Miniaturize and optimize detection devices, is one step to achieve that.

So, the aim of this thesis was to evaluate the efficacy of microfluidic devices, by changing their geometries to separate RBCs from plasma and at same time evaluated the deformation of RBCs, using passive methods, and a low-cost microfabrication technique.

The cardiovascular diseases, diabetes and other blood diseases have been grown increasingly in the last years. The most common way to detect blood diseases is in a clinical laboratory, but the costs and the efficacy of the system could be improved. Some microfluidic devices have been developed to overcome these problems. Blood is full of information and many biomarkers could be found with the help of microfluidic devices. Hence, the goal of this PhD thesis is to create an efficient microfluidic device that separate blood cells and at the same time measure mechanical biomarkers such as the deformability and recovery time of individual blood cells by means of passive methods, to manipulate multiphase flows and as a result to develop an efficient microfluidic device able to separate and assess blood cells deformability in one single step.

The major scientific and technological objectives that should be accomplished are:

- to design and fabricate PDMS microchannels by using different microfabrication techniques such as soft-lithography and micromilling;
- to measure the rheology of blood in a shear rheometer in order to quantify the shear viscosity, as a function of blood hematocrit (Hct). This involves not only the use of healthy blood but also of diseased and drug treated RBCs which will change the deformability of the cells;
- to optimize the existing biomimetic methods to perform blood cells separations;
- to study possible effects of chemicals and nanoparticles on the blood cells;
- to quantify the separated cells by using a spectrophotometric method.

1.2 State of the art

This chapter corresponds to parts of already published review papers about the main topics of this thesis. First topic will be focus on different fabrications techniques for biomedical microfluidic devices, focusing on the low-cost fabrication. The second topic will be the passive separation of blood cells in the biomedical microfluidic devices. The third topic will be focus on the deformation methods in biomedical microfluidic devices and the last one, will be the challenges in biomedical microfluidic devices for Passive cells separations and deformation.

Chapter 2

Biomedical microfluidic devices by using low-cost fabrication techniques: a review[1]

2.1 Introduction

In the last 20 years, microfabrication technologies have become an important research area of for microfluidic applications in different scientific and industrial areas (Hansen and Quake 2003; Stone et al. 2004; Zare and Kim 2010), from environment (Mehta et al. 2006; Bridle et al. 2014), to pharmaceutics (Postier et al. 2008) or biomedical engineering (Fujii 2002; Ruffien-Ciszak et al. 2008; Sackmann et al. 2014). In particular, biomedical microsystems technologies for diagnosis applications have an extremely enhanced potential for being used as point-of-care devices (Kopp et al. 1997; Ribeiro et al. 2005; Urban 2009) since these systems typically feature high analytical performance, high system integration, improved potential for automation and control, small volume of analytes and reagents, safety, reduced cost, greater sensitivity, disposability and shorter analysis times, when compared to the conventional size systems (Lauks 1998; Figeys and Pinto 2000; Ziaie et al. 2004; Squires and Quake 2005; Whitesides 2006; Haeberle and Zengerle 2007; Melin and Quake 2007; Urban 2009). Manz et al. (1990) proposed the first miniaturized total analysis system (TAS) (Manz et al. 1990), able to automatically perform the sampling, transport, chromatographic separations and detection of samples at a microscale level. Since then, many authors have proposed micro total analysis systems, for different applications, and have explored different microfabrication techniques.

In the 90's decade, photolithography and micromachining in silicon were the most popular microfabrication techniques due to their vast use for microelectronics integrated circuits and

---

microelectromechanical systems (MEMS). This popularity, lead to adapt them to the fabrication of microstructures on glass and oxidized silicon (Terry et al. 1979; Wilding et al. 1994; Whitesides et al. 2001) for biological and biomedical applications, such as deoxyribonucleic acid (DNA) arrays, cells, proteins and clinical diagnostics studies (Schena et al. 1995; Chen et al. 1998; Duffy et al. 1998; Westin et al. 2000; Taylor et al. 2003; Rhee et al. 2005; Qin et al. 2010; Zare and Kim 2010; Mitra and Chakraborty 2011). Although glass and silicon technologies offer high precision, the fabrication methods are complex, time consuming and costly, since the use of cleanroom facilities is required each time a device is made (Duffy et al. 1998; Ziaie et al. 2004; Patel et al. 2008). Additionally, glass and silicon are fragile and too expensive materials for disposable devices. It is important to notice that silicon is optically opaque and semiconductor and, consequently, inappropriate for certain types of separation and detection mechanisms (with risk of sample carry-over and cross contamination) (Duffy et al. 1998). These limitations increased the research into alternative materials (Patel et al. 2008). Therefore, in the second half of the 90's decade, polymers started to be used for microfluidic structures fabrication (Xia et al. 1997; Duffy et al. 1998; Whitesides et al. 2001; Fujii 2002; Patel et al. 2008; Pinto et al. 2014b), and emerged as an attractive alternative to glass and silicon, due to their low-cost, wide range of mechanical and chemical properties, flexibility and easy processing (Whitesides 2006; Patel et al. 2008; Wong and Ho 2009; Pinto et al. 2014b). The fabrication processes using polymers are based on replication, which makes them faster and less expensive than those used with glass and silicon (McCormick et al. 1997; Duffy et al. 1998; Becker and Locascio 2002). The most popular polymers for microfluidic systems are poly(dimethylsiloxane) (PDMS), poly(methyl methacrylate) (PMMA), high-density polyethylene (HDPE), low-density polyethylene (LDPE), polyamide 6 and SU-8 (Becker and Locascio 2002; Ziaie et al. 2004).

Photolithography is a highly developed technology for micropatterning and microfabrication (Levinson 2005; Bhushan 2007). The photolithography process begins with producing a mask (typically a chromium pattern layer on a glass plate), and covering the substrate (such as silicon, glass or GaAs) with an Ultraviolet (UV) light sensitive polymer – photoresist. Ultraviolet light is then emitted through the mask onto the photoresist and it is developed, transferring the mask pattern to the photoresist layer above the substrate (Bhushan 2007; Fraden 2010). Two different kinds of photoresist are available: positive and negative. In a positive resist, the UV-exposed areas are dissolved in the subsequent development stage, whereas in a negative photoresist, the exposed areas remain intact after development (Bhushan 2007). Although photolithography is by far the

6

most common lithography technique in microelectronic fabrication, electron-beam (Broers et al. 1996) and X-ray lithography (Heuberger 1988) are two other alternatives which have attracted considerable attention in the MEMS and high resolution nanofabrication areas. However, photolithography, electron-beam and X-ray lithography techniques have high cost, the necessity of cleanrooms that increase the fabrication cost, limited control over surface properties, long time from the design to the prototype and inaccessible techniques to most biologists. Those features are slowing down the interest of the industrial community to commercialize these kinds of devices, and consequently, are limiting the use of this technology in biological applications (Whitesides et al. 2001; Ziaie et al. 2004; Bhushan 2007). Hence, it is crucial to develop low-cost alternatives for the fabrication of microstructures, avoiding the use of cleanroom facilities. A large number of research groups that are developing new microdevices do not have expensive cleanroom facilities and, as a result, do not have equipment frequently used in photolithography such as the mask aligner. This review focus on the selection of the most recent lithographic and non-lithographic low- cost techniques to fabricate microfluidic structures, where special attention is devoted on the features and limitations of each technique. Note that, in this review only microfabrication methods that do not require the use of cleanrooms are considered. Methods that involves cleanroom facilities have been reviewed elsewhere (Xia and Whitesides 1998; Whitesides et al. 2001; Rogers and Nuzzo 2005; Kim et al. 2008a; Rodrigue et al. 2015). Additionally, this review shows current and potential applications of these microfluidic devices in biomedical engineering.

2.2 Soft lithography

One of the most popular methods to fabricate biomedical microfluidic devices is by using soft lithography techniques (Duffy et al. 1998; Whitesides et al. 2001; Abdelgawad et al. 2008; Kim et al. 2008a; Feng and Tsai 2010; Pinho et al. 2013b; Faustino et al. 2014b; Rodrigues et al. 2015b), with organic and polymeric materials (Whitesides et al. 2001; Becker and Locascio 2002; Patel et al. 2008; Pinto et al. 2014b). The term "soft lithography" was first referred in 1998 (Xia and Whitesides 1998), and this technique is based on printing and replica moulding using elastomeric (mechanically soft) materials photomasks, stamps or moulds with the patterns of interest (Anderson et al. 2000; Whitesides et al. 2001; McDonald and Whitesides 2002; Ziaie et al. 2004; Abdelgawad et al. 2008), for the fabrication of microfluidic devices. Soft lithography represents a conceptually different approach to rapid and low-cost prototyping of various types of both microscale and nanoscale structures and devices on planar, curved, flexible and soft

substrates (Qin et al. 2010). It allows complex biochemical patterning (Chen et al. 1997; Bernard et al. 1998; Whitesides et al. 2001), in opposition to the photolithography, a high- cost microfabrication technology based, mainly, on glass and silicon substrates through relevant techniques such as patterning, etching, bonding and integration (Chen et al. 1997).

The soft lithography technology overcomes the main photolithography limitations usually found for biological and biomedical applications. Soft lithography allows the control of the molecular structure of the surfaces, the micropatterning of complex molecules and the fabrication of microfluidics channel structures (Xia et al. 1997; Whitesides et al. 2001). Additionally, the use of elastomeric materials allows the micropatterned surface to come into conformal contact with the surfaces over large areas, replicating the three-dimensional topography of a patterned, solid surface by replica moulding (which is successful even with features that are only one nanometer, as achieved by Gates and Whitesides (Whitesides et al. 2001; Gates and Whitesides 2003; Gates et al. 2004; Gates 2005)) (Anderson et al. 2000; Gates and Whitesides 2003; Gates et al. 2004; Gates 2005; Abdelgawad et al. 2008). Since the typical moulds are rigid, the use of an elastomer enables an easy detachment of the mould and replica. Polymeric stamps can also be used as moulds for fabrication with rigid materials that cannot be moulded and separated on conventional, brittle moulds. One of the main advantages of soft lithography is the easy bonding of the moulds to polymeric, elastomeric or glass substrates, regarding the sealing process, which can be reversible or irreversible (Becker and Locascio 2002).

PDMS has become popular among researchers because it has many favourable properties for prototypes fabrication: the material is inexpensive, optically clear (transparency to visible light makes it compatible with optical detection systems), and biocompatible; its moulding procedure is safe and easy to learn; and its flexibility allows the integration of elastomeric actuators and optical elements into devices (McDonald and Whitesides 2002; Fiorini and Chiu 2005; Wong and Ho 2009). Additionally, PDMS has excellent sealing properties, making it very suitable for microfluidics, and can be easily bonded to itself, allowing the fabrication of multilayer structures (Becker and Locascio 2002; Ziaie et al. 2004; Qin et al. 2010).

Soft lithography includes a large number of patterning techniques, all of them based on printing, moulding and embossing with an elastomeric stamp (Qin et al. 2010): replica moulding (Xia et al. 1997), microcontact printing (Kumar and Whitesides 1993), nanotransfer printing (Jeon et al. 2004), microtransfer moulding (Zhao et al. 1996), micromoulding in capillary (Kim et al. 1995), solvent-assisted micromolding (King et al. 1997), phase-shifting edge lithography (Rogers

et al. 1997), nanoskiving (Xu et al. 2008) and decal transfer lithography (Childs and Nuzzo 2002). One of the most used materials for the fabrication of moulds for microfluidic structures is the epoxy- based negative photoresist SU-8 (del Campo and Greiner 2007; Dey et al. 2010; Pinto et al. 2014b), due to its excellent properties, discussed in section 2.2.2 (del Campo and Greiner 2007; Pinto et al. 2014b). However, the fabrication of the moulds to produce microfluidic devices, such as SU- 8 moulds (Feng and Tsai 2010), usually requires a cleanroom environment that can be quite costly. Recently, low-cost techniques without cleanroom facilities that feature more than 20:1 aspect ratios (height/width), for fabricating those SU-8 moulds have being reported (Feng and Tsai 2010; Pinto et al. 2014b; Lim et al. 2015). With these aspect ratios, it is possible to obtain 100 µm width structures up to 2 mm height (Pinto et al. 2014b). For different authors, aspect ratios higher than 5:1 are already considered high aspect ratios (Patel et al. 2008; Kung et al. 2015). These techniques allow the fabrication of structures with dimensions appropriate for microfluidics: 10-100 µm, without the need of cleanroom facilities (Anderson et al. 2000; Pinto et al. 2014b). The production of prototype patterns and structures is rapid and inexpensive (Whitesides et al. 2001).

2.2.1 PDMS processing

PDMS has been widely reported for microfluidic systems (Delamarche et al. 1997, 1998; Chen et al. 1998; Duffy et al. 1998; Jackman et al. 1998; Anderson et al. 2000; Whitesides et al. 2001; Kim et al. 2008b). The PDMS processing, as well as the processing of other elastomeric materials, begins with the creation and printing of a high-resolution transparent photomask containing the design of the microchannels (Xia et al. 1997; Xia and Whitesides 1998; McDonald and Whitesides 2002). This photomask is used in soft lithography to create a master in positive relief photoresist with the desired patterning (Duffy et al. 1998; McDonald and Whitesides 2002). The PDMS cast against the master yields a polymeric replica containing the microfluidic structure. This technique can create a variety of microstructures prototypes, rapidly and at low-cost (Xia et al. 1997; Xia and Whitesides 1998). The entire fabrication process, from concept to realization, takes less than 24 hours, which is a significant decrease on the time required to develop a working prototype of a microfluidic structure, when compared with photolithography (Duffy et al. 1998). Figure 1 displays a schematic of soft lithography patterning by preparation of a PDMS stamp using replica moulding. First, the negative photoresist deposited on a substrate is exposed to UV light through a mask. The unexposed photoresist is dissolved, and the cured photoresist remains on the

substrate, with the pattern defined by the mask. This resultant structure is called master. At this stage, the master is exposed to a chemical treatment to reduce its tendency to adhere to the stamp. Then, an elastomer (typically PDMS) is poured over the master and cured. After curing, the PDMS stamp can be peeled off the master (Whitesides et al. 2001).
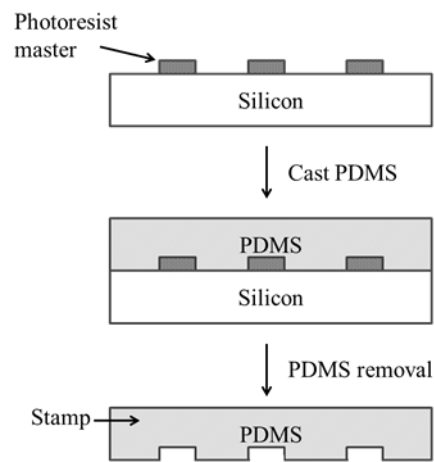
Figure 1. Schematic of patterning by preparation of a PDMS stamp using replica moulding.

The fabrication of microfluidic structures using soft lithography follows four main steps: pattern design, fabrication of the mask and the master, fabrication of the PDMS stamp and fabrication of micro- and nanostructures with the stamp by printing, moulding and embossing (Qin et al. 2010).

In conclusion, the soft lithography technique for PDMS microdevices brings several advantages to the fabrication of microfluidic prototypes. Some of the benefits of the described approach are the low-cost (low-cost transparencies are used as masks in photolithography to create masters, and channels are created by moulding a low-cost polymer against these masters), fast processing of prototypes, ease of designing, direct moulding and sealing of devices, reusability of the masters, design of complex 3D systems, easy installation of fluidic interconnects, as well as the applicability to a variety of biological and cellular processes due to the polymers biocompatibility (Duffy et al. 1998; McDonald and Whitesides 2002; Fiorini and Chiu 2005). Figure 2 displays some examples of PDMS microstructures for fluidic applications.

The main disadvantages of the PDMS soft lithography technique for prototyping are the vulnerability to the defects of the moulds (since the softness of PDMS can create distortions), limited temperature range and instability at high temperatures (Xia and Whitesides 1998; Whitesides et al. 2001). Additionally, PDMS fabrication through soft lithography, as described above, despite being a proper choice for prototypes, is not the best option for mass production, when

compared with non-lithographic techniques, since it takes a long time to produce a large number of microstructures.
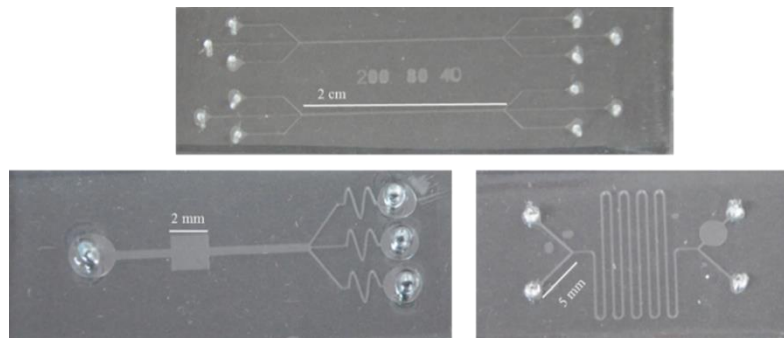
Figure 2. Photography of PDMS microfluidic structures.

2.2.2 SU-8 moulds processing

SU-8 is an epoxy-based negative photoresist, commonly used as a material for moulds, as well as for structures (Lin et al. 2002; Han et al. 2004; Lee et al. 2008; Alghane et al. 2011; Pinto et al. 2014b; Lim et al. 2015). SU-8 photosensitivity allows its patterning by UV photolithography. Therefore, in the SU-8 processing with soft lithography (and in the absence of cleanroom facilities), an UV exposure equipment, commonly used in the Printed Circuit Board (PCB) industry, can replace the more expensive and less available Mask Aligner that has been used in the last 15 years for SU-8 patterning. Furthermore, high transparency masks, printed in a photomask, can be used, instead of expensive chromium masks (Madou et al. 2001; Lin et al. 2002; Pinto et al. 2014b). Moreover, it is biocompatible and mechanically and chemically stable (Dey et al. 2010; Pinto et al. 2014b).

Relatively to the photomasks fabrication, although chromium masks have been widely employed for lithography processes, since they present excellent spatial resolution (<1 μm), they have a high-cost fabrication (Lau et al. 2013). Therefore, several authors have developed alternative not chromium based lithographic masks, in order to reduce the costs of the photomasks fabrication (including facilities). The patterns to be created in photoresist can be designed using commercial computer drawing packages (Whitesides et al. 2001). These transparencies can generate features of photoresist with dimensions of 50 μm as well as features as small as 20 μm (Whitesides et al. 2001). Additionally, several authors have approached other methods for photomasks fabrication: Orabona et al. (2013) developed a procedure for fabrication of photomasks on photographic films, and achieve a minimum resolution of 20 μm (Orabona et al. 2013); Cabriales et al. (2014) developed custom-made grayscale transparent patterns in polymeric layers with embedded

11

absorbing carbon nanopowder coated on a transparent glass substrate, using a setup based on the optical unit of a compact disc–digital versatile disc burner and a low-energy infrared laser beam (Cabriales et al. 2014).

Recently, Pinto et al. (2014b) demonstrate the successful fabrication of low-cost, well-defined SU-8 microstructures with aspect ratios higher than 20:1 in the absence of cleanroom facilities, by optimizing the SU-8 type, prebake and postbake time and temperature, as well as exposure and development time(Pinto et al. 2014b). The SU-8 processing follows the traditional soft lithography processing steps (see Figure 3). In a simple description, the process starts as the polymer is deposited into a silicon or glass substrate using a spin-coater, followed by a thermal treatment (prebake) with a hot plate, UV exposure, postbake and development of the SU-8 microstructure. Since SU-8 is a negative photoresist, the exposed areas become rigid and insoluble, while the non-exposed areas are removed (Pinto et al. 2014b; Lim et al. 2015). The removal and hardbake steps are optional steps, since the hardbake is used to further harden the SU-8 structure when it is used in a final device and the removal step is used to obtain free SU-8 microstructures, without the substrate (Pinto et al. 2014b; Lim et al. 2015). The substrate removal and, consequently, obtaining free standing SU-8 microstructures can be performed when the final microdevices involve combinations of metals and polymers or when mechanical flexibility is required for the microstructure application (Patel et al. 2008).

Other authors reported the fabrication of microstructures, based on SU-8 moulds, without cleanroom facilities: Huntington and Odom (2011) reported the fabrication of PDMS channels with SU-8 moulds, using UV LEDs (light emitting diodes) for phase-shifting photolithography. The authors converted an array of LEDs into a homogenous source by placing a diffuser after the LED array and in front of the substrate to be exposed, eliminating the need for a sophisticated exposure optics system and decreasing the power consumption of the system (Huntington and Odom 2011). Li et al. (2015) also used UV LED lithography for fabricating a microfluidic chip with acceptable results for mixing, droplet generation and blood typing and avoiding cleanroom facilities. Yang et al. (2014) also developed a low-cost portable system for fabricating PDMS fluidic structures in the millimetre range, using the photoresist OBM-309 and UV LEDs.
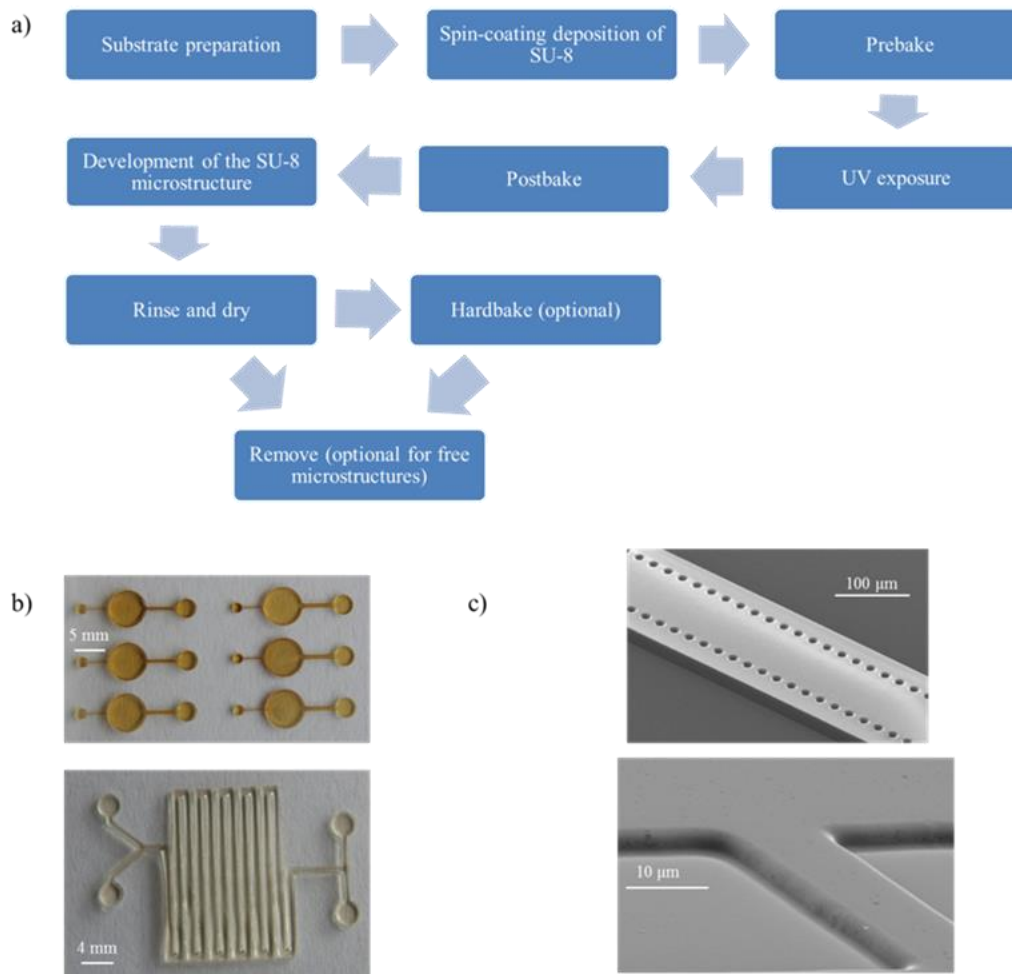
Figure 3. a) Basic procedure for the SU-8 negative photoresist processing with low-cost and without cleanroom facilities. b) Photography of SU-8 microstructures on glass substrate. c) Scanning electron microscope (SEM) images of SU-8 microstructures.

SU-8 is very sensitive to the processing parameters and, consequently, each step of the process strongly affects the results, particularly when no cleanroom facilities are available. Therefore, it is important to find the optimal processing conditions of equipment and environment for the fabrication of SU-8 moulds and structures (Pinto et al. 2014b; Lim et al. 2015).

The patterning of the SU-8 by soft lithography allows low-cost microstructures of almost any kind of shape and size, i.e., it allows not only planar microstructures, but also multilayer and 3D microstructures (del Campo and Greiner 2007; Pinto et al. 2014b).

SU-8 has been used for different microfluidic applications, for fabrication of microchannels, micropumps, valves and micromixers. Additionally, SU-8 (or other elastomeric material) moulds fabricated through soft lithography can be used, almost up to hundred times, to fabricate microchannels in other materials, such as PDMS, using the previously described techniques.

2.2.3 3D Soft lithography

Besides planar microstructures, 3D soft lithographic techniques have been used in the last years for fabricating multilayer and 3D microstructures (Kane et al. 1999; Rodrigue et al. 2015), based on layer-by-layer multi exposure (Becker and Locascio 2002; del Campo and Greiner 2007; Lee et al. 2008), inclined/rotated (Han et al. 2004), holographic and grey-scale lithography (del Campo and Greiner 2007; Rammohan et al. 2011) technologies. In particular, soft lithography using the grey-scale technology in the photomasks is based on the principle that different grey levels lead to different values of the structure thickness (del Campo and Greiner 2007; Rammohan et al. 2011). 3D soft lithography with photosensitive polymers was the key technology for the fabrication of 3D parts with complex shapes (as internal structures) and high resolution (Rodrigue et al. 2015). 3D microstructures can have applications in biomicrofluidic applications, as pumping valves (Nge et al. 2013), polymer scaffolds with networks of channels (Kim et al. 1998) or L shaped serpentine microchannels for improving mixing, as suggested in (Ansari 2009; Nge et al. 2013). By combining soft lithography with other mechanical non-lithographic techniques (Wu et al. 2003), for defining the moulds (as micromilling (Wilson et al. 2011)), it is possible to obtain complex 3D structures with curved cross sections (Wilson et al. 2011), which can be useful to recreate blood vessels for hemodynamic studies. Other authors have used 3D micromachining for patterning substrates with regionally selective cell adhesion (Park et al. 1998).

2.3 Non-lithography microfabrication techniques

From the beginning of the twenty first century, different authors started to fabricate their own devices, using non-lithographic microfabrication techniques, known as low-cost techniques. Due to its simplicity, low-cost and availability in almost all laboratories and offices, these techniques are a potential alternative to produce biomedical microdevices to researchers who have difficulty to access specialized fabrication facilities and equipment. Equipment regularly used by these low- cost techniques are laserjet printers, inkjet printers, solid ink printers, cutting plotters and micromilling machines.

2.3.1 PAP (Print and Peel)

Print and Peel methods (PAP) are low-cost fabrication techniques able to perform direct printing of the masters for casting polymer device components using regular office equipment such as laserJet printers, inkjet printers and cutting plotters (Thomas et al. 2010). Although, this

low- cost method is an attractive technique due to its fast and easy prototyping, it has a major constrain concerning the durability of the master moulds in mass production (Thomas et al. 2010). The main limitations of this fabrication method are established by the resolution of the printers used to print the masters and control the amount of toner or ink deposited during the printing process (Thomas et al. 2010). In the literature, it was found that the smallest dimension achieved by the printed masters is just a little narrower than 100 μm (Thomas et al. 2010) and the aspect ratio (relationship between its width and height) is from 20 up to 100 (Tan et al. 2001; Bao et al. 2005; Vullev et al. 2006; Kaigala et al. 2007). Laserjet and solid ink are the most popular techniques to produce microsystems.

2.3.1.1 Laserjet and Solid ink

Generally, the fabrication by using this nonlithography technique is by printing the computer-aided design (CAD) drawings directly on the polystyrene transparency films to produce the masters (Vullev et al. 2006). The main characteristics of the masters printed by laserjet printers is the use of toner particles, comprising binder polymers, colorants and charge-controlling agents (Tyagi et al.; Natsuhara et al. 2001) deposited on a substrate, such as papers or transparency films (Vullev et al. 2006). The polymer glues the particles together and adhere the printed features to the surface of the substrate due the elevated temperature and subsequent cooling and solidification (Vullev et al. 2006). In general, the toner polymer contains polyesters, polystyrene and epoxy resins (Fukuda et al. 1974; Amering et al. 1990; Natsuhara et al. 2001), but the composition of the tonner binder polymers depends on the manufacturers. During the fabrication process, the master mould cannot be used more than 5 times as the quality of the mould tends to decrease and the roughness of the channel walls tend to increase with the replication of the mould (Vullev et al. 2006). On the other hand, by using this technique it is possible to obtain trapezoidal and round bottom cross sections that could be a potential advantage for several microfluidic applications (Bao et al. 2005; Vullev et al. 2006). Vullev et al. (2006) in their studies could not reproduce channels thinner than about 70 μm, by means of a LaserJet Printer. Additionally, they have observed that the depth of the channels tends to decrease as the microstructures become narrower than 200 μm (Vullev et al. 2006). In these particular techniques, the dimensions and shapes are strongly linked with the characteristics of the printer, and for high quality printers it is possible to achieve heights down to 5 μm. Note that it is possible to increase the height of the microstructure by repeatedly printing layer by layer. However, special attention should be devoted

to the alignment of the layers (Vullev et al. 2006). Experiments performed by both techniques (LaserJet and Solid Ink Printers) have shown that maximum height of the master moulds is about 15 µm (Thomas et al. 2010). Thomas et al. (2010) have performed microvisualization studies to compare the quality between both methods and they have found that solid ink printer generates features with improved smoothness. Hence, by using a solid ink printer, it is possible to integrate 3D elements into the printed features and consequently to produce a continuous flow microfluidic biosensor (Vullev et al. 2006).

2.3.1.2 Xurography

Xurography is a technique that has emerged, as others mentioned in this review, from the low-cost necessity and impossibility of having a cleanroom facility. The first study using xurography was performed by Tan et al. (2001), Pinto et al. (2014a) and Greer et al. (2007) and they have shown to be an effective, low-cost (material and equipment), and rapid technique to fabricate microfluidic channels without the need of a cleanroom. Overall, xurography uses a cutting plotter machine and adhesive vinyl films to generate master moulds or mask and it can be used as simple soft-lithography technique to produce microfluidic devices in elastomeric polymer (Pinto et al. 2014a). The master moulds will be dependent on the cutting plotter and the foil used. Bartholomeusz et al. (2005) made experiments where it was possible to fabricate structures with widths down to 6 µm and thickness of 25 µm. However, these extremely small dimensions are difficult to achieve and manipulate, in particular when the structures have complex geometries. A recent work performed by Pinto et al. (2014a) has shown that this technique has poor resolution for dimensions smaller than 500 µm. Figure 4 shows the main steps of the fabrication procedure performed by Pinto and his colleagues. Additionally qualitative visualization results of the cross section for microchannels with different widths are also shown. To evaluate quantitatively the produced mould masters and correspondent PDMS microchannels several microscopic images and measurements were obtained in the middle of straight microchannels having different widths (see Figure 5). The results have shown that the difference between the expected dimensions of a drawing performed in AutoCAD and the real dimensions measured in the microchannel cross section tend to increase by decreasing the width of the PDMS microchannels.
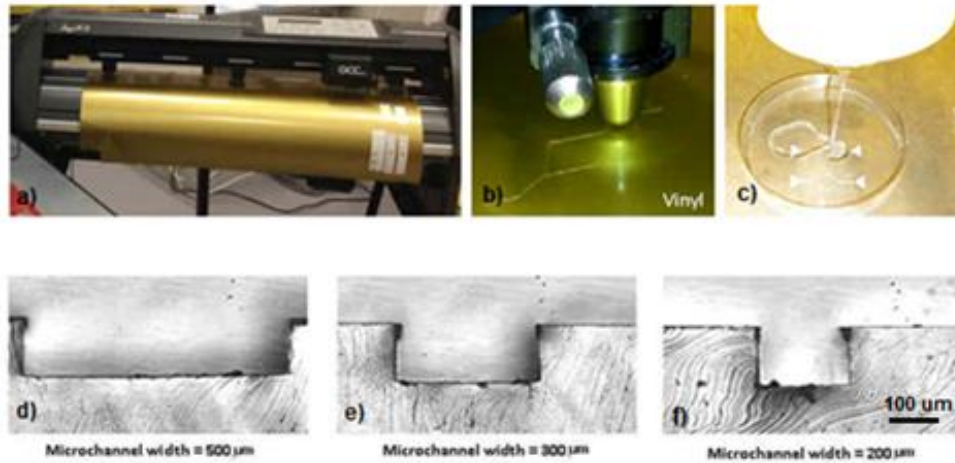
Figure 4. Main steps used by the xurography technique and microscopic images obtained at the cross section of PDMS microchannels having different widths: a) Cutting plotter machine used to cut the drawings performed in a CAD software; b) The plotter cuts the vinyl film to produce the correspondent moulds; c) By using an adhesive film the mold in moved to a petri to pour the PDMS on the mold and consequently to obtain the proposed microchannel; d) Cross section for microchannels with 500 µm width; e) Cross section for microchannel with 300 µm width; f) Cross section for microchannel with 200 µm width (Pinto et al. 2014a).
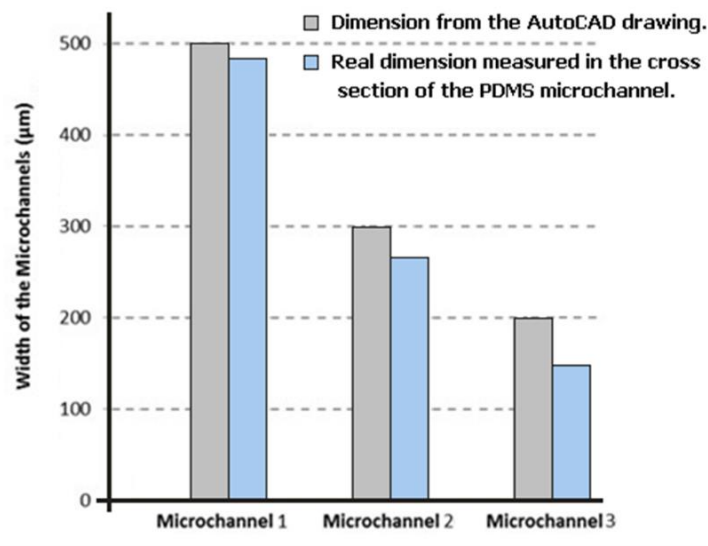
Figure 5. Comparison between the values projected from AutoCAD and the real widths of the produced PDMS microchannels (Pinto et al. 2014a).

2.3.2 Micromilling

Micromilling is a technique that uses a high precision computer numerical controlled (CNC) motion system, a high-speed spindle with rotational speed and micromills (Bordatchev and Nikumb 2008). The micromills are tools where the cutting edge can have dimensions smaller than 100 µm. Hence, this tool can remove material in micron range and, as a result, it is possible to produce structures down to 5 µm without the use of complicated environment such as cleanroom facilities (Bordatchev and Nikumb 2008). A recent study performed by Lopes (2014) and Lopes et al.

17

(2015a) has shown the ability of a micromilling machine to manufacture microchannels with widths down to 30 µm (see Figure 6). Note that, micromilling should be used with hard materials, like thermoplastics, PMMA and COC (Cyclic Olefin Copolymer), as long as the milling does not heat the material too much (Lopes 2014). Additionally, they have shown the capability of the developed microfluidic device to perform separation of red blood cells (RBCs) from plasma. These phenomena occur due to the increase of the cell free layer (CFL) that can be observed upstream the contraction and close to the microchannel walls. This is a well-known phenomenon that happens in both microvessels (Kim et al. 2009) and microchannels (Sollier et al. 2010; Rodrigues et al. 2016b), and is attributed to the shape and deformability of the red blood cells that tend to migrate to the middle of the microchannel. More detailed description about this phenomenon can be found at Kim et al. (2009) and Rodrigues at al. (2016b). Although this technique looks promising, several disadvantages such as complex tool alignment and easily tool breakage are slowing down the application of this method in the fields of bio-engineering and biomedical engineering (Lopes 2014; Lopes et al. 2015a).
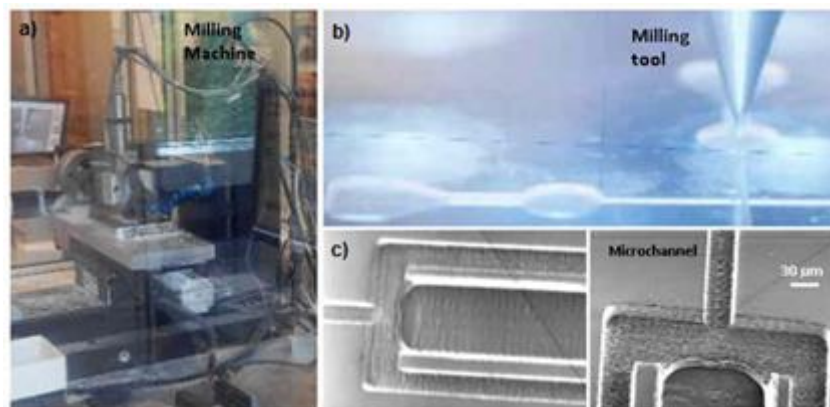
Figure 6. Main steps of the micromilling process: a) Micromilling machine used to fabricate microchannels with widths down to 30 µm (Right side); b) During the fabrication of the device, two different milling tools with the diameter of 30 (for smaller parts) and 100 µm (for bigger parts), this process was only possible due to the assistance of a small microscope able to observe the movements of the microtools; c) After the fabrication of the microfluidc device and in order to evaluate the milling fabrication process, images from the microchannels were obtained by using a scanning electron microscope (SEM) (Lopes et al. 2015a).

2.3.3 Direct Laser Plotting

An attractive technique used to create microstructures or microchannels is by using a laser plotter. In general, lasers are expensive but when compared with the high costs associated to cleanroom facilities, the laser fabrication technique is a potential alternative to conventional soft lithography. Briefly, the microstructures generated by this technique are based upon thermal degradation effect that engraves the surface of the desired material. This micromachining

18

technique can use long pulse (Kim et al. 2009) or short pulse laser beams (Sollier et al. 2010) and all the parameters are controlled by using a software. Hence, this technique is simple and very fast and consequently as a great potential to produce mass-manufacturable disposable microfluidic devices (Sollier et al. 2010). Typically, by using long pulse lasers this method can generate microchannel widths down to 100 μm (Khan Malek et al. 2009; Wang et al. 2012), however, by using ultra-short laser pulses, it is possible to reach structures down to 10-20 μm (Khan Malek et al. 2009; Wang et al. 2012). Other interesting characteristic of this technique is the possibility to use different materials. For instance, Wang et al. have used PDMS as substrate, that can be suitable to fabricate microchannels for biomedical applications (Wang et al. 2012). As already mentioned, the time required to produce microstructures with this technique is also a great advantage, in only 1 hour we can produce several microfluidic devices (Wang et al. 2012). The most critical parameters of this technique are the laser power, moving speed, and pulses per inch, as all of them will affect the final profile of microchannels. Hence, before the fabrication of the desired microstructures it is crucial to test the above parameters as they may change from plotter to plotter (Wang et al. 2012). Another, important drawback of this technique is the difficulty to control the desired cross section geometry of the microchannels. The most common geometry produced by this technique is a trapezoidal cross section.

2.3.4 Techniques to fabricate circular microchannels

In *in vitro* blood experiments it is important to fabricate microchannels with geometries close to *in vivo* environments. Hence, it is crucial to fabricate microchannels with circular or elliptical cross sections. By using the above techniques such kind of geometries are extremely difficult to achieve. In the last century, the majority of experimental blood flow studies have performed in glass capillaries and promoted *in vitro* rheological findings happening at a microscale (Goldsmith 1971; Goldsmith and Marlow 1979; Reinke et al. 1987; Pries et al. 1992; Suzuki et al. 1996). Additional information on *in vitro* blood flowing through glass capillaries can be found in reviews by Goldsmith et al. (1989), Chien et al. (1984), Maeda (1996) and more recently by Lima et al. (2012). Nowadays, glass capillaries still a popular methodology to perform experimental flow studies mainly due to low cost of acquiring the capillaries. Some examples are the confocal micro-PIV studies performed by Lima et al. (Lima et al. 2006, 2008a; Pinho et al. 2013a) and Saadatmand et al. (2011). However, during the last decade the number of studies that uses capillaries is decreasing mainly due to the novel low-cost alternatives to produce microchannels

and to several limitations associated to the glass capillaries such as rigid walls, geometry simplicity, difficulty to control flows and culture cells at small dimensions. Recently, in order to overcome the limitations of the glass capillaries, several researchers were able to fabricate circular microchachannels by casting PDMS around templates (Verma et al. 2006; Perry et al. 2007; Jia et al. 2008; Lima et al. 2009c) or by reshaping rectangular microchannels (Kangsun et al. 2007; Fiddes et al. 2010).

2.3.4.1 Microwire-moulding

This is an extremely simple and popular technique to manufacture circular PDMS microchannels. The microwire-moulding strategy generates the circular cross-section by casting PDMS around different kinds of templates such as glass rods (Perry et al. 2007), nylon theards (Verma et al. 2006) and metal microwires (Jia et al. 2008; Lima et al. 2009c). In general, these microchannels can be generated by embedding microwires within the PDMS and after the curing of the PDMS the microwires can be removed from it (see Figure 7). More details about this technique can be found at Jia et al. (2008) and Lima et al. (2009c). Both studies were able to fabricate microfluidic devices comprising microchannels with diameters down to 50 μm. In the former study they have applied their device to perform micro-PIV flow studies and to generate microdroplets (Jia et al. 2008), whereas the latter work a confocal micro-PTV system was used to perform flow visualization measurements of labelled and non-labelled RBCs (Lima et al. 2009c). The main advantage of this technique is the ability to fabricate microchannels from a single piece of PDMS, thus avoiding alignment and bonding problems. However, this method also has several drawn backs such as the difficulty to fabricate complex geometries and the strong dependence on the size and geometries available in the market.

Figure 7. Schematic of the microwire-moulding methodology to fabricate PDMS circular cross-section microchannels. The microwire embedded in the PDMS (right side) is removed after the curing of the PDMS. As a result, it is possible to produce a circular microchannel (left side).

2.3.5 Reshaping rectangular microchannels

An alternative technique to produce circular and elliptical cross sections is by reshaping original rectangular microchannels. Kangsun et al. (2007) were able to fabricate both circular and elliptical cross-section microchannels by using the PDMS surface tension. In brief, when the PDMS layer is cured, it contacts with a liquid PDMS film and as result a meniscus is formed due to surface tension. The meniscus of the liquid PDMS can be adjusted and form cross-sectional shapes such as ellipses and circles. By using this technique a serpentine three-dimensional micromixer was developed and tested (Kangsun et al. 2007). The main drawn back of this method is the large number of complicated steps to fabricate the microchannels. Another alternative method was proposed by Fiddes et al. (2010), where they were able to modify rectangular SU-8 masters into PDMS circular cross-section microchannels. Briefly, this method includes the following steps (i) fabrication of the original square or rectangular microchannel in SU-8; (ii) introduction in the microchannel a solution of silicone oligomer in hexanes and a stream of nitrogen gas; and (iii) polymerization of PDMS and evaporation of hexanes. It is worth mentioning, that the gas stream is the main responsible to control the shape and the diameter of the circular cross-section microchannels. Fiddes et al. (2010) have shown the ability to not only fabricate microchannels with diameters down to 39 μm but also to grow endothelial cells inside the microchannels. However, this method requires nitrogen gas which might be difficult to find in conventional laboratories. Additionally, expertise is needed to control the pressure of the nitrogen stream.

2.4 Discussion and comparison of the reported low-cost techniques

This section presents a comparison between the previously described low-cost lithographic and non-lithographic techniques for fabrication of microfluidic structures. Table 1 shows a summary comparing the main features of the reported low-cost techniques that can be successfully used without cleanroom. Representative features for comparison are the microfluidic device dimensions highlighting the aspect ratio, minimum resolution, allowed materials, moulds re- usability. Some advantages and disadvantages are also reported.

Overall, some methods including glass capillaries and microwire-moulding technique are extremely simple. Others require more sophisticated equipment such as soft lithography and the techniques used to reshape rectangular microchannels. In microfluidic devices, the replication of the moulds is a feature that we should have in mind due the influence of the channels surface in the flow behaviour of the tested fluids. For the majority of the techniques covered in this review,

the replication is possible. Note that, the PAP technique more precisely the laserjet and solidink print the roughness of the walls increased with replication of the mould (Vullev et al. 2006). Others like xurography and micromilling the microchannels sometimes have little imperfections associated to the tools used to fabricate the microchannels, as we can in Figure 4 and Figure 6. It is worth mentioning, that the moulds used to reshape rectangular microchannels can only be used once.

Table 1. Low-cost lithographic and non-lithographic techniques comparison.

Lithographic Techniques	Dimensions	Resolution	Materials	Advantages	Disadvantages
Soft lithography	Down to 1 nm (Gates and Whitesides 2003; Gates et al. 2004; Gates 2005). Aspect ratio > 20:1 (Whitesides et al. 2001).	Limited by the resolution of the mask printer (Xia and Whitesides 1998). The resolution can be improved at nanoscale by defining the masks by a focused laser or electron beam (Betancourt and Brannon-Peppas 2006).	Polymers – PDMS, SU-8 and organic materials.	High-resolution and 3D geometries (del Campo and Greiner 2007; Rammohan et al. 2011). Excellent micro size precision. Moulds used hundred times.	Pattern deformation and vulnerability to defects (Xia and Whitesides 1998; Whitesides et al. 2001). Inappropriate for mass production.
Non-Lithographic Techniques					
PAP: Laserjet and Solid ink print	Height 5-15 µm (Vullev et al. 2006; Thomas et al. 2010). Channels width thinner than about 70 µm width (Vullev et al. 2006).	Aspect ratio width/height is 20 up to 100 (Tan et al. 2001; Bao et al. 2005; Vullev et al. 2006; Kaigala et al. 2007).	Toner polymer contains polyesters, polystyrene and epoxy resins (Fukuda et al. 1974; Amering et al. 1990; Natsuhara et al. 2001).	Trapezoidal and round bottom cross sections (Bao et al. 2005; Vullev et al. 2006). Possible to integrate 3D elements (Bao et al. 2005).	Resolution of the printers (Thomas et al. 2010). Controller of the amount of toner/ink deposited (Thomas et al. 2010). Durability of the master moulds in mass production (Thomas et al. 2010).
PAP: Xurography	Width down to 6 µm and thickness of 25 µm (Bartholomeusz et al. 2005).	Poor resolution for dimensions smaller than 500 µm (Pinto et al. 2014a).	Adhesive vinyl films (Pinto et al. 2014a).	Low-cost (material and equipment), and rapid technique (Tan et al. 2001; Greer et al. 2007; Pinto et al. 2014b).	Extremely small dimensions are difficult to achieve and manipulate.

Micromilling	Width down to 30 µm (Lopes 2014; Lopes et al. 2015a).	Limited by the milling tool.	Possibility to use different materials, such as PMMA, aluminium and machinable wax (Lopes 2014; Lopes et al. 2015a).	Moderate micro size precision. Moulds used hundred times.	Complex tool alignment and easily tool breakage (Lopes 2014; Lopes et al. 2015a).
Direct Laser Plotting	Structures down to 10-20 µm (Bao et al. 2005; Wang et al. 2012).	Limited by kind of laser beam.	Possibility to use different kind of polymeric materials, such as, acrylic and PDMS (Wang et al. 2012).	It is possible to produce 3D structures (Bao et al. 2005). Within 1 hour we may have a microfluidic device (Wang et al. 2012).	Usually trapezoidal cross sections. Lasers are expensive (Bao et al. 2005; Wang et al. 2012)
Glass Capillaries	Down to 5 µm	Aspect ratio 1	Borosilicate, clear-Fused Quartz, Synthetic Fused Silica.	Excellent micro size precision and economic method.	Only for simple and straight geometries. Rigid walls. Difficulty to control flows and culture cells at small dimensions.
Microwire-moulding technique	Down to 50 µm (Jia et al. 2008; Lima et al. 2009c)	Aspect ratio 0.95-1 (Lima et al. 2009c).	Glass, stainless steel, nylon, aluminum (Verma et al. 2006; Perry et al. 2007; Jia et al. 2008; Lima et al. 2009c)	Circular cross section. Simple and economic method (Lima et al. 2009c).	Only for simple geometries. (Lima et al. 2009c). Market dependent. Low versatility.
Reshaping rectangular microchannels technique	Down to 39 µm (Fiddes et al. 2010).	Aspect ratio close to 1.	PDMS, SU-8 (Kangsun et al. 2007; Fiddes et al. 2010).	Circular and elliptical cross section. Possible to change the dimensions and geometry of the original microchannel. Easy bonding process (Kangsun et al. 2007; Fiddes et al. 2010).	Mainly simple geometries (Kangsun et al. 2007; Fiddes et al. 2010). Complex to control fabrication parameters (Kangsun et al. 2007). Requires nitrogen gas.

2.5 Biomedical Applications

During the last decade, several research works have applied low-cost techniques into the biomedical field. Applications of out of cleanroom microfabrication in biomedical research can be found in recent reviews performed by Li et al. (2012) and Pan and Wang (2011). However, both reviews did not focus on issues related to blood flow mechanics. Therefore, in this review we address several recent applications into the blood on chip field. Note that, the majority of the presented examples were developed by elements of the authors' research groups.

Recently, Pinto et al. (2012), by using xurography, have successfully fabricated microchannels with bifurcations followed by confluences and by means of a high-speed microvisualization system they were able to perform blood flow visualizations measurements. Figure 8 shows the visualization of *in vitro* blood flowing in a microchannel fabricated by xurography.
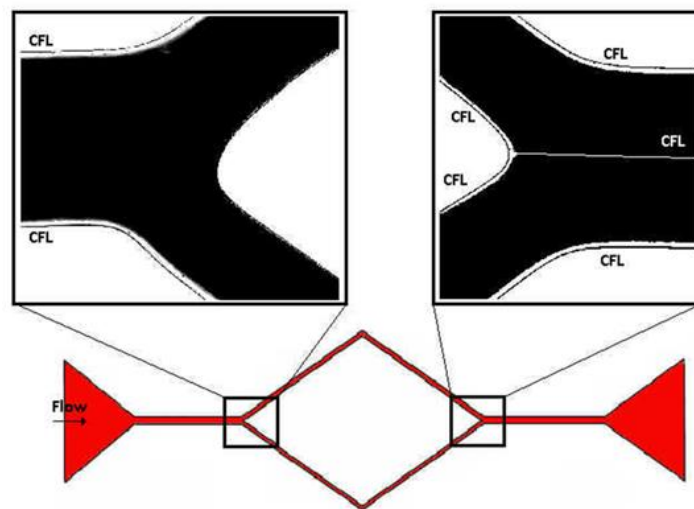
Figure 8. Visualization of *in vitro* blood flowing in a microchannel geometry fabricated by xurography with a diverging bifurcation and converging bifurcation. It was considered a constant flow rate of 10 μl/min and constant pressure. This microchannel was tested with 3 different width: 200, 300 and 500 μm (Pinto 2012).

This research work has shown that by using microchannels fabricated by xurography it is possible to observe physiological phenomena that happens in both *in vivo* an *in vitro* experiments (Pinto 2012). Additionally, by using these kind of microchannels Pinto et al. (2012) have found the formation of a cell depleted region immediately downstream of the apex of the convergent bifurcation. This phenomenon was also observed by the research works performed by Ishikawa et al. (2011) and Leble et al. (2011), where they have used microfluidic devices fabricated by a soft lithography technique. Those research studies have shown that main reason for the observed phenomenon is mainly due to the cell depleted layers that are originated around the walls of the

24

confluence daughter branches. More detailed information about this phenomenon can be found at Leble et al. (2011).

Another very recent work was the study performed by Lopes (2014), Lopes et al. (2015a) and Jaron et al. (2016), where the authors have shown the ability of a micromilling machine to produce a microfluidic device able to perform separation of red blood cells from plasma due to the CFL created upstream the contraction (Figure 9). They have shown that the contraction produced by this technique was able to enhance the CFL and consequently may result in an efficient way to separate blood cells from plasma at low-cost.
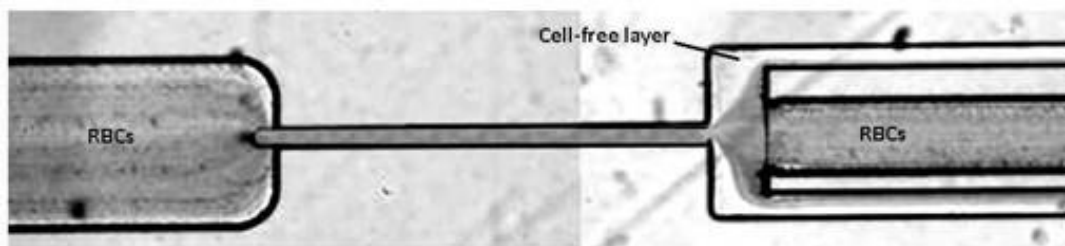
Figure 9. Visualization of the effect a contraction produced by a micromilling machine in the CFL. RBCs solution was used as working fluid in the microchannel at a constant flow rate. The inlet width is 300 μm, the contraction width is 30 μm, the outlet width is 160 μm and total length of the channel is 1300 μm (Lopes 2014; Lopes et al. 2015a).

In the last century, glass capillaries were the most popular way to investigate blood flow phenomena happening at a microscale level. The major findings in mechanics of blood flow in glass capillaries can be found in reviews by Goldsmith et al. (1989), Chien et al. (1984), Maeda (1996) and Lima et al. (2012). The recent popularity and the associated benefits of using polymeric microfluidic devices to perform blood flow studies have promoted the development of new alternative microdevices. A successful examples were the microfluidic devices developed by Jia et al. (2008) and Lima et al. (2009c), where they were able to manufacture circular PDMS microchannels by using a microwire-moulding technique. By using a confocal micro-PTV system individual RBCs were successfully tracked through a 75 μm circular PDMS microchannel. Figure 10 shows the trajectories of individual labelled RBCs flowing through the PDMS microtube for a feed Hct of 3%, and 23% (Lima et al. 2009c). It is clear that for solutions with higher RBC concentrations (e.g. 23% Hct) the trajectories of flowing RCBs exhibit higher fluctuations in the direction normal to the flow. Additionally, this study has shown that the RBCs flowing in a crowded environment (e.g. 23% Hct) tend to undergo multi-body collisions which increases the amplitude of the RBC's lateral motion and a result the RBC lateral dispersion increases with the Hct.
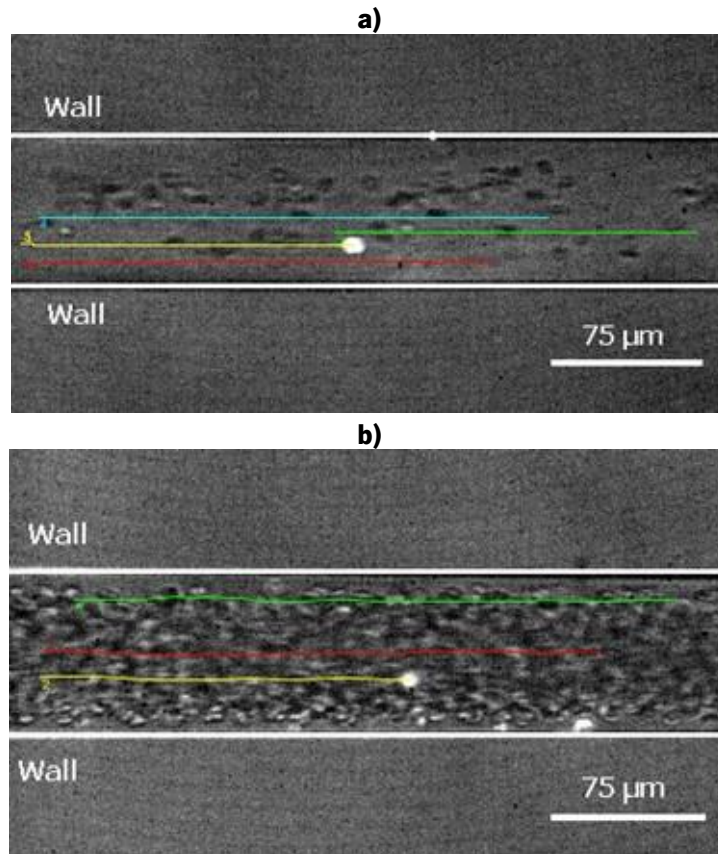
Figure 10. Trajectories of individual labeled RBCs flowing through a 75 µm circular PDMS microchannel for: a) a feed Hct of 3%; b) a feed Hct of 23%. The unlabeled RBCs appear as dark gray ellipsoids and the labeled RBCs appear as bright spots.

The inability of the glass capillaries to culture living cells have motivated researchers such as Fiddes et al. (2010) to develop PDMS circular cross-section microchannels able to culture cells on their walls. By using nitrogen gas Fiddes et al. (2010), were able to modify rectangular SU-8 masters into PDMS circular microchannels. Additionally, they were able to successfully culture endothelial cells on the surfaces of circular PDMS microchannels. It is therefore clear that ability to culture endothelial cells on the microchannel surface represents a more realistic way of the cell flow phenomena that happens in *in vivo* environments.

Chapter 3

Passive methods for cell separation

3.1 Introduction

Microfluidic devices became an important tool for researchers because of the enormous potential of their features, such as high analytical performance, high system integration, improved potential for automation and control, small volume of analytes and reagents, safety, reduced cost, greater sensitivity, disposability and shorter analysis times, when compared to the conventional size systems (Lauks 1998; Figeys and Pinto 2000; Ziaie et al. 2004; Whitesides 2006; Haeberle and Zengerle 2007; Melin and Quake 2007; Urban 2009; Sackmann et al. 2014).

The first miniaturized total analysis system (TAS) was proposed by Manz et al. (1990) and was able to automatically perform the sampling, transportation, chromatographic separations and detection of samples at a microscale level. It was in the same decade that photolithography and micromachining in silicon became the most popular technique in microfabrication. So, with the increasing interest on microfluidic devices, the advances on microfabrication techniques, materials and applications grew. Nge et al. (2013) wrote a complete review of microfluidic systems on materials, functions, integration, and applications for microfluidic since 2008. Other authors focused their reviews in different topics, like fabrication techniques and applications making the information more resumed and allowing the research more easily (Nge et al. 2013; Faustino et al. 2016). The physical phenomena such as the Reynolds, Peclet, Grashof, and Knudsen numbers, among others, can be used for characterizing the fluid behaviour inside microfluidic devices. This topic is very well reviewed by Squires and Quake (2005) combining the physical explanation with practical examples.

The fabrication of microdevices allowed us to mimic the microcirculation and study the blood circulation, to physically and biologically understand the blood behavior, in the way that we find biomarkers for early detection of blood diseases. Blood is an interesting fluid that provides us

a lot of information related with our body and health. All the components of blood, such as platelets, erythrocytes, leucocytes and plasma have an amount of biological, biomechanical and biochemical information that could help us in the discovering of many diseases like cancer, diabetes mellitus, malaria or cardiovascular disorders (Cho et al. 2008; Hou et al. 2011).

The complexity and peculiar characteristics of blood make it a very complicated and interesting fluid to study. It was shown that blood behaves as a single-phase homogeneous fluid or a multiphase, non-homogeneous fluid (Garcia et al. 2012). For example, when blood passes through large diameter vessels could be thought of as homogeneous and treat as a single-phase fluid, in the other hand, in smaller diameters blood change is behaviour and start to exhibit multi-phase, nonhomogeneous and non-Newtonian characteristics, mainly caused by the components of blood, particularly the RBCs, which are present in large quantity (Tripathi et al. 2015a). The apparent viscosity is a result of non-Newtonian characteristics and depends of different factors such as haematocrit, plasma viscosity, RBCs aggregation and the mechanical properties of RBCs (Reinke et al. 1986; Baskurt and Meiselman 2003; Chakraborty 2005; Tripathi et al. 2015b).

Phenomena like cell free layer (CFL), Fahraeus Effect, Fahraeus - Lindquist Effect and phase separation of single bifurcation were observed in microcirculation and could be replied and obtained by physical and geometrical effects created in hydrodynamic microdevices for study blood plasma separation (Tripathi et al. 2015a). The Fahraeus Effect is the tendency of the concentration of RBCs (haematocrit) to decrease with the decrease of diameter of vessels, and generally occurs in diameters smaller than 500 μm (Park et al. 2006). The Fahraeus - Lindquist Effect is related to the viscosity of blood, so the viscosity decreases with the decrease of diameter of vessel, and normally happens in vessels between 10 and 300 μm in diameter (Fåhræus and Lindqvist 1931). The CFL appears around the walls of the microchannels and it is a tendency of RBCs to migrate to the centre of the microchannel increasing the cells concentration in that region (axial migration) and, consequently, leaves a space around the walls empty of cells (Thurston 1989; Goldsmith et al. 1989; Cokelet and Goldsmith 1991; Park et al. 2006; Zhang et al. 2009; Fedosov et al. 2010). The concentration of cells, deformability and diameter of the vessels influence the thickness of the CFL, leading to an increase of the CFL with the increase of the diameter and decrease of the cells concentration. The flow rate also has influence in the CFL thickness, increasing the CFL with the increase of the flow rate (McHedlishvili and Maeda 2001; Park et al. 2006).

The velocity profile of blood flow in microcirculation is something challenging due the high concentration of cells. However, for low haematocrit, it can be considered as parabolic and behaves

according to Poiseuille's law (Baskurt and Meiselman 2003; Sugii et al. 2005; Lima et al. 2012). So, some factors such as Hct, shear rate, flow rate, aggregation and diluting medium influence the velocity profile and it is possible that the dilution factor is the most important factor in the blood behaviour studies.

The separation of the blood components from the plasma could give us tools to discover new biomarkers and new ways to analyse the blood components (RBC, WBC or even particles) separately but in the same microdevice. However, blood is a complex fluid that must be very well prepared for *in vivo* studies to overcome some challenges when inside the microchannels. For example, Chen et al. (2008) used pillars in their microchannels to avoid cells clogging and jamming and, at the same time, to create the crossflow effect and a multilevel filtration barriers, that simultaneously separate the WBCs, RBCs and the plasma. Other authors used hyperbolic shapes to measure RBCs deformability (Yaginuma et al. 2013; Faustino et al. 2014b) and used diluted blood to have the minimum cells inside the microchannels in order to improve the measurements. Recently, Pinho et al. (2013b) have proposed a continuous microfluidic device for partial separation of RBCs and subsequent measurement of the RBC deformability in one single device. The geometries used in this device were slightly smaller than the size of the cells and, as a result, this methodology was able to generate mechanical stimuli close to *in vivo* capillaries.

In the next section it will be present some techniques for cell separation, with focus on the passive separation.

3.2 Techniques used for cells separation using microfluidic tools

Microfluidic tools were used until now for different kinds of purposes, such as micropumps, valves, mixers and separation devices (Rife et al. 2000; Haeberle and Zengerle 2007; Cardoso and Minas 2012), overcoming a lot of challenges concerning the miniaturization of the lab on a chip. The techniques of cell separation were mostly developed for cell concentration purposes (mainly haematocrit concentration or plasma separation); blood fractioning (separation of blood components); or cell sorting (separation of different types of cells) (Wyatt Shields Iv et al. 2015).

The techniques used for separation of cells, can be active, passive or both (label-free cell sorting mechanism) (Catarino et al. 2019). Figure 11 show the different methods that can be used.
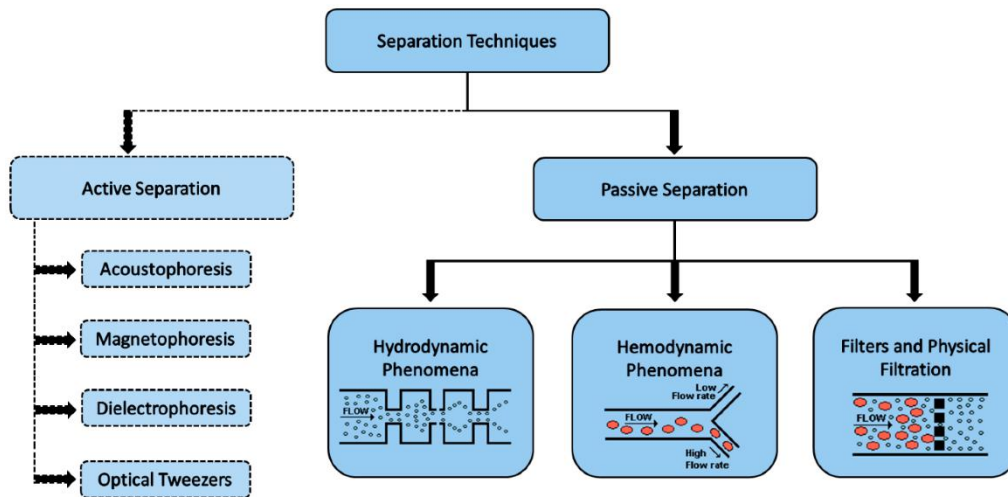
Figure 11. Classification of the main active and passive separation techniques used in microfluidic systems (Catarino et al. 2019)

Other methods also can be used in cell separation, such as paper based (Songjaroen et al. 2012; Kim et al. 2013) and CD based (Haeberle et al. 2006; Amasia and Madou 2010), that are mostly to separate plasma from blood (Kersaudy-Kerhoas and Sollier 2013).

The passive methods used in microfluidic devices are more interesting than the active methods because its precise manipulation, low-cost fabrication, simple structure (without external forces), simple integration and lower maintenance in lab on chip devices and high throughput (Chung et al. 2004; Squires and Quake 2005; Khosravi Parsa et al. 2014; Rodrigues et al. 2015b). The passive method use the geometry of channels (Shevkoplyas et al. 2005; Yang et al. 2006a; Ishikawa et al. 2011; Karimi et al. 2013; Kersaudy-Kerhoas and Sollier 2013; Martel and Toner 2014; Zhang et al. 2016) or intrinsic hydrodynamic forces, such as punch flow fraction, deterministic lateral displacement, inertial forces and intrinsic physical property of the cells (Pamme and Manz 2004; Pamme 2007; Suh and Kang 2010; Lee et al. 2011a; Martel and Toner 2014; Zhang et al. 2016). The different passive techniques can be divided by the phenomenon: hydrodynamic phenomena (as punch flow, inertial forces or deterministic lateral displacement); hemodynamic phenomena (based on the intrinsic physical properties of the cells); and filters and physical filtration (based on micropores, microweirs, membranes and the gap between micropillars) as can be seen in Figure 11 (Catarino et al. 2019).

3.2.1 Hydrodynamic Separation and Sorting Techniques

In microfluidic devices the hydrodynamic separation is more suitable for low Reynolds number flows (Re<1). The laminar flows that occurs in this conditions allow that particles or cells follow different paths achieving size-based separation (Tsutsui et al. 2009).

Many factors can influence the particles or cells exposed to a shear flow experience a lift force perpendicular to the flow direction and a force from the wall, such as channel geometry, flow rate, rheological properties of the carrier fluid and mechanical properties of the elements (Catarino et al. 2019). So, it is possible to achieve size-based cell separation and sorting, by controlling the flow rates of the inlets (Gossett et al. 2010).

Deterministic lateral displacement (DLD) is one of the hydrodynamic separation methods, that is based in arrays of pillars placed within a microchannel. This effect combined with laminar flow, force the particles or cells following specific trajectories through the device. The gap between the array of pillars sorted the particle or cells by their size. So, when particles and/or cells are smaller compared with the gap of the pillars, they tend to flow through the array gaps without net displacement from the original central streamline. In other hand, when particles are bigger than the gap of the pillars, they will displace laterally, traveling at an angle predetermined by the posts offset distance (Gossett et al. 2010). The isolation of cancer cells from whole blood using a rapid label-free microfluidic structure, based in DLD arrays, was made by Liu et al. (2013) and they achieved a cells separation efficiency between 80 and 99%.

3.2.2 Hemodynamic Phenomena on Cell Separation Techniques

The hemodynamic phenomena on cell separation techniques can be observed *in vivo*, inspiring microfluidic structures that mimic these effects. In some microfluidic systems have been found effects, such as:

- Fåharaeus–Lindqvist effect, that is the decrease of the apparent viscosity of blood in small vessels) which causes the tendency of the RBCs to migrate toward the centre of the microchannel, creating the cell-free layer (CFL) (Lima et al. 2012; Pinho et al. 2017);
- leukocyte margination, since leukocytes are less deformable than RBCs, they tend to flow near the wall due the collisions between them (Bhagat et al. 2010)[86];
- Zweifach–Fung bifurcation effect occur in asymmetric bifurcations in which the vessel with the smaller flow rate gets a higher concentration of plasma) (Kersaudy-Kerhoas and Sollier 2013; Pinho et al. 2017).

Fahraeus effect was study by Faivre et al. (2006) using a microchannel with a constriction-expansion region and they obtained almost pure plasma with a 16% Hct at a flow rate of 200 μL/h. It was also studied the behaviour of RBCs in a 75 μm circular PDMS microchannel by Lima et al.

(2009c). In this study it was used 3% and 23% Hct and it was observed trajectories of the solutions with higher RBC concentrations exhibit higher fluctuations in the direction normal to the flow (Lima et al. 2009c).

Other microdevices were developed for blood plasma separation using the bifurcation law. Jaggi et al. (2007) obtained for 4.5% and 45% Hct (whole blood), at a flow rate of 5 mL/min-1, separation efficiency of 92% and 30%, respectively. The separation of RBCs from plasm due to CFL created upstream a contraction in a microchannels was developed by Lopes et al. (2015a). The authors used a micromilling technique to produce the microchannels and concluded that the geometric contraction was able to increase the CFL resulting in an efficient way to separate blood cells from plasma (Lopes et al. 2015a). Other authors, such as Yang et al. (2006a) also described a PDMS microfluidic device based on the Zweifach–Fung bifurcation law. They obtained a separation efficiency of 100% for a 45% Hct at a flow rate of 10 µL/h.

Some relevant studies were performed *in vitro* with blood in simple microchannels with asymmetric bifurcations by Ishikawa et al., (2011), Leble et al., (2011) and Pinto et al., (Pinto et al. 2014a) and more recently Bento et al. (2018a, 2019) have performed similar studies in more complex geometries. They had observed a clear cell-depleted layer at the region of the confluence apex that can be used to perform blood plasma separation.

3.2.3 Microfluidic Filters-Physical Filtration Techniques

The microfluidic filters can be combined with the already mentioned separation techniques in order to improve the efficiency of the microfluidic device (Squires and Quake 2005; Tripathi et al. 2015a). Those filters, such as, micropillar arrays, microweir structures or microporous membranes, are able to separate cells and particles based on their size and/or deformability. They can be adjusted to the needs, but some challenges may show up, like clogging, fouling and heterogeneity of the cell sizes (Gossett et al. 2010). The use of cross-flow filters (Lee and Clark 1998; Keskinler et al. 2004; Chen et al. 2008; Tsutsui et al. 2009) can minimize the clogging since the fluid tangentially rather than through the filter as it does in membrane filtration. A set of microfluidic chips based on cross-flow filtration principle were developed by Chen et al. (2008). Plasma, RBCs and WBCs can be separated and collected at different outlets. These microfluidic chips had micropillar-array and parallel microweirs that were used to separate cells by their sizes obtained 95% of RBCs separated from the initial whole blood and 27.4% of WBCs (Chen et al. 2008). Other authors, such as Zhang et al. (2012) combined the passive filters with hydrodynamic

forces in a chip using microbarriers with a range size of 15 to 7 µm, to promote the separation of cells. They reported the separation of cancer cells based on their deformability and the microscale geometry of the flow channels ensured that the fluid flow is laminar, resulting in continuous cell movement and deformation in the device (Zhang et al. 2012).

A summarized comparison of the already mentioned methods was made by Catarino et al. (2019) and it is presented in Table 2.

Table 2. Comparison between the passive separation phenomena (Catarino et al. 2019).

Method	Hydrodynamic Separation	Hemodynamic Separation	Physical Filtration
Separation criteria	Size	Size, deformability, cells concentration (hematocrit), cell aggregation (Haeberle et al. 2006)	Size, shape, deformability
Target sample	Cells, microparticles	RBCs, WBCs, plasma	Cells, particles
Separation Efficiency	Above 90% (Kuntaegowdanahalli et al. 2009; Wang et al. 2013) 80–99% (Liu et al. 2013) 62.2% (Lee et al. 2011b)	100% separation efficiency with 15–25% plasma separation volume (Yang et al. 2006a) 92% separation efficiency with diluted blood (Hct 4.5%) and 37% with whole blood (Hct 45%) (Jäggi et al. 2007)	More than 95% of the RBCs and 27% of the WBCs removed from whole blood (Chen et al. 2008) 65–100% (Haeberle et al. 2006) 98%, 8% (plasma from whole blood) (VanDelinder and Groisman 2006, 2007)
Throughput	2 mL/min (Liu et al. 2013) 10^6cells/min (Kuntaegowdanahalli et al. 2009) 1.2 mL/h (10^{10} cells/min) (Lee et al. 2011b	3–4 µL/min(VanDelinder and Groisman 2007) 5 mL/min (Jäggi et al. 2007)	2×10^3 cells/s (VanDelinder and Groisman 2006, 2007)
Potential effects on cells	Shear stress	Shear stress	Clogging, fouling, shear stress
Required instrumentation	Fluidic pumps	Fluidic pumps	Fluidic pumps
Processing layout	Continuous flow	Continuous flow	Batch; Continuous flow

The perfect lab-on-a-chip should be small, simple and portable, and with the passive separation methods it can be possible this achievement to separate cells due its simplicity to integrated in a microdevice (Yang et al. 2006a; Streets and Huang 2013).

Although, there is still some challenges to overcome, such as, the integration of passive separation techniques in autonomous, functional and portable microdevices (Catarino et al. 2019). Other challenges such clogging or hematocrit (in case of using blood samples) also have to be considered in the design and implementation of the microfluidic structures (Kersaudy-Kerhoas and Sollier 2013; Catarino et al. 2019).

Chapter 4

Deformation of Red Blood Cells, Air Bubbles, and Droplets in Microfluidic Devices: Flow Visualizations and Measurements[2]

4.1 Introduction

Blood flow behavior in microcirculation is strongly influenced by red blood cell (RBC) deformability as they occupy almost half of whole blood volume. When RBCs are subjected to large external flow forces, they elongate without rupture and tend to return to their original shape when the external forces are removed. Some major determinants of RBC deformability include external flow forces, cell geometry, cell internal viscosity, and membrane viscoelastic properties (Mokken et al. 1992). RBC-related diseases, such as malaria, sickle cell disease, and diabetes, can also promote significant alteration in the RBC deformability. Ever since the deformability of RBCs became a potential biomarker for several blood diseases, various experimental techniques have been developed to measure the deformation of blood cells (see Table 3). There have been several reviews discussing different techniques for measuring RBC deformability under a variety of experimental and diseased conditions (Musielak; Mokken et al. 1992; Lee and Lim 2007; Kim et al. 2012). The recent progress in microfabrication and high-speed microvisualization technology made it possible to produce microfluidic devices able to directly visualize and characterize the mechanical properties of individual cells flowing through constriction microchannels (Abkarian et al. 2008; Faustino et al. 2016). However, there are still few reviews focusing on the use of these kinds of microfluidic devices to measure cell deformability. Most of the recent reviews, performed by Zheng et al. (2013), Tomaiuolo (2014), and Xue et al. (2015), have focused on single-cell devices, cylindrical glass capillaries, and in microdevices, where the shear effect is dominant. Due

to the growing interest of combining the shear and extensional effect to perform deformability measurements, this review focuses on the most recent findings performed by our research group related to the deformation of RBCs flowing through hyperbolic, smooth, and sudden-contraction microchannels. Moreover, deformations of air microbubbles flowing within *in vitro* blood microfluidic devices are also measured and compared with RBC deformability.

Table 3. Techniques to measure RBC deformability under different diseased conditions.

Measurement Technique	Human Diseases	Main Key Features	References
Micropipette aspiration	Sickle cell anemia, malaria	Enables accurate mechanical response of single RBCs, labor-intensive, time-consuming, and involves a typically difficult process of manipulation.	(Nash et al. 1989; Paulitschke and Nash 1993; Glenister et al. 2002; Kim et al. 2012)
Optical tweezers	Malaria, sickle cell anemia, diabetes mellitus	Ability to obtain a mechanical response of single RBCs down to the piconewton level; labor-intensive, time-consuming, and special human technical skills are required.	(Suresh et al. 2005; Kim et al. 2012; Agrawal et al. 2016)
Atomic force microscopy	Cancer, spherocytosis, thalassemia, diabetes mellitus, sickle cell anemia	Ability to apply forces to RBC surfaces at the nanoscale level; labor-intensive; time-consuming and requires expensive equipment.	(Dulińska et al. 2006; Fornal et al. 2006; Maciaszek and Lykotrafitis 2011; Kim et al. 2012)
Microfluidic ektacytometer	Diabetes mellitus	Homogenous flow, ability to differentiate healthy and diseased cells, labor-intensive and time-consuming process. It is required to label the RBCs to identify them. This latter process may change the RBCs' mechanical properties.	(Shin et al. 2007; Pinho et al. 2017)
Microfluidic constriction channel	Diabetes mellitus, malaria, cancer, abdominal obesity and metabolic syndrome	Reduced space, homogenous flow, label-free, ability to measure a large amount of cells in one single run, potential to precisely control and detect small deformability changes, needs a high-speed video microscopy system combined with an image analysis technique; blockage is likely to happen at constriction microchannels with dimensions similar to the RBC diameter.	(Tsukada et al. 2001; Shelby et al. 2003; Shin et al. 2007; Hou et al. 2009; Huang et al. 2013; Zeng et al. 2016; Pinho et al. 2017)

4.2 Deformation of RBCs in Microfluidic Devices

Most of the proposed microfluidic devices to perform RBC deformability characterization focus on the shear effect. Some examples from the literature are the measurements of the RBCs' deformation under a transient high shear stress in a sudden-contraction microchannel (Zhao et al. 2006) and the RBCs' deformability through a microfluidic device with a microchannel diameter comparable to RBC size (Tomaiuolo et al. 2011). In addition to the shear effect, the extensional effect and the combination of both can be encountered in the human body, e.g., in microstenosis, in microvascular networks composed of small, irregular vessel segments, in pulmonary microvessels, and in medical instrumentation, such as the flow through syringes and syringe needles. Hence, it is important to understand the RBC mechanical properties under both shear and extensional effect.

Flows of blood cells through microfluidic contractions generate complex flow phenomena despite their simple geometry. The flow involves a reduction in the cross-sectional area, which generates strongly-converging flows as the fluid goes through the contraction and the blood cells exhibit a variety of shapes, such as circular, ellipse, and parachute, which depend on the rheological properties of the fluid, geometric configuration, and dimensions of the contraction. The schematic illustration in Figure 12 shows the fluid flow behavior in different kinds of microfluidic constriction channels through which the RBCs travel. In general, the flow exhibits mixed kinematics with strong extensional flow (the fluid accelerates as it is going through the contraction) along the centerline and shear flow close to the walls. The major advantage of microfluidic hyperbolic-shaped contraction (Figure 12c) is the ability to impose a constant strain rate along the centerline of the contraction, as well as to achieve high extensional and shear flows. Relevant works in the context of blood flow and RBC deformability are those performed by Sousa et al. (2011), Lee at al. (2009), Yaginuma et al. (2013), Rodrigues et al. (2016b), Rodrigues et al. (2015b), Rodrigues et al. (2016a), Faustino et al. (2014b), Pinho et al. (2017), and Calejo et al. (2015), who studied the effects of the extensional flow in hyperbolic converging microchannels using blood analog fluids and *in vitro* blood containing different kinds of blood cells. Other works have used cross-slot microfluidic devices to investigate the deformability of different kinds of cells under the application of extensional flows (Gossett et al. 2012; Henon et al. 2014; Guillou et al. 2016).
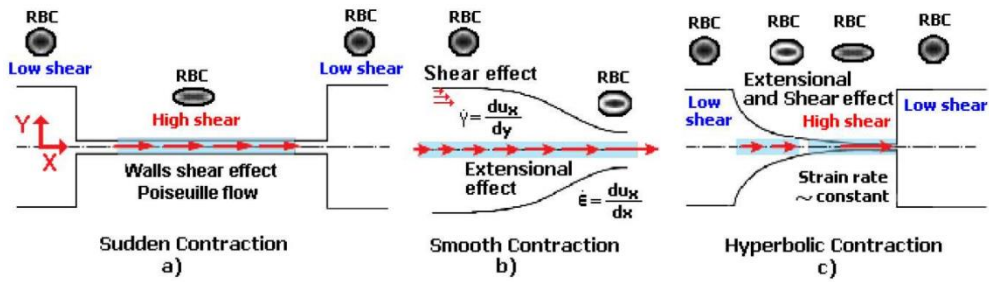
Figure 12. Blood flow and RBC deformability in microfluidic contractions at different geometries: (a) sudden contraction; (b) smooth contraction; and (c) hyperbolic contraction, adapted from (Faustino et al. 2014a).

RBCs flowing through microfluidic contractions are, most of the time, subjected to high shear and extensional effects and, as a result, they tend to elongate into ellipsoid shapes with their major axis aligned to the flow direction. When the cells leave the constriction region, the fluid shear forces created by the wall are removed and, consequently, RBCs tend to return to their normal resting biconcave disc shape. The deformation under controlled flow conditions provides an efficient method to generate cellular-scale mechanical stimuli. Hence, microfluidic constrictions due to the ability of performing precise control and manipulation of a small volume of samples have been gaining increasing interest to measure the deformability of RBCs for clinical proposes (Abkarian et al. 2008; Lee et al. 2009; Zheng et al. 2013; Yaginuma et al. 2013; Faustino et al. 2014b; Tomaiuolo 2014; Rodrigues et al. 2015b, 2016b, a; Pinho et al. 2017).

The classical method to quantify the degree of deformability is by using an ellipse-fitting program. The deformation index (DI), also known as elongation index, most of the times is calculated by $(X - Y)/(X + Y)$ where X and Y represent the major and minor lengths of the ellipse, respectively (see Figure 13). However, in microchannel capillaries, where the dimensions of the channels are smaller than the diameters of the cells, the degree of deformability should be measured as the ratio between the length of the major axis and the length of the minor axis as the RBC tends to deform in a parachute shape, as shown in Figure 13 (Tsukada et al. 2001; Jeong et al. 2006). This latter definition is designated as the deformation ratio (DR).
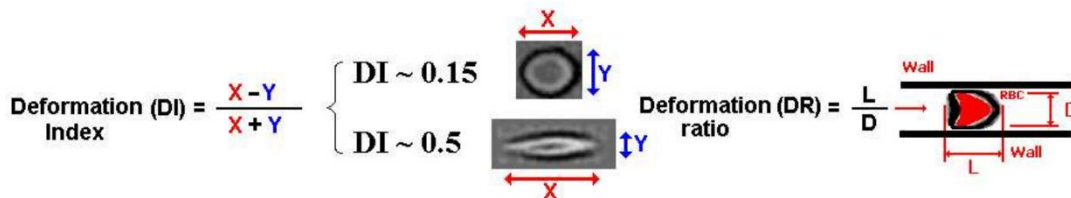
Figure 13. Schematic diagram of the deformation index (DI) and deformation ratio (DR) definition, adapted from (Maciaszek and Lykotrafitis 2011).

4.2.1 Deformation of RBCs in Hyperbolic Contractions

Since RBC deformability became a potential clinical biomarker, several single-cell microfluidic methodologies have been developed to perform flow measurements on RBCs (Zheng et al. 2013; Tomaiuolo 2014; Xue et al. 2015; Faustino et al. 2016). The majority of the methods to measure the RBCs' deformability have focused on the response of the cells under simple shear flow. However, it is well known that extensional flow also plays an important role in the blood cells' flow dynamics in both *in vivo* and *in vitro* environments. Extensional effects, or a combination of shear and extensional effects, can happen in several situations, such as in micro-contractions (due to velocity transition), in bifurcations (around the apex region and small branch), and when cells flow from a wide blood vessel to a narrow catheter or needles. This latter situation can generate extremely high extensional flows, which can promote hemolysis and, as a result, can lead to clogging and jamming within the devices (Lee et al. 2009; Gossett et al. 2012). Hence, recently, several extensional flow studies have been performed not only to assess cell deformability (Lee et al. 2009; Yaginuma et al. 2013; Faustino et al. 2014b; Rodrigues et al. 2015b, 2016a; Pinho et al. 2017), but also to separate blood cells from plasma (Yaginuma et al. 2013; Rodrigues et al. 2016b). The majority of these studies were performed at hyperbolic converging microchannels where single-cell deformability was assessed under a controlled homogeneous extensional flow field. Figure 14 shows RBCs flowing through the expansion region (A) and hyperbolic contraction region (B) for two different flow rates, i.e., 9.45 µL/min and 66.15 µL/min. These qualitative flow visualizations clearly show that the RBC deformability is higher in the hyperbolic contraction region (B) where the RBCs are subjected to a strong extensional flow. Right after the exit of the contraction, RBCs tend to recover their initial shape (A), which corresponds to a minimal value of the deformation and where the RBCs are no longer exposed to a strong extensional flow. Another expected result is that the RBCs have a tendency to increase the deformation as the flow rate increases. More detailed information can be found in the work performed by Yagimuma et al. (2013) where they have investigated the influence of the extensional flow on the motion and deformability of individual RBCs in the full length of a hyperbolic microchannel.
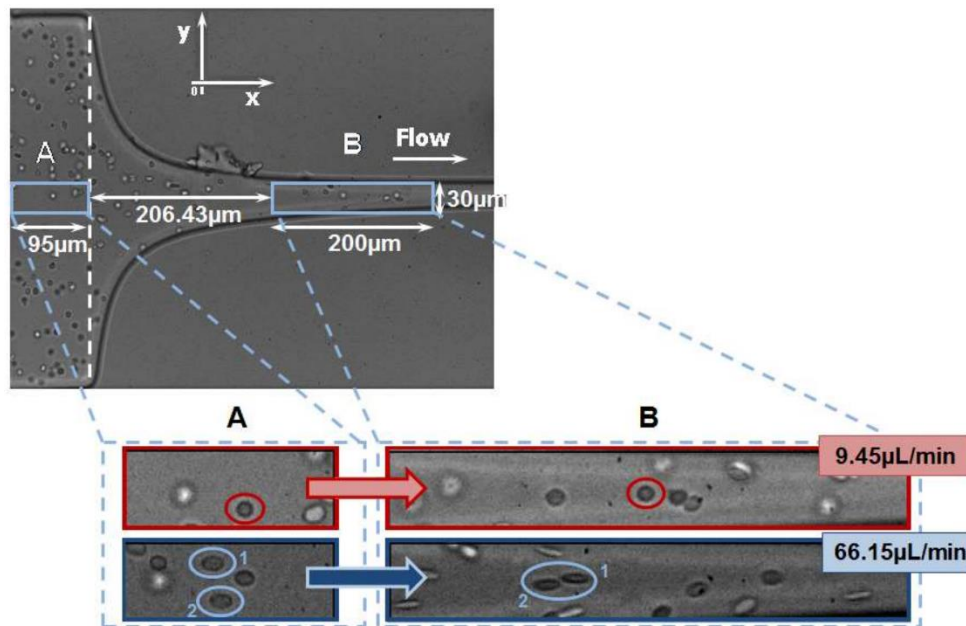
Figure 14. RBC deformability in a hyperbolic converging microchannel at two different regions (A) and (B) and flow rates (9.45 L/min and 66.15 L/min) (adapted from (Yaginuma et al. 2011)).

Figure 15 shows a quantitative description of the degree of deformation of human RBCs under a homogenous extensional flow field. We have measured the DI, as well as the velocity of the RBCs flowing through the expansion and hyperbolic contraction regions, for two different flow rates. For an inlet flow rate of 9.45 μL/min the RBCs do not suffer any significant deformation and the DI values are fairly constant along the full length of the microchannel. However, for a flow rate of 66.15 μL/min it is clear that when the RBCs enter the contraction region, RBCs start to elongate and, consequently, their DI values start to increase until the end of the hyperbolic contraction region. The latter results clearly show that when the RBCs are subjected to strong extensional flows RBCs tend to elongate up to a maximum value. Another interesting result shown in Figure 15b is that when RBCs reach the hyperbolic contraction region their velocities increase almost linearly, which corresponds to a constant strain rate. This phenomenon happens for the both tested flow rates. These *in vitro* blood experiments show the potential of using hyperbolic-shaped microchannels to precisely control and assess changes in RBC deformability in physiological and pathological situations. However, the selection of the geometry and the identification of the most suitable region to evaluate the changes on the RBC deformability under strong extensional flows are crucial and further studies need to be performed in more detail in the near future.
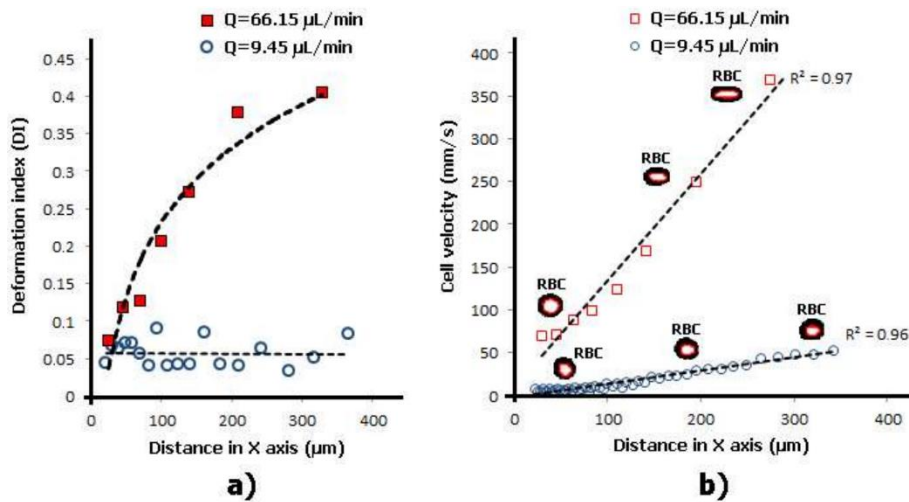
Figure 15. Individual RBCs' (a) DI and (b) velocity flowing through a hyperbolic contraction microchannel for two different flow rates: 9.45 μL/min and 66.15 μL/min.

Lee and his collaborators (2009) have compared the deformability response of the RBCs to simple shear and extensional flows. Their results have shown that extensional flows generate higher RBC deformability than simple shear flows. Recently, Faustino and her colleagues (2014b), (2014a) have performed RBC deformation measurements in a hyperbolic-shaped contraction with a low aspect ratio (AR), where RBCs were submitted to both extensional and shear flow. By comparing the DI results performed by Faustino et al. (2014b), (2014a) with the results obtained with extensional flows (Yaginuma et al. 2011, 2013) it is clear that the combination of both extensional and shear flow promote higher RBC deformability. Although hyperbolic converging microchannels with low AR show the most suitable approach to assess the clinical meaning of RBC deformability, further studies should be performed with different flow rates and microchannel dimensions.

4.2.2 Deformability in Smooth and Sudden Contractions

During the years, a large number of studies on *in vitro* blood rheology and particularly in the deformation of RBCs under a simple shear flow were performed by using rotational rheometers (Kim et al. 2012; Pinho et al. 2016, 2017; Sousa et al. 2016; Muñoz-Sánchez et al. 2016). However, RBCs flowing in microvessels, due to the confined microenvironment, deform not only due to shear effect but also to extensional effect. Hence, from the beginning of the 21st century, and due to the progress in microfabrication (Wong et al. 2012; Zheng et al. 2013; Rodrigues et al. 2015a; Faustino et al. 2016), microflow visualization techniques (Kim and Lee 2006; Lima et al. 2006, 2008b, 2009a, 2012; Vennemann et al. 2006; Williams et al. 2010; Pitts et al. 2012; Garcia et al. 2012; Sackmann et al. 2014; Stauber et al. 2017), and image analysis methods (Kim et al.

40

2006; Pinho et al. 2013a; Chenouard et al. 2014; Taboada et al. 2016; Bento et al. 2018a; Mehri et al. 2018), several microfluidic devices containing microchannels have been proposed to study RBC deformability in environments closer to *in vivo* microcirculation. Most of the proposed microfluidic devices to perform RBC deformability characterization can be classified as fluid-induced deformation microchannels (when the dimensions of the channels used to generate deformability are larger than the tested cells) and as structure-induced deformation microchannels (constriction channels with dimensions similar or smaller than the diameter of tested cells). To the best of our knowledge, the first application of a microfluidic constriction channel to perform RBC deformability measurements was done by Tsukada et al. (2001). In this study they measured RBC deformability of diabetic RBCs flowing through constriction microchannels and they reported that the deformability of diabetic RBCs was lower than healthy RBCs. A few years later, Shelby et al. (2003) used a polydimethylsiloxane constriction microchannel to investigate the deformability changes between malaria infected RBCs and healthy RBCs. As expected, they have confirmed that the deformation of the infected RBCs decreases as the parasite progresses. After these two deformability research studies several microfluidic devices, having constriction microchannels, were proposed to measure the deformation of RBCs (Abkarian et al. 2008; Lee et al. 2009; Forsyth et al. 2011; Tomaiuolo et al. 2011; Pinho et al. 2013b, 2017; Yaginuma et al. 2013; Faustino et al. 2014b; Tomaiuolo 2014; Rodrigues et al. 2016a), white blood cells (WBCs) (Rosenbluth et al. 2008; Gossett et al. 2012; Rodrigues et al. 2015b), and cancer cells (Hou et al. 2009; Guillou et al. 2016). Although, the majority of the proposed microfluidic devices to perform RBC deformability characterization have focused on the strong shear effects created by the walls, these kinds of devices, due to the extremely small dimensions of the microchannels, have several critical difficulties, including fabrication complexity, flow control, and microflow visualizations. One way to overcome such experimental difficulties is by using fluid-induced deformation microfluidic devices. These kinds of devices are easier to fabricate (Faustino et al. 2016) and, most of the time, produce a combination of shear and extensional flows. Some successful examples, by using abrupt or sudden contractions, are the studies performed by Zhao et al. (2006), Forsyth et al. (2010), and Fujiwara et al. (2009). Zeng and Ristenpart (2014) have performed measurements of the RBCs' deformation in a sudden-contraction microchannel and they have reported that under different flow rates, RBC elongation reached a maximum value and could not deform any further. Forsyth et al. (2010), by using a microfluidic constriction channel, have studied the deformability and dynamic behavior of both healthy and hardened RBCs and they have found different types of flow motion

due to the increased shear rate in the constriction microchannel. The effect of RBCs deformability on the cell-free layer (CFL) thickness, by hardening RBCs, was also investigated at an abrupt microfluidic constriction channel by Fujiwara et al. (2009). They have found that the RBC deformability plays an important role on the asymmetry of the CFL thickness and they have reported that the motions of RBCs are strongly affected by the deformability, haematocrit, and the channel geometry. However, abrupt constriction microchannels fail to produce homogeneous extensional flows and, as a result, several researchers have been assessing RBC deformability using hyperbolic converging microchannels (Lee et al. 2009; Yaginuma et al. 2013; Faustino et al. 2014b; Rodrigues et al. 2015b, 2016b, a; Calejo et al. 2015; Pinho et al. 2017). RBC deformability changes in response to shear and extensional flows strongly depend on the geometric configuration and dimensions of the constriction. For instance, the motion and deformation of a RBC passing through a sudden constriction is different from a RBC passing through a smooth or hyperbolic constriction. Pinho et al. (2013b) have developed a partial cell separation microfluidic device, where RBC deformability was assessed in different kinds of constriction channels. Figure 16 shows RBCs flowing through a smooth and a sudden (or abrupt) constriction microchannel.
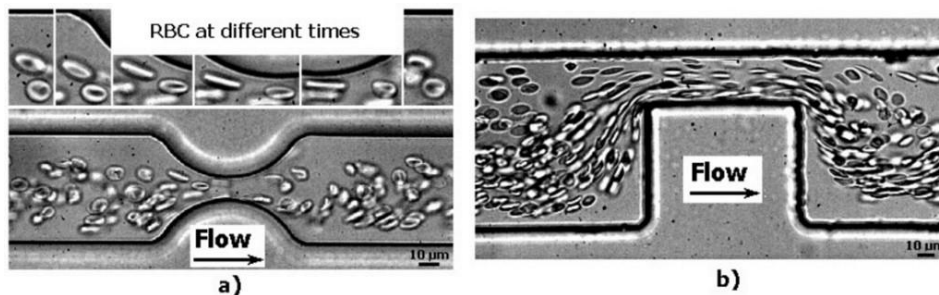
Figure 16. RBCs flowing through a microchannel with (a) a smooth and (b) a sudden (or abrupt) contraction (adapted from (Pinho et al. 2013b)).

In Figure 17 and Figure 18 it is possible to observe the DIs and velocities of two individual RBCs flowing through a smooth and a sudden constriction microchannel, respectively. These results show that for both situations when the RBCs start to enter the constriction region the cells velocities increase and, consequently, they deform up to a maximum value. The measurements performed in a sudden contraction (see Figure 18) show that the RBCs' elongation tends to reach to a maximum value and, afterwards, do not deform any further due to the constant velocity that cells possess when they flow within the contraction. These latter results are in accordance with the findings performed by Zhao et al. (2006). However, recent results performed by Zeng and Ristenpart (2014) have shown that the deformability of the RBCs tend to decrease slightly as they progress within the contraction region. Hence, these contradictory results show that there is a need

for further research in this field. However, it is clear that the RBCs flowing through this kind of contraction are not subjected to constant strain rates. This is in contrast to the flow phenomenon that happens in hyperbolic contractions.
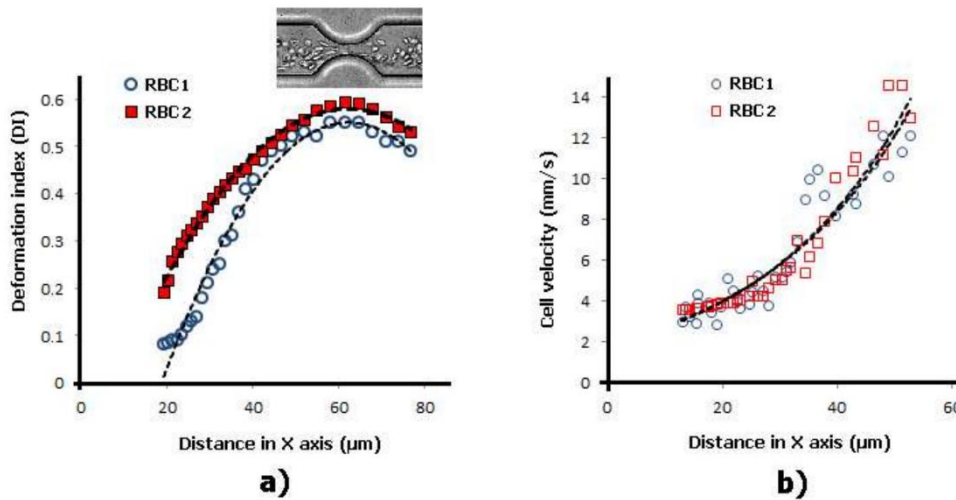
Figure 17. Individual RBCs (a) DI and (b) velocity flowing through a smooth contraction microchannel for the same flow rate. The X axis correspond to the main flow direction.
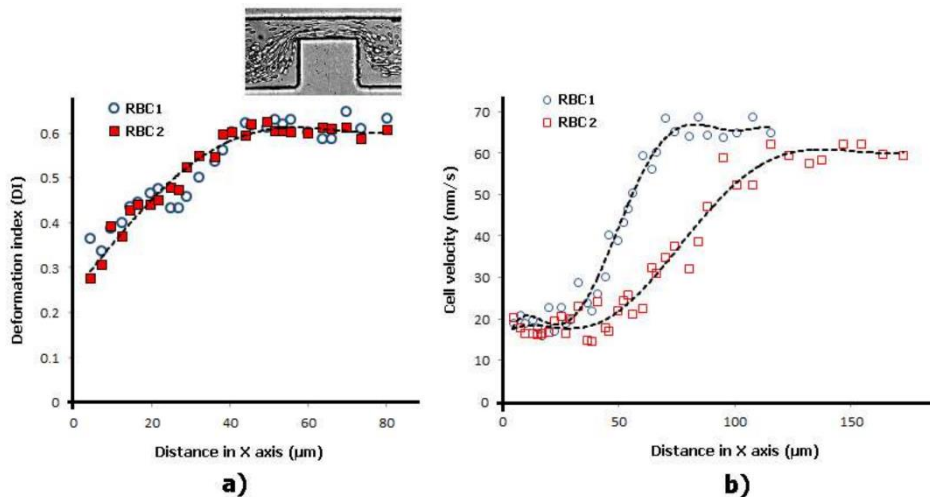
Figure 18. Individual RBCs (a) DI and (b) velocity flowing through a sudden contraction microchannel for the same flow rate. The X axis correspond to the main flow direction.

It is known that RBCs' rigidity has been correlated with malaria, sickle cell disease, diabetes mellitus, and others haematological disorders and diseases that affect RBC deformability (Mokken et al. 1992; Lee and Lim 2007; Kim et al. 2012). Therefore, several flow studies with rigid RBCs (Forsyth et al. 2011; Pinho et al. 2017), or with microparticles that simulate rigid RBCs, have been investigated due to the important role that they play in clarifying the hemodynamic behavior of diseased cells in microcirculation. Pinho et al. (2014) have performed a study in order to clarify the flow behavior of both healthy RBCs and rigid microparticles when subjected to high shear rates. In this study, they have investigated the trajectories and DI in a microchannel with a pronounced

43

microstenosis (75%). By using a microfluidic device fabricated by a soft lithography technique, they have used a solution of Dextran 40 containing a mixture of 0.5% polystyrene (PS) latex microspheres (10 μm), that mimic rigid RBCs (arRBCs) mixed with 1% of healthy ovine RBCs (diameter: ~5 μm). The *in vitro* experiments were performed under different flow rates (1, 10, 20 μL/min) and the DI of both arRBCs and healthy RBCs were measured and compared. More detailed information about the experimental setup can be found elsewhere (Pinho et al. 2014).

In Figure 19 it is shown that, for both RBCs (rigid and healthy), the maximum DI was obtained at the highest flow rate used in this study and within the stenosis region (represented by Section 2, Section 3 and Section 4). As expected, healthy RBCs had higher DIs when compared with rigid microparticles (arRBCs). In addition, it was at the highest flow rate of 20 μL/min that healthy RBCs obtaining a maximum DI of 0.38 in comparison to the 0.09 obtained by the arRBCs. These results are consistent with the ones obtained by Pinho et al. (2013b), where healthy human RBCs were investigated using different kinds of constrictions. Additionally, in this study, they have observed that some of the ovine RBCs have changed their normal shape to a parachute or umbrella shape when passing through the sudden constriction microchannel. In contrast, the rigid microparticles did not exhibit any noteworthy change from their original shape. Note that the measured residual values of the arRBC DIs were mainly due to image distortions of the high-speed microparticles.
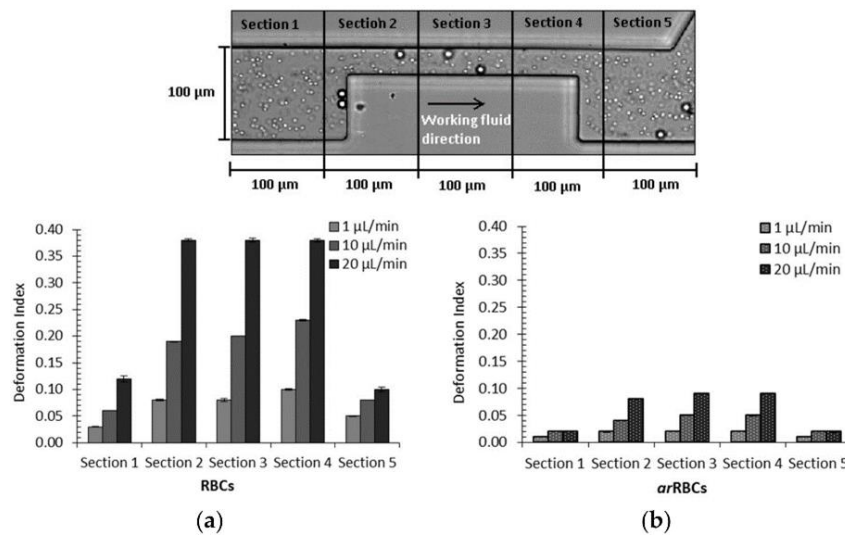
Figure 19. DI measured at five different sections of the stenosed microchannel for different flow rates: (a) healthy ovine RBCs; and (b) particles mimicking rigid RBCs (arRBCs). Error bars represent a 95% confidence interval (adapted from (Pinho et al. 2014)).

4.2.3 Deformability in Rectangular PDMS Microcapillaries and Micropillars

Although it is difficult to fabricate and control the flow in constriction microchannels with dimensions similar to RBC diameters, this kind of geometry is one the most popular ways to measure the deformability of RBCs. As it is possible to observe in Figure 20, RBCs flowing through structure-induced deformation microchannels, the RBCs tend to deform into a parachute shape or umbrella shape. Researchers, such as Tsukada et al. (2001), Jeong et al. (2006), and Tomaiuolo et al. (2011), have calculated the RBCs' deformability by applying the formula L/D, where L and D represent the length and diameter of a deformed RBC, respectively (see Figure 20). Note that, in the present study, this measurement approach is designated as the deformation ratio (DR). By following this approach, we have analyzed and measured the DR of two individual RBCs flowing through a structure-induced deformation microchannel (see Figure 21).
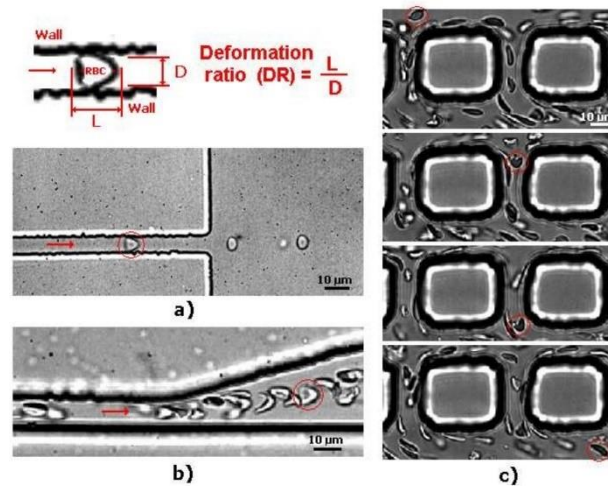
Figure 20. RBCs flowing through (a) rectangular PDMS microcapillary (b) divergent region upstream of a rectangular PDMS microcapillary; and (c) micropillars, adapted from (Rodrigues et al. 2015b).
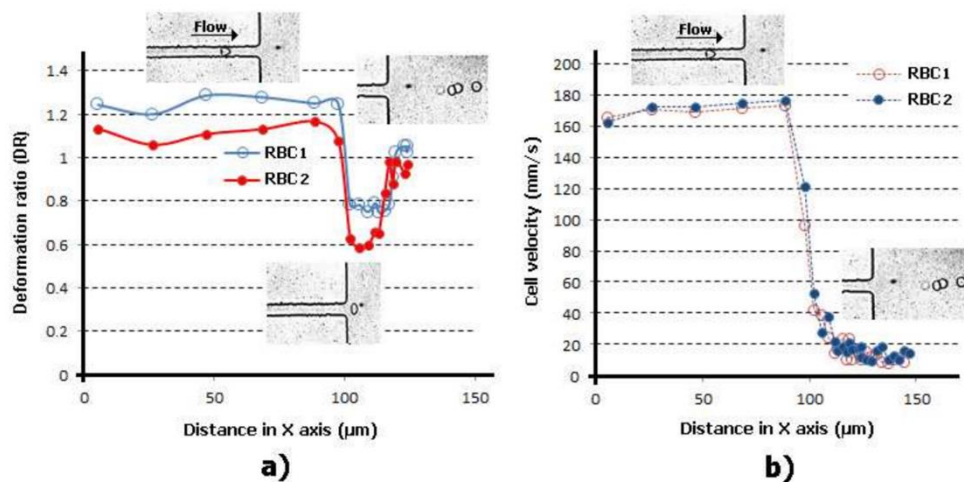
Figure 21. Individual RBCs' (a) DR and (b) velocity flowing through a rectangular PDMS microcapillary for the same flow rate. The X axis corresponds to the main flow direction.
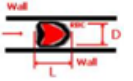
Figure 21 shows the DRs and correspondent velocities of two individual RBCs flowing through a microchannel with dimensions similar to the RBC diameter. The results clearly show an abrupt decrease of both DRs and velocities when the RBCs leave the constriction and enter into an expansion region. It is worth mentioning that as soon as the RBC leaves the constriction region, the RBC changes from a parachute to a nearly circular shape. However, this latter behavior is not always true as it is possible to visualize in Figure 20. In Figure 20a, due to the low local haematocrit and abrupt expansion when the RBC leaves the constriction region, the RBC changes its shape to a circle. In contrast, when the RBC flows within a high local haematocrit and smooth expansion, the RBC tends to keep its parachute shape for a certain period of time. Eventually, when the shear stress induced by the walls decrease the RBC tend to change to a nearly circular shape. Figure 20c shows that, besides the effect of the geometry and local haematocrit, the orientation is also a parameter that plays an important role on the RBC deformability. Although several numerical blood flow studies (YAMAGUCHI et al. 2006; Lima et al. 2009b; Nakamura et al. 2013; Bento et al. 2015; Omori et al. 2015; Gambaruto 2016; Imai et al. 2016; Ye et al. 2016) have been proposed to better understand the RBCs' flow behavior in microchannels and microvessels, our understanding of the RBC motion, orientation, and deformability at the microcirculation level is still far from complete.

4.2.4 Comparison of Cells' Deformability Studies

Table 4 shows a summary comparing the main features of several cells deformability studies performed in microfluidic devices. Representative features for comparison are the microfluidic technique, blood cell types, main flow phenomenon and the used approach to measure the degree of deformability of the cells.

Table 4. Comparison of several cells deformability studies performed in microfluidic devices.

Microfluidic Technique	Cell Types	Main Flow Phenomenon	Approach to Measure the Degree of Deformability	Main Advantages	Main Disadvantages	References
Fluid-induced deformation channel	Human RBCs	Poiseuille flow	Deformation (DI) Index $= \frac{X-Y}{X+Y}$	Homogenous flow; ability to measure large amount of cells in one single run.	The extensional flow is not homogenous; expensive micro-visualization equipment.	(Zhao et al. 2006)
Fluid-induced	Human and rabbit	Extensional flow (hyperbolic channel)	Deformation ratio (DR) $= \frac{L}{D}$	Homogenous extensional flow; high-	Expensive micro-visualization equipment.	(Lee et al. 2009; Yaginuma et

deformation channel	RBCs, WBCs			sensitivity tool; potential to precisely control and detect small deformability changes; ability to measure large amount of cells in one single run.		al. 2011, 2013; Faustino et al. 2014b, a; Rodrigues et al. 2016a; Pinho et al. 2017)
Fluid-induced deformation channel	RBCs and WBCs	Extensional flow (cross slot channel)	Deformation ratio (DR) = $\frac{L}{D}$	Extensional flow; capacity to differentiate healthy and diseased cells; ability to measure large amount of cells in one single run.	Expensive micro-visualization equipment; the numerical models may need to be validated with *in vitro* experiments.	(Gossett et al. 2012; Henon et al. 2014)
Fluid-induced deformation channel	RBCs	Poiseuille flow	Elongation Index (EI1) = $\frac{Length\ (L)}{Initial\ Length\ (L_0)}$	Homogenous flow; ability to measure large amount of cells in one single run.	The extensional flow is not homogenous; expensive micro-visualization equipment.	(Forsyth et al. 2010; Zeng and Ristenpart 2014)
Structure-induced deformation channel	RBCs	Poiseuille flow	Deformation ratio (DR) = $\frac{L}{D}$	Homogenous flow; ability to differentiate healthy and diseased cells.	Complex to control the flow; difficult fabrication; blockage is likely to happen; expensive micro-visualization equipment.	(Tsukada et al. 2001; Tomaiuolo et al. 2011)
Structure-induced deformation channel	Cancer cells	Poiseuille flow	Elongation Index (EI1) = $\frac{Length\ (L)}{Initial\ Length\ (L_0)}$	Homogenous flow; ability to differentiate healthy and diseased cells.	Complex to control the flow; difficult fabrication; blockage is likely to happen; expensive micro-visualization equipment.	(Hou et al. 2009)

Part II

Design and fabrication of microfluidic structures

Chapter 5

Fabrication process

This chapter will describe the main fabrication technique and the different parameters to take into account in order to choose the most efficient geometries to separate and assess the deformability of RBCs.

5.1 Equipment and procedure

The procedure used to fabricate the microfluidic devices was based in previews works (Pinto et al. 2014b; Faustino et al. 2016). However, due to the complexity of the microchannels, it was necessary to optimize the procedure in order to obtain the perfect microfluidic device. Figure 22 shows a schematic diagram of the main steps to produce the SU-8 moulds, that will serve as the mould for the PDMS microfluidic devices.
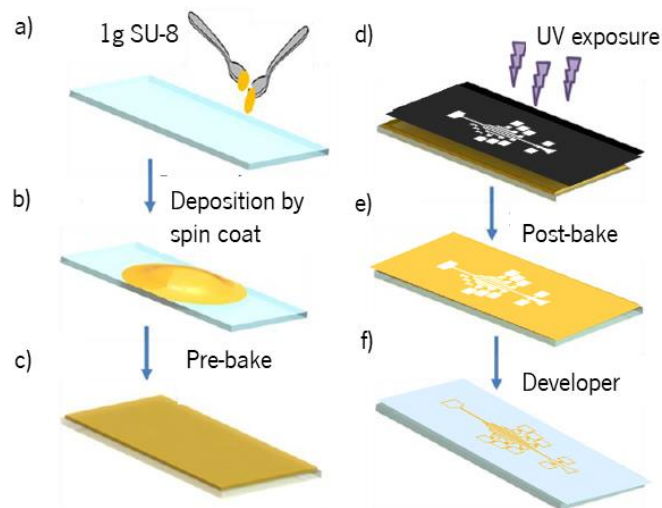
Figure 22. Main steps to produce the SU-8 moulds.

In this procedure it was used a high-resolution film photo mask drawn in a computer design software (Figure 23 a)) and sent to print at Microlitho company located in UK. This mask was used in all the fabrication procedures. After the acquisition of the mask, it was evaluated the most

suitable SU-8 to produce the moulds. As the dimensions and aspect ratio of the structures were small, it was decided to use the SU-8 25 (Microchem Corp., Newton, MA) in order to obtain microfluidic devices with 10 to 50 µm height (Pinto et al. 2014b). The SU-8 was placed in a slide glass (Figure 22 a)), previously clean with isopropyl alcohol (IPA), and then placed in a spin coat (Polos 200, ATP GmbH, Bienenbüttel, Germany). The pre-bake and post-bake were made in a hot plate (Präzitherm type PZ28-2, 1100 W, Harry Gestigkeit GmbH, Düsseldorf, Germany), and for exposure it was used a mask aligner (Karl Suss mask aligner, with a 290-400nm UV lamp) (Figure 23 b)). After all these steps, the structures were revelled by means of a SU-8 developer (Microchem Corp., Newton, MA).

a)

b)
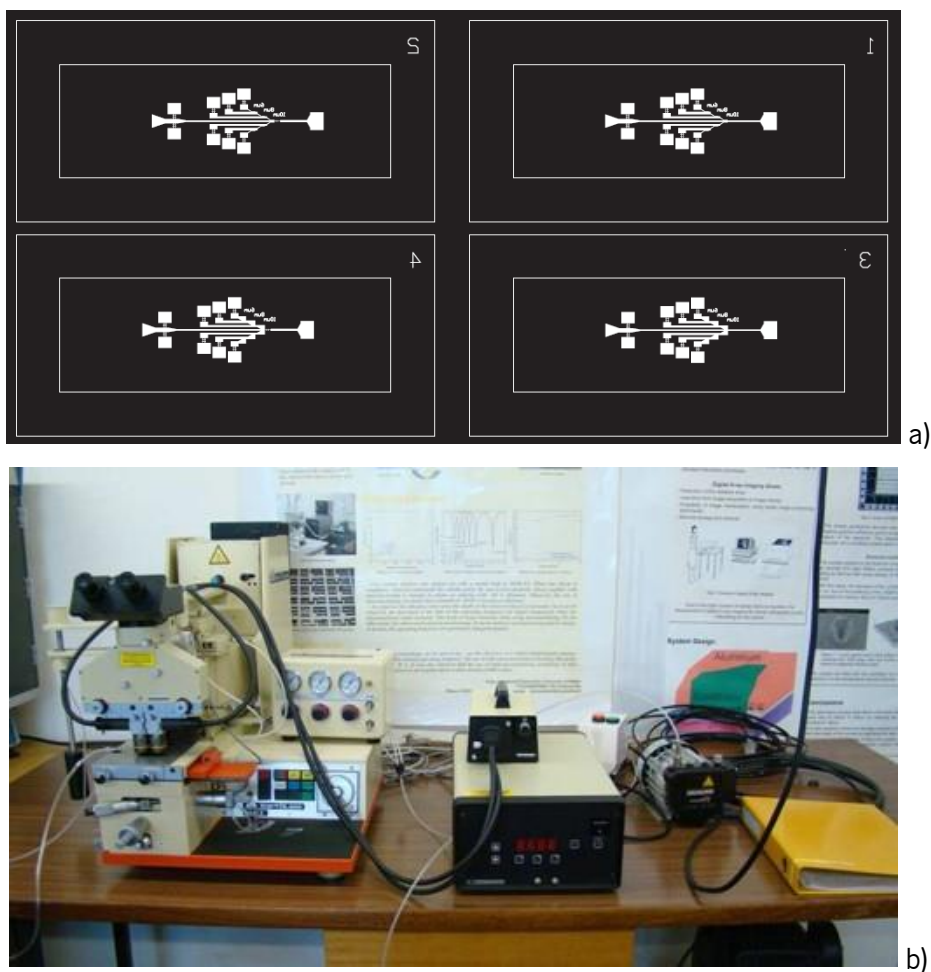
Figure 23. a) Example of CAD Design of microchannels to print the photo mask; b) mask aligner set-up.

The specific parameters used to obtain the microchannels are presented in Table 5. It was used a profilometer (Veeco Dektak 150) to measure the height of the microchannels and a Microscope (Leica) to analyse the smaller structures of the microchannels.

Table 5. Parameters used in microfabrication procedure and their results

Spin coat (rpm, s)	Pre-bake (°C, min)	Exposure (s)	Post bake (°C, min)	Developer (min)	Room Temp. (°C)	Height (µm)	observations
1st 500, 5 2nd 3000, 30	65, 10 95, 15	30	65, 5 95, 6	3	23	13	Not good definition of pillars
1st 500, 5 2nd 2000, 30	65, 10 95, 15	30	65, 5 95, 6	3	23	19	Not good definition of pillars
1st 500, 5 2nd 2000, 30	65, 10 95, 15	40	65, 5 95, 6	3	20	29	Not good definition of pillars
1st 500, 5 2nd 2000, 30	65, 10 95, 15	45	65, 5 95, 6	2	22	24	Perfect
1st 500, 5 2nd 1800, 30	65, 10 95, 15	50	65, 5 95, 6	2	23	30	Not good definition of pillars
1st 500, 5 2nd 1900, 30	65, 10 95, 15	60	65, 5 95, 6	2	23	30	Perfect
1st 500, 5 2nd 1000, 20	65, 5 95, 20	30	65, 3 95, 6	3	23	52	Not good definition of pillars and hyperbolic
1st 500, 5 2nd 1000, 20	65, 5 95, 20	40	65, 3 95, 6	3	23	55	Not good definition of pillars and hyperbolic

After some attempts it was found the most suitable parameters to obtain the microchannels with good enough definition at the smaller parts. Initially, it was planned the lowest height possible, between 10 and 20 µm. In Table 5 it corresponds to the lines with light blue. Due to the purpose of microchannels, that was measure separation and also deformability, and considering too, the average size of RBCs is 8 µm. However, the best structure obtained was 24 µm, which lead us to optimize the heigh to 30 µm, which corresponds in the Table 5 to darker blue. The most suitable were the ones with a height of 30 µm height.

The SU-8 moulds were replicated by using the soft-lithography method, by following the procedure already reported in previews research works (Pinto et al. 2014b; Faustino et al. 2016). Generally, it was used PDMS, in a 10:1 ratio, and it was cured at 80 °C, for 20 minutes. By using microfluidic punchers (Darwin microfluidics, Paris, France), it was made the connecting holes at the microdevices and then PDMS replicas were adhered to a slide glass by means of an oxygen plasma (Plasma Systems ZEPTO, Diener electronic). After this procedure, the biomedical microdevices were ready to be used to perform experimental biomicrofluidic tests.

More detailed information about the dimensions and design can be find in Chapter 6.

Chapter 6

Geometry effect in multi-step crossflow microfluidic devices for red blood cells separation and deformability assessment[3]

6.1 Introduction

The global interest in microfluidics has been increasing, in the last decades, due to its multidisciplinary and versatility in multiple applications, such as in biomedical, mechanical, electronics, chemical analysis, nanotechnology and nanomedicine (Rodrigues et al. 2016a, 2020; Bento et al. 2019; Catarino et al. 2019; Zhu et al. 2019; Kung et al. 2020; Gonçalves et al. 2021; Sadek et al. 2021). Regarding biomedical applications, microfluidics have gained a special interest due to the possibility of, in a single chip, integrate different functionalities for the detection of molecules, cells and, ultimately, different types of blood diseases (Bento et al. 2018b; Nasiri et al. 2020).

A typical lab-on-chip device for blood analysis includes various functional modules, such as sample transport and preparation, filtration, separation, detection and analysis. In particular, the separation and analysis of blood cells are two extremely important modules of such devices. For blood analysis, the blood samples need, in a first step, to be filtrated, through the separation of the cells from the plasma and, in a second stage, those cells need to be carefully analyzed, by means of either biosensors or image analysis techniques, to help diagnosis (Sajeesh and Sen 2014; Catarino et al. 2019; Carvalho et al. 2021).

In such systems, regarding the separation of cells from plasma, microfluidic devices are gaining popularity as a tool to accomplish that purpose, due to several well-known advantages, including the need for small volumes of samples, portability and ability to perform multiple and

parallel features (Tripathi et al. 2015b). Blood plasma separation can be accomplished by active or passive microfluidic methods (Sajeesh and Sen 2014; Yan et al. 2017; Karimi et al. 2021; Liu et al. 2021). The active methods include the application of external forces to increase the separation efficiency, such as acoustic, magnetic, dielectrophoretic stimuli or the combination of them (Dalili et al. 2019). On the other hand, passive separation methods do not require external forces, and their performance is mainly promoted by geometrical effects and nonlinear hydrodynamic forces in the microstructures (Karimi et al. 2013; Catarino et al. 2019). Thus, these latter methods are much simpler and have lower fabrication costs, enhancing the continuous gaining interest of these microfluidic technologies in the blood-on-a-chip and biomicrofluidics research fields. There are several approaches to perform the passive separation of red blood cells (RBCs), plasma or white blood cells (WBCs), as well as their sorting. These techniques include micro-trench (Dimov et al. 2011), deterministic lateral displacement (DLD) structures (Davis et al. 2006), curved series of microchannels (Tripathi et al. 2016), microchannels geometric constrictions (Faivre et al. 2006; Sollier et al. 2010; Pinho et al. 2013b; Yaginuma et al. 2013; Lopes et al. 2015b; Rodrigues et al. 2015b, 2016b; Rubio et al. 2019), laminar micro-vortices (Sollier et al. 2010) and the bifurcation law phenomenon (Yang et al. 2006b; Ishikawa et al. 2011; Leble et al. 2011; Bento et al. 2019). Recently, Trypathi et al. (2016) have studied both biophysical and geometrical effects and proposed a hydrodynamic microfluidic device to obtain plasma separation from whole blood. More recently, Karimi et al. (2021) have applied geometrical effects (pillars) to improve the blood cells separation. However, although this method is simple, the use of physical filtration microstructures promotes the appearance of clogging and jamming problems within the microfluidic device (Alvankarian et al. 2013; Catarino et al. 2019). One simple way to minimize such problems is by using crossflow filters (Lee and Clark 1998; Keskinler et al. 2004; Chen et al. 2008; Tsutsui et al. 2009), which force the fluid to flow tangentially, in contrast with the classical filtration approaches, where the fluid flows through the filter.

Besides cells' separation, the assessment of the cells mechanical features has an important role in diagnostics. Blood related diseases, such as malaria, sickle cell disease, and diabetes, can affect the RBCs membrane and, as a result, contribute to different levels of stiffness of the RBCs membrane and lead to changes in the cells' rigidity and deformability (Bento et al. 2018b; Boas et al. 2018a). These different levels of stiffness can be potentially detected by microfluidic devices with multiple sequential steps, which would allow to separate blood plasma and cells, with different mechanical stiffness. For instance, in the presence of a micropillar array

structure, a healthy and deformable cell has the tendency to pass throughout the smaller micropillars, whereas the rigid cells have more tendency to flow through larger microchannel branches, where the flow resistance will be lower and the velocities higher (Faustino et al. 2018).

In this study, by using a soft lithography technique, it is proposed the design and fabrication of three different multi-step microfluidic devices, based on crossflow filtration. For the three approached geometries, it will be analyzed not only the separation efficiency but also the RBC velocities and cell-free layer (CFL). The selected geometries have small differences between their dimensions, in order to evaluate the most suitable geometry to simultaneously perform the RBCs separation and deformability assessment. The authors have been working on the field for a few years, and have, previously, developed different microfluidic structures for cells separation (Rodrigues et al. 2015b; Faustino et al. 2018). Thus, the main novelty of this work is the analysis of the effect of the downstream structural design of crossflow filters. In particular, in this work, we have designed different configurations of the downstream region, with different areas and aperture angles, as well as several other geometrical features, and compared them regarding their separation efficiency. To the best of our knowledge, this is the first reported work that shows how to optimize a multi-step microfluidic device, based on crossflow filtration, and with the purpose of simultaneously performing blood plasma separation and RBCs deformability assessment based on CFL and optical absorbance measurement.

The article is organized as follow: The Materials and Methods section presents the geometry and main dimensions of the proposed multi-step crossflow microfluidic devices, as well as the details of the blood samples preparation, experimental set-up and image analysis. The following section (Results and Discussion) presents the main results regarding the separation efficiency of the microfluidic devices, as well as the discussion aiming the selection of the most suitable geometry to perform the deformability measurements of individual RBCs. In the last section (Conclusion and Future Perspectives), the most relevant findings achieved from this study are presented, and some topics discussed for further developments.

6.2 Materials and methods

This section presents the geometry description, experimental setup and materials used in the procedures for evaluating the RBCs separation and deformability.

6.2.1 Microchannels geometry and experimental set-up

The microchannels were fabricated in polydimethylsiloxane (PDMS) (Sylgard® 184 Silicone Elastomer, from Dow Corning) at the CMEMS Research Unit (University of Minho), using a soft lithography technique with SU-8 moulds (Pinto et al. 2014b; Rodrigues et al. 2015b; Faustino et al. 2016). Three different geometries were proposed, where the main geometry was similar to all. In general, the devices have a main channel with symmetrical crossflow filters with multiple rows of ten pillars (see Figure 24). All the proposed devices have three step stages, with sequential crossflow filters, in order to reduce the amount of RBCs flowing to each of the outlets located at the sides of the microchannel (outlets O1, O2, O3, O7, O8 and O9). The aim of this sequential separation is not to perform a complete separation of the RBCs from the plasma, but rather a partial RBCs separation, to reduce the number of cells and allow to assess their deformability at a set of hyperbolic constrictions located at the upstream part of the outlets (see Figure 24).
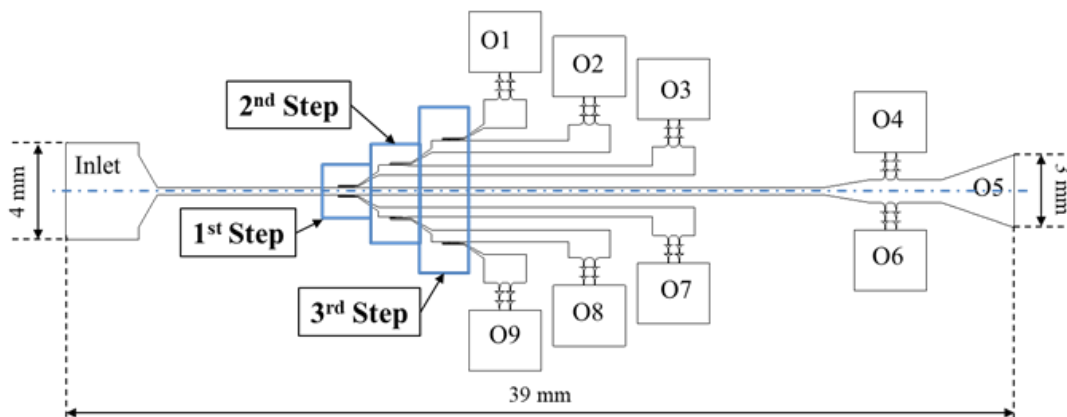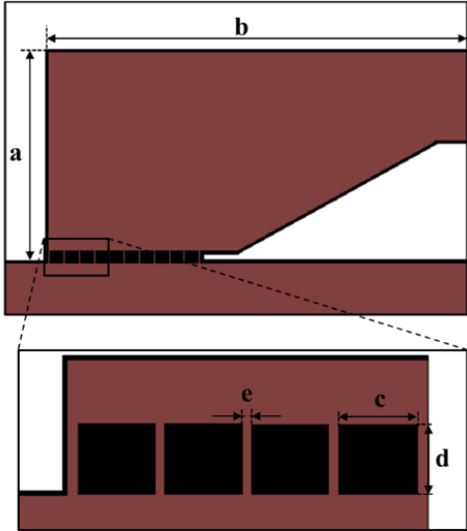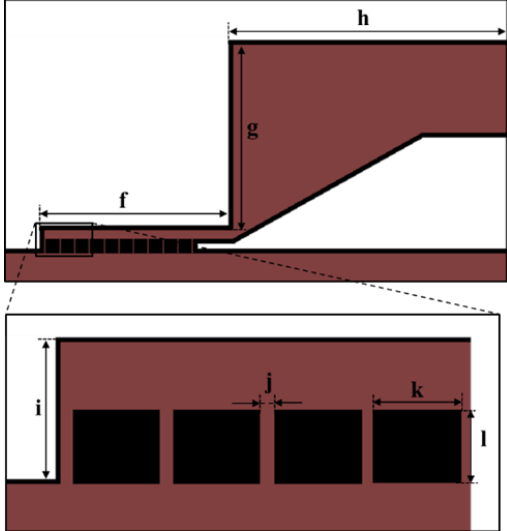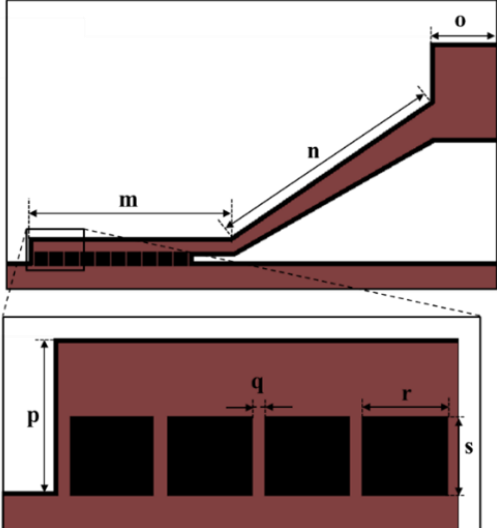
Figure 24. Overall view of the proposed multi-step microfluidic device for cell separation and deformability assessment. The microfluidic device has one inlet and 9 outlets (O1 – O9).

The main difference between the three proposed geometries is mainly related to the downstream structural design of crossflow filters. These differences and the main dimensions of each microfluidic device (MD) are represented in Table 6.

The three microfluidic devices have a total length of 39 mm, one inlet, three levels of pillars (steps 1, 2 and 3) and nine outlets (O1 to O9). At each outlet upstream, there are hyperbolic constrictions that will further allow the measurement of the RBCs deformability. Note that, at the first step, all devices have crossflow filters with a gap of 10 µm between pillars, whereas the second step has a gap of 8 µm and, finally, the third step has a gap of 6 µm between pillars.

Table 6. Design and main dimensions of the three multi-step microfluidic devices (MD) tested in this study.

Microfluidic Device (MD 1)	Dimensions		
	Step 1	a = 920 µm b = 1020 µm c = 55 µm	d = 50 µm e = 10 µm
	Step 2	a = 1020 µm b = 2166 µm c = 55 µm	d = 50 µm e = 8 µm
	Step 3	a = 1020 µm b = 2165 µm c = 55 µm	d = 50 µm e = 6 µm
Microfluidic Device (MD 2)			
	Step 1	f = 830 µm g = 819 µm h = 1335 µm i = 100 µm	j = 10 µm k = 55 µm l = 50 µm
	Step 2	f = 855 µm g = 920 µm h = 1310 µm i = 100 µm	j = 8 µm k = 55 µm l = 50 µm
	Step 3	f = 880 µm g = 920 µm h = 838 µm i = 100 µm	j = 6 µm k = 55 µm l = 50 µm
Microfluidic Device (MD 3)			
	Step 1	m = 830 µm n = 1030 µm o = 482 µm p = 100 µm	q = 10 µm r = 55 µm s = 50 µm
	Step 2	m = 848 µm n = 1030 µm o = 464 µm p = 100 µm	q = 8 µm r = 55 µm s = 50 µm
	Step 3	m = 866 µm n = 1030 µm o = 400 µm p = 100 µm	q = 6 µm r = 55 µm s = 50 µm

Hyperbolic Constrictions (similar to all MDs)	
	t = 2500 μm u = 3000 μm v = 318.8 μm x = 19.9 μm

For the experimental assays, the high-speed video microscopy system used in the present study consisted of an inverted microscope (IX71; Olympus Corporation, Tokyo, Japan) combined with a high-speed camera (Fastcam SA3, Photron, Motion Engineering Company, Westfield, IN, USA), as shown in Figure 25. Each PDMS microchannel was positioned and fixed in the microscope plate and the flow rate of the working fluids was kept constant at 50 μL/min using a syringe pump (KD Scientific Inc., Holliston, MA, USA), with a 5 mL syringe (CETONI GmbH, Korbussen, Germany). At the same time, the images of the flowing cells at the established flow rate were captured by the high-speed camera with an 10x objective lens, at a frame rate of 2000 frames/s and a shutter speed ratio of 1/60000, which minimized the dragging of the cells at the high flow rate in study. All the experimental assays were performed at room temperature (T= 22 ± 1°C).
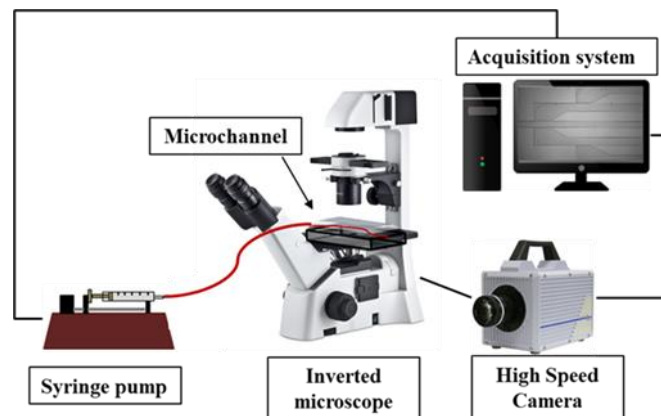
Figure 25. Schematic representation of the experimental setup, comprising a high-speed camera, inverted microscope, syringe pump system and acquisition system.

6.2.2 Working Fluids

Human blood of a healthy donor was collected into 2.7 mL tubes (S-Monovette®, Sarstedt) containing ethylenediaminetetraacetic acid (EDTA). All procedures for the collection of blood and

for the *in vitro* blood experiments were carried out in compliance with the EU directives 2004/23/CE, 2006/17/CE. The whole blood was centrifuged at 1500 rpm for 20 min at room temperature. Plasma and the buffy coat were removed and the RBCs were re-suspended and washed once in physiological salt solution (PSS) (from Braun Medical, Melsungen, Germany) with 0.9% NaCL. The working fluid used was a Dextran 40 (Dx40) (Sigma-Aldrich, USA) solution containing 2% Hct (Hematocrit). Each outlet of the microchannel device was connected to an Eppendorf tube for collection of the samples. After the separation steps, in the microfluidic device, were concluded, and in order to assure equal conditions for each optical assay, it was collected the same volume from each Eppendorf tube (50 μL) and diluted with Dx40 (3 mL) to be analyzed in the spectrophotometry equipment.

6.2.3 Image analysis

The recorded videos were converted to a sequence of 500 frames and analyzed using an image handling software ImageJ (1.46r, NIH, USA) (Rasband 1997). Then, the same post-processing was applied to all the images.

First, to visualize the cell-free layer (CFL), intensity level distinction was used to identify the CFLs since it is relatively clear that RBCs are represented as dark (low intensity) spherical shapes against bright (high intensity) background in the images. Therefore, the minimum intensity level was selected from all the images at each pixel position and only one image replaced with these minimum intensity values was created by means of "Z Project" function in ImageJ, as shown in Figure 26a). After this process, the obtained grayscale images were converted to binary frames (black and white), in order to improve the visualization and definition of, not only the CFL (white pixels), but also the walls and the flowing RBCs (black pixels), as exemplified in Figure 26b). More details about this image analysis method can be found elsewhere (Pinho et al. 2017; Faustino et al. 2019).

To determine the RBCs velocities, it was used a manual tracking plugin available at ImageJ – MtrackJ (Meijering et al. 2006), to track individual RBCs in order to determine their average velocities for each region of interest (ROI). In Figure 26c), it is shown the ROI (A, A1, A2 and A3) at the first crossflow filter, i.e, at the first separation step of the MD. For the second and third separation steps, the ROI were similar to the first step ones, but here identified as B, B1 and B2 and C, C1 and C2, respectively, as seen in Figure 26d). The ROI was selected at the center of the main channel. In particular, for section A, B and C, the ROI has an area of around 50 μm × 100

μm (upstream the pillars), for section A1 and A2 is about 330 μm × 100 μm, for section B1 and C1 is 660 μm × 100 μm, and for section A3, B2 and C2 is 100 μm × 100 μm (downstream the pillars).
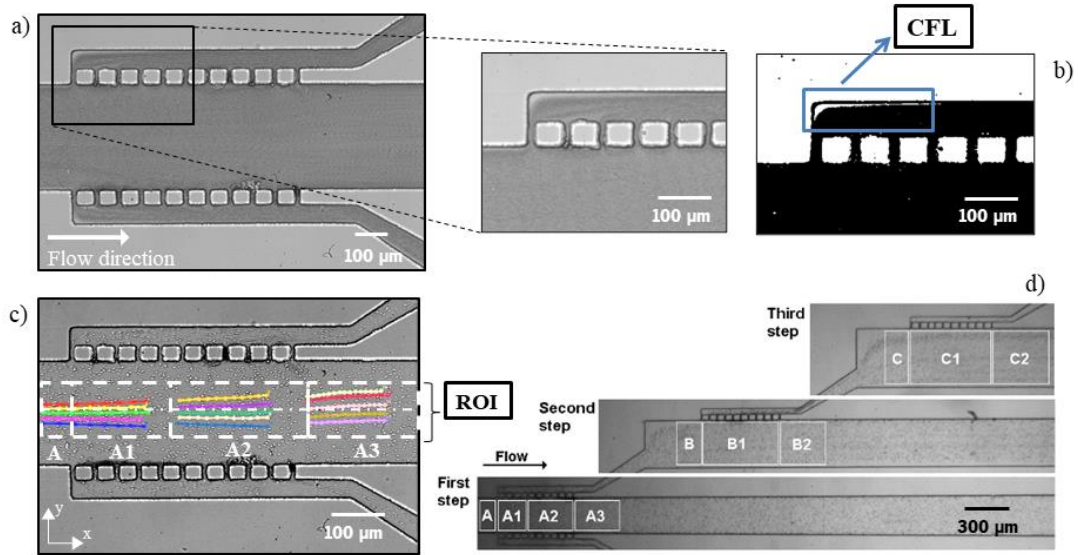
Figure 26. Image analysis and tracking process: a) image stack with minimum intensity; b) CFL binary image; c) tracking of individual RBCs to calculate their average velocities; d) Regions of interest (ROI) locations for each separation step.

Figure 27 presents the original image of each microfluidic device at the third step separation level (Figure 27a), b) and c)), its correspondent stack image (Figure 27d), e) and f)) and the resultant binary image (Figure 27g), h) and i)).
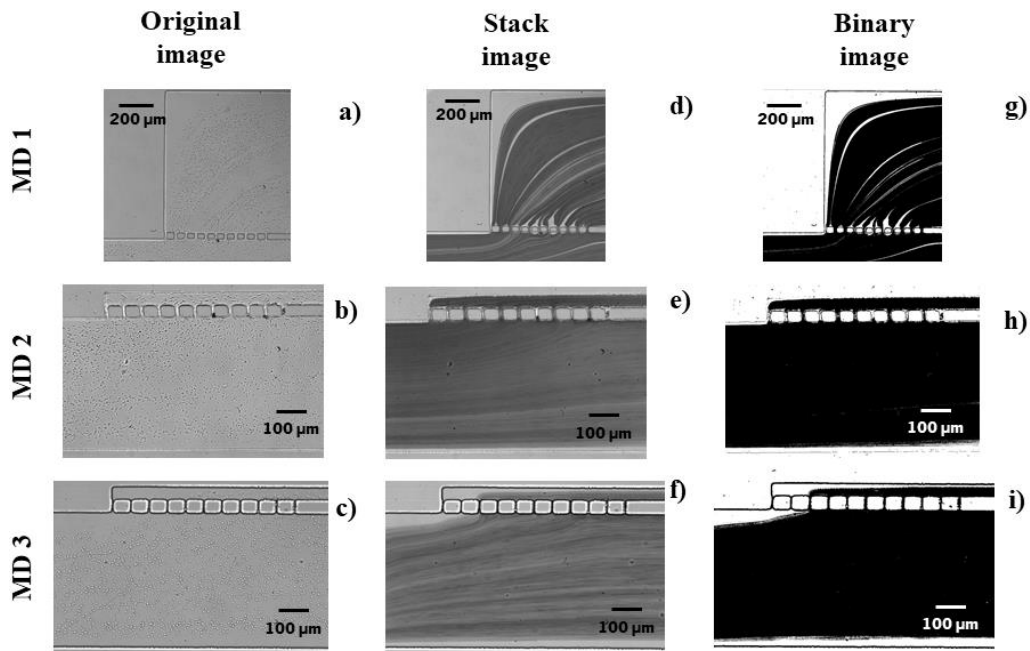
Figure 27. Microfluidic devices MD 1, MD 2 and MD 3 at the third step separation level. a), b) and c) original images; d), e) and f) stack images; and g), h) and i) binary images.

By using the ImageJ, we have also performed several steps of pre-processing and image segmentation to obtain a well-defined color binary cell shape, in order to measure the major (X) and minor (Y) axis lengths of each individual cell. After measuring both major and minor lengths of the cells, their deformation indexes (DIs) were calculated using the equation DI = (X-Y)/(X+Y). Note that, the DI will present values between 1 and 0, where 0 means a perfect circle and higher values correspond to a more deformed shape. In this work, a sample of 20 cells was evaluated to calculate the mean DI. More detailed information can be found in Faustino et al. (2014b).

6.2.4 Spectrophotometric setup and data analysis

For quantifying the separation efficiency, it was considered a spectrophotometry setup that consisted on an Oriel/Newport 68931 power supply, a model 487 picoammeter/voltage source from Keithley, an ultraviolet (UV) light source, an Oriel Newport (model 74125) monochromator, an optical fiber and a photodetector. The photodetector converts the light that passes through a sample (in a 1 cm optical path quartz cuvette) into electric current. That current is measured by the picoammeter, and then exported to a computer using a data acquisition customized application developed in LabView software. The transmittance ($T = I/I_0$) was then used to calculate the optical absorbance: $A = -\log_{10}(T)$, where A is the absorbance, I the intensity of light transmitted through the sample and I_0 the intensity of the incident light. As the optical absorbance of the sample is directly proportional to the Hct, the separation efficiency was estimated by calculating the Hct at each outlet, based on the absorbance values at 450 nm.

6.3 Results and discussion

Figure 28 shows the binary images of all the microfluidic devices (MD 1, MD 2 and MD 3) in each step showing, qualitatively, the CFL throughout all the three steps. In this way, it is possible the comparison between the sequential separation steps and the different microfluidic devices geometry.
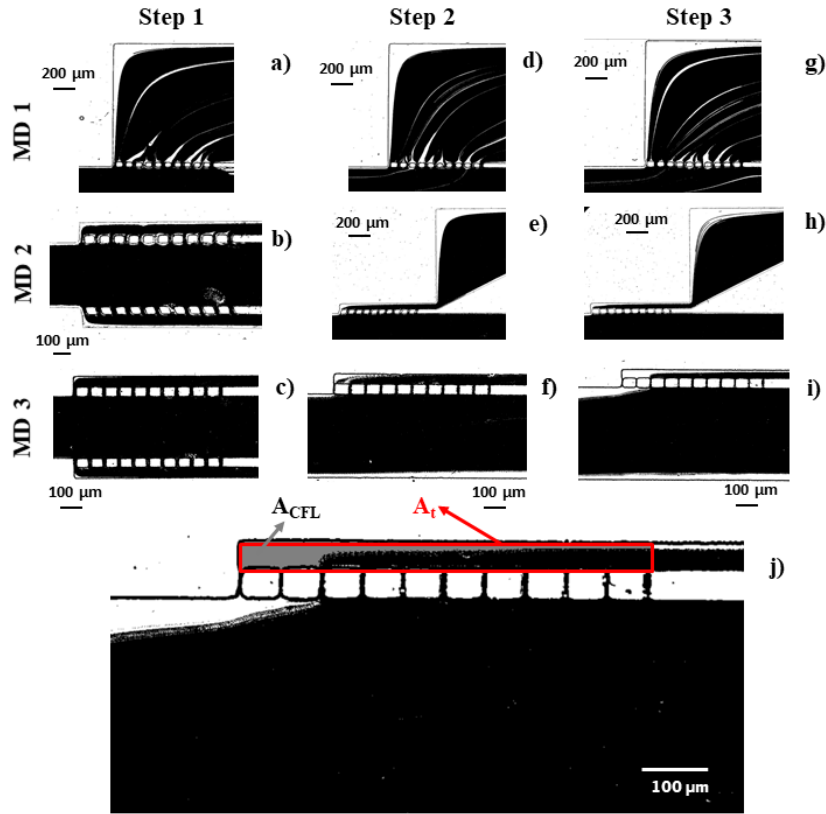
Figure 28. Binary images of CFL in MD 1, MD 2 and MD 3; a), b) and c) step 1; d), e) and f) step 2; and g), h) and i) step 3; j) Representation of total area – At (red square) and CFL area – ACFL (light gray color).

Since the microfluidic devices have different structural geometries, it was necessary, besides the qualitative data, already presented in Figure 28, to quantify the CFL. Several authors have studied the CFL separation efficiency, and they have obtained high CFL values at the downstream region, when they have applied a contraction (Faivre et al. 2006; Yaginuma et al. 2013; Rodrigues et al. 2016b; Pinho et al. 2017, 2019). Generally, the quantification of the CFL area corresponds to a layer depleted of cells that can be directly correlated with the separation of cells from plasma. In this study, this quantification was performed by means of image analysis and by measuring the CFL area obtained from recorded images (Figure 28. Binary images of CFL in MD 1, MD 2 and MD 3; a), b) and c) step 1; d), e) and f) step 2; and g), h) and i) step 3; j) Representation of total area – At (red square) and CFL area – ACFL (light gray color).Figure 28, A_{CFL}). The definition of the CFL aspect ratio (CFL_{AR}) was based on the CFL area located at the downstream part of the crossflow filters, and given as $CFL_{AR} = A_{CFL}/A_t$, where At is the total area and A_{CFL} is the CFL area, both located at the downstream part of the filters, as represented in Figure 28j). By using the CFL_{AR}, comparisons between the developed MD´s can be made.

Figure 29 represents the CFL_{AR} of all the microfluidic devices, in each step, as well as the total CFL_{AR} of each MD, representing the cumulative effect of all the separation stages.
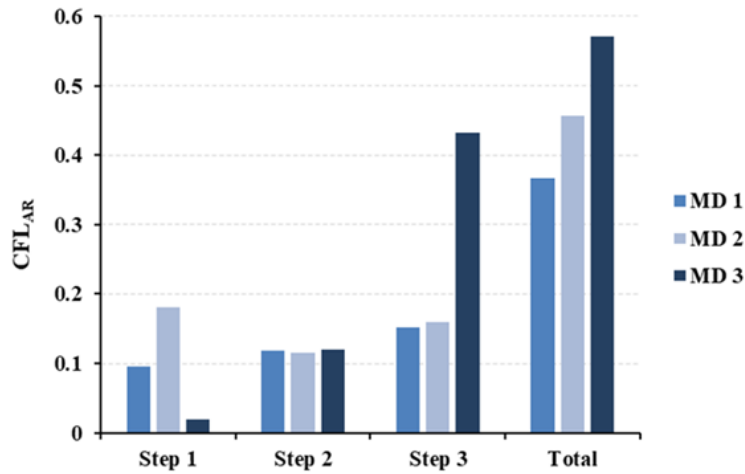
Figure 29. CFL aspect ratio for step 1, 2 and 3, and total CFL for each microfluidic device (MD 1, MD 2 and MD 3).

The results, from Figure 29, show that MD 3 presents the highest CLF area and, consequently, the highest separation of RBCs at the cumulative end of the three separation steps (column "total"). In addition, it also possible to observe that MD 1, MD 2 and MD 3 have an increase of CFL_{AR} with the increment of separation steps. Note that, MD 3 presents a high CFL_{AR} (about 0.58) and consequently corresponding to a high CFL area, i. e., MD 3 has less RBCs flowing into the correspondent outlets and as result MD 3 is the most appropriate device to assess the RBCs deformation index.

The velocities were obtained by tracking individual RBCs flowing within the microchannels, upstream the crossflow filters (see Figure 30). After determining the instantaneous velocities of the RBCs, the average velocities of RBCs were obtained at each ROI. It is relevant to note that all the selected RBCs were flowing at the center of the main microchannels, where the RBCs have the highest velocities.

Globally, from Figure 30, it can be observed that the highest velocities are located at the main channel, upstream of the first step. As the RBCs flow through this main channel, the velocities tend to decrease, reaching the lowest values at the region A3. It is interesting to observe that the MD 1 has the lowest average velocity at A3, due to a decrease of the local flow rate. After passing the crossflow filters (steps 1, 2 and 3), the RBCs velocities at all MD have tendency to decrease mainly due to the hydrodynamic resistance and bifurcation law. It is worth mentioning that the average velocities shown in Figure 30, correspond to only one side of the microchannels. This way, the initial flow rate entering the main branch is the highest. At the main branch the flow is divided

in two daughter channels and, as a result, the average velocity will be lower in step 1 and 2 when compared with the main branch, as shown in Figure 30. It is relevant to note that the average velocities of MD 3 have a smoother behavior, when compared with the other devices and, as a result, MD 3 is expected to be the most stable device to perform the blood flow experiments.
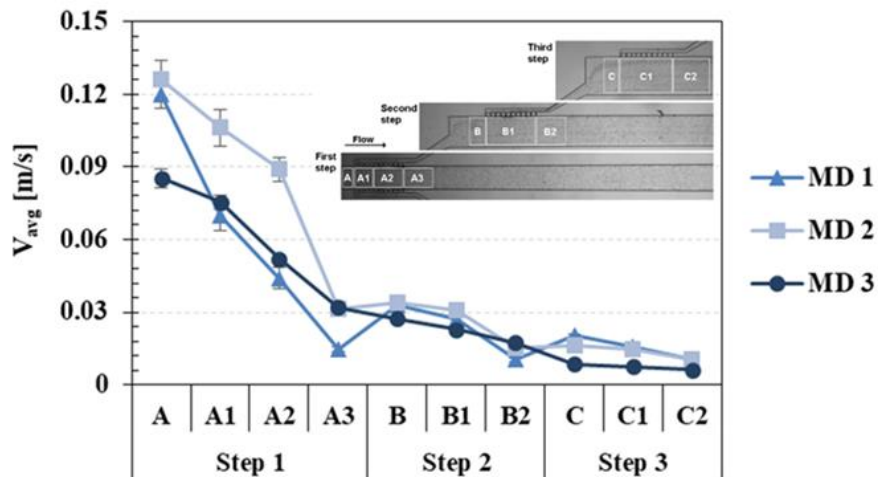
Figure 30. Average velocities along the steps 1, 2 and 3, with respective standard deviations (SD) for the microfluidic devices MD1, MD2 and MD3.

Along the years, several research works have measured the blood cells deformability by using hematocrit values lower than 1% (Bento et al. 2018b; Faustino et al. 2019). In this study, one of the main goals was to select the most suitable device to perform, simultaneously, both the RBCs separation and deformability assessment, for inlet hematocrit higher than 1%. The results from Figure 31 reinforce the data obtained from Figure 28 (CFL). In Figure 31 it is possible to observe the amount of RBCs flowing through the hyperbolic constrictions located upstream the outlet O1. It is clearly observed that the separation achieved by the device MD 1 is not enough to perform cell deformability measurements, as the amount of cells flowing through the hyperbolic constriction is too high to perform accurate cell visualizations (Yaginuma et al. 2013; Faustino et al. 2014b). By using the devices MD 2 and MD 3, the number of cells flowing through the hyperbolic constrictions is much lower, when compared to the MD 1. Nevertheless, from this qualitative result, the device MD 3 is the most suitable to perform both RBCs partial separation and deformability assessment, as it was extremely rare to observe interactions between the RBCs and RBCs flowing next to each other. Note that, to perform accurate cell deformability measurements, it is crucial to avoid nearby cells and interactions between them. Thus, the cells' DI was measured in the smallest part of the hyperbolic contractions (represented by dashed rectangles in Figure 31), as this section corresponds to the highest strain rates and DI values. Hence, for all the tested devices, the DI

results obtained at this section are similar and in good agreement with the works performed by Faustino et al. (2014b) and Carvalho et. al. (2018). The deformability values obtained at the MD 1 corresponds to the smaller DI of 0.71, followed by MD 2 with 0.73 and MD 3 with 0.75.

DI = 0.71 ± 0.03   DI = 0.73 ± 0.07   DI = 0.75 ± 0.06
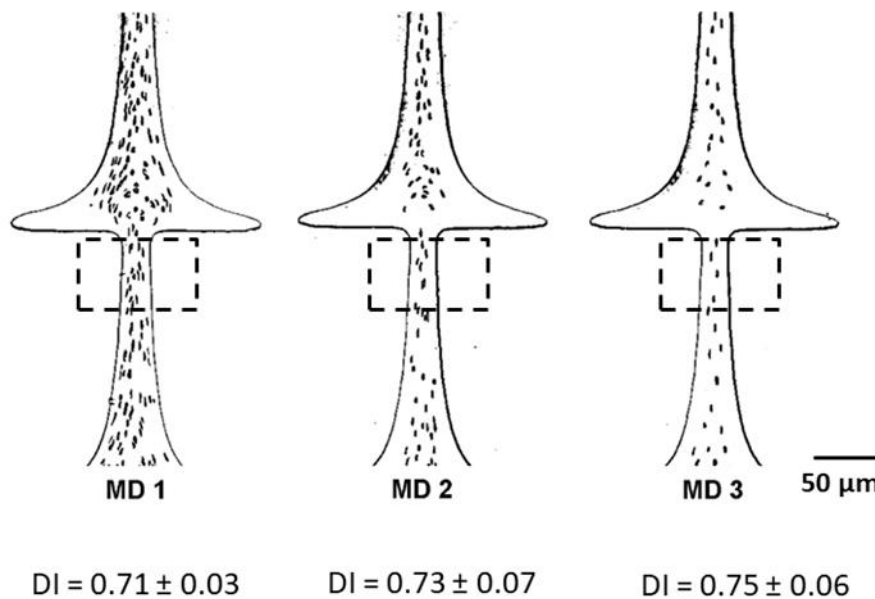
Figure 31. RBCs flowing through the hyperbolic constrictions located upstream the outlet O1 for the microfluidic devices MD 1, MD 2 and MD 3, and respective mean and standard deviation DI values (n = 20).

To quantify the RBCs presented at the outlets of the microfluidic devices, several RBCs samples, collected from the inlet and from all the outlets were measured. As all microfluidic devices have symmetric geometries, the results from the outlets were combined, so it is expected that a sample collected at O1 is equal to O9, O2 is equal to O8, and O3 is equal to O7. The O4 and O6 were not considered because there was not any fluidic sample to collect, so just O5 was considered.

The samples, which were collected into Eppendorfs, were then optically characterized. A 50 µL sample volume was used to measure the optical absorbance, as previously described in the Materials and Methods section. From the spectral curves, it was selected the wavelength of 450 nm (which is one of the highest absorption blood peak (Silva et al. 2017)), to quantify the RBCs in each outlet and inlet. Thus, Figure 32 represents the optical absorbance of the samples collected at the inlet and at the outlets O5, O3/O7, O2/O8 and O1/O9, for each of the microdevices (MD1, MD2 and MD3).

At the inlet, the Hct was about 2% and, as expected, it was the highest in this study, which was confirmed by the highest optical absorbance at 450 nm. According to the data, 2% of Hct has an optical absorbance, at 450 nm, around 0.26. As the cells flow through the devices, it is expected an Hct reduction along the outlets. The optical absorbance results corroborate such expectation,

as in Figure 32 it is shown a decrease of the amount of RBCs at all the outlets when compared to the inlet. As the Hct relates to the concentration of RBCs in the sample, and their optical absorbance is directly proportional to the cells' concentration, from the optical absorbance results, it was estimated the Hct at each outlet. For MD 1, the Hct was 1.15% at O1/O9, 1.08% at O2/O8, 1.08% at O3/O7 and 1% at O5. For MD 2, it was estimated a Hct of 1% at O1/O9, 1% at O2/O8, 1% at O3/O7 and 0.92% at O5. For MD 3 it was estimated a Hct of 0.85% at O1/O9, 1% at O2/O8, 1.15% at O3/O7 and 1.23% at O5. This phenomenon happened in all the tested microfluidic devices. However, these results show that MD 3 is more efficient in the separation of the plasma from the cells, as the Hct tends to reduce (also decreasing the optical absorbance) as the filter step increases. This is clear in MD 3, since O9 and O1 (outlets at third separation step) have the lowest Hct. In contrast, the Hct obtained from the outlets of the devices MD 1 and MD 2 did not show such sequential decrease of the Hct but rather an oscillating behavior. These results suggest that the devices MD 1 and MD 2 are not efficient enough to separate plasma from an *in vitro* blood sample.
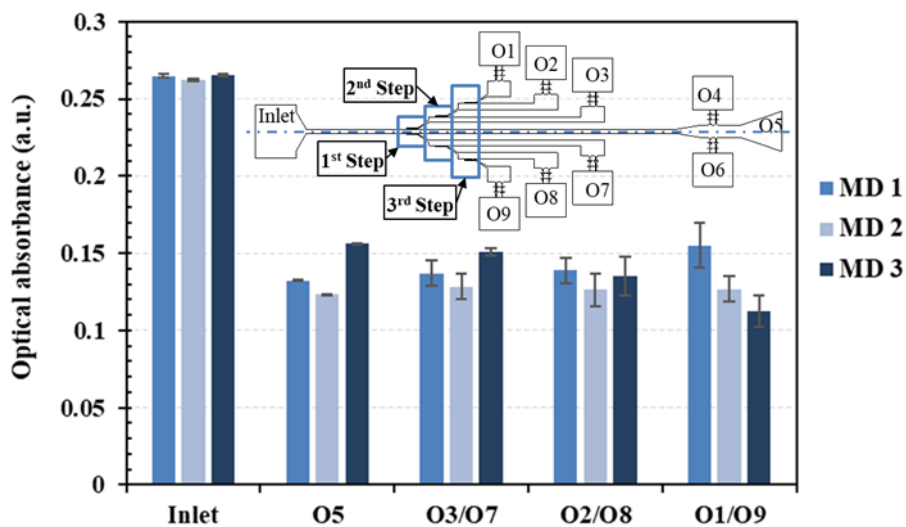
Figure 32. Optical absorbance (a.u.) at 450 nm for the inlet and outlets O5/O4/O6, O7/O3, O8/O2 and O9/O1.

For the intended application, it was important to assure a good separation performance, aiming to achieve the lowest number of cells in each separation step (1, 2 and 3) in order to visualize and measure the deformability of individual cells at each level. Therefore, the herein proposed strategy allows to perform, using one single microdevice, both the separation and the measurement of the cells deformation index.

Part III

Results and discussion of the cell separation and deformation work

Chapter 7

A Passive Microfluidic Device Based on Crossflow Filtration for Cell Separation Measurements: A Spectrophotometric Characterization[4]

7.1 Introduction

Microfluidic devices have been widely reported to perform blood separation experiments (Tanaka et al. 2012; Chen et al. 2014; Tripathi et al. 2015a; Catarino et al. 2016; Faustino et al. 2016). Some diseases, such as malaria, diabetes mellitus and sickle cell disease, influence the red blood cells (RBCs) stiffness and, consequently, their deformability (Suresh et al. 2005; Chen et al. 2008; Hou et al. 2010; Faustino et al. 2014b; Tomaiuolo 2014; Xue et al. 2015; Guo et al. 2016; Agrawal et al. 2016; Bento et al. 2018b; Boas et al. 2018a; Li et al. 2018). However, the complexity and peculiar characteristics of blood make it a very complicated and interesting fluid to study. It has been shown that blood behaves as a single phase, homogeneous fluid or a multiphase, non-homogeneous fluid (Gidaspow and Huang 2009; Sankar et al. 2015).

Malaria is a parasitic disease with more than half of the world's population at risk that causes around 500 thousand deaths per year, with 80% of infections occurring in children under five years old. The control, effective treatment, and elimination of this disease require an early and accurate diagnosis. The malaria parasite lifecycle passes from the mosquito vector to the human host by entering the liver cells where it matures, is released into the blood stream, and invades the RBCs. At this stage, the infected RBCs suffer biochemical, optical, and morphological changes (Diez-Silva et al. 2010; Saha et al. 2012), making these cells thicker and more rigid, resulting in a decrease of the cells' deformability (Handayani et al. 2009). Hemodynamic studies help to obtain

information regarding the presence, stage, and evolution of the disease. Particularly, the RBCs' deformability can work as relevant biomarkers for malaria diagnostic applications (Boas et al. 2018a), since they are directly related to the changes that the parasite causes throughout the evolution of the disease (Shelby et al. 2003).

The separation of the blood components from the plasma could give us tools to discover new biomarkers and new ways to analyze the blood components (RBCs, white blood cells (WBCs) or even particles) separately by using one single microdevice. However, blood is a complex fluid that involves careful preparation for *in vitro* studies to overcome several blood flow challenges that happen within the microchannels, such as coagulation and sedimentation (Garcia et al. 2012). For example, Chen et al. (2008) used cross-flow pillars in their microchannels to avoid cell clogging and jamming, and at the same time to create the cross-flow effect and multilevel filtration barriers that simultaneously separate the WBCs, RBCs, and the plasma (Chen et al. 2008). Other authors have used microchannels with hyperbolic shape contractions to measure RBC deformability in both physiological and pathological situations (Chen et al. 2008; Lee et al. 2009; Gossett et al. 2012; Pinho et al. 2013b, 2017; Yaginuma et al. 2013; Faustino et al. 2014b; Henon et al. 2014; Rodrigues et al. 2015b, 2016a; Guillou et al. 2016) and they have used low concentrations to improve their measurements. Recently, Pinho et al. (2013b) have proposed a continuous microfluidic device for the partial separation of RBCs and the subsequent measurement of their deformability in one single device. The geometries used in this device were slightly bigger than the size of the cells and as a result this methodology was able to generate mechanical stimuli close to *in vivo* capillaries.

The device implemented by Pinho et al. (2013b) follows the work published by Rodrigues et al. (2015b), where the authors developed a microfluidic device with pillars to separate and collect RBCs based on their deformability, with the expectation in the future to use this device with real malaria effects in RBCs. To validate and quantify the separation of the cells based on their deformability, the present work proposes the use of an optical absorption spectrophotometric setup to compare the optical absorption of the healthy RBCs (as studied in (Silva et al. 2017)) with the optical absorption of glutaraldehyde chemically modified RBCs. By obtaining different absorption spectra for the samples according to the rate of the healthy/glutaraldehyde-induced rigid RBCs (mimicking the malaria effects) that were collected in each Eppendorf tube. Hence, this study aims to show the potential for a cross-flow microfluidic device with pillars, not only to perform the partial separation of RBCs, but also to deform cells and assess their deformability. To the best of our

knowledge, there is no work in the literature quantifying RBC separation using spectrophotometric approaches (and, thus, differentiating between healthy and glutaraldehyde-induced rigid RBCs), showing the innovation of the proposed methodology.

7.2 Experimental Procedure

This section presents the geometry, experimental setup, and materials used in the procedures for evaluating RBC separation.

7.2.1 Microchannel Geometry and Experimental Set-Up

A polydimethylsiloxane (PDMS) (Sylgard® 184 Silicone Elastomer, from Dow Corning, Midland, Michigan) microchannel with 3×2 rows of 10 pillars (with distances between them of 17 µm, 16 µm, and 14 µm, respectively) and a depth of approximately 30 µm was used in this study, as shown in Figure 33a). The microchannel was fabricated in the CMEMS Research Unit at the University of Minho, using soft lithography techniques with SU-8 molds (Pinto et al. 2014b). The rows of pillars were placed in different levels on the microchannel to create different levels of separation. In this work, three different sets of pillars were considered (leading to the O1, O2, O3, O7, O8, and O9 outlets with hyperbolic contractions), and three additional outlets represented fluid paths with no pillars (although O4 and O6 also have hyperbolic contractions to allow deformability assessments).
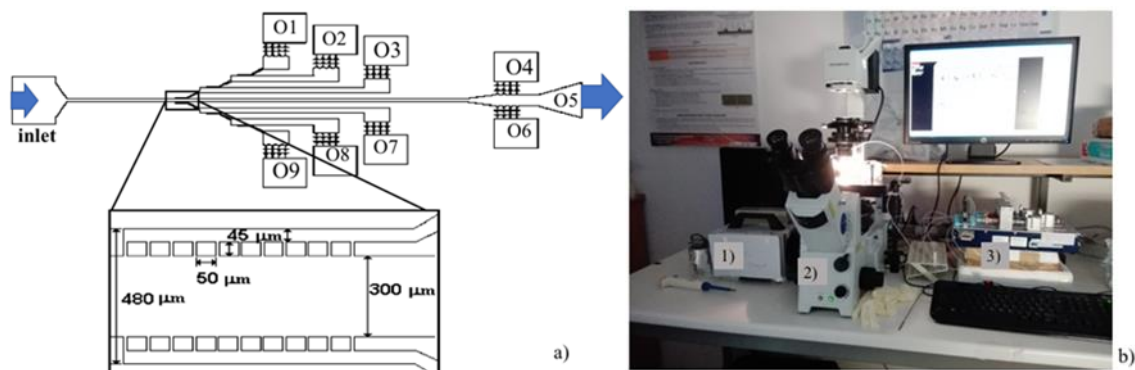
Figure 33. (a) Microchannel geometry with nine outlets (O1–O9). The arrows indicate the positioning of the rows of pillars in the microfluidic device. The left arrow indicates the region where the pillars have a 17 µm spacing between them, the central arrow indicates the region where the pillars have a 16 µm spacing between them, and the right arrow indicates the region where the pillars have a 14 µm spacing between them. The zoomed area beneath the microfluidic device represents two rows of pillars where each pillar has a 50×50 µm dimension and is separated from its neighbors by 17 µm; (b) Experimental setup comprising a 1) high-speed camera, 2) inverted microscope, and 3) syringe pump system.

The high-speed video microscopy system used in the present study consisted of an inverted microscope (IX71, Olympus, Tokyo, Japan) combined with a high-speed camera (Fastcam SA3, Photron, CA, USA), as shown in Figure 33b. The PDMS microchannel was placed and fixed in the microscope and the flow rate of the working fluids was kept constant at 50 µL/min using a syringe pump (NEMESYS) with a 5 mL syringe. At the same time, the images of the flowing cells at the established flow rate were captured by the high-speed camera at a frame rate of 2000 frames/s and a shutter speed ratio of 1/75,000, which minimized the dragging of the cells at the high-flow rate in study. All the experimental assays were performed at room temperature (T = 22 ± 1 °C).

7.2.2 Working Fluids

Human blood from a healthy donor was collected into 2.7 mL tubes (S-Monovette®, Sarstedt, Germany) containing ethylenediaminetetraacetic acid (EDTA). The RBCs were taken from a female volunteer. All procedures for the collection of blood and *in vitro* blood experiments were carried out in compliance with the EU directives 2004/23/CE and 2006/17/CE. The whole blood was centrifuged at 1500 rpm for 15 min at 20 °C. The plasma and the buffy coat were removed and the RBCs were resuspended and washed once in physiological salt solution (PSS) with 0.9% NaCL (B. Braun Medical, Melsungen, Germany). A RBC solution of 1% of Hematocrit (Hct) with 0.02% of glutaraldehyde was prepared in PSS and incubated for 10 min. The working fluid used was Dex40 (Sigma-Aldrich, St. Louis, MO, USA) solution containing 1% of healthy RBCs and 1% of RBCs incubated with glutaraldehyde (from now on, this solution will be referred to as the initial solution). It was used with a low Hct compared with the physiological because by using this low concentration of cells, it was possible to perform better visualizations of the flowing RBCs and consequently to obtain more accurate measurements. Each outlet of the microchannel device was connected to an Eppendorf tube to collect the samples. Once separation within the microfluidic device was finished, and in order to assure equal conditions for each optical assay, the same volume was collected from each Eppendorf tube (50 µL) and diluted with Dex40 (3 mL) to be analyzed in the spectrophotometry equipment.

7.2.3 Spectrophotometric Set-Up and Data Analysis

To quantify the separation efficiency, a spectrophotometric set-up was used that consisted of an Oriel/Newport 68,931 power supply, a model 487 picoammeter/voltage source (Keithley Instruments, Cleveland, OH, USA), an ultraviolet (UV) light source, an Oriel Newport (model 74125)

monochromator, an optical fiber, and a photodiode. The photodiode converts into a current the light that passes through a sample placed inside a 1 cm optical path quartz cuvette. This photodiode current measured by the picoammeter was then exported to a computer using a data acquisition application developed in the LabView software. The transmittance (T = I/I0) was then used to calculate the optical absorbance: A = −log10(I/I0), where A is the absorbance, I the intensity of light transmitted through the sample, and I0 the intensity of the incident light in the sample.

7.3 Results and Discussion

The proposed device was primarily evaluated by comparing the shape of the RBCs and the volume of samples collected in each outlet of the device. Figure 34 presents an overview of the samples collected in each outlet of the microfluidic device (Figure 34a), as well as microscope images of RBCs in each of those outlets and pillars.
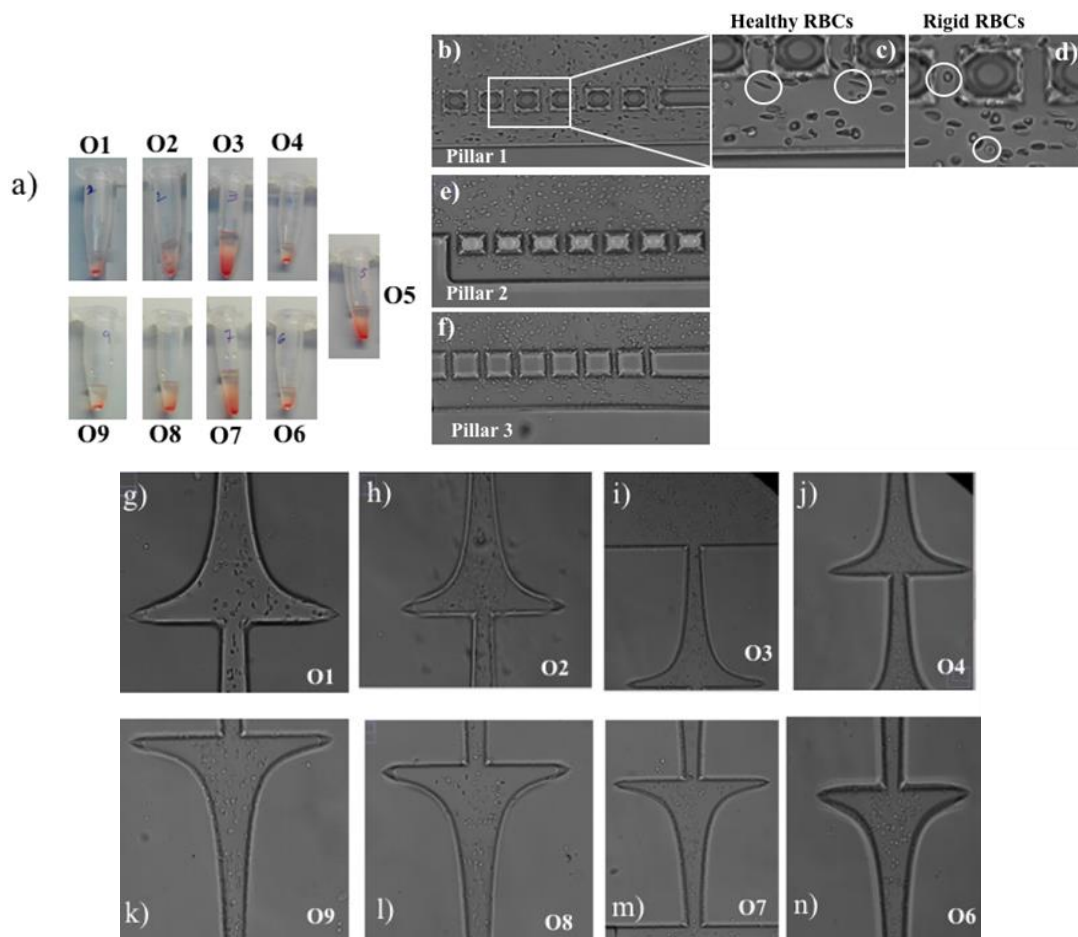
Figure 34. (a) Photo of the Eppendorf tubes with the samples collected in each outlet of the device; (b) pillars with a spacing of 17 µm; (c) elongated RBC; (d) rigid RBC; (e,f) pillars with spacing of 16 µm and 14 µm, respectively; (g- n) RBCs in each outlet O1‑O9 of the microchannel (except for O5, where there was no hyperbolic contraction).

From Figure 34 it can be observed that the separation device was able to transport the RBCs through the microfluidic channels and pillars according to their deformability. Figure 34b– f present instantaneous frames of RBCs crossing the three rows of pillars of the microfluidic device. Additionally, Figure 34c,d (magnified figures of Figure 34b) show, respectively, deformable RBCs and rigid RBCs flowing within the first row of pillars (cells located inside the white circles). By analyzing these figures, it is clear that the healthy RBCs have a high elongation when subjected to high shear flow (Figure 34c), and as a consequence it is reflected in the high deformability of these cells. On the other hand, in Figure 34d, we can see that the RBCs kept their almost spherical shape, indicating their difficulty to deform, which is a result of their glutaraldehyde-induced rigidity. These qualitative results indicate that the proposed device has the potential to measure the RBCs' deformation index within the pillars and at the hyperbolic contractions located at the outlets, as displayed in Figure 2g–n. Additional and detailed measurements of RBCs' deformability under hyperbolic contractions can be found in (Faustino et al. 2014b; Rodrigues et al. 2016b). Figure 34a shows the Eppendorf volume of each outlet collected during the experiment.

The Eppendorf volumes present some differences between the symmetric outlets (O1–O9; O2–O8; O3–O7; O4–O6), as shown in Figure 35. It was expected that the central outlets (considering O5 as the central outlet, as in Figure 35) would have higher collected volumes, and that these volumes would gradually decrease towards O1 and O9. On the upper side of the device (see Figure 33a), O1, O2, and O3 were the outlets following the 14 µm, 16 µm, and 17 µm pillar paths and, as expected, as the spacing between the pillars increased, the collected volume also increased. It was expected that the symmetric outlets would obtain similar volumes in both Eppendorf tubes, however, this phenomenon was not observed. This may indicate that the flow inside the microchannel was not fully steady. Regarding the central outlets (O4, O5, and O6), since there were no pillars in their way, the RBCs followed the easiest path, avoiding the hyperbolic contractions of O4 and O6, and explaining the higher volume of O5.
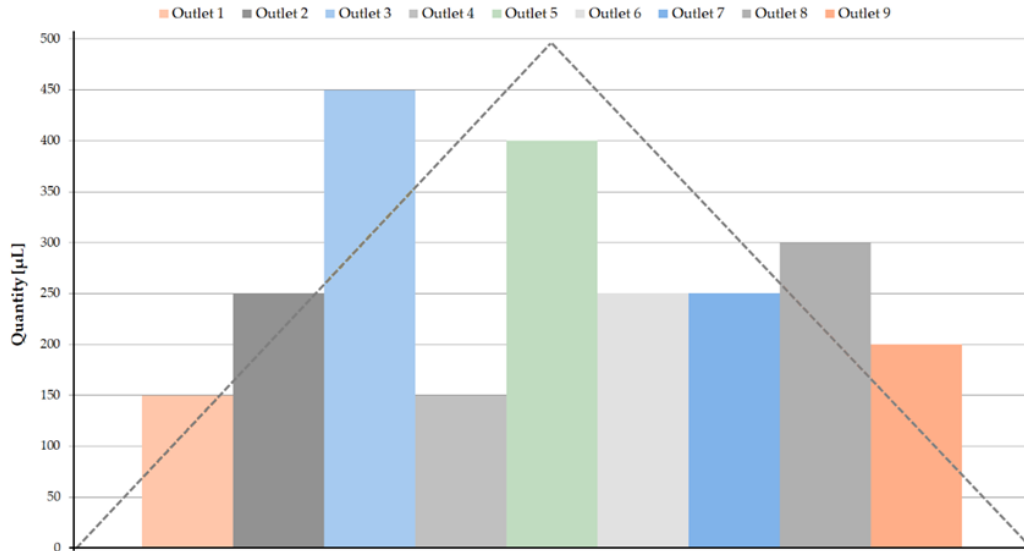
Figure 35. Volumes of the samples collected in the Eppendorf tubes. The dashed line represents an approximation of the expected behavior of the collected sample volumes in each outlet.

With the aim of quantifying the separation process, Figure 36 presents the average values of the absorption spectra curves of the samples collected in the outlets (O1–O9) and their standard deviation. Each spectrum curve represents the average of three measurements. Additionally, the blood, glutaraldehyde, and initial solution spectra in the UV range (between 220 nm and 450 nm) are also presented.
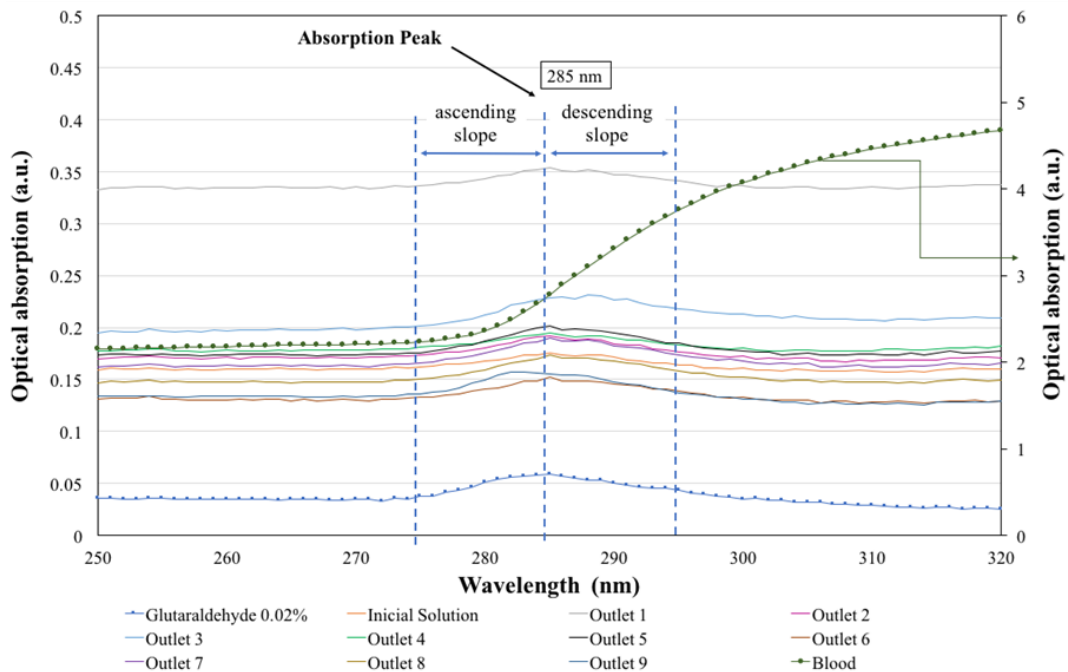
Figure 36. Average curves (n = 3) of the optical absorption spectra (a.u.) in the UV region of blood, glutaraldehyde, the initial working solution, and the samples collected in all the microchannel outlets (O1–O9). Note that the blood sample has an absolute optical absorption higher than all the other curves and, as a consequence, a secondary axis of optical absorption was added to the graphic (right axis).

Firstly, the optical absorption of blood, glutaraldehyde and the initial solution (working fluid with both healthy and rigidified RBCs that enters the microfluidic device) in the UV region of the optical spectrum was measured. These measurements showed the different typical spectra of these solutions and function as a reference for the quantification of the separation efficiency. The main absorption peaks of the blood are located at 540 nm and 574 nm (Silva et al. 2017), both located in the visible region of the optical spectrum, and are therefore not shown in this Figure 36 plot. In the UV region, the blood (dashed green line) showed an absorption increase, with a wavelength of up to 320 nm. On the other hand, glutaraldehyde at 0.02% concentration (dashed blue line) had an absorption peak around 285 nm. Additionally, the initial solution (orange line with arrows in the plot) had, as expected, an intermediate shape, i.e., had the same spectrum peak as glutaraldehyde, but with a higher absorbance value (closer in intensity to the blood absorbance curve). This way, by quantifying the slopes in the glutaraldehyde peaks in all the solutions collected in the outlets, it was possible to quantify the relative proportion of rigidified RBCs and healthy RBCs in each region of the microfluidic device, helping to quantify the efficiency of the RBC separation. To clarify the values of optical absorption, Table 7 presents the average optical absorption values (a.u.) at the glutaraldehyde absorption peak (285 nm) with the respective standard deviation values.

Table 7. Average of the optical absorption values (a.u.) at the glutaraldehyde absorption peak (285 nm) obtained for each curve and respective standard deviations.

Samples	Average (n = 3)	Standard Deviations (n = 3)
Glutaraldehyde	0.059	$\pm 1.41x\text{-}08$
Initial Solution	0.175	$\pm 1.85x\text{-}08$
01	0.353	$\pm 2.51x\text{-}06$
02	0.192	$\pm 1.30x\text{-}08$
03	0.228	$\pm 8.14x\text{-}09$
04	0.195	$\pm 1.53x\text{-}08$
05	0.201	$\pm 1.50x\text{-}08$
06	0.152	$\pm 1.71x\text{-}08$
07	0.190	$\pm 1.40x\text{-}08$
08	0.173	$\pm 1.59x\text{-}08$
09	0.156	$\pm 1.20x\text{-}08$

Observing Figure 36, it is difficult to directly distinguish the optical absorption peaks of the samples collected in each outlet, making it hard to evaluate the proportion of healthy and chemically modified RBCs in the microchannel outlets in order to evaluate the separation efficiency. However, from Figure 36 it is observed that while the blood optical absorption curve increased with the wavelength in the entire UV range, the glutaraldehyde sample presented an absorption peak at 285 nm. Therefore, by evaluating the absorption peak intensities of each sample, composed of RBCs with glutaraldehyde and healthy RBCs, it was possible to obtain the quantity of glutaraldehyde

within the samples and, as a consequence, to evaluate the amount of RBCs chemically modified at each outlet. Using this strategy, it was possible to determine the ascending and descending slopes for each measured sample, using the expression slope = $(y2 - y1)/(x2 - x1)$, where the x values correspond to the wavelength and the y values to the optical absorption. Table 8 presents the slopes calculated for two different regions, the ascending slope between 274 nm and 285 nm and descending slope between 285 nm and 296 nm. By evaluating the ascending slope region, it was observed that both glutaraldehyde and blood presented a positive slope, making it difficult to distinguish the effects of blood and glutaraldehyde in the obtained spectra. Therefore, we compared the slope in the descending region for all the samples (the slope in the blood sample was still positive, while in the presence of glutaraldehyde it became negative). Higher absolute values of this slope mean that the glutaraldehyde peak is more significant and, therefore, the sample has a larger quantity of modified RBCs and, consequently, is less deformable.

Table 8. Average ascending (274–285 nm) and descending slopes (285–296 nm) calculated for each sample.

Samples	Ascending Slope (274–285 nm)	Descending Slope (285–296 nm)
Blood	0.04979	0.09607
Glutaraldehyde	0.00217	−0.00165
Initial Solution	0.00130	−0.00109
O1	0.00165	−0.00129
O2	0.00172	−0.00149
O3	0.00249	−0.00105
O4	0.00138	−0.00111
O5	0.00237	−0.00171
O6	0.00182	−0.00141
O7	0.00233	−0.00168
O8	0.00214	−0.00155
O9	0.00183	−0.00177

Due to the microchannel geometry, it was expected that the values at the outlets 1, 2, 3, and 4 would be symmetric to the values at the outlets 9, 8, 7, and 6, respectively. However, the results in Table 8 show slight differences, probably related to the stabilization of the flow inside the microchannel. Additionally, it was expected a decrease of RBCs with glutaraldehyde (and consequently a decrease in the absolute value of the descending slope) would correspond to the decrease in the gaps between pillars. For example, from outlet 1 to outlet 3, as the pillars gaps decreased from 17 μm to 14 μm, the quantity of modified RBCs in the outlet should have been lower, since for shorter distances between pillars only the highly deformable cells are able to cross these obstacles. Therefore, in O1 we should have had more glutaraldehyde than in O3, and in O9 we should have had more glutaraldehyde than in O7, in agreement with the results of Table 8. Furthermore, O5 should have had a higher value of glutaraldehyde-modified RBCs, since that outlet

does not have any pillars working as obstacles and, therefore, less deformable RBCs are still able to reach that region. This is in agreement with the higher descending slope presented by the sample collected in this outlet. However, the results in Table 2 show some discrepancies from the expected results. O2 should have had a value between O1 and O3, and O8 should have had a value between O7 and O9. The discrepancies were likely caused by flow instabilities, some possible clogging problems due to the presence of stagnant flow regions, as well as some difficulties in microchannel fabrication, particularly when keeping equal distances between the pillars, which may have affected the separation results. These discrepancies were particularly common when comparing the left side of the microchannel (O9, O8, and O7) with the right side (O1, O2, and O3). Hence, further research on some critical parameters such as pillar spacing, layout, and orientation is needed. Nevertheless, the results obtained from this study are promising and are a starting point to develop an efficient microfluidic device based on cross-flow filtration for the partial separation of RBCs.

For the final intended application, concerning healthy and malaria-infected RBCs, additional tests must be performed in order to deal with real malaria parasite-affected RBC samples (at different disease stages) to compare disease and glutaraldehyde artificially impaired RBCs, establish target values, and fully validate this approach. Although it is well known that malaria leads to a decrease in RBC deformability, the target values are not yet clear, i.e., which deformability index values are achieved, since not many works can be found in the literature regarding this behavior (with testing in similar conditions). Barber et al. (2018) is one of the few studies found by the authors showing experimental data regarding the deformation index of controls and malaria-infected RBCs. This study shows that, as expected, the malaria-infected cells are less deformable than the healthy cells (controls), and that RBC deformability is reduced in humans with malaria in proportion to the disease severity. However, absolute values cannot be compared, since the experimental work was performed under different stretching conditions.

7.4 Limitations and Future Perspectives

Future work must focus on increasing the cell quantity in order to define the average property of the entire cell population with higher accuracy, since the physical properties of individual RBCs within the same RBC population can vary significantly. Additionally, since the ultimate goal is to develop an efficient separation device, more blood samples from different donors will be assessed to increase the RBCs' variability and to include more independent data, as well as to increase the blood cells' concentration in order to approximate to the physiological values. It will

be also interesting to compare, for validation purposes, the quantification of the separation efficiency using deformability data for the RBCs measured within the microfluidic device outlets. For this purpose, the microdevice was already fabricated considering hyperbolic contractions before each outlet, since this is one of the most common methods to assess cells deformability (Rodrigues et al. 2013a; Faustino et al. 2014b; Bento et al. 2018b). Finally, it is intended to test real parasite-affected RBC samples to compare their behavior with the glutaraldehyde-modified RBCs (Hosseini and Feng 2012), establish target values, and fully validate the proposed approach. This improved correlation will be used to relate the RBC behavior according to the various stages of malaria and to develop integrated sensors in microfluidic devices.

Chapter 8

Label-free multi-step microfluidic device for mechanical and rheological characterization of blood: diabetes type II[5]

8.1 Introduction

Currently, microfluidic technologies are a powerful way to rapidly and efficiently manipulate blood samples at low cost. In particular, it allow portable and low cost *in vitro* clinical devices for efficient blood fractionation into its different components, using small volumes of samples for the diagnosis of pathologies (Yu et al. 2014; Choi et al. 2015; Tripathi et al. 2016; Faustino et al. 2019). The separation of red blood cells (RBCs) from plasma and the quantification of proteins, cholesterol and glucose are examples of conventional routine assays for the diagnosis and monitoring of many diseases, such as malaria, cardiovascular disease and type II diabetes mellitus (Bhagat et al. 2010; Hou et al. 2010, 2011; Zeng et al. 2016).

Blood cells can be severely affected by several pathologies. For example, white blood cells (WBCs) play an important role in the immune response to allergies and infections, and contain a wealth of information about the immune status of the body (Liu and Wang 2004; Rosenbluth et al. 2008). Also, regarding RBCs, several biomechanical properties (e.g. deformability, shape, density or aggregability) are important functional biomarkers with significant potential to be applied in the biomedical and clinical research of diseases, such as diabetes, cholesterol, malaria, coronary diseases and obesity (Sabo et al. 1993; Suwanarusk et al. 2004; Bhagat et al. 2010; Yaylali et al. 2013; Tomaiuolo 2014; Zeng et al. 2016). Hence, easy optical visible access to microfluidic devices make them powerful tools to perform direct visualizations of the cells shape and deformability at geometries with similar conditions as *in vivo* microcirculation, and to help a better understanding of the diseases' abnormal deformability behavior (Hou et al. 2010; Yaylali et al. 2013; Zeng et al. 2016; Pinho et al. 2020).

Microfluidic approaches to perform blood cells and plasma separation can be based on passive or active separation techniques (Toner and Irimia 2005; Tripathi et al. 2016; Catarino et

---

[5] Pinho D, **Faustino V**, Catarino SO, et al (2022) Label-free multi-step microfluidic device for mechanical characterization of blood cells: Diabetes type II. Micro Nano Eng 16:100149. https://doi.org/https://doi.org/10.1016/j.mne.2022.100149

al. 2019). Some authors have reported efficient cell separation (95% RBCs removed from the initial whole blood (Chen et al. 2008), 99.55 ± 0.35% of plasma separation (Tripathi et al. 2016)) and sorting taking into account the size, shape, deformability and sedimentation of cells (Chen et al. 2008; Layton et al. 2012; Tripathi et al. 2016). Other separation techniques are based on hemodynamic and geometrical effects, such as the existence of a cell-free layer (CFL) and the bifurcation law for hematocrit (Hct) reduction (Yang et al. 2006a). Some authors have also achieved the separation of tumor cells from healthy cells based on geometric effects (Chen et al. 2008; Layton et al. 2012; Lee et al. 2013; Hyun et al. 2013; Prabhakar et al. 2015; Tripathi et al. 2015a). However, regarding the sorting of WBCs and RBCs and, simultaneously, the measurement of their deformability and shape, few studies were found. Sethu et al. (2006) have developed a microfluidic device based on geometric filters to separate cells by size and obtain leucocytes from whole blood, but did not measure any physical characteristics of the separated cells. Rosenbluth et al. (2008) have developed a microfluidic device based on biophysical flow cytometry to measure the WBCs deformability, previously isolated from a blood sample with leukemia, using the histopaque method. Similarly, Rodrigues et al. (2015b) have first separated WBCs from whole blood (to obtain higher concentration of WBCs than in the initial solution), and then performed flow tests in a continuous pillar-type filtration microfluidic device to measure the deformation index of both WBCs and RBCs.

Diabetes mellitus type II is a disorder characterized by high blood sugar (hyperglycemia) and is commonly associated with alterations in the blood cells deformability and blood viscosity, that may cause serious microvascular complications (Cho et al. 2008; Tomaiuolo 2014). Blood viscosity depends on the interaction between the molecules and cells and is proportional to the resistance to the free sliding of the blood layers within the circulation (Irace et al. 2014). An increase of the blood viscosity can promote high blood pressure with harmful consequences to the heart activity and walls of the vascular network. Also, following Poiseuille's law, blood viscosity is inversely proportional to flow rate and might, therefore, reduce the delivery of insulin and glucose to peripheral tissues, leading to insulin resistance and/or diabetes (Irace et al. 2014). Most of the diabetes-focused studies performed to date in rheometers and microfluidic devices have been based on the ability of RBCs to deform (Shin et al. 2007; Agrawal et al. 2016) or on the increase of blood viscosity (Riquelme et al. 2005). Overall, these studies have shown that the presence of a high blood glucose level contributes to disturbances of the whole blood viscosity and in particular to the RBCs deformability and agglomeration (de Cindio et al. 2007). Fundamental rheological tests, such as steady shear tests (Kostova et al. 2012), small and large amplitude oscillatory shear

tests (Sousa et al. 2013; Campo-Deaño et al. 2013) and creep tests (de Cindio et al. 2007) have proven their relevance and can provide a better understanding and characterization of blood properties and the relation with their microstructure (Riquelme et al. 2005; Kostova et al. 2012; Pinho et al. 2020).

To go a step further, it is necessary to combine blood rheology with the deformability measurements. Such goal is attempted here by performing, first, the rheological characterization of the fluids, specifically, steady shear viscosity tests of whole blood from healthy and type II diabetic donors. The viscous behavior of the working fluids used in the separation experiments is also evaluated. By using the developed multi-step microfluidic device, sorting and deformability analysis of WBCs and RBCs are also performed with healthy (n=5) and pathological (n=15) blood samples, diluted at both 5 and 20% Hct.

8.2 Materials and methods

8.2.1 Microfluidic device design and working principle

The developed multi-step microfluidic device is a polydimethylsiloxane (PDMS) microchannel bonded to a glass substrate coated with a thin layer of PDMS. The PDMS microchannel was fabricated through replica moulding, from SU-8 moulds using a low-cost soft-lithography method [36], without the need for cleanroom facilities, and with ultraviolet exposure equipment (Pinto et al. 2014b; Faustino et al. 2016). Inlet and outlet holes were performed by using a 1.5 mm biopsy punch.

The microfluidic device comprises several stages of cross-flow filtration barriers (zones A, B and C in Figure 37), with a 35 µm height (normal to the plane of the figure). The main channel has a length of 27.66 mm and a width of 300 µm (see Figure 37). The cross-flow filtration takes place at various sequential pillar arrays, each made of ten rectangular pillars (50 × 55 µm) defining eleven channels of 12 µm width. These arrays are used in all stages of separation, A, B and C. The microchannel has nine outlets, eight of them preceded by four parallel sets of three hyperbolic contractions, as exhibited in zone D of Figure 37. The hyperbolic contraction geometry has a 19 µm width at the smallest contraction size and a length of 375 µm, following the equation proposed by James et al. (1990), to impose a constant strain rate along the centerline of the microchannel outlets. The multi-step microdevice has geometric symmetry relative to the main streamwise center plane (dashed line in Figure 37), and we found the flow field to be symmetric relative to that plane.

This geometry results from previous works (Rodrigues et al. 2015b; Faustino et al. 2018) in which the number of pillars, gap sizes, levels of separation and downstream geometry shape was heuristically optimised, leading to the present design as the most suitable for the purpose of reducing cell concentration, from an inlet blood sample, to a minimum amount of individual cells in order to perform reliable cell deformability analysis at the outlets. This design can be further optimised especially if the objective is changed, for instance, to ensure total plasma separation or enhanced separation efficiency.
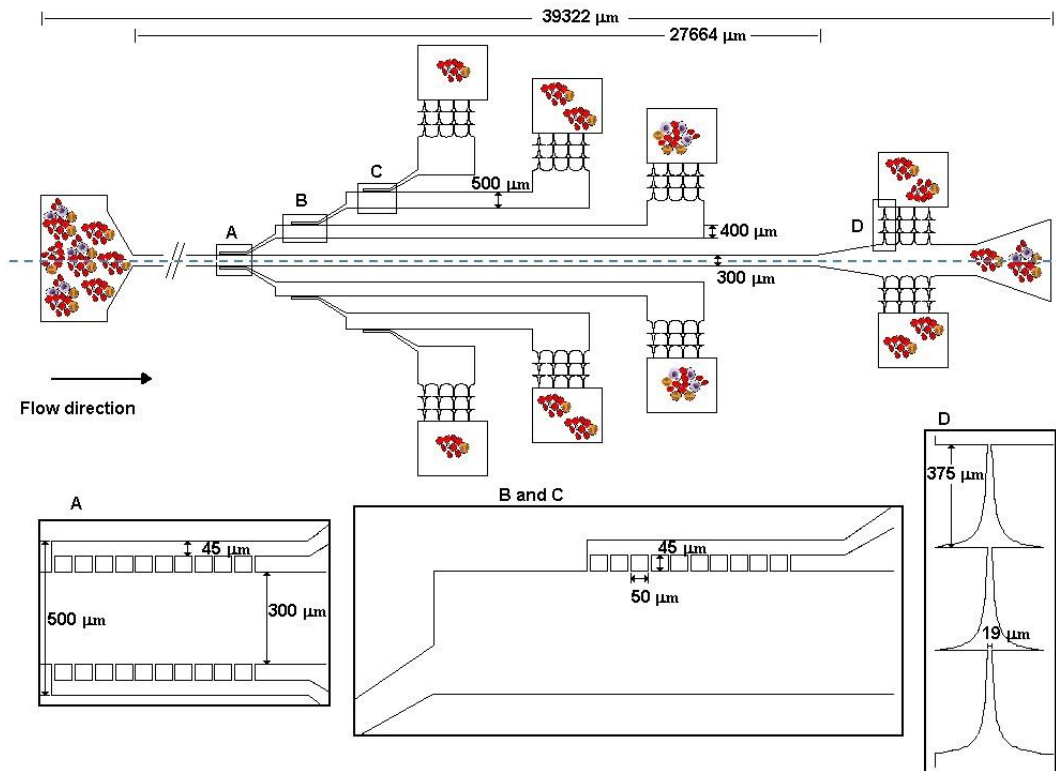
Figure 37. Schematic views of the microchannel design and its main dimensions. Details of zones A, B, C and D. The blue dashed line represents the axis of symmetry of the multi-step microdevice.

<u>Cross-flow filtration and hydrodynamic effects (size, density, deformability and morphology)</u>

By implementing a cross-flow filtration approach combined with the Zweifach-Fung effect, an efficient cell sorting along the sequential separation regions (zones A, B and C at Figure 37) is expected. The device design takes into consideration the dimensions of the cells and the hydrodynamic effects: RBCs have a biconcave discoid shape, with a major diameter of about 8 μm and WBCs can be roughly spherical, with diameters between 8 and 20 μm (Lima et al. 2012); in addition, WBCs present a lower density (~1090 Kg m-3) than RBCs (~1100 Kg m-3) (Kersaudy-Kerhoas and Sollier 2013). For that purpose, the cross-flow region comprises an array of 11 parallel 12 μm wide channels, which promote the separation of cells with dimensions up to the gap size

(12 μm). Since these channels are perpendicular to the main channel flow, the larger cells tend to flow tangentially, rather than flowing through the gaps (Chen et al. 2008; Gossett et al. 2010).

Extensional flow and cell deformability assessment

The nine outlets were numerated from O1 to O9, as shown in Figure 38. At each outlet, four parallel sequences of hyperbolic microchannels impose a strong extensional flow. These characteristics allow the assessment of the cells deformability. Cells moving along the centreline of the hyperbolic-shaped contractions do not suffer from other complex motions, such as rotation and tumbling (Lee et al. 2009; Yaginuma et al. 2013; Faustino et al. 2014b; Rodrigues et al. 2016b). Also, the hyperbolic micro-contraction generates a region of nearly constant strain rate and strong homogenous extensional flow away from its walls, thus constituting a promising strategy to assess single-cell deformability. It can be used as a simple and inexpensive platform suitable to detect and diagnose several diseases related to cells deformability.
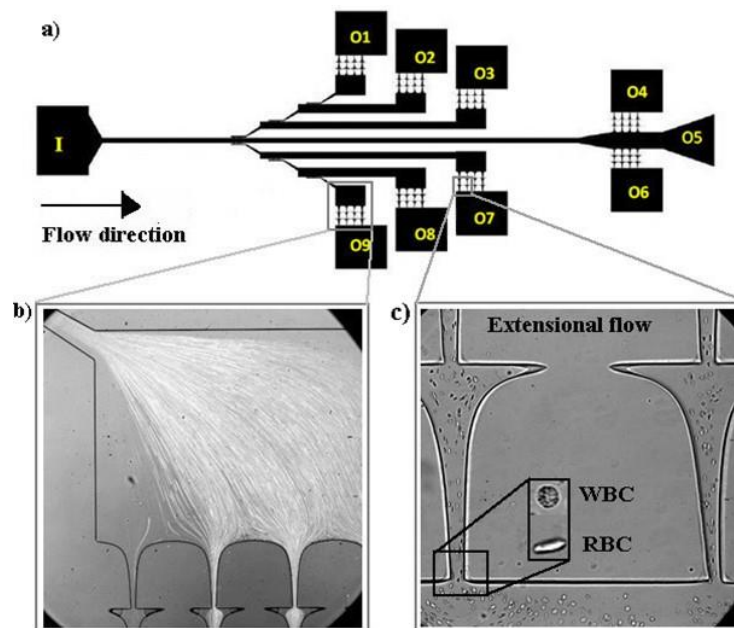
Figure 38. Schematic representation and numeration of the microchannel outlets (O1 to O9) a); and microscope image of: b) the flow at the Outlet 9 and c) RBCs and WBCs under extensional flow at the Outlet 7.

8.2.2 Blood samples preparation

All blood samples were collected into 2.7 mL BD-vacutainer tubes. The experiments were performed with healthy (n = 5) and pathological (n = 15) human blood, donated from different voluntary donors. To reduce donor-to-donor variability our pathological samples were collected from patients of middle age (38-48), with a clinical follow-up of several years and with the indication that the disease was under control. Hematocrit concentrations of 5 % and 20% in Dextran 40 (Dx 40) were used from healthy and pathological samples acquired from donors with a diabetes mellitus

type II diagnosis, for separation and deformability assays. For the whole blood viscosity measurements, for standardization purposes, only blood samples (both healthy and pathological) with 48% Hct were prepared. Note that Dx 40 was used to reduce cells agglomeration and sedimentation during the experimental assays. All procedures were performed after patient informed consent and approval by the Ethics Committee of Bragança Hospital.

8.2.3 Rheometer characteristics and measurements

Samples viscosity was measured using a rotational rheometer (Bohlin CVO, Malvern, Worcestershire, UK), with a 55 mm diameter cone-plate geometry and a gap of 50 μm. Steady shear flow curves were obtained in a range of shear rates of $1 \leq \dot{\gamma} / s^{-1} \leq 10{,}000$ at temperatures of 37 °C and 22 °C, which correspond to the body temperature and *in vitro* blood experiments, respectively.

8.2.4 Experimental set-up

The high-speed video microscopy system used in the present study consisted of an inverted microscope (IX71, Olympus) combined with a high-speed camera (Fastcam SA5, Photron, USA), Figure 39. The PDMS microdevice was placed and fixed in the microscope and the images were acquired by using objective lens of 10 and 20 X. The stage of the microscope allowed us to move and adjust the device for interrogation of the region of interest. Images of the flowing cells were captured by the high-speed camera at a frame rate of 2000 frames/s and a shutter speed of 1/50000 s. All the experimental assays for cells separation were performed at room temperature (T = 22 ± 2 °C).

The flow rate of the working fluids through the microchannel was kept constant, at 100 μL/min, by means of a syringe pump (PHD Ultra, Harvard Apparatus, USA) fitted with a 5 mL syringe (Terumo, Japan). Inlet and outlet connections were performed by tubing. As the blood samples flowed within the microfluidic device, the cells were collected at the nine outlets into different reservoirs in order to evaluate the cell separation. The outlet orifices were made with a 1.5 mm diameter biopsy punch and connected to the reservoirs (Eppendorf) by tygon tubes.
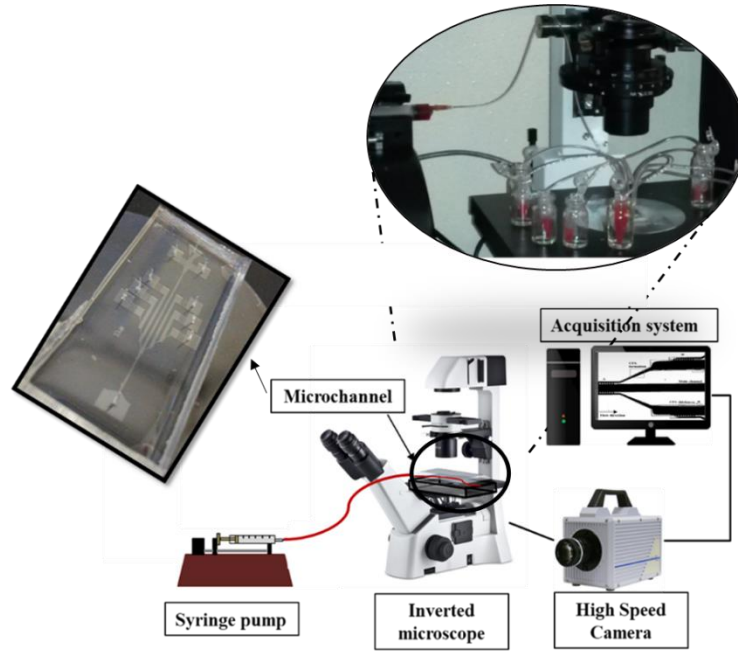
Figure 39. Schematic representation of the experimental setup, comprising an inverted microscope coupled with a syringe pump system and a high-speed camera acquisition system.

To quantify the concentration of cells (WBCs and RBCs) in the source sample and at each outlet, an automatic hematology analyzer system (Sysmex XT-4000i) was used. This clinical equipment relies on fluorescent flow cytometry and hydrodynamic focusing technologies to allow the reliable identification and counting of cells. For each outlet, three samples of 150 µL were collected in order to perform the measurements three times and evaluate the results reproducibility. The cell concentration (E_x) defined by Eq. (1) was quantified as the ratio between the number of cells of a given type (x) captured at the outlet (N_{out_x}) over the total number of the same type of cells in the source blood (N_{in_x}). Three types of cells were considered with subscript x referring to RBCs, WBCs and M (RBCs plus WBCs).

$$E_x = \left(\frac{N_{out\_x}}{N_{in\_x}}\right) \times 100\% \tag{1}$$

8.2.5 Image analysis

The image sequences recorded during the flow visualizations were analyzed and processed using the image processing tools from the software ImageJ (1.46r, NIH, USA) (Abramoff et al.). Several steps of pre-processing and image segmentation were performed in order to reduce static artifacts, an average background image was created from the original stack images, by averaging each pixel over the sequence of static images while using the ImageJ function Z project (Abramoff

et al.; Faustino et al. 2014b), and then subtracted from the individual stack images, so that at the end only the RBCs of interest remain. Brightness/Contrast adjustment was also applied to enhance the image quality, and the greyscale images were converted to binary images adjusting the threshold level. For that purpose, the Otsu threshold method (Kim et al. 2006) was as applied and, when required, the level was manually adjusted, resulting in well-defined cells as black ellipsoidal objects against a white background. At the end, the flowing cells in the binary images were manually measured frame by frame with the wand tool function in ImageJ. The main output results of these measurements were the major and minor axis length of each individual cell (WBC and RBC from healthy and diabetic donors' blood) and the x-y coordinates of their centroids. More details about the image processing steps can be found in (Faustino et al. 2014b, a, 2019). The deformation indexes (DI) of the samples were then calculated using:

$$DI = \frac{L_{major} - L_{minor}}{L_{major} + L_{minor}} \qquad (2)$$

where L_{major} and L_{minor} refer to the lengths of the major and minor axis of the blood cell, respectively. Finally, the MTrackJ plugin from ImageJ was also used to assess the velocities and trajectories of the cells (Meijering et al. 2006).

8.3 Results and discussion

8.3.1 Whole blood and working fluids rheology

Steady shear tests with healthy and pathological blood samples were performed at 37 and 22 ℃. The samples hematocrit was standardized to 48% in order to minimize the influence of the cells concentration. Diabetes mellitus type II is a disease characterized by elevated glucose in the blood circulation and it is generally accepted that blood viscosity is increased, as a result of the disease (Kostova et al. 2012). Although the relation between blood glucose, diabetes and blood viscosity is still not completed understood, several works have demonstrated that patients with high levels of blood glucose have higher plasma viscosity, higher RBCs rigidity and higher aggregation, (Kostova et al. 2012; Irace et al. 2014; Deng et al. 2020). Figure 40 a) and b) shows a comparison between the viscosity measured for both pathological and healthy blood samples, as a function of the shear rate. The whole blood viscosity (WBV) of diabetic patients is higher for all the tested shear rates, in line with experiments performed by Kostova et al. (2012). At low shear rates, the blood viscosity is strongly dependent on the RBCs aggregation while at high shear rates, the aggregated structures tend to breakdown and cells tend to elongate and align with the flow, being influenced

by cells deformability. Pathological cells are less deformable and, consequently, will increase the blood viscosity.
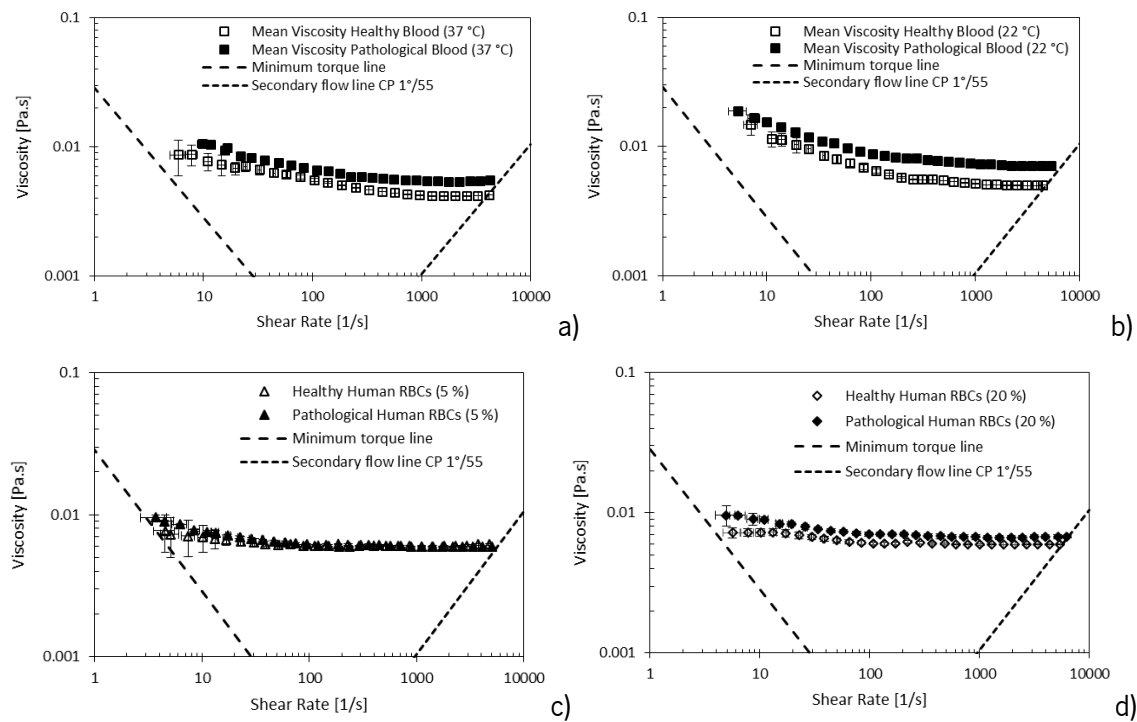
Figure 40. Mean WBV for the patients with diabetes type II (n = 15) and for the control group of healthy individuals (n = 5) at: a) 22 °C and b) 37 °C. Viscosity curves of diluted blood in dextran 40 at: c) 5% and d) 20% of Hct obtained at 22 °C. Error bars represent the mean standard deviation at 95%.

By analyzing the viscosity at a single shear rate, it is clearly observed that the pathological WBV shows higher values. For example, at a shear rate of 25 s^{-1}, the mean WBV for pathological and healthy blood is 0.0118 Pa.s and 0.0096 Pa.s, respectively, at a temperature of 22 °C. In the same way, for a higher shear rate of 520 s^{-1}, the WBV presents values of 0.0079 Pa.s for pathological blood and 0.00565 Pa.s for healthy blood samples.

Regarding the working fluids (5 and 20% of Hct in Dx 40) used for the separation and deformability tests, their viscosity curves at T = 22 °C are shown in Figure 40 c) and d). Despite blood dilution in Dx 40, a higher viscosity at low shear rates is still observed for all samples especially at the hematocrit of 20% (Figure 40 d)). This high viscosity at low shear rates can now be related to both cell aggregation and the reduced cells deformability. Therefore, by performing the separation and deformability assays, it will be an essential step for the characterization of the fluid and to obtain more detailed insights about the blood rheological properties and correlate them with the results of individual cell behavior.

8.3.2 Cell separation phenomena at the multi-step device

The cell separation and deformability experiments were performed at the same flow conditions without observing significant sedimentation, clogging, jamming or leakage problems that are likely to arise at microfluidic devices with multiple filters and bifurcations (see Figure 41). The Reynolds number (Re), based on the viscosity of the carrier fluid (5.2 mPa.s for Dx 40) and the hydraulic diameter, was below 1 at the smallest microchannel. Additionally, velocities obtained in this device for the dextran suspensions, to be presented in sub-section 8.3.4, are of the same order as the velocities observed in *in vivo* microvessels having diameters ranging from 80 to 500 µm (Rodrigues et al. 2015b).

The proposed multi-step microfluidic device comprises a sequence of cross-flow filters that plays a major role in the separation of cells based on their size. Besides the hydrodynamic mechanisms, it is well known that the combination of RBCs deformability and high wall shear rates promotes RBCs migration to the center of the microchannel. Also the cells interaction and the margination process lead some WBCs toward the microchannel wall (Wong et al. 2012; Yazdani et al. 2016). Thus, smaller WBCs and some deformable RBCs, when flowing near the pillars, tend to pass through the cross-flow filter barrier into the branch channels. Yet, when cells reach an asymmetric bifurcation, according to the bifurcation law, they tend to prefer the daughter channel with the higher flow rate (Yang et al. 2006a; Yu et al. 2014). The smaller dimensions of the branch channels, complemented with the cross-flow filters, help to create differences in the local flow rates. The combination of both effects can be seen in Figure 41, where the local flow rate in the main channel is ~ 75.6 µL/min and at the daughter channels the smaller mean flow rate is ~20.6 µL/min.
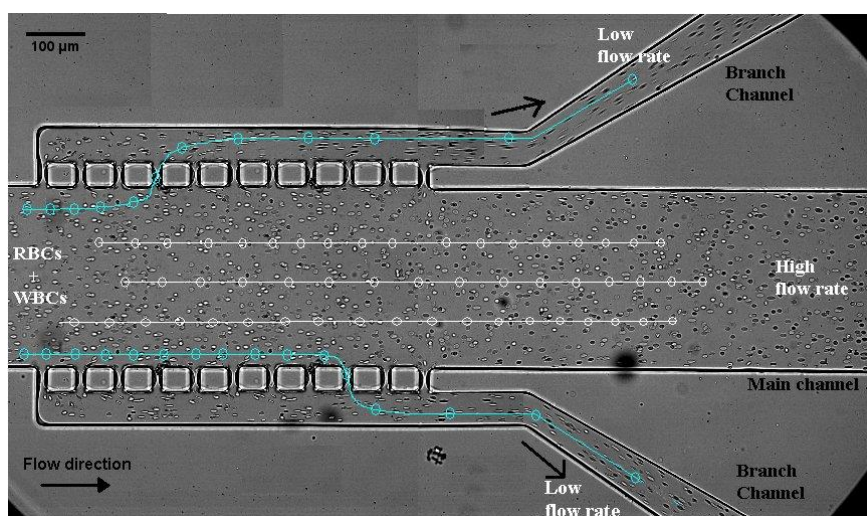
Figure 41. Microscope image (20× objective) at zone A of the microdevice. The lines with symbols represent schematically expected trajectories of different blood cells flowing through the main and branch microchannels.

Figure 41 shows the combination of several hydrodynamics effects taking place inside the microdevice, as well as flow pattern variations over the various obstacle arrays in zones A, B and C (Figure 37). The CFL developed in the straight channel grows in size, not only downstream, but also when this fluid has the chance to flow laterally through the filter on the side wall, subsequently flowing through constrictions-expansions. In fact, it can be seen in Figure 42 a), b) and c), that the blood fraction passing through the successive divergent branches leads to an increase of the CFL thickness and, as a result, the amount of cells that are able to move to the next daughter channel is reduced. Hence, by combining all the hydrodynamics phenomena, it is possible not only to obtain a low concentration of cells at the outermost outlets (Figure 42 d)), but also to measure accurately the cell deformability of each individual cell.
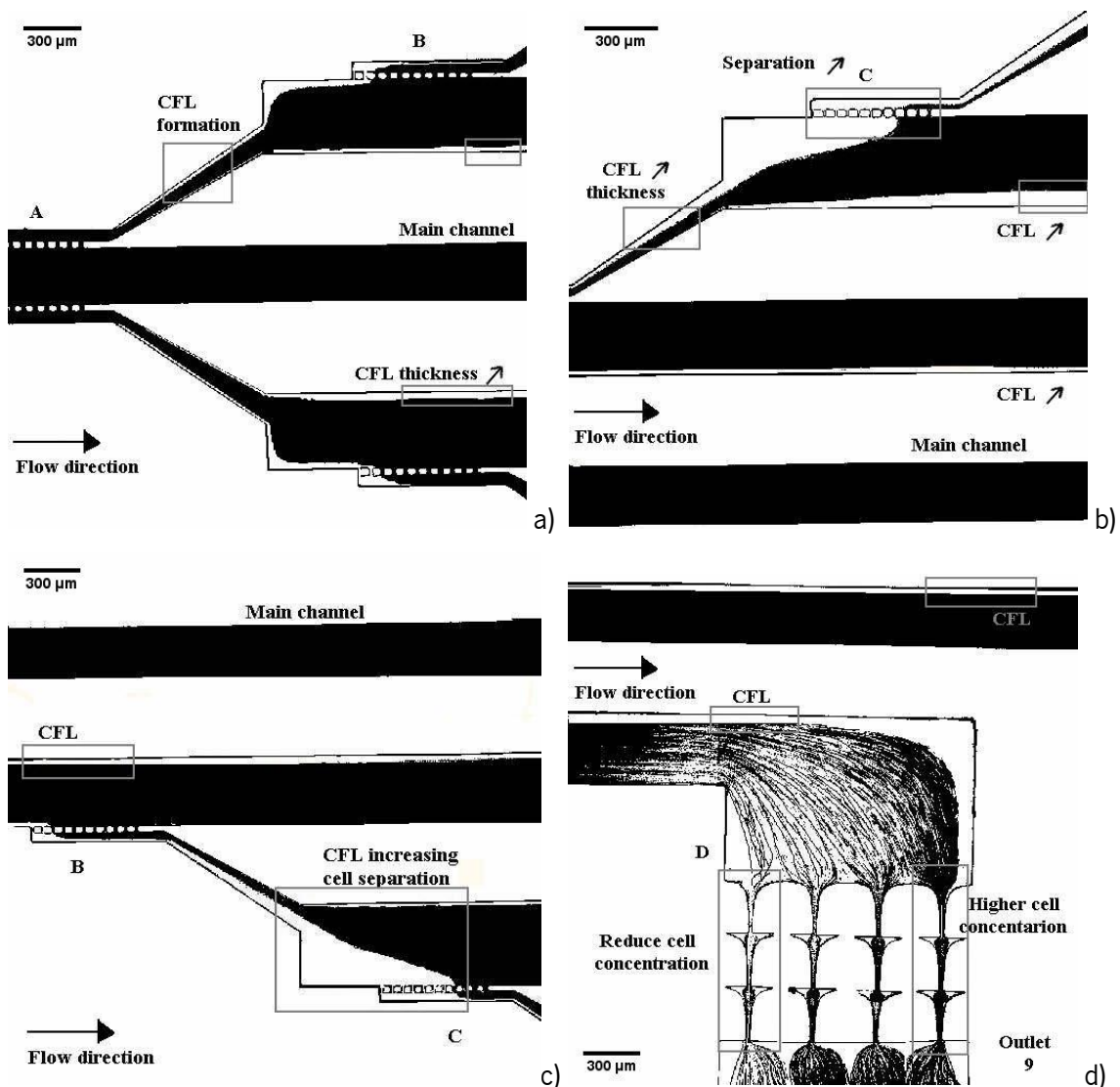
Figure 42. Threshold microscopic images (10x objective) of the microchannel: a) zone A; b) zone C; c) zones B and C and d) zone D of the Outlet 9, for the flow visualizations, at 20% Hct.

8.3.3 Microdevice cell separation

The counting of WBCs and RBCs was performed off-chip, using an automated hematology system. By taking into account the values obtained at the hematology system, it was possible to estimate the cells concentration, by considering the difference between the cells collected at the outlets and inlets. Table 9 lists the concentration of cells at the outlet of the experimental assays performed for the healthy donors (n = 5). The cell counting was performed three times for each sample.

Table 9. Microdevice cell concentration at each outlet for healthy blood dilution (5 and 20% Hct) and the standard deviation at 95% for n = 5.

Microdevice Outlets	Healthy blood at 5% Hct				Healthy blood at 20% Hct			
	E_{RBCs} (%)	E_{WBCs} (%)	E_M (%)	SD (95%)	E_{RBCs} (%)	E_{WBCs} (%)	E_M (%)	SD (95 %)
O1	1.00	0.82	1.00	0.04	3.59	1.13	3.58	0.19
O2	11.67	9.79	11.67	1.41	5.64	5.36	5.64	0.30
O3	14.30	16.15	14.31	1.94	19.83	23.00	19.84	1.27
O4	5.14	4.40	5.14	0.91	5.64	4.85	5.64	0.62
O5	32.25	35.07	32.25	1.94	31.28	30.64	31.27	2.04
O6	7.15	5.06	7.15	1.65	5.33	4.88	5.33	0.84
O7	18.44	19.58	18.45	0.88	16.14	19.15	16.15	1.48
O8	9.28	8.65	9.28	1.14	8.97	9.30	8.97	0.36
O9	0.75	0.49	0.75	0.05	3.59	1.69	3.58	0.72

The lowest concentrations were obtained through outlets O1 and O9, regardless of hematocrit, but for 5% Hct it was possible to get almost pure plasma, with a very low concentration of all cells (less or equal to 1%). For 20% Hct, the device was still able to achieve a good separation and the cell concentration at those outlets was $E_M = 3.58$ % (cf. Table 9). For both dilutions, around 44% of cells exited through outlets O4, O5 and O6. The cells that pass through the first cross-flow filters to the branch channels encounter the second pillar array and the majority of them are oriented to outlets O3 and O7, where the cell concentration was about 16 and 18%, for 5 and 20% Hct, respectively. For the outlets with two levels of pillar-array filtration (O2 and O8), the cells concentration can reach mean values of 10% and 7%, for 5 and 20% Hct, respectively. Overall, the sequence of cross-flow filters combined with the hydrodynamic effects allowed a gradual increment of the cell separation, where the lowest cell concentration was found at the outermost outlets (O1 and O9).

The results of cell separation with pathological blood from diabetic II patients are listed in Table 10. The results are qualitatively similar to those of healthy cells. However, quantitatively, they exhibited minor differences between the various outlets of the device. The outlets located at the end of the main channel (O4, O5 and O6) have the highest total cell concentration, in the same

way as for healthy cells flow separation, but outlet O5 has far less cells (19% to 21% against 32% to 35% for healthy cells). The outermost outlets O1 and O9 also exhibit the lowest concentrations of the device, at around 4% and 6 % of cells for 5% and 20% Hct, but the pure plasma separation was not achieved as occurred with healthy cells (concentration at or below 1%).

Table 10. Microchannel cell concentration, in each outlet for diabetic blood dilution (5 and 20% Hct) with standard deviation at 95% for n = 15.

Microdevice Outlets	Blood of diabetic patients at 5% Hct				Blood of diabetic patients at 20% Hct			
	E_{RBCs} (%)	E_{WBCs} (%)	E_M (%)	SD (95 %)	E_{RBCs} (%)	E_{WBCs} (%)	E_M (%)	SD (95 %)
O1	5.05	7.27	5.05	0.62	6.02	3.37	6.01	0.19
O2	12.63	12.73	12.63	0.87	10.65	13.20	10.63	0.30
O3	14.14	14.55	14.14	0.81	12.50	15.73	12.48	1.21
O4	11.11	12.36	11.11	0.54	7.87	8.71	7.86	0.62
O5	18.69	17.09	18.68	0.30	21.30	16.29	21.26	1.67
O6	11.11	9.09	11.11	0.54	10.65	10.39	10.63	0.84
O7	12.12	13.09	12.12	0.90	12.50	14.33	12.48	1.31
O8	11.11	10.18	11.10	0.10	12.04	13.76	12.02	0.36
O9	4.04	3.64	4.05	0.92	6.48	4.21	6.47	0.30

In the flow tests performed with the 5% Hct of pathological blood samples, residual formation of agglomerates was observed at the cross-flow filters, whereas considerable agglomerates were observed at 20% Hct. This aggregation of pathological RBCs could be the result of their higher tendency to form large cell agglomerates that partially block the array gaps. However, after some time, the agglomerates tend to disaggregate due to the high local fluid velocities. In order to minimize these effects each experiment was limited to a maximum time of 30 minutes, and in the initial 20 minutes we could not observe any cell agglomeration.

8.3.4 Deformability and cell velocity

The aim of the proposed microfluidic device is, not only to separate blood cells from the plasma, but also to measure the deformability of RBCs and WBCs at the hyperbolic contractions located upstream the outlets. Variations in blood cell deformability have been associated with several human diseases and, for the particular case of diabetes, the possible genetic and molecular causes for cell deformability alteration are still unclear. Hence, it is necessary to better understand this correlation. Figure 43 shows cell deformability results at all outlets (60 cells per outlet) with hyperbolic geometries (15 cells per hyperbolic contraction), together with the corresponding centerline cell velocities, which were measured by tracking the RBCs and WBCs. The image sequences used to obtain the DI measurements were recorded during the flow of healthy and

pathological blood with a 20% Hct. Most of the fluid exited through outlet O5, which has no hyperbolic contraction, while a low amount of cells cross the pillar barrier and the cell deformability can be analyzed. Note that cells flowing close to the walls, cells exhibiting rotational motion upstream the hyperbolic contraction or rotating along the middle of the contraction were not measured.
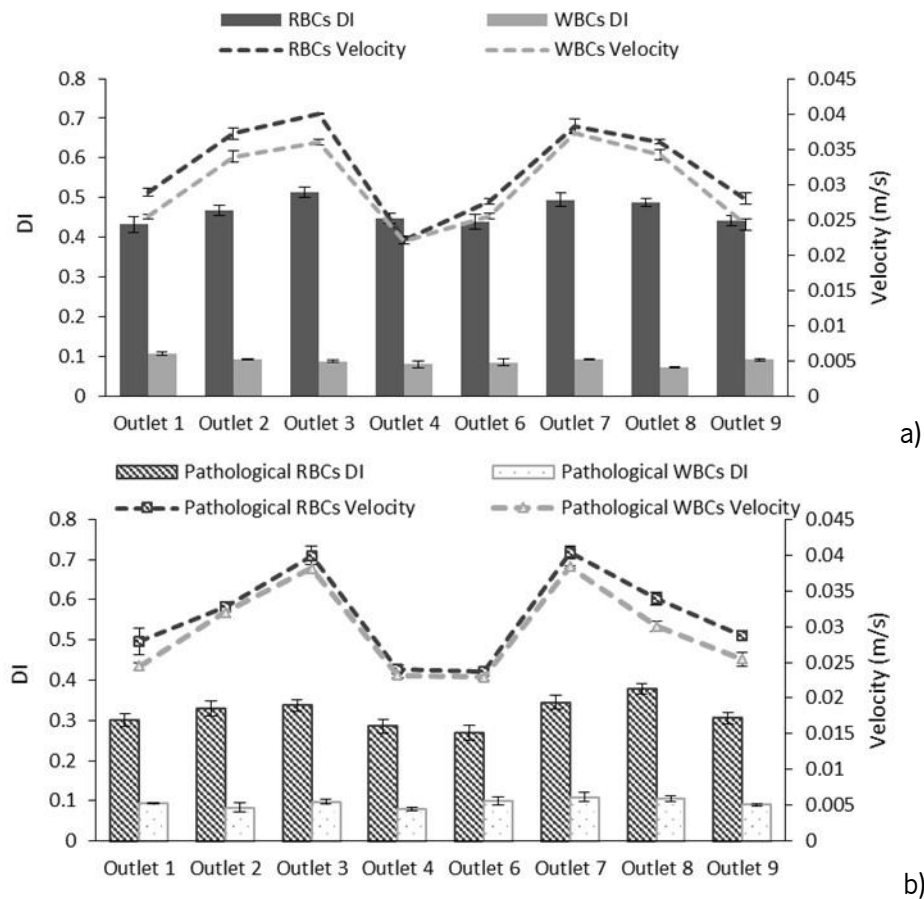
Figure 43. Deformation index (DI) (a.u.) measurements at each outlet (total of 60 cells) and corresponding velocity (m/s) for the RBCs and WBCs with 20% Hct: a) healthy and b) pathological blood.

The velocity data demonstrate near symmetry between the up-down outlets, as expected due the device design, showing that the flow experiments were in equilibrium, Figure 43 a) and b). This is even more obvious with pathological cells, as shown in Figure 43 b). This equilibrium is extremely important to perform accurate comparison of the cells deformability. In addition, the velocities measured at the tested hyperbolic microchannel outlets are similar to those found in *in vivo* microvessels (Rodrigues et al. 2015b), therefore, this microdevice is able to deform cells is similar to what happens in *in vivo* environments.

The DI results show a significant difference between the behavior of healthy and pathological RBCs, with the deformability of the latter being 25% less that of the former (and relative to healthy RBCs), therefore confirming the correlation between the loss of RBCs deformability and

the pathological condition. Specifically, the healthy RBCs reach peak DI values of 0.51 ± 0.01 at O3 and of 0.49 ± 0.02 at O7 (mean shear rate of 1609.33 s^{-1}), which corresponds to the two outlets with highest velocities, cf. Figure 43 a). For the outlets with lower velocities, O1, O4, O6 and O9, we measured lower DI values for the healthy RBCs, around 0.44 ± 0.02. On the other hand, the RBCs from diabetic type II blood samples have a mean DI of 0.3 ± 0.01 and, even at the outlets with higher velocities, their deformability does not have a significant increase, demonstrating that these cells are more rigid, therefore less able to elongate with the applied normal stress.

In contrast, the differences between healthy and pathological WBCs are negligible. The WBCs submitted to the same strong extensional flow and high shear rates as the RBCs reach a maximum DI of 0.11 (Outlets 3 and 7), corresponding to a mean shear rate of 1521 s^{-1}, $\dot{\gamma} = U/D_h$. In addition, the deformability measurements showed WBCs flow trajectories taking place close to the walls of the hyperbolic geometries, subject to rotational motion. The WBCs cytoskeleton structure, internal composition and their *in vivo* function are the main reasons for the rolling and arrest phenomena, allowing their capture from the blood flow to the endothelial cells. This flow behavior is one of the reasons why WBCs have consistently lower velocities than RBCs, as shown in Figure 43. Note that the deformation of WBCs is usually a consequence of immune system activity (Rodrigues et al. 2015b). Here, the deformability results reveal that, under the applied in vitro conditions, WBCs behaved as non-deformable cells due to the absence of immune activation even though there is a blood disease, diabetes, that affects RBCs.

Chapter 9

A microfluidic deformability assessment of pathological red blood cells flowing in a hyperbolic converging microchannel[6]

9.1 Introduction

Blood is a complex and an extremely information-rich fluid that can be used to diagnose different kinds of blood diseases with multiple biophysical techniques and tools (Lee and Lim 2007; Tomaiuolo 2014). Under normal healthy conditions, the red blood cells (RBCs) comprise about 42% in adult females and 47% in adult males of the total blood volume (Tripathi et al. 2015a). As RBCs are the most abundant cells in blood, their deformable properties strongly influence the blood rheological properties, particularly in microvessels with complex geometries and diameters of less than 300 μm (Lima et al. 2012). Several research works have found that complex microgeometries, such as contractions (Abkarian et al. 2008; Pinho et al. 2013b) and bifurcations (Shevkoplyas et al. 2006; Sosa et al. 2014; Tomaiuolo 2014; Bento et al. 2019), promote the presence of strong shear and extensional flows that elongate the RBCs without reaching the rupture.

Ever since the RBCs deformability became a potential biomarker for blood diseases, such as malaria (Shelby et al. 2003; Boas et al. 2018a), sickle cell disease (Dao et al. 2003; Lee and Lim 2007), and diabetes (Tsukada et al. 2001; Shin et al. 2007; Agrawal et al. 2016), several techniques have been developed to measure the biomechanical properties of the RBCs. Additionally, there have been several reviews that discuss different kind of experimental methods to measure the RBC deformability (Musielak; Lee and Lim 2007; Tomaiuolo 2014; Xue et al. 2015; Bento et al. 2018b). The available methods can be divided in two main kinds, i.e., the high-throughput methods that measure high concentrations or diluted suspensions of RBCs, and the single-cell techniques. The most popular high-throughput methods, which include the conventional rotational viscometer (Sousa et al. 2013; Pinho et al. 2016, 2017), ektacytometer (Shin et al. 2007; Sosa et al. 2014) and micro-pore filtration assay (Sosa et al. 2014), have been used to measure the blood viscosity and other rheological properties, but they are generally expensive,

labor intensive, and do not provide a direct and detailed source of information on the mechanical properties of the RBCs. A recent study that was performed by Sosa et al. (2014) has shown that the results from the micro-pore filtration and ektacytometry were often in disagreement, and that neither of them represent the actual blood flow conditions occurring in microvascular networks. Other methods, known as single-cell techniques, which include the micropipette aspiration and optical tweezers, are also extremely popular for measuring the mechanical properties of the RBC membrane (Lee and Lim 2007; Agrawal et al. 2016). However, these techniques also have several drawbacks, such as a low-throughput, labor intensive, and static process. Additionally, it is argued that these methods do not represent the actual RBC deformability that happens during microcirculation (Tomaiuolo 2014).

The progress in microfabrication made fabricating microfluidic devices with the ability to directly visualize, measure, and control the motion and deformation of RBCs flowing through constricted (Zheng et al. 2013; Faustino et al. 2016; Pinho et al. 2017; Catarino et al. 2019) and bifurcated microchannels (Sosa et al. 2014; Bento et al. 2019; Catarino et al. 2019) possible. The distinctive advantage of the microfluidic devices, such as the need of small sample's volumes and their ability to reproduce more realistic conditions of the microcirculation, have promoted a vast amount of studies on the cell motion and deformability, mainly under the shear flow effect (Zhao et al. 2008; Quinn et al. 2011; Pinho et al. 2013b, 2016; Zeng and Ristenpart 2014; Tripathi et al. 2015a; Bento et al. 2018b). Some examples are the deformability measurements that were performed under transient high shear stress in sudden constriction channels, (Fujiwara et al. 2009; Bento et al. 2018b) and in microchannels with dimensions that were comparable to cell size (Tomaiuolo 2014; Bento et al. 2018b). Besides the shear flow effect, the extensional flow and the combination of both can be often found in the microcirculation system, such as in microstenosis and microvascular networks. Hence, during the last decade, several extensional blood flow studies have been performed in cross slot devices (Gossett et al. 2012; Guillou et al. 2016) and in microfluidic devices with hyperbolic channels (Lee et al. 2009; Yaginuma et al. 2013; Rodrigues et al. 2015b, 2016b, a; Zografos et al. 2016). Recent studies that were performed in cross slot devices (Henon et al. 2014) and sudden constriction channels (Zeng and Ristenpart 2014) have shown that cells entrance location and angular orientation strongly affect the cells deformability. On the other hand, extensional flows, where cells are deformed at almost constant strain rates, has been demonstrated to be a microfluidic methodology that is capable of efficiently and

accurately probing singe-cell deformability with high throughputs (Gossett et al. 2012; Bento et al. 2018b).

Additionally, the ability of hyperbolic-shaped contraction channels to generate constant strain-rates makes them a promising strategy for measuring RBCs deformability under a well- controlled microenvironment. Taking these advantages into account, the present study investigates the ability of hyperbolic microfluidic channels to measure the deformation and cell motion of RBCs that were obtained from healthy and diseased individuals (having end-stage kidney disease (ESKD), with or without diabetes type II) and exploits the relevance of this flow technique to be used as a viable tool suitable for detecting and diagnosing RBC related diseases.

Chronic kidney disease (CKD) is a pathological condition that results from a gradual, permanent loss of kidney function over time, usually, months to years, which can lead to an end-stage kidney disease (ESKD) (Astor et al. 2002). This condition is associated with a decreased quality of life (Staples et al. 2009), increased hospitalization (Brines et al. 2004; Staples et al. 2009), cardiovascular complications, such as angina, left ventricular hypertrophy (LVH), and chronic heart failure, and increased mortality (Robinson et al. 2005; Yang et al. 2007).

The remainder of this paper is organized, as follows: Section 9.2 comprises several subsections to explain the experimental framework around blood samples, setups used to acquire the data, and methods used to analyze it. Sections 9.3 and 9.4 presents and results and discussion, respectively.

9.2 Materials and Methods

9.2.1 Patients

In this study, a total of 20 ESKD patients under online hemodiafiltration (OL-HDF) that voluntary accepted to participate in the study, have been tested. From those, eight additionally showed diabetic nephropathy. Patients were excluded if they: (1) did not accept to participate in the study; (2) were under 18 years old; (3) were cognitively impaired; (4) had a severe speech or hearing impairment; (5) were in the dialysis program for less than three months; and, (6) presented malignancy, autoimmune, inflammatory, or infectious diseases.

The control group included seven healthy volunteers presenting normal haematological and biochemical values, with no history of renal or inflammatory diseases, and, as far as possible, age- and gender-matched with ESKD patients. The controls did not receive any medication known to

interfere with the studied variables. Blood samples (using EDTA as anticoagulant) were drawn from the fasting controls or before the second dialysis session of the week in ESKD patients.

All of the blood samples were obtained from dialysis patients at the hemodialysis clinic of Gondomar, in Porto, Portugal. Informed consent was obtained from all the participants and this study was approved by the clinic's ethics review board.

9.2.2 Microfluidic Device, Experimental Setup and Parameters

The polydimethylsiloxane (PDMS) microfluidic devices that were evaluated in this work were fabricated by using a conventional soft-lithographic technique (Faustino et al. 2016). To perform the deformability assessment, hyperbolic converging microchannels were fabricated with 382 μm of length (Lc), as well as maximum width of 400 μm (W1) and minimum width of 20 μm (W2) at the wide and narrow sizes, respectively (cf. Figure 44). This particular geometry corresponds to a hyperbolic contraction with a Hencky strain (ε_H) of ≈3. Note that the ''H can be defined as ln (W1/W2) (Rodrigues et al. 2016a). The advantages of the use of this hyperbolic geometry for RBCs screening have already been ascribed in previous studies (Faustino et al. 2014b, a). The hyperbolic contraction geometry was chosen, mainly due to the strong extensional flow that was generated in the middle of the microchannel, which is dominant over the shear flow. The cells by passing through the hyperbolic contraction are submitted to a strong extensional flow, where the velocity almost linearly increases, but the strain rate stays approximately constant. Note that the depth was about 50 μm along the full length of the device.

Figure 44b also shows the main advantage of using hyperbolic converging microchannels. At the entrance of these kinds of geometries, the RBCs tend to exhibit a linear increase of their velocities and consequently the strain rates within the hyperbolic contractions are close to a constant. This flow phenomenon imposes a homogenous mechanical fluid behaviour to the RBCs and avoids some possible motions (tumbling, twisting, and rolling rotations), often observed in abrupt contractions (Zeng and Ristenpart 2014). Hence, by using hyperbolic converging microchannels, most of the RBCs tend to elongate when they flow through the contraction. It is worth mentioning that RBCs motions, such as tumbling, twisting, and rolling rotations, were never observed during our experiments.

96
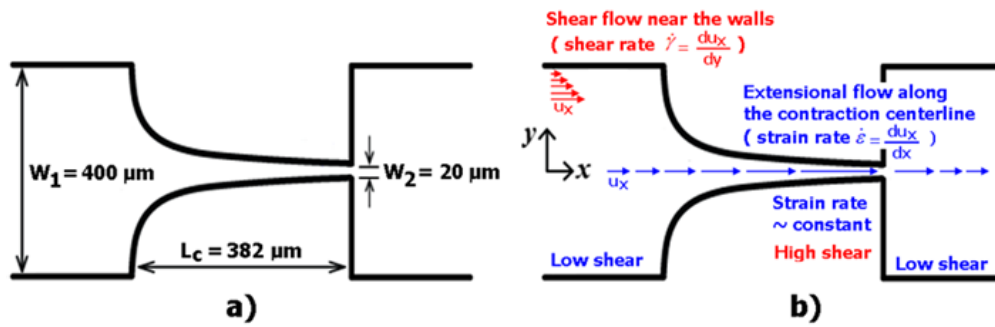
Figure 44. Microfluidic device fabricated in polydimethylsiloxane (PDMS) with a hyperbolic-shaped contraction to assess the red blood cells (RBCs) deformability: a) main dimensions; b) flow phenomena happening in this kind of geometry. Adapted with permission from (Lima et al. 2018).

The visualization and measurements of the motion of the RBCs were performed by means of a high-speed video microscopy system that includes an inverted microscope (IX71, Olympus, Tokyo, Japan) combined with a high-speed camera (Fastcam SA3, Photron, San Diego, CA, USA). The microfluidic device was placed on the microscope stage and the flow rate of the working fluids was kept constant at 3 µL/min. by using a syringe pump (PHD Ultra, Harvard Apparatus, Holliston, MA, USA) with a 1 mL disposable syringe (Terumo) (Figure 45). For all of the flow measurements, the average shear rate at the hyperbolic contraction region was about $1750 \ s^{-1}$. The average or pseudo shear rate was calculated by $\bar{\gamma} = \frac{U}{D_h}$, where U is the mean velocity of the blood cells that were obtained at the contraction region, and D_h is the hydraulic diameter at the end of the contraction region.
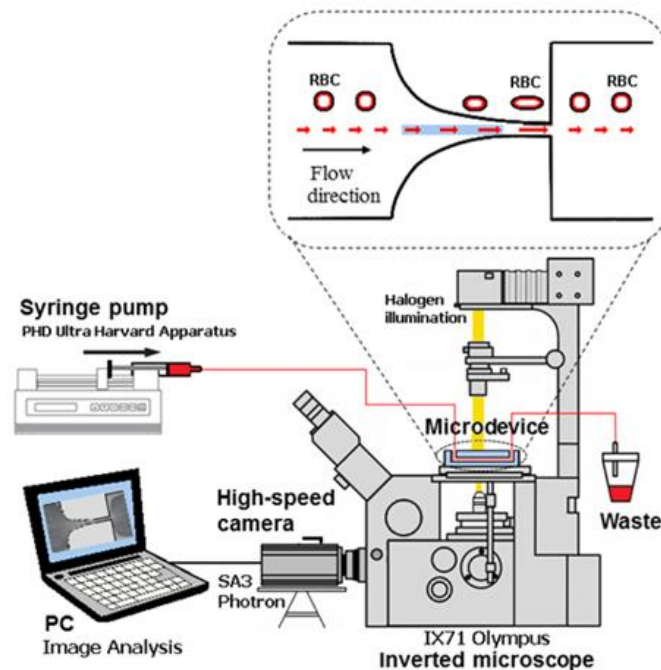
Figure 45. Experimental set-up used to perform the motion and measurements of the RBCs deformability.

The images of the RBCs flowing through the hyperbolic contraction were captured by the high-speed camera with a frame rate of 3000 frames/s and a shutter speed ratio of 1/75,000 s. These parameters were selected in order to obtain well defined RBCs and avoid possible image distortions that are caused by the high flow velocities at the contraction region. Table 11 shows the most of the relevant experimental parameters that were used to perform the RBCs deformability measurements.

Table 11. Main experimental parameters used to perform the RBCs deformability measurements.

Main experimental parameters	
Maximum width of the microchannel	400 μm
Minimum width of the microchannel	20 μm
Total length of the contraction region	382 μm
Depth of the microchannel	50 μm
Flow rate (syringe of 1 mL)	3 μL/min
Shear viscosity of the Dextran 40	4.5×10^{-3} Pa/s
Density of the Dextran 40	1046 Kg/m³
Haematocrit of the working fluid	1%
Temperature of the working fluid	22 °C
Magnification (M)	40×
Numerical Aperture (NA)	0.75
Frame rate	3000 frames/s
Exposure time	1/75000 s

9.2.3 Working Fluids

To perform the RBCs deformability studies, Dextran 40 (Sigma-Aldrich, Saint Louis, MO, USA) at 10% (w/v) solution containing 1% of haematocrit (Hct 1%, v/v) of RBCs was used as the working fluid. Briefly, venous blood samples from both patients and healthy donors were collected into 10 mL BD-Vacutainers (BD, Franklin Lakes, NJ, USA) tubes containing ethylenediaminetetraacetic acid (EDTA) to prevent coagulation. The RBCs and buffy coat were separated from the plasma after centrifugation (2500 rpm for 10 min., at 4 °C). The RBCs were then washed with physiological salt solution (PSS) and then centrifuged, with this procedure repeated twice. The RBCs were suspended in Dextran 40 to make several samples with low hematocrit levels of ∼1% by volume (cf. Figure 46) to obtain the measurements of individual RBC flowing through hyperbolic contraction. Dextran 40 was used as substitute of the blood plasma, since it prevents not only the sedimentation of the RBCs during the experimental assays, but also the cell clogging phenomenon. All of the analyses were performed within a maximum period of 12 h, with blood samples being hermetically stored at 4 °C until being used in the flow experiments.
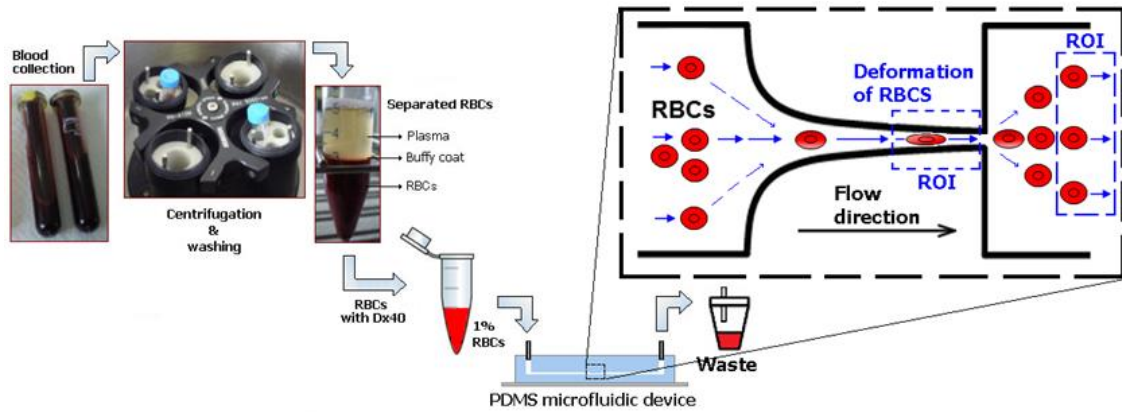
Figure 46. Schematic diagram from blood collection up to the flow microfluidic tests with RBCs. Samples with low hematocrit levels of ~1% were crucial in order to visualize individual RBC flowing through hyperbolic contraction. The ROI regions represent the regions of interest used to analyze the RBCs deformation index.

Image analysis was essential to obtain sharper, brighter, and clearer images of the RBCs flowing through the contraction, and to consequently obtain reliable velocity and deformability measurements, at the regions of interest (ROI) in both contraction and expansion regions, where the RBCs deform and recover to their normal circular shape, respectively (see Figure 47). The first step of this process involves the capture of videos with a resolution of 1024 X 576 pixels at frame intervals of 330 μs at the end of the contraction region. Figure 47a shows a typical obtained image. In order to reduce static artifacts in the images, a background image (Figure 47b) was created from the original stack images, by averaging each pixel over the sequence of static images while using an ImageJ function, called Z project, and then subtracted from the stack images. This process eliminates all the static objects including the microchannel walls and some possible attached cells, which resulted in having at the end, only the RBCs of interest (Figure 47c). Brightness/Contrast adjustment was also applied to enhance the image quality. Finally, the greyscale images were converted to binary images adjusting the threshold level (Figure 47d). At this stage, an Otsu threshold method was applied and when required, the level was manually refined. This segmentation process generates objects of interest (RBCs) as black ellipsoidal objects against a white background. At the end, the flowing RBCs in the binary images were measured frame by frame manually, by using Wand tool function in ImageJ. The main output results of these measurements were the major and minor axis lengths of the RBCs and the x-y coordinates of their centroid.
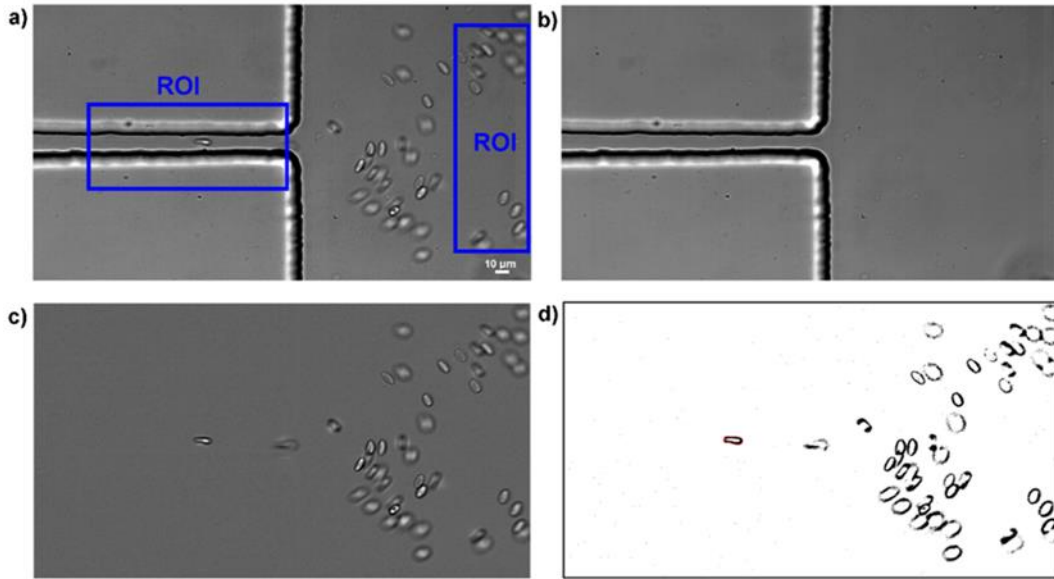
Figure 47. Images analysis sequence: a) original image at the regions of interest (ROI) regions in which moving RBCs as well as microchannel boundaries are visible, b) background image containing only static objects, c) original image after background subtraction showing only moving RBCs, and d) final binary image to perform measurements of the RBCs major and minor axis lengths.

The deformation ratio (DR) of all the measured RBCs was calculated and and saved with the cell's positions, given by their *x-y* coordinates, using the set of data obtained for the cells at the regions of interest (ROI) at both constriction and expansion locations of the microchannel. In this study, DR was defined by the equation that is shown in Figure 48, where L_{major} and L_{minor} refer to major and minor axis lengths of the RBC, respectively.

Figure 48. Definition of the deformation ratio, $DR = L_{major}/L_{minor}$, where Lmajor and Lminor are the major and minor axis lengths of the ellipse best fitted to the cell.

Although different automatic methods to track RBCs in microfluidic devices have been reported in the literature (Forsyth et al. 2010; Pinho et al. 2013a; Rodrigues et al. 2013b; Taboada et al. 2016; Lima et al. 2018), further improvements still need to be achieved to perform reliable deformability measurements. Hence, in the present study, hundreds of RBCs were manually tracked by using the ImageJ plug-in, MTrackJ. By selecting this method, it is possible to easily track the cells by a centroid based strategy and obtain their centroid position (x-y coordinates), by carefully tracking individual RBCs and consequently determine their orientations and velocities

100

within the hyperbolic contraction and downstream of the contraction region. In this study, measurements were only performed for the in focus cells flowing from the side, as it is possible to observe in the examples at the supplementary video. In this video, it is also possible to observe a RBC that flows from the top (the biconcave disc shape cell). However, the cells flowing with this orientation were not considered in our deformability measurements

9.2.4 Statistical Analysis

The statistical analysis was performed by using one-way ANOVA (Microsoft Office Excel, version Office 365 ProPlus). Before performing the ANOVA analysis, the requirements regarding normal distribution were tested by means of the Shapiro–Wilk's test. In this test, the null hypothesis that the population is normally distributed was accepted since $p > 0.05$. Overall, for the constriction region, we have measured the deformability of 1769 RBCs corresponding to 12 ESKD patients and a total of 736 measured RBCs, eight ESKDD patients and a total of 444 measured RBCs, and seven healthy controls and a total of 589 measured RBCs. All of the statistical tests were performed at a 95% confidence level; differences with $p < 0.05$ were considered to be statistically significant, and were represented as asterisks (*).

9.3 Results and Discussion

The determination of the RBC velocities plays an essential role in confirming whether the cells are deformed under similar flow conditions. Hence, before the deformability assessment of each sample, velocity measurements were performed and compared. After analyzing the average velocities of each sample at the contraction region, it was decided to compare the RBC deformability for all of the samples having similar flow conditions, i.e., both shear and extensional flows. Figure 49 shows representative RBC trajectories that were manually tracked within the hyperbolic contraction and downstream of the contraction region.

Figure 50 shows the measurements of the velocity and DR of representative RBCs flowing through the hyperbolic-shaped contraction (ROI region) for both healthy donors and ESKD patients (see also supplementary video). The majority of the RBC velocities tend to slightly increase as they move through the exit of the contraction, and then they suffer a dramatic reduction of their velocities when flowing from the narrow to the wide region of the microchannel (cf. Figure 50a). Overall, the velocities of the RBCs of both control and ESKD patients present a similar qualitative flow behavior at the tested region of the device, which results in a good agreement in the deformability results

obtained in all the samples (cf. Figure 50b). However, it should be noted that, quantitatively, the DR results indicate that the deformability of the ESKD RBCs under extensional flow tend to be smaller when compared to the control RBCs (cf. Figure 50b). These latter results are further confirmed with the measurements that were performed with several ESKD patients and healthy individual, as shown in Figure 51. Additionally, during all the flow visualization measurements at constriction region, the RBCs did not show any tumbling and rolling motion, which was mainly due to the uniform and strong extensional flow generated along the hyperbolic-shaped contraction. Note that, under shear flow, it is extremely common to observe RBCs flowing with complex dynamics, such as tumbling and rolling (Forsyth et al. 2010; Zeng and Ristenpart 2014). In the present study, the RBCs only exhibited such kind of complex flow motions at the expansion region, due to the dominant shear flow with respect to the extensional flow (cf. supplementary video). Hence, by using the proposed method, when the RBCs enter into the contraction region, they change from a circular to an elliptical shape, with a tendency to become increasingly elongated as they moved through the hyperbolic contraction. This latter flow behavior is possible to observe in Figure 50b. Additionally, in this figure, it can be observed that, at the downstream of the contraction region, the cells start to recover their nearly circular shape, exhibiting a DR that is close to one.
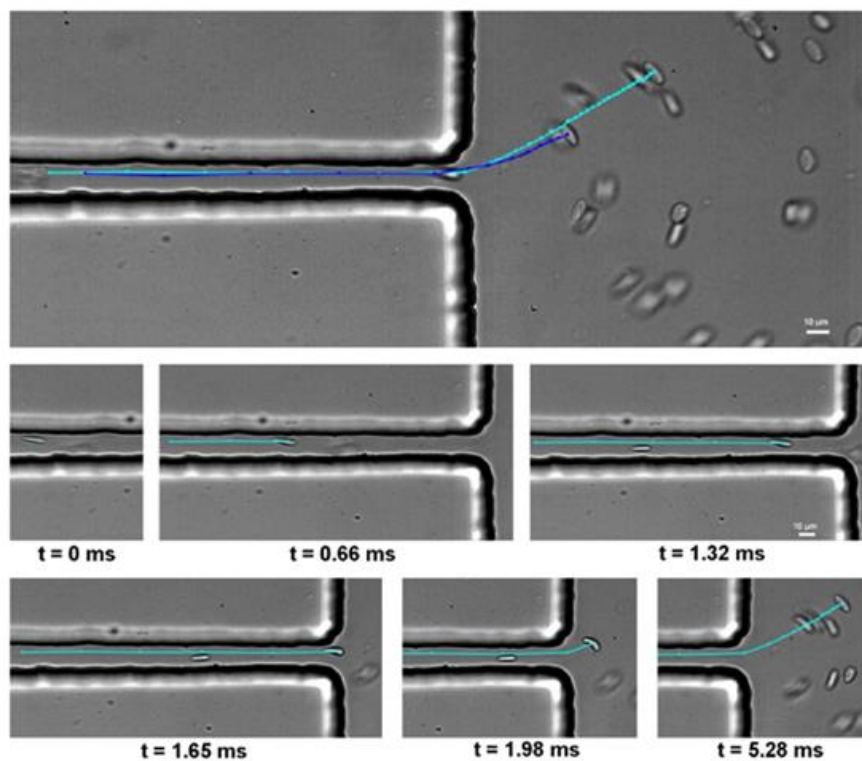
Figure 49. Trajectories of two RBCs flowing within the hyperbolic contraction and downstream of the contraction region (Upper part); detail of a representative trajectory of a RBC flowing near the microchannel wall at different times intervals (Bottom part).
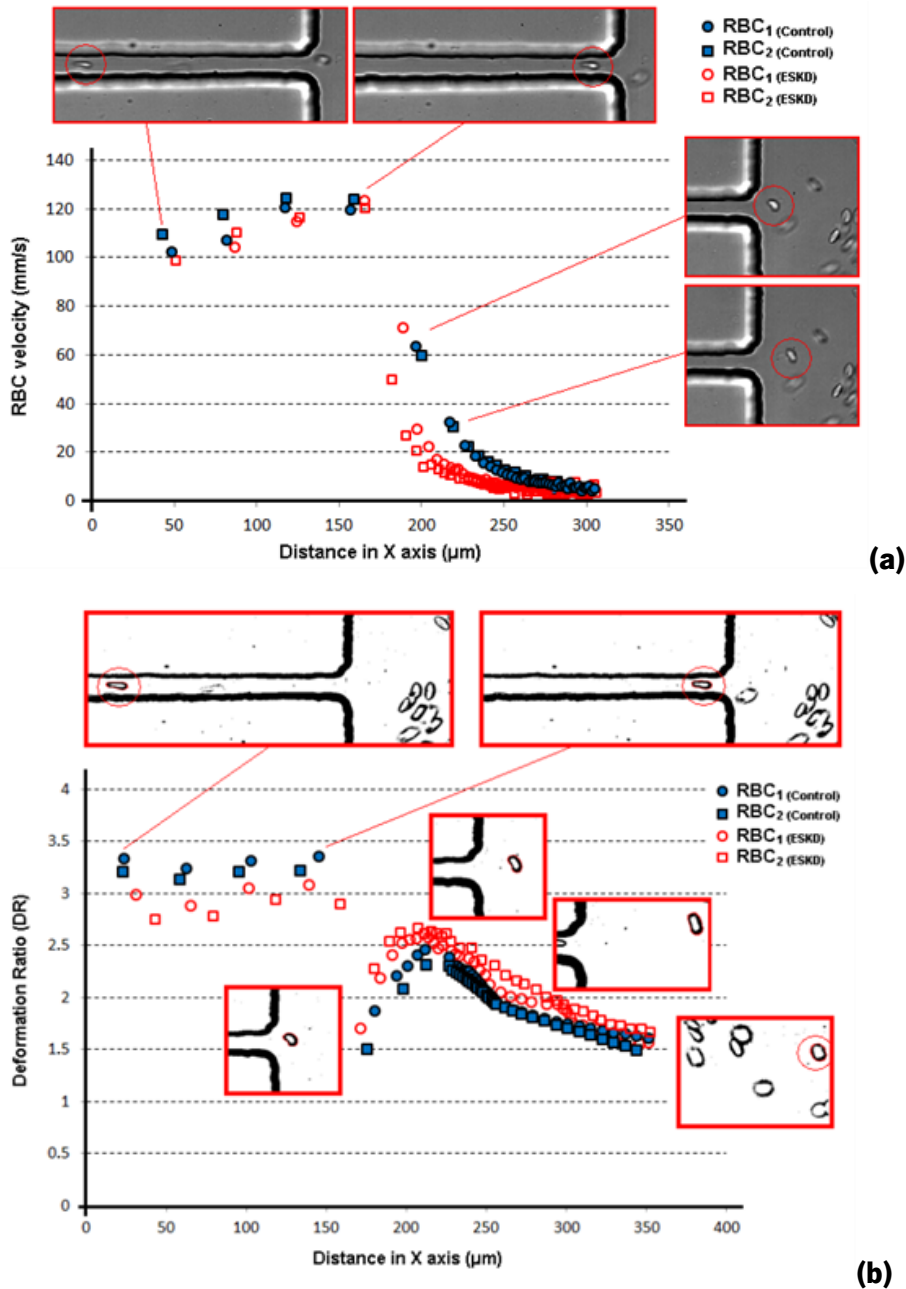
Figure 50. Measurements of RBCs from healthy donors and end-stage kidney disease (ESKD) patients, flowing within the hyperbolic contraction and downstream of the contraction region: (a) velocity measurements; (b) deformability measurements. The X axis represents the position of the cells centroid flowing through the microchannel.

Figure 51 shows the box plot of the deformation ratio (DR) for three different groups, i.e., samples of ESKD patients without diabetes type II (n = 12), samples of ESKD patients with diabetes (n = 8) type II, and samples from healthy donors (n = 7). For each patient sample, more than 60 RBCs with similar flow behavior were individually measured and analyzed at the hyperbolic constriction and recovering channel of the proposed microfluidic device (Figure 51). Additionally, Table 12 shows the data of the average DR and standard deviation (SD) of the RBCs deformation at both the contraction and expansion region for all of the tested samples. Overall, the deformability

of ESKD patients (with and without diabetes) measured at the hyperbolic constriction is lower in comparison with the RBCs from the normal healthy controls ($p < 0.05$), as shown in Figure 51b. This difference is more evident when only the group of ESKD patients with diabetes is taken into consideration. For instance, RBCs from ESKD patients without diabetes elongates, on average, 8% less within the hyperbolic contraction when compared to healthy controls, whereas RBCs from ESKD patients with diabetes elongates on average 14% less than the healthy controls (cf. Figure 51b). On the other hand, all of the cells analyzed, both healthy and diseased, have been shown to have a similar DR (nearly to 1, i.e., close to a spherical-shape) at the expansion region of the microchannel (Figure 51c,d), where cells tend to recover to their normal circular shape due to the low shear rate and a negligible strain rate. Therefore, the results from the present study demonstrate that the RBCs DR measured by using the proposed microfluidic device can be considered as a sensitive mechanical biomarker, as it was able to detect changes in DR of the RBCs from patients with different diseases in comparison with healthy ones. Moreover, this study also corroborates other previous research works (Shin et al. 2007; Agrawal et al. 2016), where, by using different deformability measurement techniques, it was shown that elongation of RBCs from patients with diabetes is lower in comparison with the non-diabetic healthy controls.

As previously mentioned, RBCs occupy almost half of the total blood volume and, under healthy conditions, they are highly deformable in order to pass through capillaries with dimensions several times lower than the RBCs size (Bento et al. 2018b)]. Hence, it is well known that the RBC deformability plays a crucial role in the rheological properties of blood in microvessels, i.e., the decrease of the RBC deformability might result in an increase of the blood viscosity and, consequently, in an increased tendency for microvascular complications and associated diseases. The results that are presented in this study indicate that the ESKD patients with and without diabetes have a tendency to decrease the RBCs deformability and, as a result, might have a substantial impact in the whole blood viscosity of these patient's health. This can result in an elicit hemolysis in the capillaries and premature sequestration of RBCs by the reticulo-endothelial system, and altering tissue oxygenation. However, a larger scale study is required to confirm whether the decrease of the RBC deformability contributes to the increase of the blood viscosity, or not.
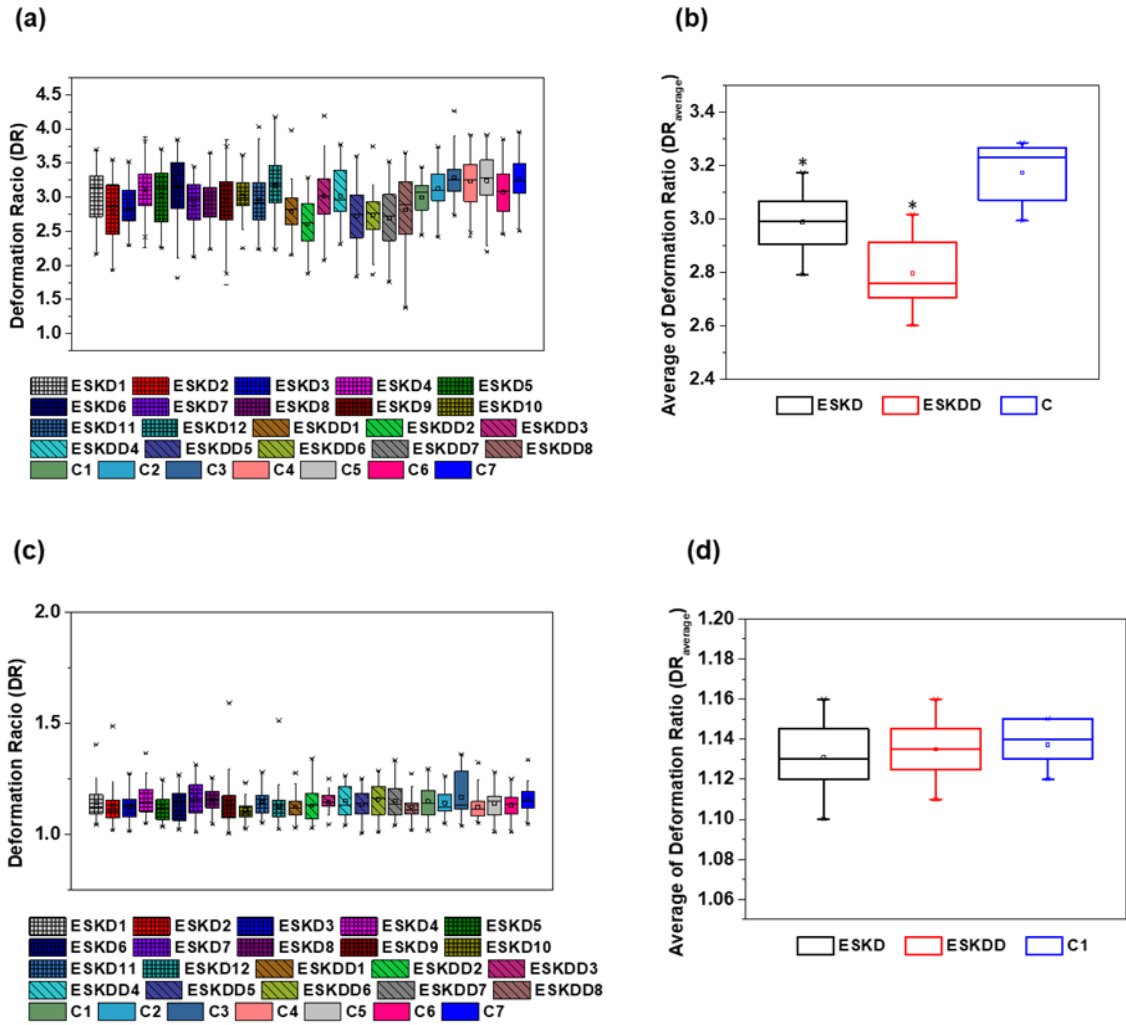
Figure 51. Box plot representation of RBC's deformation ratio (DR) measured by the proposed microfluidic device: (a) DR of individual donors, including ESKD patients, ESKD patients with diabetes and healthy donors (control) in the hyperbolic constriction, (b) Average DR of the groups of donors, including ESKD patients, ESKD patients with diabetes and healthy donors (control) in the hyperbolic constriction, (c) DR of individual donors, including ESKD patients, ESKD patients with diabetes and healthy donors (control) at the expansion region, (d) Average DR of the groups of donors, including ESKD patients, ESKD patients with diabetes and healthy donors (control at the expansion region. The asterisks (*) indicates statistically significant differences (p < 0.05) determined by Student's t test.

Table 12. Average DR and standard deviation (SD) of the flowing RBCs at both contraction and expansion region for each sample.

Blood Samples	Contraction Region DR		Expansion Region DR	
	Average	**SD**	**Average**	**SD**
ESKD1	3.03	0.34	1.12	0.08
ESKD2	2.79	0.36	1.10	0.09
ESKD3	2.86	0.26	1.13	0.06
ESKD4	3.11	0.25	1.14	0.08
ESKD5	3.03	0.39	1.12	0.06
ESKD6	3.15	0.37	1.15	0.07
ESKD7	2.89	0.31	1.15	0.08
ESKD8	2.93	0.26	1.16	0.05

ESKD9	2.94	0.35	1.13	0.10
ESKD10	3.02	0.24	1.10	0.05
ESKD11	2.96	0.32	1.14	0.06
ESKD12	3.17	0.35	1.13	0.08
ESKDD1	2.78	0.25	1.12	0.05
ESKDD2	2.60	0.27	1.13	0.07
ESKDD3	3.01	0.32	1.15	0.05
ESKDD4	3.02	0.32	1.13	0.08
ESKDD5	2.72	0.37	1.14	0.07
ESKDD6	2.74	0.28	1.16	0.08
ESKDD7	2.69	0.34	1.14	0.08
ESKDD8	2.81	0.43	1.11	0.06
C1	2.99	0.21	1.14	0.07
C2	3.12	0.23	1.13	0.06
C3	3.28	0.22	1.13	0.10
C4	3.23	0.27	1.12	0.06
C5	3.24	0.31	1.15	0.07
C6	3.07	0.30	1.14	0.07
C7	3.27	0.27	1.15	0.06

9.4 Limitations and Future Directions

The primary goal of the present work was to investigate the ability of hyperbolic converging microchannels to be used as an alternative clinical tool that is suitable to detect and diagnose RBC related diseases. To accomplish it, high speed microfluidic studies were performed in a hyperbolic contraction microchannel with a uniform depth of about 50 μm. The selection of this depth was a compromise solution mainly due to the limitation of our high-speed video camera: although, by decreasing the microchannel depth, the orientation of the cells tend to be more stable, the difficulty to measure the RBCs deformability increases due to the extremely high velocities that were generated at this region. The major advantage of this geometrical modification is the ability to use simple automatic methods, which results in a significant increase of the number of cell measurements performed under similar flow conditions. Nevertheless, in this study, we opted for manual measurements to guarantee that only adequate cells were included.

Additionally, we would like to refer that recently, Schonbrun et al. (2014) have shown that by using blue light the hemoglobin absorption makes cells extremely visible and easier to track in microchannels for low shear rates. Although this optical option looks promising, further research needs to be performed regarding the ability to measure blood cells at high shear rates. We consider that a combination of both strategies could result in a promising methodology to preform DR measurement of RBCs with high accuracy. The high-speed camera used due to its cost can be a limitation to consider the technique as a common tool; however, during the last two decades, the

cost of this technology has been decreasing in an exponential way, thus we believe that it will be possible to have in a more affordable way a high-speed system in the future. Another way can be the use of compact CCD cameras due its capacity to achieve similar sensitivity and exposure, but in an affordable way.

Chapter 10

Assessment of the deformability and velocity of healthy and artificially impaired red blood cells in narrow polydimethylsiloxane (PDMS) microchannels[7]

10.1 Introduction

Malaria is a parasitic disease with more than half the world population at risk and around 500 thousand deaths per year, with 80% of infections occurring in children under 5 years old (WHO 2016). This disease is mainly widespread in underdeveloped regions, with lack of proper infrastructure and living conditions, worsening the chances of infection for the population. The control, effective treatment and elimination of malaria require an early and accurate diagnosis. Currently, the malaria diagnosis is based on blood smear microscopy or rapid diagnostic tests (RDTs) (Wongsrichanalai et al. 2007; WHO 2017), which have limitations in the detection limit (only detect above 50 parasites/μL of blood). Additionally, microscopy has limitations in the required time to perform the assays and in the need for specialized technicians and/or laboratories, compromising the reduction of global incidence. To fulfill these needs, innovative diagnosis based on molecular assays have been developed, with detection limit below 2 parasites/μL, particularly using loop mediated isothermal amplification (Lucchi et al. 2016) or more advanced portable devices such as QuantuMDx/Q-POC. However, these techniques require disposable reagents, technicians, more than 30 minutes to get the test results and imply aseptic conditions (hard to maintain in endemic regions). Therefore, there is a huge need for fast, reagent-free and low-cost malaria diagnostic systems, without requiring special training and independent of the genetic variability of the parasite, and overall the final ideal device should comprise all these concerns.

The malaria parasite lifecycle passes from the mosquito vector to the human host by entering the liver cells where it maturates, to further being released into the blood stream, invading the red blood cells (RBCs). At this stage, the infected RBCs (iRBCs) suffer biochemical, optical and morphological changes (Diez-Silva et al. 2010; Saha et al. 2012), making these cells more rigid and thicker, resulting in a decrease of the cells velocity (when the cells are infected with Plasmodium falciparum parasite) (Handayani et al. 2009). Hemodynamic studies help to obtain information regarding the evolution of the disease. Particularly, the RBCs deformability and the RBCs velocity when crossing a geometric contraction can work as relevant markers for malaria diagnostics applications, since they are directly related to the changes that the parasite causes throughout the evolution of the disease (Shelby et al. 2003). The literature reports different methods for assessment of the RBCs deformability, including filtration (How et al. 1996), ektacytometry (Johnson 1989; Tomaiuolo 2014), optical tweezers (Grier 2003; Lim et al. 2004), micropipette aspiration (Hochmuth 2000) and microfluidic geometrical constrictions (Zhao et al. 2006; Lee et al. 2009; Hou et al. 2010; Yaginuma et al. 2013; Faustino et al. 2014b; Rodrigues et al. 2015b; Bento et al. 2018b). Some numerical and experimental studies in the literature already report the relation between RBCs deformability and hemodynamics (Chien 1987; Passos et al. 2016) or between deformability and the individual RBCs velocities in specific geometrical conditions (Shelby et al. 2003; Jeong et al. 2006; Tsai et al. 2016; Kaneko et al. 2017; Boas et al. 2018b). This work will be focused on a microfluidic system to measure the RBCs deformability and velocity, as well as to establish a relation between these properties when the cells cross geometric microcontractions, with the expectation to, in the future, compare this correlation with the real malaria effects in RBCs. The microfluidic systems are a potential alternative to the current diagnostic methods, since they are able to mimic the hemodynamic phenomena that happens in blood vessels and have advantages in terms of sample preparation and analysis (low volume of samples, easy handling, low-cost and fast processing), eliminating the need for specialized personnel (Hou et al. 2010). Additionally, microfluidic devices enhance the possibility of creating a fully automated and portable diagnostic device for malaria, when assembled in a microfluidic platform that includes microfluidic handling, control and readout electronics and data acquisition.

In order to develop and evaluate those microfluidic methods for the deformability and velocity assessment, it is essential to synthetically impair the RBCs for mimicking the malaria behavior, for testing the method's efficiency and reproducibility, without the constant need for parasites or infected samples, improving the laboratorial safety, when testing, and decreasing the

costs. For that purpose, glutaraldehyde, diamide and glucose will be used for increasing the rigidity of the RBCs and their effect in narrow constrictions will be compared (Babu and Singh 2004; Shin et al. 2008; Forsyth et al. 2010; Rodrigues et al. 2013a). When exposed to these chemicals, the RBCs will be rigidified and their dynamic behavior in narrow constrictions, relatively to deformability and velocity, will be compared to healthy RBCs. The evaluation of the RBCs velocity and deformability will be performed in a set of microchannels with abrupt constrictions, followed by abrupt expansions (Boas et al. 2018b). This approach takes advantage of the potential of these sudden geometrical contractions to deform the cells due to shear and extensional flows. The cells' behavior will be captured by a setup comprising a high-speed camera and a microscope, and the obtained images will be processed in two software tools (ImageJ and PIVLab) for determining both the RBCs' deformability and the RBCs' velocities, as well as determining the relation between those properties.

10.2 Materials and Methods

This section presents the materials and samples used to perform the experimental assays, as well as the description of the microchannels fabrication method, experimental setup and image processing techniques. In brief, RBCs samples with low concentration (low hematocrit) will be exposed to glutaraldehyde, diamide or glucose and will be tested in polydimethylsiloxane (PDMS) microchannels that comprise 8 μm widths abrupt contractions. The ability of the RBCs to flow through the microchannels contractions will be assessed.

10.2.1 Microchannels Fabrication

A polydimethylsiloxane (PDMS) microfluidic device was microfabricated by soft lithography techniques, using SU-8 molds (SU-8 purchased from Microchem Corporation, Westborough, MA, USA) (Pinto et al. 2014b; Faustino et al. 2016). PDMS (Sylgard 184 Silicone Elastomer kit obtained from Dow Corning) was chosen due to its transparency that is required to the microscope visualization, easy fabrication and low-cost for prototypes. The PDMS microchannels have a 25 μm height in order to reduce the flow volume and the number of RBCs within the microchannels making, also, easier to observe the RBCs. Each microchannel is composed by a linear transition zone followed by an abrupt contraction (at a 90° angle) with 8 μm width and 780 μm length (seen in Figure 52), designed to force the RBCs to deform and gain velocity when crossing it. The width of

the contractions mimics capillary vessels with the same average dimensions of the RBCs (around 8 µm).
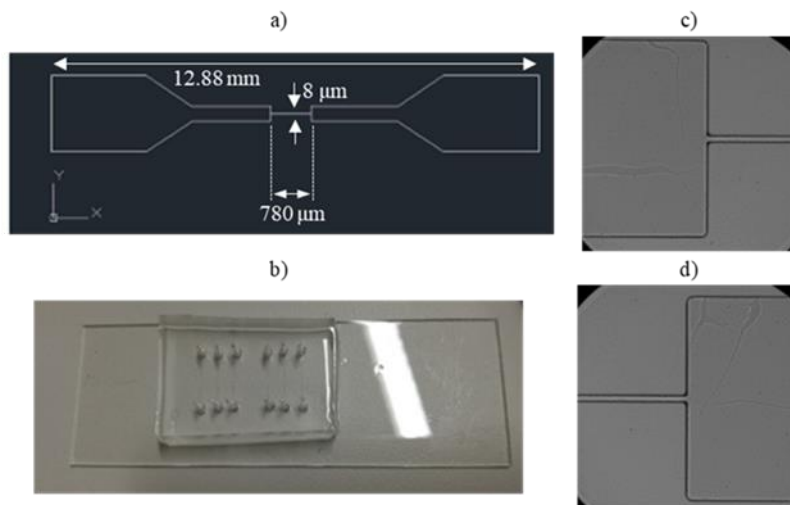
Figure 52. (a) 2D masks for the microchannels fabrication. The narrow contractions in the central region of the microchannels have 8 µm width; (b) PDMS microchannels with a 12.8 mm total length; (c) Detail of the entrance of the 8 µm width contraction of the PDMS microchannel; (d) Detail of the outlet of the 8 µm width contraction of the PDMS microchannel. Magnification: 40x.

10.2.2 Samples

For the *in vitro* assays, samples containing human RBCs (hematocrit = 0.5%) in Dextran40 (Dx40) were used. Human RBCs have a biconcave shape and typical diameters in the 6 µm – 8 µm range, being highly deformable.

The healthy human whole blood samples were taken from a female volunteer and provided by Instituto Politécnico de Bragança (Portugal). All procedures for the blood collection, transport and *in vitro* experiments were carried out in compliance with the EU directives 2004/23/CE, 2006/17/CE and 2006/86/CE and approved by the Unidade Local de Saúde do Nordeste (Bragança, Portugal). In order to evaluate the RBCs deformability and velocity in the microchannels, the RBCs were separated from the other blood constituents through centrifugation (15 minutes, 2000 rpm, at room temperature). After that, RBCs were re-suspended and washed twice in a physiological solution (PSS) (from B. Braun Medical, Germany) with a NaCl concentration of 0.9%. The Dx40 solution where the RBCs were suspended was used as a plasma-volume expander to prevent RBCs sedimentation and maintain the ideal osmotic physiological conditions for the RBCs. This solution was synthetically produced, by mixing 68 µL of CaCl2 with 201 µL of KC, 7.35 mL of NaCl and 5 g of Dx40 (for 1 M solution) (all reagents purchased from Sigma-Aldrich, USA). The 0.5% hematocrit, representing a 0.5% volume of RBCs in 5 ml of Dx40, was considered in order to assure that the RBCs are isolated when crossing the microchannel contraction. Although the 0.5%

hematocrit is significantly lower than the physiological one, it was decided to study diluted samples, to improve the visualizations and measurements of each individual RBC and, as result, to avoid effects such as interactions and aggregation of RBCs. Preliminary tests performed with hematocrit values ranging from 0.5% up to 2%, have shown that as the concentration of RBCs was increased, it was difficult to individually follow the RBCs and, consequently, to measure the RBCs velocity and deformation index. Hence, the current study was performed with a hematocrit of 0.5%.

The RBCs samples were then modified with glucose (Copan, USA), glutaraldehyde (Sigma-Aldrich, USA) and diamide (Sigma-Aldrich, USA) solutions, in order to rigidify the cells at different levels. These chemicals were selected since they are commonly used to perform deformability studies, are accessible and have simple preparation protocols, as well as they allow to rigidify the cells at different levels, according to the added concentration. To modify the RBCs with glucose, four different concentrations of glucose were considered: 2%, 5%, 10% and 20% (v/v). First, glucose (powder) was diluted in a phosphate buffered saline solution (PBS: pH 7.4). Then, the RBCs (already separated from the other blood constituents and suspended in Dx40) were incubated for 20 minutes, at room temperature, at each of the referred glucose concentrations. The cells were then washed in PSS to remove the excess of glucose from the samples and re-suspended in Dx40. To modify the cells with glutaraldehyde, at 0.00625%, 0.0125%, 0.025% and 0.08% glutaraldehyde concentrations (v/v), the RBCs (already separated from the other blood constituents and suspended in Dx40) were incubated for 10 minutes at each of the referred concentrations, washed in PSS, re-suspended in Dx40 and used right away. The RBCs were also modified with diamide, at 0.00625%, 0.0125%, 0.025%, 0.08%, 0.32% and 1% diamide concentrations (v/v), using the same protocol: incubation for 10 minutes at each of the referred concentrations, washing in PSS and re-suspension in Dx40.

10.2.3 Experimental Setup

The cells' deformability and velocity assays were performed with an experimental setup comprising the microfluidic device placed on the stage of an inverted microscope (IX71; Olympus). A flow rate of 5 µL/min was controlled using a syringe pump system (KD Scientific). For selecting the ideal flow rate, preliminarily studies were performed for four different flow rates (0.1, 1, 3 and 5 µl/min) and no significant differences were observed in the cells deformability. Additionally, it was observed that the syringe pump system presented more stability for the highest tested flow rate, i. e., the 5 µL/min. The images of the RBCs were captured using a high-speed camera

(Fastcam SA3, Photron) at a 2000 frames/s rate and exported to a computer to be analyzed. Each assay was repeated 3 times.

10.2.4 Image Processing and Analysis Techniques

The images exported from the high-speed camera to the computer were analyzed using two software tools: ImageJ (Abramoff et al.) and PIVLab (Thielicke and Stamhuis 2014; Thielicke and J. Stamhuis 2019). For each assay, a sequence of 10000 frames was considered. ImageJ was used to perform the pre-treatment of the acquired frames, in order to remove the noise and image artifacts, as well as convert them into binary images. Initially, the image sequence was imported and the crop function was executed to define the region of interest (ROI) as a rectangle with 308 × 332 μm dimension (Figure 53a)). Then, by using the Z-Project function, the selected frames were stacked to determine an average of the frames. This averaged frame was subtracted from all the frames under analysis, eliminating all static objects, which resulted in frames comprising only the visible RBCs, without any additional information. Finally, by using a threshold function, the images were converted into binary images. The ImageJ software was also used to measure the cells size in order to calculate the RBCs deformation index (DI). Using the ROI Manager and the Measure functions, it was possible to follow both the healthy and the impaired RBCs (example in Figure 53b)) and calculate their DI along the microchannel, using the expression: DI=(X-Y)/(X+Y), where X and Y represent the largest (X) and the smallest (Y) axis of the ellipse correspondent to the RBC under analysis. Typically, the RBCs' DI varies between 0 and 0.8, where 0 represents non-deformed cells and 0.8 represents cells at maximum elongation. For each assay, a group of RBCs was followed at the entrance and at the outlet of the contraction to measure their DI and determine an averaged value. Figure 53c) presents the area, at the entrance and at the outlet of the microchannel contraction (the areas inside the dashed lines in Figure 53c)), where the deformability of the RBCs is measured. These areas were chosen after performing preliminary observations of the RBCs flows. For the entrance of the contraction, it was selected a 121 × 237 μm region of interest, since it is in this area that the RBCs experience the highest extensional flow and consequently start to deform to enter the contraction. For the outlet, in the region immediately after exiting the contraction, the RBCs are at maximum deformation, and outside that region, the cells start to recover their original shape. Then, for assuring a standard area at the outlet for all assays, an 86 × 142 μm region of interest was selected. It should be noted that the evaluation area at the outlet of the contraction is significantly smaller than at the entrance. This difference is

explained by the authors' intention, in future devices and prototypes, of integrating micro-sensors in the outlet of the contraction (occupying the smallest area possible) and, therefore, in this work it was expected to obtain relevant data from a small area of evaluation in the outlet.

In order to determine the average of the velocity values of the RBCs at the entrance and at the outlet of each contraction, the sequence of frames was analyzed using the PIVLab image analysis toolbox, integrated in MATLAB. First, the pre-treated images were imported into the software and calibrated (relatively to their dimensions and time between frames), and a ROI mask was applied to remove the areas where there are no RBCs. Following, the motion of the particles between the frames was analyzed and the instantaneous velocities were calculated by the variation of the distance traveled by the RBCs between each time step. Then, the average velocity vectors (U_x and U_y) were calculated in the x and y directions and the velocity field of each sample was determined (U_{xy}) based on the equation: $|U_{xy}|=sqrt (U_{x2} + U_{y2})$. Finally, a filter was applied to smooth the images and remove the high frequencies, which could indicate spikes of velocity without physical significance. Figure 53d) presents an example of the velocity field distribution at the entrance of the contraction. It is possible to observe that the velocity of the RBCs is significantly higher in the zone of the narrowing entrance, reasoning that the abrupt transition causes the increase of the velocity of the RBCs. Note that, due to limitations of the available equipment, it was not possible to acquire frames with RBCs moving at high velocity in the interior of the microchannel contraction. As a result, almost no cells were registered in that region, explaining the 0 velocity in the interior of the contraction in the PIVLab image (Figure 53d)), this way the results section will approach and compare the DI and velocity of the RBCs at the entrance and outlet of the contractions, neglecting the study of cells inside the contraction regions. Note that both RBCs deformability and velocity are measured in the same area (as defined in Figure 53c), left and right) in order to establish a relation between the RBCs deformability and their velocity. After obtaining the velocity distribution immediately before the entrance and after the outlet of the contraction, it was defined a criterion for determining the RBCs velocity (as presented in the Results section 3): from the region of interest (Figure 53c), left and right), where the velocities are higher, the 100 pixels with highest velocity (obtained in PIVLab) were selected and those velocities were averaged, neglecting the surrounding areas with lowest velocities.

Additional details on the ImageJ and PIVLab procedures for determination of RBCs deformability and velocity can be found in (Boas et al. 2018b).

114
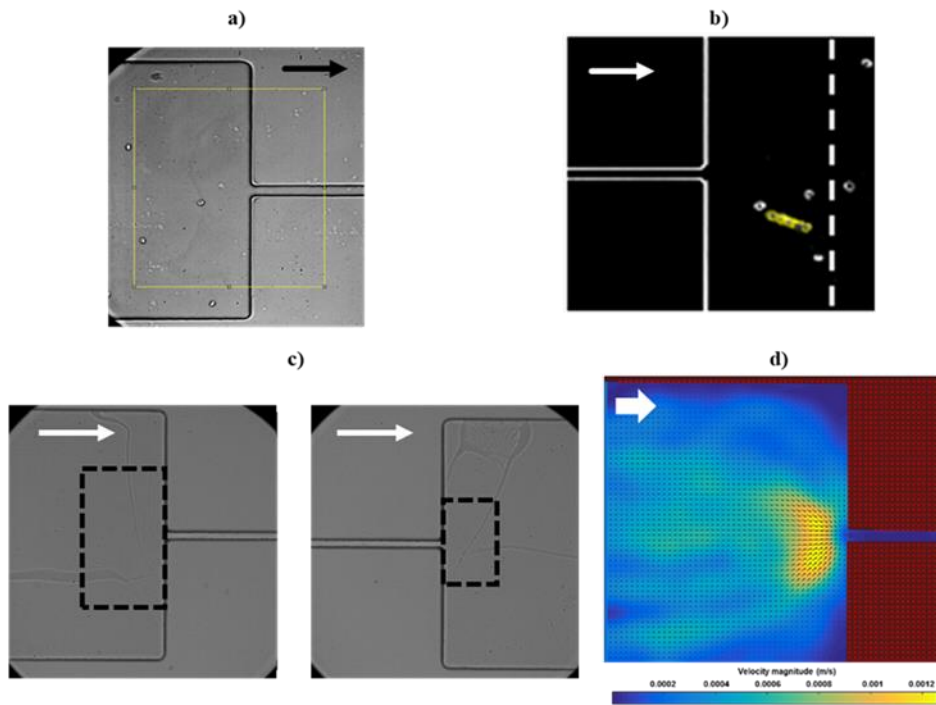
Figure 53. (a) Example of a cut-off of a transfer zone (308 × 332 µm) in the entrance of the microchannel contraction, using the crop function of ImageJ; (b) Example of a tracked RBC at the outlet of the microchannel contraction, using ImageJ, where the dashed line represents a region where the RBCs expand after the outlet (relaxation area); (c) Definition of the areas (inside the dashed lines) for measuring the RBCs deformability and velocity at the entrance (left - 121 × 237 µm region) and at the outlet (right - 86 × 142 µm region) of the microchannel contraction (Magnification: 40x); (d) Example of the velocity distribution, obtained with PIVLab, of healthy RBCs (non modified) at the entrance of the microchannel contraction (the arrows indicate the flow direction in each frame). Note that, due to limitations of the available equipment (frame rate acquisition), it was not possible to acquire frames with RBCs moving at high velocity in the interior of the microchannel contraction and, as a result, no cells were registered in that region, explaining the 0 velocity in the image.

10.3 Results and Discussion

This section presents the deformability and velocity results (obtained as in section 10.2.4) of the comparison between healthy and chemically modified RBCs with glucose, glutaraldehyde and diamide. All the presented results are an average of 3 assays. For each assay, a sequence of 10000 frames was considered and around 10 RBCs were followed to measure their DI. Figure 54 shows examples of RBCs from different assays at the entrance and at the outlet of the contraction in the PDMS microchannel, for different percentages of glucose, considering a 5 L/min flow rate, and for a healthy RBCs sample (for control - 0% glucose). From Figure 54a), it is possible to detect a difference between the RBCs deformability as the glucose percentage increases, i. e., the RBCs change from a deformed/stretched shape to a non-deformed shape as the cells have more difficulties to deform and tend to keep their original shape.

115

(a)
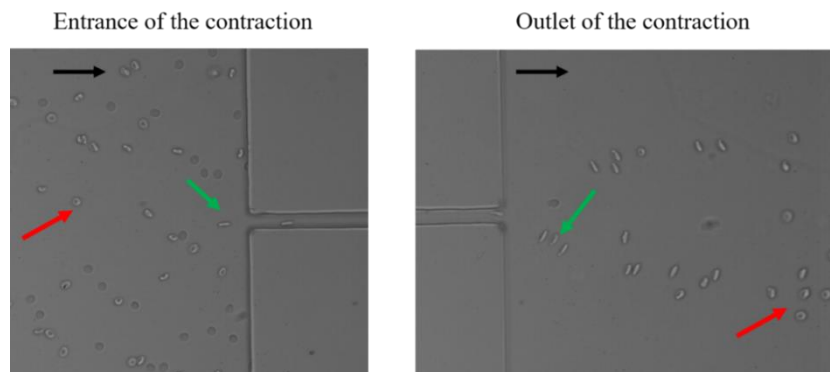
(b)
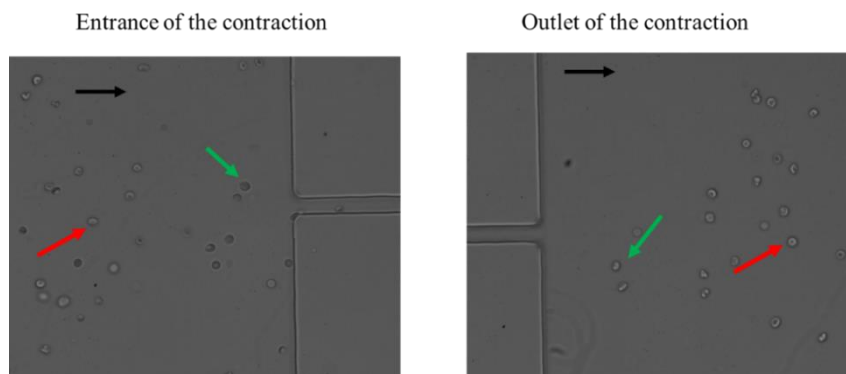
(c)

Figure 54. a) Examples of healthy RBCs and RBCs modified with different glucose percentages at the entrance and at the outlet of the microchannel contraction, extracted from three assays; b) Healthy RBCs (red arrow, left) deforming at the entrance of the contraction (green arrow, left), leaving the contraction still deformed (green arrow, right) and recovering their original shape following the outlet on an expansion area (red arrow, right); c) 10% glucose modified RBCs (red arrow, left) with almost no deformation at the entrance of the contraction (green arrow, left) and leaving the contraction (green arrow, right), recovering their original shape on an expansion area (red arrow, right). The black arrows indicate the flow direction.

116

These results suggest that the glucose concentration affects the RBCs' deformability, in agreement with several past studies regarding the influence of glucose over the RBCs deformability (Babu and Singh 2004; Shin et al. 2008). The increase of glucose (hyperglycemia) in the RBCs causes damage in the RBCs membranes and increases the blood viscosity, also increasing the cells aggregation, which leads to a significant decrease on the RBCs DI. When the RBCs were modified with glutaraldehyde or diamide the results were similar to the ones observed for glucose (shown in Figure 54), and, therefore, only the glucose images are presented. Following the outlet of the microchannel contraction, the RBCs start to recover their shape, decreasing again their deformation index, as shown in Figure 54b) and c), for an assay with healthy RBCs and one assay with 10% glucose modified RBCs.

Figure 55 presents the DI for healthy and modified RBCs (with glucose, glutaraldehyde and diamide), at the entrance and at the outlet of the microchannel 8 µm contraction, as well as at the relaxation area (see Figure 53 b)), for the 5 µL/min flow rate.

The results show that, as the percentage of glucose, glutaraldehyde or diamide increases, the cells tend to become more rigid, decreasing their DI (Rodrigues et al. 2013a). While the healthy cells deformed at the entrance of the contraction to pass throughout the contraction and then recovered to their initial shape after reaching the microchannel expansion area, the modified RBCs did not deform and it was observed some aggregation of the cells, increasing the difficulty to cross the contraction. At the outlet of the contraction, where the deformability was measured, the RBCs tend to start to recover their original shape, which is verified in Figure 55: the RBCs at the outlet have lower DI than at the entrance of the contraction. As the rigidity of the cells increases, the difference between the DI at entrance and at the outlet of the contraction decreases. Since the evaluation regions at entrance and at the outlet have a different total area (as defined in Figure 53c)) it may also help to explain the hysteresis in the results between entrance and outlet (the entrance evaluation area is larger than the outlet evaluation area).

Table 13 presents the differences between the averaged RBC deformability at the entrance of the contraction and at the relaxation area, for all the tested conditions. This allows us to observe the cells' maximum deformability, passing from their deformed shape entering the contraction, until their recovered shape after relaxation. The results show that, as the rigidity of the cells increases, the difference in the deformability between the entrance and the relaxation area (DDI) decreases, and this behavior is similar for the three chemicals tested: Glucose, glutaraldehyde, and diamide.

Glucose

$y = 0.0008x^2 - 0.0436x + 0.609$
$R^2 = 0.9484$

$y = 0.0012x^2 - 0.0472x + 0.5236$
$R^2 = 0.9646$

● Entrance of the contraction ▲ Outlet of the contraction ◆ Relaxation Area

(a)

Glutaraldehyde

$y = 0.3981e^{-86.14x}$
$R^2 = 0.9387$

$y = 0.4602e^{-78.68x}$
$R^2 = 0.9318$

● Entrance of the contraction ▲ Outlet of the contraction ◆ Relaxation Area

(b)

Diamide

$y = 0.538e^{-1.628x}$
$R^2 = 0.9935$

$y = 0.4382e^{-1.655x}$
$R^2 = 0.959$

● Entrance of the contraction ▲ Outlet of the contraction ◆ Relaxation Area

(c)

Figure 55. DI and error bars for healthy and a) glucose, b) glutaraldehyde and c) diamide modified RBCs, at the entrance (blue series), at the outlet (orange series) and at the relaxation area (green series) of the microchannel contraction and trend lines. In b), the X represents the clogging of the microchannel, with no deformability or velocity data. Each point of the plots is the average of 30 RBCs (3 assays for each condition and 10 RBCs followed in each assay).

Table 13. Difference of the deformation index (Δ DI) between the RBCs deformability at the entrance of the contraction (Figure 53c), left) and at the relaxation area (Figure 53b)) for all the tested conditions, obtained from the data presented in Figure 55.

Sample	Concentration (%)	ΔDI
Healthy RBCs	0	0.479
RBCs + Glucose	2	0.463
	5	0.410
	10	0.139
	20	0.041
RBCs + Glutaraldehyde	0.00625	0.196
	0.0125	0.074
	0.025	0.034
	0.08	X
RBCs + Diamide	0.00625	0.493
	0.0125	0.482
	0.025	0.464
	0.08	0.396
	0.32	0.267
	1	0.068

It was also observed that, for 0.08% (v/v) glutaraldehyde modified RBCs, the rigidified cells clogged the entrance of the contraction and no deformability or velocity data could be extracted (this is represented by X in Figure 55 b)). Therefore, for a high concentration of glutaraldehyde, it was unable to measure the transiting velocity of the cells. Figure 56 presents an example of clogging at the entrance of the contraction, when the RBCs were modified with a 0.08% (v/v) concentration of glutaraldehyde.
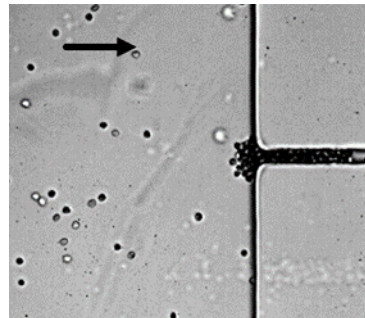
Figure 56. Detail of clogging at the entrance of the 8 μm contraction when the RBCs were modified with a 0.08% (v/v) concentration of glutaraldehyde.

Elevated blood glucose in the RBCs alters RBCs membrane proteins through glycosylation and oxidation. Glutaraldehyde penetrates into cell membranes and non-specifically cross-links the cytosol, the cytoskeletal, and the transmembrane proteins, acting on all components of the cell and increasing the effective viscosity of the cytoplasm and lipid membrane. Diamide is a spectrin- specific cross-linker, oxidizing thiol groups while forming disulfide bonds within the structural region (Forsyth et al. 2010). The obtained results indicate that viscous effects in the

cytoplasm and/or lipid membrane are a dominant factor when dictating dynamic responses of RBCs in pressure-driven flows, explaining the higher effect of the glutaraldehyde in damaging the RBCs and the microchannel clogging, when compared to diamide and glucose (Forsyth et al. 2010).

Figure 57 presents the average cell velocity for healthy and modified RBCs (with glucose, glutaraldehyde and diamide), at the entrance and at the outlet of the microchannel 8 µm contraction, for the 5 µL/min flow rate.

Overall, the results agree with the ones of the deformability. When it was evaluated the average velocity at the high velocity regions, it was found that the impaired RBCs (by adding glucose, glutaraldehyde or diamide) presented lower velocities than healthy RBCs, indicating that the increase of the RBCs rigidity causes the non-deformed cells to follow streamlines that on average have lower velocity, while the stretched and healthy RBCs follow streamlines that on average have higher velocity. Supplementary material videos show how the cells gain velocity when entering the contraction, explaining the higher velocity immediately at the outlet of the contraction (when compared to the velocity at the entrance), before starting to relax and recover their original shape. Similarly to the deformability results, for 0.08% (v/v) glutaraldehyde modified RBCs, the rigidified cells clogged at the entrance of the contraction and, as a result, no velocity data could be extracted (this is represented by X in Figure 57 b)).

Additionally, it would be interesting to quantitatively study the relation between deformation index and velocity inside the microchannel contraction, besides the data presented at entrance and outlet (Figure 55 and Figure 57). However, due to technical limitations of the high-speed acquisition system, it was not possible to acquire an enough number of RBCs with high quality contrast to perform the measurements of RBCs deformability and velocity with the software tools referred in section 10.2. Despite that limitation, some RBCs could still be observed within the contraction. Examples of RBCs (healthy, with 0.025% diamide and with 10% glucose) flowing within the contraction are shown in Figure 58.

(a)

(b)

(c)
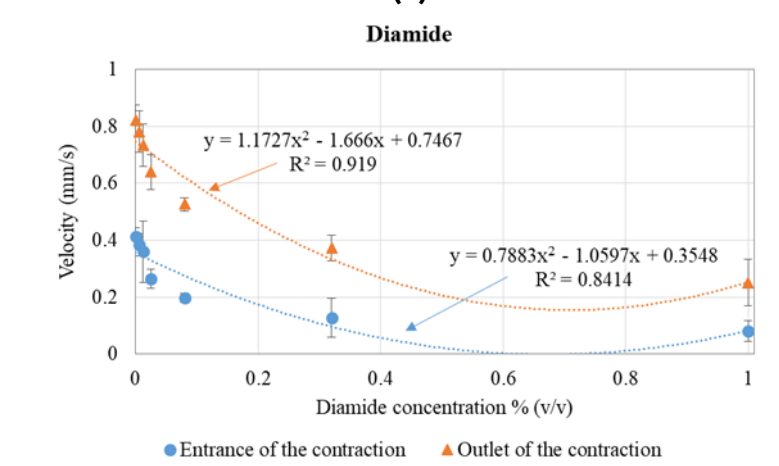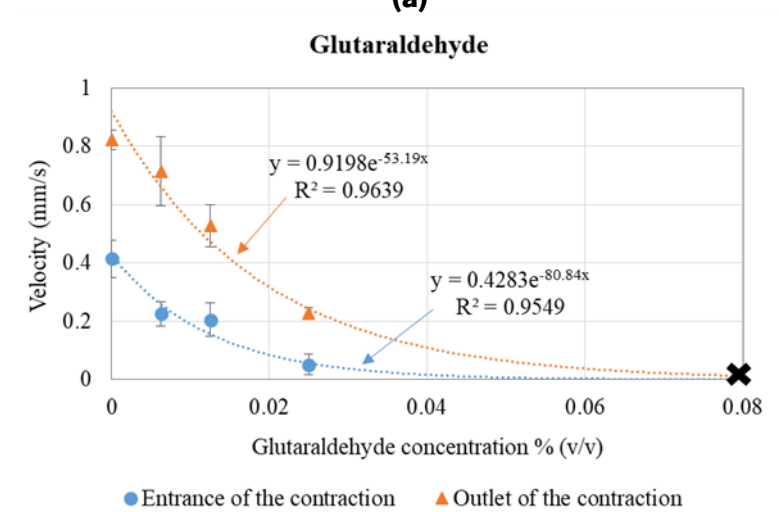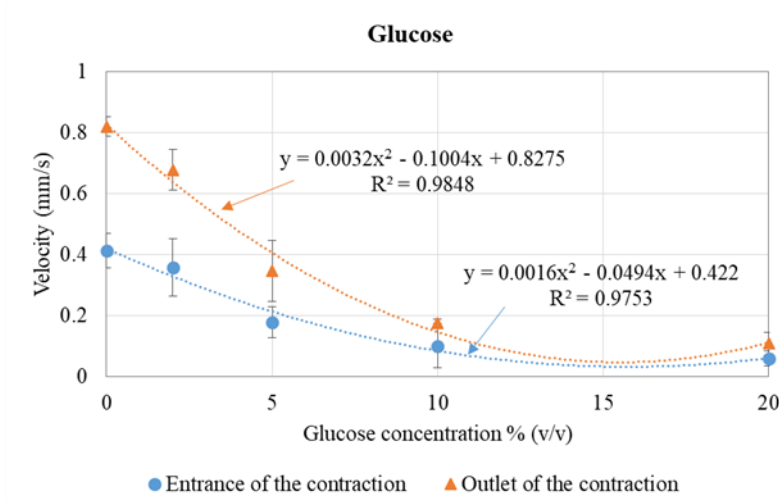
Figure 57. Velocity (mm/s) and error bars for healthy and a) glucose, b) glutaraldehyde and c) diamide modified RBCs, at the entrance (blue series) and at the outlet (orange series) of the microchannel contraction and trend lines. In b), the X represents the clogging of the microchannel, with no deformability or velocity data.
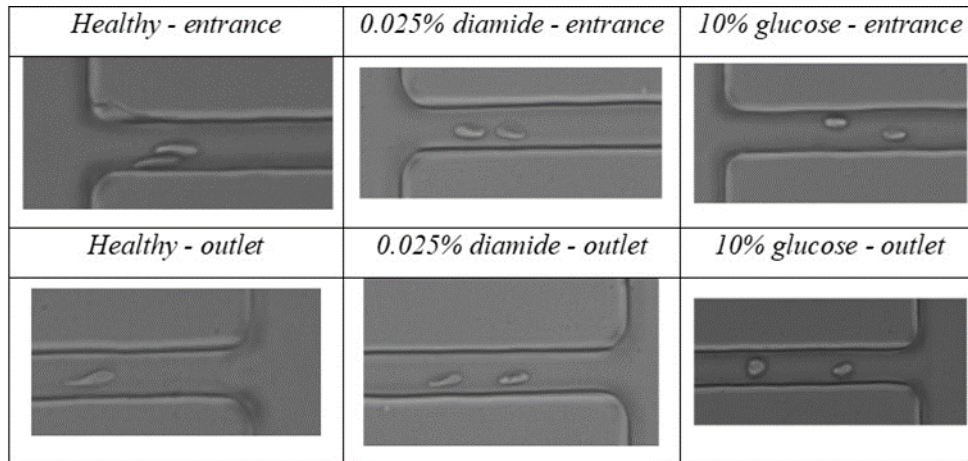
Figure 58. Examples of healthy RBCs, RBCs modified with 0.025% diamide and RBCs modified with 10% glucose inside the 8 μm width microchannel contraction, at different areas (entrance and outlet of the contraction).

A qualitative analysis of the presented results shows that healthy RBCs cross the microchannel contraction in a more deformed shape than the 0.025% diamide and 10% glucose samples, and the 10% glucose samples are less deformable than the 0.025% diamide ones, which corroborates the quantitative results (before the entrance and after the outlet) presented in Figure 57. Supplementary material presents videos of healthy and modified RBCs flowing at the entrance and at the outlet of the contraction, allowing a better observation of the RBCs behavior at the different regions of the microchannel contraction.

Since one of the main objectives of this work was to establish a relation between the RBCs deformability and their velocity, Figure 59 presents the velocity vs DI calibration curves for glucose, glutaraldehyde and diamide modified RBCs at the entrance and at the outlet of the microchannel contraction. This figure purpose is to show the dispersion that occurs between the cells. Therefore, instead of presenting all RBCs averaged together (as in Figure 55 and Figure 57), it is intended to evaluate how each small group of cells fits the deformability vs velocity curve, in order to understand their individualized behavior. Therefore, from the performed assays, the RBCs were gathered in groups of 3 cells measured under the same conditions and their average was calculated (each blue dot of the plots). Consequently, each plot of Figure 59 gathers data from a high number of RBCs (3 RBCs × number of dots in each plot, leading to a range of RBCs between 3 x 16 = 48 in Figure 8 d) and 3 x 28 = 84 in Figure 59 e)), measured in the areas defined in Figure 53.

Based on the results, it is observed that, overall and as expected, for all synthetically modified RBCs, an increase of the cells deformation index leads to an increase of the cells velocity, both at the entrance and at the outlet of a microchannel contraction. When comparing the velocity with the deformability correlation at entrance and at outlet, it is clear, for all the tested methods,

122

that the results at the outlet present a better fitting to the linear tendency curve than at the entrance (based on the R2 values). Therefore, in the future, when advancing for a diagnostic tool, the analysis must be performed at the outlet of the contraction (the place to integrate a sensor), where the RBCs behavior is more trustful. Additionally, our results indicate that diamide is the most interesting approach for mimicking the malaria effects on RBCs with the intention of exploring sensor applications, as the velocity vs DI results show a better fitting to the linear tendency curve (R2 = 0.89) and, consequently, it is easier to control the velocity vs deformability curve. These results are a promising step to help the development of integrated sensors in microfluidic devices that allow the design of an autonomous malaria detection system, of high sensitivity, precise, low-cost, portable and with low energy consumption.
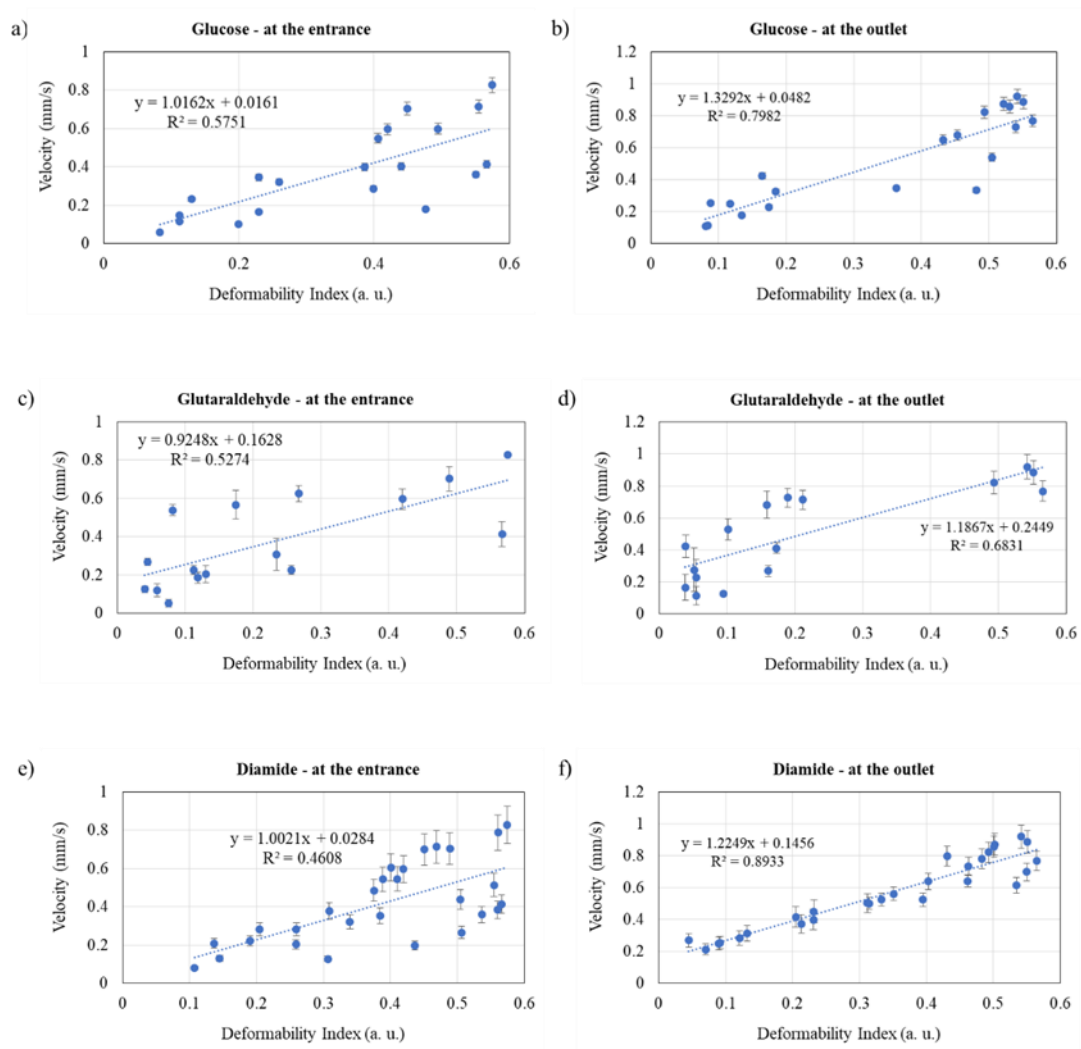
Figure 59. Velocity (mm/s) vs Deformability (a.u.) curve, measured at the entrance and at the outlet of the 8 μm contraction, for the RBCs samples modified with a) at entrance; glucose, b) at outlet; glucose c) at entrance; glutaraldehyde; d) at outlet; glutaraldehyde, e) at entrance; diamide and f) at outlet; diamide.

10.4 Future Perspectives

Future works will include the increase of the cell quantity in order to define the average property of the entire cell population with higher accuracy, since the physical properties of individual RBCs within the same RBC population can vary significantly (Picot et al. 2015). Additionally, since the ultimate goal is to develop a clinical tool, more blood samples from different donors will be assessed to increase the RBCs variability and to include more independent data. It is also planned to improve our high-speed video microsystem allowing the capture of good enough quality images to quantitatively measure both velocity and deformability of the RBCs flowing across the microchannel contraction. This improvement will allow to develop an improved association between RBC deformability and transiting velocity through the narrow constrictions. Finally, after obtaining an improved correlation with synthetically modified samples, it is intended to test real parasite-affected RBCs samples (Barber et al. 2018) to measure their deformability and velocity, compare disease and artificially impaired RBCs, stablish target values and fully validate the proposed approach. This improved correlation will be used to relate the RBCs behavior according to the various stages of malaria and to develop integrated sensors in microfluidic devices for RBCs velocity measurements.

Part IV

Conclusion and Future work

Chapter 11

Conclusion and Future Work

11.1 Final remarks

In this thesis, the fabrication of microfluidic structures was extremely important and as result, it was presented not only the fundamentals of lithography and non-lithography low-cost techniques but also the main features, advantages and limitations of each technique. The fabrication methods without need of clean room facilities were the most applied in this research work. Some insights were taken, such as soft lithographic techniques allow the fabrication of both 2D and 3D structures with high resolution, with dimensions down to a few nanometers. However, this technique has associated high maintenance costs and is inadequate for mass production. On the other hand, non-lithographic techniques, in spite of being appropriate for mass production, only can achieve microstructures with dimensions on the micrometric range. The selection of best technique for a specific microstructure was easier when we take into account all the features described above. It was also important, to perform detailed investigation on the current cell separation and deformation techniques, that are also reviewed and described in Chapter 3 and Chapter 4 of this thesis.

The cells separation can be applied in microfluidic devices by using passive methods or active methods. The passive separation methods were presented in Chapter 3 due its main advantages, such as the non-application of external forces and its simple way to separate cells avoiding their destruction. However, there are still several challenges to overcome, such as clogging, hematocrit limitations, the amount of the sample and preparation time. Despite these limitations, the passive separation method has a huge potential to be applied in microfluidic devices, mainly because of the simple integration on the microfluidic devices, the reduced size of these microdevices when compared with active methods that will need integration external actuators, increasing the complexity and compromising the portability of the microfluidic device.

I

It was concluded that passive microfluidic devices have many advantages in performing both separation and deformation cell assessments in the same microfluidic device. These devices have the ability to detect small changes in RBC deformability in a more efficient and less time-consuming way when compared with other deformability measurement techniques, such as micropipette aspiration, rheoscope, and optical tweezers. By comparing different geometries and by taken into account both flow visualization and RBCs deformability results it was concluded that the geometry have a strong impact on the results and as result it was selected the structure more suitable for our purpose (more details can be found in Chapter 4).

11.2 Conclusion

One of the main aims of this thesis was investigate the effect of different geometries in the separation and deformation of healthy and pathological cells. The Part III is mainly the results divided by chapters with papers, already published or submitted where the main conclusions are the following:

• The microfluidic device MD3 was the most suitable to perform plasma/RBCs separation as it showed the highest CFL aspect ratio, which corresponds to the flow of lesser RBCs into the outlets O1/O9, as it was confirmed by optical absorbance. It was also observed that the RBCs separation efficiency increases with the number of crossflow filter steps and, as a result, it was possible to assess the RBCs deformability at the hyperbolic contractions located at the outlets of the device.

• The spectrophotometry method by optical absorbance, allowed to quantify the RBCs at each outlet. This method was also used to quantify the chemical change of RBCs, with glutaraldehyde. Although this method was shown to be effective, the protocol needs to be improved due to the application of different kinds of fluids frequently used for the separation process.

• Hyperbolic microfluidic channels were shown to be a successful method to measure the RBC deformation of pathological blood samples from patients with ESKD (with and without diabetes type II). It was shown that this method has potential to be a viable clinical tool suitable to detect and diagnose RBC related disease. Another important finding was related to the comparison of the cells at the expansion region, where the RBCs have recovered their normal circular shape. At this region, the cells were deformed under low shear rate and negligible strain rate. Under those conditions, we have not found any difference between the ESKD patients and the healthy controls. This latter result indicates that the RBCs need to be submitted to high mechanical stresses to

deform the cells and, consequently, to detect different state of blood diseases. Although the proposed microfluidic tool requires further improvements, the results that were obtained from the present study suggest that this technique is able to assure a simple and efficient cell deformability assessment at both physiological and pathological situations.

 • From another study where it was chemically modified RBCs (to mimic malaria), it was concluded that, by adding glucose, glutaraldehyde or diamide, the RBCs membrane tends to become stiffer, decreasing the cells deformability and, consequently, decreasing the cell shape recovery capacity. Additionally, when the RBCs rigidity increased, the RBCs velocity decreased. A relationship between deformability and velocity was evaluated and it was concluded that, for all synthetically modified RBCs, an increase of the cells deformation index led to an increase of the cells velocity. It was also verified that diamide was the most interesting approach to impair the cells and mimic the malaria effects on RBCs, as the velocity vs deformation index results have shown the best fitting to a linear tendency curve and, consequently, it would be easier to control the deformability and velocity of the cells based on this method.

11.3 Future work

For future works, it will be interesting study separation and deformation with different pathologic blood, besides diabetes. It will be interesting to use blood with different stages of malaria, to assess not only the deformation of the RBCs at different stages, but also separate the different stages of malaria using the pillars and the levels in the microchannel.

The improvement of the separation efficiency can be achieved by using active forces, such as acoustic waves produced by piezoelectric actuators. The vibration could be helpful when the hematocrit is high (total blood), in order to prevent the clogging at the pillars section.

The deformation index could be also analysed by using smaller microchannels but for that we will need a much better high-speed camera.

Another future work could be to perform mesh less numerical simulations of these complex microfluidic channels, in order to improve the design of the separation levels, evaluate different flow rates, cells, or even particles.

References

Abdelgawad M, Watson MWL, Young EWK, et al (2008) Soft lithography: masters on demand. Lab Chip 8:1379–1385

Abkarian M, Faivre M, Horton R, et al (2008) Cellular-scale hydrodynamics. Biomed Mater 3:34011

Abramoff MD, Magalhães PJ, Ram SJ Image processing with ImageJ. 11:36–42

Agrawal R, Smart T, Nobre-Cardoso J, et al (2016) Assessment of red blood cell deformability in type 2 diabetes mellitus and diabetic retinopathy by dual optical tweezers stretching technique. Sci Rep 6:15873. https://doi.org/10.1038/srep15873

Alghane M, Chen BX, Fu YQ, et al (2011) Experimental and numerical investigation of acoustic streaming excited by using a surface acoustic wave device on a 128° YX-LiNbO3 substrate. J Micromechanics Microengineering 21:15005

Alvankarian J, Bahadorimehr A, Yeop Majlis B (2013) A pillar-based microfilter for isolation of white blood cells on elastomeric substrate. Biomicrofluidics 7:14102. https://doi.org/10.1063/1.4774068

Amasia M, Madou M (2010) Large-volume centrifugal microfluidic device for blood plasma separation. Bioanalysis 2:1701–1710. https://doi.org/10.4155/bio.10.140

Amering AR, Smith DE, Spence JM (1990) Toner composition and method of making

Anderson JR, Chiu DT, Wu H, et al (2000) Fabrication of microfluidic systems in poly (dimethylsiloxane). Electrophoresis 21:27–40

Ansari MA (2009) Parametric study on mixing of two fluids in a three-dimensional serpentine microchannel. Chem Eng J 146:439–448

Astor BC, Muntner P, Levin A, et al (2002) Association of Kidney Function With Anemia. Arch Intern Med 162:1401. https://doi.org/10.1001/archinte.162.12.1401

Babu N, Singh M (2004) Influence of hyperglycemia on aggregation, deformability and shape parameters of erythrocytes. Clin Hemorheol Microcirc 31:273–280

Bao N, Zhang Q Fau - Xu J-J, Xu Jj Fau - Chen H-Y, Chen HY (2005) Fabrication of poly(dimethylsiloxane) microfluidic system based on masters directly printed with an office laser printer. J Chromatogr A TA - A, J Chromatogr 1089:270–275. https://doi.org/10.1016/j.chroma.2005.07.001

Barber BE, Russell B, Grigg MJ, et al (2018) Reduced red blood cell deformability in Plasmodium knowlesi malaria. Blood Adv 2:433 LP – 443

Bartholomeusz DA, Boutte RW, Andrade JD (2005) Xurography: rapid prototyping of microstructures using a cutting plotter. J Microelectromechanical Syst 14:1364–1374. https://doi.org/10.1109/JMEMS.2005.859087

Baskurt OK, Meiselman HJ (2003) Blood Rheology and Hemodynamics. Semin Thromb Hemost 29:435–450. https://doi.org/10.1055/s-2003-44551

Becker H, Locascio LE (2002) Polymer microfluidic devices. Talanta 56:267–287

Bento D, Fernandes CS, Miranda JM, Lima R (2019) In vitro blood flow visualizations and cell-free layer (CFL) measurements in a microchannel network. Exp Therm Fluid Sci 109:109847. https://doi.org/10.1016/j.expthermflusci.2019.109847

Bento D, Lima R, M. Miranda J (2015) Computation of a Three-Dimensional Flow in a Square Microchannel: A Comparison Between a Particle Method and a Finite Volume Method. Micro Nanosyst. 7:142–147

Bento D, Pereira AI, Lima J, et al (2018a) Cell-free layer measurements of in vitro blood flow in a microfluidic network: an automatic and manual approach. Comput Methods Biomech Biomed Eng Imaging Vis 6:629–637. https://doi.org/10.1080/21681163.2017.1329029

Bento D, Rodrigues RO, Faustino V, et al (2018b) Deformation of red blood cells, air bubbles, and droplets in microfluidic devices: Flow visualizations and measurements. Micromachines 9:151

Bernard A, Delamarche E, Schmid H, et al (1998) Printing patterns of proteins. Langmuir 14:2225–2229

Betancourt T, Brannon-Peppas L (2006) Micro- and nanofabrication methods in nanotechnological medical and pharmaceutical devices. Int J Nanomedicine 1:483–495

Bhagat AAS, Bow H, Hou HW, et al (2010) Microfluidics for cell separation. Med Biol Eng Comput 48:999–1014. https://doi.org/10.1007/s11517-010-0611-4

Bhushan B (2007) Springer Handbook of Nanotechnology. Springer

Boas L, Faustino V, Lima R, et al (2018a) Assessment of the Deformability and Velocity of Healthy and Artificially Impaired Red Blood Cells in Narrow Polydimethylsiloxane (PDMS) Microchannels. Micromachines 9:384. https://doi.org/10.3390/mi9080384

Boas LV, Lima R, Minas G, et al (2018b) Imaging of Healthy and Malaria-Mimicked Red Blood Cells in Polydimethylsiloxane Microchannels for Determination of Cells Deformability and Flow Velocity BT - VipIMAGE 2017. In: Tavares JMRS, Natal Jorge RM (eds). Springer International Publishing, Cham, pp 915–922

Bordatchev E, Nikumb S (2008) Fabrication of Moulds and Dies Using Precision Laser Micromachining and Micromilling Technologies . J Laser Micro/Nanoengineering 3:. https://doi.org/10.2961/jlmn.2008.03.0009

Bridle H, Miller B, Desmulliez MPY (2014) Application of microfluidics in waterborne pathogen monitoring: A review. Water Res 55:256–271. https://doi.org/http://dx.doi.org/10.1016/j.watres.2014.01.061

Brines M, Grasso G, Fiordaliso F, et al (2004) Erythropoietin mediates tissue protection through an erythropoietin and common β-subunit heteroreceptor. Proc Natl Acad Sci U S A 101:14907–14912. https://doi.org/10.1073/pnas.0406491101

Broers AN, Hoole ACF, Ryan JM (1996) Electron beam lithography—Resolution limits. Microelectron Eng 32:131–142

Cabriales L, Hautefeuille M, Fernández G, et al (2014) Rapid fabrication of on-demand high-resolution optical masks with a CD–DVD pickup unit. Appl Opt 53:1802–1807

Calejo J, Pinho D, Galindo-Rosales F, et al (2015) Particulate Blood Analogues Reproducing the Erythrocytes Cell-Free Layer in a Microfluidic Device Containing a Hyperbolic Contraction. Micromachines 7:4. https://doi.org/10.3390/mi7010004

Campo-Deaño L, Dullens RPA, Aarts DGAL, et al (2013) Viscoelasticity of blood and viscoelastic blood analogues for use in polydymethylsiloxane in vitro models of the circulatory system. Biomicrofluidics 7

Cardoso VF, Irusta S, Navascues N, Lanceros-Mendez S (2016) Comparative study of sol-gel methods for the facile synthesis of tailored magnetic silica spheres. Mater Res Express 3:1–7. https://doi.org/10.1088/2053-1591/3/7/075402

Cardoso VF, Minas G (2012) Micro Total Analysis Systems. In: Mitra SK, Chakraborty S (eds) Fabrication, Implementation, and Applications, 1st edn. pp 319–365

Carvalho DAM, Rodrigues ARO, Faustino V, et al (2018) Microfluidic Deformability Study of an Innovative Blood Analogue Fluid Based on Giant Unilamellar Vesicles. J Funct Biomater 9:70. https://doi.org/10.3390/jfb9040070

Carvalho V, Gonçalves IM, Souza A, et al (2021) Manual and automatic image analysis segmentation methods for blood flow studies in microchannels. Micromachines 12:1–20. https://doi.org/10.3390/mi12030317

Catarino S, Lima R, Minas G (2016) Smart devices: Lab-on-a-chip. Elsevier Ltd.

Catarino SO, Rodrigues RO, Pinho D, et al (2019) Blood cells separation and sorting techniques of passive microfluidic devices: From fabrication to applications. Micromachines 10:. https://doi.org/10.3390/mi10090593

Chakraborty S (2005) Dynamics of capillary flow of blood into a microfluidic channel. Lab Chip 5:421–430. https://doi.org/10.1039/B414566F

Chen CS, Mrksich M, Huang S, et al (1998) Micropatterned surfaces for control of cell shape, position, and function. Biotechnol Prog 14:356–363

Chen CS, Mrksich M, Huang S, et al (1997) Geometric control of cell life and death. Science (80-) 276:1425–1428

Chen J, Chen D, Yuan T, et al (2014) Blood plasma separation microfluidic chip with gradual filtration. Microelectron Eng 128:36–41. https://doi.org/10.1016/j.mee.2014.05.032

Chen X, Cui D, Liu C, Li H (2008) Microfluidic chip for blood cell separation and collection based on crossflow filtration. Sensors Actuators B Chem 130:216–221. https://doi.org/10.1016/j.snb.2007.07.126

Chenouard N, Smal I, De Chaumont F, et al (2014) Objective comparison of particle tracking methods. Nat

Methods 11:281–289. https://doi.org/10.1038/nmeth.2808

Chien S (1987) Red Cell Deformability and its Relevance to Blood Flow. Annu Rev Physiol 49:177–192. https://doi.org/10.1146/annurev.ph.49.030187.001141

Chien S, Usami S, R S (1984) Blood flow in small tubes. In: Eds GRR (ed) Handbook of physiology – The cardiovascular system. American Physiological Association , pp 217–249

Childs WR, Nuzzo RG (2002) Decal transfer microlithography: a new soft-lithographic patterning method. J Am Chem Soc 124:13583–13596

Cho YI, Mooney MP, Cho DJ, et al (2008) Hemorheological disorders in diabetes mellitus. J Diabetes Sci Technol 2:1130–8. https://doi.org/10.1177/193229680800200622

Choi J, Hyun J, Yang S (2015) On-chip Extraction of Intracellular Molecules in White Blood Cells from Whole Blood. Sci Rep 5:15167. https://doi.org/10.1038/srep15167

Chung YC, Hsu YL, Jen CP, et al (2004) Design of passive mixers utilizing microfluidic self-circulation in the mixing chamber. Lab Chip 4:70–77. https://doi.org/10.1039/b310848c

Cokelet GR, Goldsmith HL (1991) Decreased hydrodynamic resistance in the two-phase flow of blood through small vertical tubes at low flow rates. Circ Res 68:1 LP – 17

Dalili A, Samiei E, Hoorfar M (2019) A review of sorting, separation and isolation of cells and microbeads for biomedical applications: microfluidic approaches. Analyst 144:87–113. https://doi.org/10.1039/c8an01061g

Dao M, Lim CT, Suresh S (2003) Mechanics of the human red blood cell deformed by optical tweezers. J Mech Phys Solids 51:2259–2280. https://doi.org/10.1016/j.jmps.2003.09.019

Davis JA, Inglis DW, Morton KJ, et al (2006) Deterministic hydrodynamics: Taking blood apart. Proc Natl Acad Sci 103:14779 LP – 14784. https://doi.org/10.1073/pnas.0605967103

de Cindio B, Gabriele D, Catapano G, et al (2007) The blood rheology in renal pathology. Ann Ist Super Sanita 43:156–163

del Campo A, Greiner C (2007) SU-8: a photoresist for high-aspect-ratio and 3D submicron lithography. J Micromechanics Microengineering 17:R81. https://doi.org/10.1088/0960-1317/17/6/R01

Delamarche E, Bernard A, Schmid H, et al (1997) Patterned delivery of immunoglobulins to surfaces using microfluidic networks. Science (80-) 276:779–781

Delamarche E, Bernard A, Schmid H, et al (1998) Microfluidic networks for chemical patterning of substrates: design and application to bioassays. J Am Chem Soc 120:500–508

Deng Y, Papageorgiou DP, Li X, et al (2020) Quantifying Fibrinogen-Dependent Aggregation of Red Blood Cells in Type 2 Diabetes Mellitus. Biophys J 119:900–912. https://doi.org/10.1016/j.bpj.2020.07.026

Dey PK, Pramanick B, RaviShankar A, et al (2010) Microstructuring of SU-8 resist for MEMS and bio-applications. Int J Smart Sens Intell Syst 3:118–129

Diez-Silva M, Dao M, Han J, et al (2010) Shape and Biomechanical Characteristics of Human Red Blood Cells in Health and Disease. MRS Bull 35:382–388. https://doi.org/DOI: 10.1557/mrs2010.571

Dimov IK, Basabe-Desmonts L, Garcia-Cordero JL, et al (2011) Stand-alone self-powered integrated microfluidic blood analysis system (SIMBAS). Lab Chip 11:845–850. https://doi.org/10.1039/C0LC00403K

Duffy DC, McDonald JC, Schueller OJA, Whitesides GM (1998) Rapid prototyping of microfluidic systems in poly (dimethylsiloxane). Anal Chem 70:4974–4984. https://doi.org/10.1021/ac980656z

Dulińska I, Targosz M, Strojny W, et al (2006) Stiffness of normal and pathological erythrocytes studied by means of atomic force microscopy. J Biochem Biophys Methods 66:1–11. https://doi.org/10.1016/j.jbbm.2005.11.003

Fåhræus R, Lindqvist T (1931) The Viscosity of the Blood in Narrow Capillary Tubes. Am J Physiol – Leg Content 96:

Faivre M, Abkarian M, Bickraj K, Stone HA (2006) Geometrical focusing of cells in a microfluidic device: an approach to separate blood plasma. Biorheology 43:147–159

Faustino V, Catarino SO, Lima R, Minas G (2016) Biomedical microfluidic devices by using low-cost fabrication techniques: A review. J Biomech 49:2280–2292. https://doi.org/10.1016/j.jbiomech.2015.11.031

Faustino V, Catarino SO, Pinho D, et al (2018) A Passive Microfluidic Device Based on Crossflow Filtration for Cell Separation Measurements: A Spectrophotometric Characterization. Biosensors 8:125. https://doi.org/10.3390/bios8040125

Faustino V, Pinho D, Yaginuma T, et al (2014a) Flow of red blood cells suspensions through hyperbolic microcontractions

Faustino V, Pinho D, Yaginuma T, et al (2014b) Extensional flow-based microfluidic device: Deformability assessment of red blood cells in contact with tumor cells. BioChip J 8:42–47. https://doi.org/10.1007/s13206-014-8107-1

Faustino V, Rodrigues RO, Pinho D, et al (2019) A microfluidic deformability assessment of pathological red blood cells flowing in a hyperbolic converging microchannel. Micromachines 10:. https://doi.org/10.3390/mi10100645

Fedosov DA, Caswell B, Popel AS, Karniadakis GE (2010) Blood flow and cell-free layer in microvessels. Microcirculation 17:615–628. https://doi.org/10.1111/j.1549-8719.2010.00056.x

Feng G-H, Tsai M-Y (2010) Acoustic emission sensor with structure-enhanced sensing mechanism based on micro-embossed piezoelectric polymer. Sensors Actuators A Phys 162:100–106

Fiddes LK, Raz N, Srigunapalan S, et al (2010) A circular cross-section PDMS microfluidics system for replication of cardiovascular flow conditions. Biomaterials 31:3459–3464. https://doi.org/http://dx.doi.org/10.1016/j.biomaterials.2010.01.082

Figeys D, Pinto D (2000) Lab-on-a-chip: a revolution in biological and medical sciences. Anal Chem 72:330-A

Fiorini GS, Chiu DT (2005) Disposable microfluidic devices: fabrication, function, and application. Biotechniques 38:429–446

Fornal M, Lekka M, Pyka-Fościak G, et al (2006) Erythrocyte stiffness in diabetes mellitus studied with atomic force microscope. Clin Hemorheol Microcirc 35:273–276

Forsyth AM, Wan J, Owrutsky PD, et al (2011) Multiscale approach to link red blood cell dynamics, shear viscosity, and ATP release. Proc Natl Acad Sci U S A 108:10986–10991. https://doi.org/10.1073/pnas.1101315108

Forsyth AM, Wan J, Ristenpart WD, Stone HA (2010) The dynamic behavior of chemically "stiffened" red blood cells in microchannel flows. Microvasc Res 80:37–43. https://doi.org/10.1016/j.mvr.2010.03.008

Fraden J (2010) Handbook of Modern Sensors: Physics, Designs, and Applications. Springer

Fujii T (2002) PDMS-based microfluidic devices for biomedical applications. Microelectron Eng 61–62:907–914. https://doi.org/http://dx.doi.org/10.1016/S0167-9317(02)00494-X

Fujiwara H, Ishikawa T, Lima R, et al (2009) Red blood cell motions in high-hematocrit blood flowing through a stenosed microchannel. J Biomech 42:838–843. https://doi.org/10.1016/j.jbiomech.2009.01.026

Fukuda M, Kishi I, Nakano TNV-UA (1974) Binder resins for electron photography and the like and method of productive thereof

Gambaruto AM (2016) Flow structures and red blood cell dynamics in arteriole of dilated or constricted cross section. J Biomech 49:2229–2240. https://doi.org/10.1016/j.jbiomech.2015.11.023

Garcia V, Dias R, Lim R (2012) In Vitro Blood Flow Behaviour in Microchannels with Simple and Complex Geometries. In: Applied Biological Engineering - Principles and Practice. InTech, pp 393–416

Gates BD (2005) Nanofabrication with molds & stamps. Mater Today 8:44–49. https://doi.org/http://dx.doi.org/10.1016/S1369-7021(05)00701-7

Gates BD, Whitesides GM (2003) Replication of vertical features smaller than 2 nm by soft lithography. J Am Chem Soc 125:14986–14987

Gates BD, Xu Q, Love JC, et al (2004) Unconventional nanofabrication. Annu Rev Mater Res 34:339–372

Gidaspow D, Huang J (2009) Kinetic Theory Based Model for Blood Flow and its Viscosity. Ann Biomed Eng 37:1534–1545. https://doi.org/10.1007/s10439-009-9720-3

Glenister FK, Coppel RL, Cowman AF, et al (2002) Contribution of parasite proteins to altered mechanical properties of malaria-infected red blood cells. Blood 99:1060–1063. https://doi.org/10.1182/blood.V99.3.1060

Goldsmith HL (1971) Deformation of human red cells in tube flow. Biorheol TA - Biorheol 7:235–242

Goldsmith HL, Cokelet GR, Gaehtgens P (1989) Robin Fahraeus: evolution of his concepts in cardiovascular physiology. Am J Physiol - Hear Circ Physiol 257:H1005–H1015

Goldsmith HL, Marlow JC (1979) Flow behavior of erythrocytes. II. Particle motions in concentrated suspensions of ghost cells. J Colloid Interface Sci 71:383–407. https://doi.org/http://dx.doi.org/10.1016/0021-9797(79)90248-0

Gonçalves I, Souza R, Coutinho G, et al (2021) Thermal conductivity of nanofluids: A review on prediction models, controversies and challenges. Appl Sci 11:. https://doi.org/10.3390/app11062525

Gossett DR, Tse HTK, Lee SA, et al (2012) Hydrodynamic stretching of single cells for large population mechanical phenotyping. Proc Natl Acad Sci U S A 109:7630–7635. https://doi.org/10.1073/pnas.1200107109

Gossett DR, Weaver WM, Mach AJ, et al (2010) Label-free cell separation and sorting in microfluidic systems. Anal Bioanal Chem 397:3249–3267. https://doi.org/10.1007/s00216-010-3721-9

Greer J, Sundberg SO, Wittwer CT, Gale BK (2007) Comparison of glass etching to xurography prototyping of microfluidic channels for DNA meltinh analysis. J Micromechanics MicroengineeringComparison Glas Etch to xurography Prototyp Microfluid channels DNA melting Anal 17:2407–2413. https://doi.org/10.1088/0960-1317/17/12/003

Grier DG (2003) A revolution in optical manipulation. Nature 424:810–816. https://doi.org/10.1038/nature01935

Guillou L, Dahl JB, Lin J-MG, et al (2016) Measuring Cell Viscoelastic Properties Using a Microfluidic Extensional Flow Device. Biophys J 111:2039–2050. https://doi.org/10.1016/j.bpj.2016.09.034

Guo Q, Duffy SP, Matthews K, et al (2016) Deformability based sorting of red blood cells improves diagnostic sensitivity for malaria caused by Plasmodium falciparum. Lab Chip 16:645–654. https://doi.org/10.1039/C5LC01248A

Haeberle S, Brenner T, Zengerle R, Ducrée J (2006) Centrifugal extraction of plasma from whole blood on a rotating disk. Lab Chip 6:776–781. https://doi.org/10.1039/b604145k

Haeberle S, Zengerle R (2007) Microfluidic platforms for lab-on-a-chip applications. Lab Chip 7:1094–1110

Han M, Lee W, Lee S-K, Lee SS (2004) 3D microfabrication with inclined/rotated UV lithography. Sensors Actuators A Phys 111:14–20

Handayani S, Chiu DT, Tjitra E, et al (2009) High deformability of Plasmodium vivax-infected red blood cells under microfluidic conditions. J Infect Dis 199:445–450. https://doi.org/10.1086/596048

Hansen C, Quake SR (2003) Microfluidics in structural biology: smaller, faster... better. Curr Opin Struct Biol 13:538–544. https://doi.org/http://dx.doi.org/10.1016/j.sbi.2003.09.010

Henon Y, Sheard GJ, Fouras A (2014) Erythrocyte deformation in a microfluidic cross-slot channel. RSC Adv 4:36079–36088. https://doi.org/10.1039/C4RA04229H

Heuberger A (1988) X-ray lithography. J Vac Sci Technol B 6:107–121

Hochmuth RM (2000) Micropipette aspiration of living cells. J Biomech 33:15–22. https://doi.org/10.1016/S0021-9290(99)00175-X

Hosseini SM, Feng JJ (2012) How malaria parasites reduce the deformability of infected red blood cells. Biophys J 103:1–10. https://doi.org/10.1016/j.bpj.2012.05.026

Hou HW, Bhagat AAS, Chong AGL, et al (2010) Deformability based cell margination—a simple microfluidic design for malaria-infected erythrocyte separation. Lab Chip 10:2605–2613. https://doi.org/10.1039/c003873c

Hou HW, Bhagat AAS, Lee WC, et al (2011) Microfluidic devices for blood fractionation. Micromachines 2:319–343. https://doi.org/10.3390/mi2030319

Hou HW, Li QS, Lee GYH, et al (2009) Deformability study of breast cancer cells using microfluidics. Biomed Microdevices 11:557–564. https://doi.org/10.1007/s10544-008-9262-8

How T, Black RA, Hughes P (1996) Hemodynamics of vascular prostheses

Huang S, Undisz A, Diez-Silva M, et al (2013) Dynamic deformability of Plasmodium falciparum-infected erythrocytes exposed to artesunatein vitro. Integr Biol 5:414–422. https://doi.org/10.1039/c2ib20161e

Huntington MD, Odom TW (2011) A Portable, Benchtop Photolithography System Based on a Solid-State

Light Source. Small 7:3144–3147. https://doi.org/10.1002/smll.201101209

Hyun K-A, Kwon K, Han H, et al (2013) Microfluidic flow fractionation device for label-free isolation of circulating tumor cells (CTCs) from breast cancer patients. Biosens Bioelectron 40:206–212. https://doi.org/10.1016/J.BIOS.2012.07.021

Imai Y, Omori T, Shimogonya Y, et al (2016) Numerical methods for simulating blood flow at macro, micro, and multi scales. J Biomech 49:2221–2228. https://doi.org/10.1016/j.jbiomech.2015.11.047

Irace C, Carallo C, Scavelli F, et al (2014) Blood viscosity in subjects with normoglycemia and prediabetes. Diabetes Care 37:488–492. https://doi.org/10.2337/dc13-1374

Ishikawa T, Fujiwara H, Matsuki N, et al (2011) Asymmetry of blood flow and cancer cell adhesion in a microchannel with symmetric bifurcation and confluence. Biomed Microdevices 13:159–167. https://doi.org/10.1007/s10544-010-9481-7

Jackman RJ, Duffy DC, Ostuni E, et al (1998) Fabricating large arrays of microwells with arbitrary dimensions and filling them using discontinuous dewetting. Anal Chem 70:2280–2287

Jäggi RD, Sandoz R, Effenhauser CS (2007) Microfluidic depletion of red blood cells from whole blood in high-aspect-ratio microchannels. Microfluid Nanofluidics 3:47–53. https://doi.org/10.1007/s10404-006-0104-9

James DF, Chandler GM, Armour SJ (1990) A converging channel rheometer for the measurement of extensional viscosity. J Nonnewton Fluid Mech 35:421–443. https://doi.org/10.1016/0377-0257(90)85063-5

Jeon S, Menard E, Park J, et al (2004) Three-Dimensional Nanofabrication with Rubber Stamps and Conformable Photomasks. Adv Mater 16:1369–1373

Jeong JH, Sugii Y, Minamiyama M, Okamoto K (2006) Measurement of RBC deformation and velocity in capillaries in vivo. Microvasc Res 71:212–217. https://doi.org/10.1016/j.mvr.2006.02.006

Jia Y, Jiang J, Ma X, et al (2008) PDMS microchannel fabrication technique based on microwire-molding. Chinese Sci Bull 53:3928–3936. https://doi.org/10.1007/s11434-008-0528-6

Johnson RM (1989) Ektacytometry of red blood cells. Methods Enzymol 173:35–54. https://doi.org/10.1016/s0076-6879(89)73004-4

Kaigala G V, Ho S, Penterman R, Backhouse CJ (2007) Rapid prototyping of microfluidic devices with a wax printer. Lab Chip 7:384–387. https://doi.org/10.1039/B617764F

Kane RS, Takayama S, Ostuni E, et al (1999) Patterning proteins and cells using soft lithography. Biomaterials 20:2363–2376

Kaneko M, Ishida T, Tsai CHD, et al (2017) On-chip RBC deformability checker embedded with vision analyzer. 2017 IEEE Int Conf Mechatronics Autom ICMA 2017 2005–2010. https://doi.org/10.1109/ICMA.2017.8016126

Kangsun L, Choong K, Kyeong SS, et al (2007) Fabrication of round channels using the surface tension of PDMS and its application to a 3D serpentine mixer. J Micromechanics Microengineering 17:1533

Karimi A, Yazdi S, Ardekani AM (2013) Hydrodynamic mechanisms of cell and particle trapping in microfluidics. Biomicrofluidics 7:1–23. https://doi.org/10.1063/1.4799787

Karimi S, Mojaddam M, Majidi S, et al (2021) Numerical and experimental analysis of a high-throughput blood plasma separator for point-of-care applications. Anal Bioanal Chem. https://doi.org/10.1007/s00216-021-03190-1

Kersaudy-Kerhoas MM, Sollier E (2013) Micro-scale blood plasma separation: from acoustophoresis to egg-beaters. Lab Chip 13:3323–3346. https://doi.org/10.1039/C3LC50432H

Keskinler B, Yildiz E, Erhan E, et al (2004) Crossflow microfiltration of low concentration-nonliving yeast suspensions. J Memb Sci 233:59–69. https://doi.org/10.1016/j.memsci.2003.12.014

Khan Malek C, Robert L, Salut R (2009) Femtosecond laser machining and lamination for large-area flexible organic microfluidic chips. Eur Phys J - Appl Phys 46:5. https://doi.org/10.1051/epjap/2009027

Khosravi Parsa M, Hormozi F, Jafari D (2014) Mixing enhancement in a passive micromixer with convergent-divergent sinusoidal microchannels and different ratio of amplitude to wave length. Comput Fluids 105:82–90. https://doi.org/10.1016/j.compfluid.2014.09.024

Kim E, Xia Y, Whitesides GM (1995) Polymer microstructures formed by moulding in capillaries. Nature 376:581–584

Kim GB, Lee SJ (2006) X-ray PIV measurements of blood flows without tracer particles. Exp Fluids 41:195–200. https://doi.org/10.1007/s00348-006-0147-4

Kim JH, Woenker T, Adamec J, Regnier FE (2013) Simple, miniaturized blood plasma extraction method. Anal Chem 85:11501–11508. https://doi.org/10.1021/ac402735y

Kim P, Kwon KW, Park MC, et al (2008a) Soft lithography for microfluidics: a review. BioChip J 2:1–11

Kim S, Kong RL, Popel AS, et al (2006) A computer-based method for determination of the cell-free layer width in microcirculation. Microcirculation 13:199–207. https://doi.org/10.1080/10739680600556878

Kim S, Ong PK, Yalcin O, et al (2009) The cell-free layer in microvascular blood flow. Biorheology 46:181

Kim SM, Lee SH, Suh KY (2008b) Cell research with physically modified microfluidic channels: a review. Lab Chip 8:1015–1023

Kim SS, Utsunomiya H, Koski JA, et al (1998) Survival and function of hepatocytes on a novel three-dimensional synthetic biodegradable polymer scaffold with an intrinsic network of channels. Ann Surg 228:8

Kim Y, Kim K, Park Y (2012) Measurement Techniques for Red Blood Cell Deformability: Recent Advances. In: Terry E. Moschandreou (ed) Blood Cell – An Overview of Studies in Hematology. IntechOpen, pp 167–194

King E, Xia Y, Zhao X, Whitesides GM (1997) Solvent-assisted microcontact molding: A convenient method for fabricating three-dimensional structures on surfaces of polymers. Adv Mater 9:651–654

Kopp MU, Crabtree HJ, Manz A (1997) Developments in technology and applications of microsystems. Curr Opin Chem Biol 1:410–419

Kostova V, Antonova N, Velcheva I, Ivanov B (2012) Comparative analysis of the rheological properties of blood in patients with type 2 diabetes. Ser Biomech 27:80–85

Kumar A, Whitesides GM (1993) Features of gold having micrometer to centimeter dimensions can be formed through a combination of stamping with an elastomeric stamp and an alkanethiol '"ink"'followed by chemical etching. Appl Phys Lett 63:2002–2004

Kung C Te, Gao H, Lee CY, et al (2020) Microfluidic synthesis control technology and its application in drug delivery, bioimaging, biosensing, environmental analysis and cell analysis. Chem Eng J 399:125748. https://doi.org/10.1016/j.cej.2020.125748

Kung Y-C, Huang K-W, Fan Y-J, Chiou P-Y (2015) Fabrication of 3D high aspect ratio PDMS microfluidic networks with a hybrid stamp. Lab Chip 15:1861–1868

Kuntaegowdanahalli SS, Bhagat AAS, Kumar G, Papautsky I (2009) Inertial microfluidics for continuous particle separation in spiral microchannels. Lab Chip 9:2973–2980. https://doi.org/10.1039/B908271A

Lau KH, Giridhar A, Harikrishnan S, et al (2013) Releasing high aspect ratio SU-8 microstructures using AZ photoresist as a sacrificial layer on metallized Si substrates. Microsyst Technol 19:1863–1871

Lauks IR (1998) Microfabricated biosensors and microanalytical systems for blood analysis. Acc Chem Res 31:317–324

Layton BE, Lynch B, Peter T, Jamieson B (2012) Red blood cell sorting with a multi-bed microfabricated filter. J Micromechanics Microengineering 22:. https://doi.org/10.1088/0960-1317/22/2/025009

Leble V, Lima R, Dias R, et al (2011) Asymmetry of red blood cell motions in a microchannel with a diverging and converging bifurcation. Biomicrofluidics 5:44115–44120. https://doi.org/10.1063/1.3672689

Lee CY, Chang CL, Wang YN, Fu LM (2011a) Microfluidic mixing: A review. Int J Mol Sci 12:3263–3287. https://doi.org/10.3390/ijms12053263

Lee GYH, Lim CT (2007) Biomechanics approaches to studying human diseases. Trends Biotechnol 25:111–118. https://doi.org/10.1016/j.tibtech.2007.01.005

Lee JA, Lee SW, Lee K-C, et al (2008) Fabrication and characterization of freestanding 3D carbon microstructures using multi-exposures and resist pyrolysis. J Micromechanics Microengineering 18:35012

Lee MG, Choi S, Kim HJ, et al (2011b) Inertial blood plasma separation in a contraction-expansion array microchannel. Appl Phys Lett 98:. https://doi.org/10.1063/1.3601745

Lee MG, Shin JH, Bae CY, et al (2013) Label-free cancer cell separation from human whole blood using

inertial microfluidics at low shear stress. Anal Chem 85:6213–6218. https://doi.org/10.1021/ac4006149

Lee SS, Yim Y, Ahn KH, Lee SJ (2009) Extensional flow-based assessment of red blood cell deformability using hyperbolic converging microchannel. Biomed Microdevices 11:1021–1027. https://doi.org/10.1007/s10544-009-9319-3

Lee Y, Clark MM (1998) Modeling of flux decline during crossflow ultrafiltration of colloidal suspensions. J Memb Sci 149:181–202. https://doi.org/10.1016/S0376-7388(98)00177-X

Levinson HJ (2005) Principles of Lithography. Society of Photo Optical

Li H, Papageorgiou PD, Chang H-Y, et al (2018) Synergistic Integration of Laboratory and Numerical Approaches in Studies of the Biomechanics of Diseased Red Blood Cells. Biosensors 8:76

Li X, Ballerini DR, Shen W (2012) A perspective on paper-based microfluidics: Current status and future trends. Biomicrofluidics 6:11301–11313. https://doi.org/10.1063/1.3687398

Li Y, Wu P, Luo Z, et al (2015) Rapid fabrication of microfluidic chips based on the simplest LED lithography. J Micromechanics Microengineering 25:55020

Lim CT, Dao M, Suresh S, et al (2004) Large deformation of living cells using laser traps. Acta Mater 52:1837–1845. https://doi.org/10.1016/j.actamat.2003.12.028

Lim YC, Kouzani AZ, Kaynak A, et al (2015) A protocol for improving fabrication yield of thin SU-8 microcantilevers for use in an aptasensor. Microsyst Technol 21:371–380

Lima R, Ishikawa T, Imai, et al (2012) Blood Flow Behavior in Microchannels: Past, Current and Future Trends. In: Ricardo Dias Rui Lima, Mata, T.M. AAM (ed) In Single and two-Phase Flows on Chemical and Biomedical Engineering. Bentham science, pp 513–547

Lima R, Ishikawa T, Imai Y, et al (2008a) Radial dispersion of red blood cells in blood flowing through glass capillaries: The role of hematocrit and geometry. J Biomech 41:2188–2196. https://doi.org/http://dx.doi.org/10.1016/j.jbiomech.2008.04.033

Lima R, Ishikawa T, Imai Y, et al (2009a) Measurement of Individual Red Blood Cell Motions Under High Hematocrit Conditions Using a Confocal Micro-PTV System. Ann Biomed Eng 37:1546–1559. https://doi.org/10.1007/s10439-009-9732-z

Lima R, Nakamura M, Omori T, et al (2009b) Microscale Flow Dynamics of Red Blood Cells in Microchannels: An Experimental and Numerical Analysis BT - Advances in Computational Vision and Medical Image Processing: Methods and Applications. In: Tavares JMRS, Jorge RMN (eds). Springer Netherlands, Dordrecht, pp 203–220

Lima R, Oliveira MSN, Ishikawa T, et al (2009c) Axisymmetric polydimethysiloxane microchannels for in vitro hemodynamic studies. Biofabrication 1:35005

Lima R, Wada S, Tanaka S, et al (2008b) In vitro blood flow in a rectangular PDMS microchannel: Experimental observations using a confocal micro-PIV system. Biomed Microdevices 10:153–167. https://doi.org/10.1007/s10544-007-9121-z

Lima R, Wada S, Tsubota K, Yamaguchi T (2006) Confocal micro-PIV measurements of three-dimensional profiles of cell suspension flow in a square microchannel. Meas Sci Technol 17:797

Lima RA, Saadatmand M, Ishikawa T (2018) Microfluidic Devices Based on Biomechanics. Elsevier

Lin C-H, Lee G-B, Chang B-W, Chang G-L (2002) A new fabrication process for ultra-thick microfluidic microstructures utilizing SU-8 photoresist. J Micromechanics Microengineering 12:590

Liu SC, Yoo PB, Garg N, et al (2021) A microfluidic device for blood plasma separation and fluorescence detection of biomarkers using acoustic microstreaming. Sensors Actuators, A Phys 317:112482. https://doi.org/10.1016/j.sna.2020.112482

Liu XH, Wang X (2004) The deformation of an adherent leukocyte under steady shear flow: A numerical study. J Biomech 37:1079–1085. https://doi.org/10.1016/j.jbiomech.2003.11.015

Liu Z, Huang F, Du J, et al (2013) Rapid isolation of cancer cells using microfluidic deterministic lateral displacement structure. Biomicrofluidics 7:1–10. https://doi.org/10.1063/1.4774308

Lopes AR, Rodrigues RO, Pinho D, et al (2015a) Low cost microfluidic device for partial cell separation: micromilling approach. In: IEEE International Conference on Industrial Technology. Seville, Spain

Lopes AR, Rodrigues RO, Pinho D, et al (2015b) The study of the effect of microcontractions in the separation of blood cells: soft lithography and micromilling. Instituto Politécnico de Bragança

Lopes ARJ (2014) The study of the effect of microcontrations in the separation of blood cells: soft lithography

and micromilling

Lucchi NW, Ljolje D, Silva-Flannery L, Udhayakumar V (2016) Use of malachite green-loop mediated isothermal amplification for detection of plasmodium spp. parasites. PLoS One 11:1–9. https://doi.org/10.1371/journal.pone.0151437

Maciaszek JL, Lykotrafitis G (2011) Sickle cell trait human erythrocytes are significantly stiffer than normal. J Biomech 44:657–661. https://doi.org/10.1016/j.jbiomech.2010.11.008

Madou MJ, Lee LJ, Koelling KW, et al (2001) Design and fabrication of polymer microfluidic platforms for biomedical applications. ANTEC-SPE 59th 3:2534–2538

Maeda N (1996) Erythrocyte Rheology in Microcirculation. Jpn J Physiol 46:1–14. https://doi.org/10.2170/jjphysiol.46.1

Manz A, Graber N, Widmer H áM (1990) Miniaturized total chemical analysis systems: a novel concept for chemical sensing. Sensors actuators B Chem 1:244–248

Martel JM, Toner M (2014) Inertial focusing in microfluidics. Annu Rev Biomed Eng 16:371–396. https://doi.org/10.1146/annurev-bioeng-121813-120704

McCormick RM, Nelson RJ, Alonso-Amigo MG, et al (1997) Microchannel electrophoretic separations of DNA in injection-molded plastic substrates. Anal Chem 69:2626–2630

McDonald JC, Whitesides GM (2002) Poly (dimethylsiloxane) as a material for fabricating microfluidic devices. Acc Chem Res 35:491–499

McHedlishvili G, Maeda N (2001) Blood Flow Structure Related to Red Cell Flow: Determinant of Blood Fluidity in Narrow Microvessels. Jpn J Physiol 51:19–30. https://doi.org/10.2170/jjphysiol.51.19

Mehri R, Niazi E, Mavriplis C, Fenech M (2018) An automated method for dynamic red blood cell aggregate detection in microfluidic flow. Physiol Meas 39:. https://doi.org/10.1088/1361-6579/aaa0ad

Mehta A, Shekhar H, Hyun S, et al (2006) A micromachined electrochemical sensor for free chlorine monitoring in drinking water. Water Sci Technol 53:403–410

Meijering E, Smal I, Danuser G (2006) Tracking in molecular bioimaging. Signal Process Mag IEEE 23:46–53. https://doi.org/10.1109/MSP.2006.1628877

Melin J, Quake SR (2007) Microfluidic large-scale integration: the evolution of design rules for biological automation. Annu Rev Biophys Biomol Struct 36:213–231

Mitra SK, Chakraborty S (2011) Microfluidics and Nanofluidics Handbook: Fabrication, Implementation, and Applications. CRC Press

Mokken FC, Kedaria M, Henny CP, et al (1992) The clinical importance of erythrocyte deformability, a hemorrheological parameter. Ann Hematol 64:113–22

Muñoz-Sánchez BN, Silva SF, Pinho D, et al (2016) Generation of micro-sized PDMS particles by a flow focusing technique for biomicrofluidics applications. Biomicrofluidics 10:014122. https://doi.org/10.1063/1.4943007

Musielak M Red blood cell-deformability measurement: review of techniques

Nakamura M, Bessho S, Wada S (2013) Spring-network-based model of a red blood cell for simulating mesoscopic blood flow. Int j numer method biomed eng 29:114–128. https://doi.org/https://doi.org/10.1002/cnm.2501

Nash G, O'Brien E, Gordon-Smith E, Dormandy J (1989) Abnormalities in the mechanical properties of red blood cells caused by Plasmodium falciparum. Blood 74:855–861. https://doi.org/10.1182/blood.v74.2.855.855

Nasiri R, Shamloo A, Ahadian S, et al (2020) Microfluidic-Based Approaches in Targeted Cell/Particle Separation Based on Physical Properties: Fundamentals and Applications. Small 16:1–27. https://doi.org/10.1002/smll.202000171

Natsuhara T, Tanino K, Ohno YNV-UB (2001) Toner for toner-jetting

Nge PN, Rogers CI, Woolley AT (2013) Advances in microfluidic materials, functions, integration, and applications. Chem Rev 113:2550–2583. https://doi.org/10.1021/cr300337x

Omori T, Imai Y, Kikuchi K, et al (2015) Hemodynamics in the Microcirculation and in Microfluidics. Ann Biomed Eng 43:238–257. https://doi.org/10.1007/s10439-014-1180-8

Orabona E, Caliò A, Rendina I, et al (2013) Photomasks fabrication based on optical reduction for microfluidic applications. Micromachines 4:206–214

Pamme N (2007) Continuous flow separations in microfluidic devices. Lab Chip 7:1644–1659.

https://doi.org/10.1039/b712784g

Pamme N, Manz A (2004) On-chip free-flow magnetophoresis: Continuous flow separation of magnetic particles and agglomerates. Anal Chem 76:7250–7256. https://doi.org/10.1021/ac049183o

Pan T, Wang W (2011) From Cleanroom to Desktop: Emerging Micro-Nanofabrication Technology for Biomedical Applications. Ann Biomed Eng 39:600–620. https://doi.org/10.1007/s10439-010-0218-9

Park A, Wu B, Griffith LG (1998) Integration of surface modification and 3D fabrication techniques to prepare patterned poly (L-lactide) substrates allowing regionally selective cell adhesion. J Biomater Sci Polym Ed 9:89–110

Park CW, Shin SH, Kim GM, et al (2006) A Hemodynamic Study on a Marginal Cell Depletion Layer of Blood Flow Inside a Microchannel. Key Eng Mater 326–328:863–866. https://doi.org/10.4028/www.scientific.net/KEM.326-328.863

Passos A, Sherwood J, Agrawal R, et al (2016) The effect of RBC stiffness on microhaemodynamics. 44:2016

Patel JN, Kaminska B, Gray BL, Gates BD (2008) PDMS as a sacrificial substrate for SU-8-based biomedical and microfluidic applications. J Micromechanics Microengineering 18:95028. https://doi.org/10.1088/0960-1317/18/9/095028

Paulitschke M, Nash GB (1993) Membrane rigidity of red blood cells parasitized by different strains of Plasmodium falciparum. J Lab Clin Med 122:581–589

Perry H, Greiner C Fau - Georgakoudi I, Georgakoudi I Fau - Cronin-Golomb M, et al (2007) Simple fabrication technique for rapid prototyping of seamless cylindrical microchannels in polymer substrates. Rev Sci Instrum TA - Rev Sci, Instrum 78:. https://doi.org/10.1063/1.2719626

Picot J, Ndour PA, Lefevre SD, et al (2015) A biomimetic microfluidic chip to study the circulation and mechanical retention of red blood cells in the spleen. Am J Hematol 90:339–345. https://doi.org/10.1002/ajh.23941

Pinho D, Campo-Deaño L, Lima R, Pinho FT (2017) In vitro particulate analogue fluids for experimental studies of rheological and hemorheological behavior of glucose-rich RBC suspensions. Biomicrofluidics 11:54105. https://doi.org/10.1063/1.4998190

Pinho D, Carvalho V, Gonçalves IM, et al (2020) Visualization and measurements of blood cells flowing in microfluidic systems and blood rheology: A personalized medicine perspective. J Pers Med 10:1–18. https://doi.org/10.3390/jpm10040249

Pinho D, Lima R, Pereira AI, Gayubo F (2013a) Automatic tracking of labeled red blood cells in microchannels. Int j numer method biomed eng 29:977–987. https://doi.org/10.1002/cnm.2526

Pinho D, Muñoz-Sánchez BN, Anes CF, et al (2019) Flexible PDMS microparticles to mimic RBCs in blood particulate analogue fluids. Mech Res Commun 100:18–20. https://doi.org/10.1016/j.mechrescom.2019.103399

Pinho D, Rodrigues RO, Faustino V, et al (2016) Red blood cells radial dispersion in blood flowing through microchannels: The role of temperature. J Biomech 49:2293–2298. https://doi.org/10.1016/j.jbiomech.2015.11.037

Pinho D, Rodrigues RO, Yaginuma T, et al (2014) Motion of rigid particles flowing in a microfluidic device with a pronounced stenosis: Trajectories and deformation index. In: 11th World Congress on Computational Mechanics, WCCM 2014, 5th European Conference on Computational Mechanics, ECCM 2014 and 6th European Conference on Computational Fluid Dynamics, ECFD 2014

Pinho D, Yaginuma T, Lima R (2013b) A microfluidic device for partial cell separation and deformability assessment. BioChip J 7:367–374. https://doi.org/10.1007/s13206-013-7408-0

Pinto E (2012) Experimental flow studies in microchannels fabricated by xurography. Instituto Politécnico de Bragança

Pinto E, Faustino V, Rodrigues RORO, et al (2014a) A Rapid and Low-Cost Nonlithographic Method to Fabricate Biomedical Microdevices for Blood Flow Analysis. Micromachines 6:121–135. https://doi.org/10.3390/mi6010121

Pinto VC, Sousa PJ, Cardoso VF, Minas G (2014b) Optimized SU-8 processing for low-cost microstructures fabrication without cleanroom facilities. Micromachines 5:738–755. https://doi.org/10.3390/mi5030738

Pitts KL, Mehri R, Mavriplis C, Fenech M (2012) Micro-particle image velocimetry measurement of blood flow: Validation and analysis of data pre-processing and processing methods. Meas Sci Technol 23:. https://doi.org/10.1088/0957-0233/23/10/105302

Postier B, DiDonato Jr R, Nevin KP, et al (2008) Benefits of in-situ synthesized microarrays for analysis of gene expression in understudied microorganisms. J Microbiol Methods 74:26–32. https://doi.org/http://dx.doi.org/10.1016/j.mimet.2007.07.004

Prabhakar A, Kumar YVBV, Tripathi S, Agrawal A (2015) A novel, compact and efficient microchannel arrangement with multiple hydrodynamic effects for blood plasma separation. Microfluid Nanofluidics 18:995–1006. https://doi.org/10.1007/s10404-014-1488-6

Pries AR, Neuhaus D, Gaehtgens P (1992) Blood viscosity in tube flow: dependence on diameter and hematocrit. Am J Physiol - Hear Circ Physiol 263:H1770–H1778

Qin D, Xia Y, Whitesides GM (2010) Soft lithography for micro-and nanoscale patterning. Nat Protoc 5:491–502

Quinn DJ, Pivkin I, Wong SY, et al (2011) Combined simulation and experimental study of large deformation of red blood cells in microfluidic systems. Ann Biomed Eng 39:1041–1050. https://doi.org/10.1007/s10439-010-0232-y

Rammohan A, Dwivedi PK, Martinez-Duarte R, et al (2011) One-step maskless grayscale lithography for the fabrication of 3-dimensional structures in SU-8. Sensors Actuators B Chem 153:125–134

Ran Q, Xiang Y, Liu Y, et al (2015) Eryptosis Indices as a Novel Predictive Parameter for Biocompatibility of Fe3O4Magnetic Nanoparticles on Erythrocytes. Sci Rep 5:1–15. https://doi.org/10.1038/srep16209

Rasband W (1997) ImageJ - Image processing and analysis in java

Reinke W, Gaehtgens P, Johnson PC (1987) Blood viscosity in small tubes: effect of shear rate, aggregation, and sedimentation. Am J Physiol - Hear Circ Physiol 253:H540–H547

Reinke W, Johnson PC, Gaehtgens P (1986) Effect of shear rate variation on apparent viscosity of human blood in tubes of 29 to 94 microns diameter. Circ Res 59:124 LP – 132. https://doi.org/10.1161/01.RES.59.2.124

Rhee SW, Taylor AM, Tu CH, et al (2005) Patterned cell culture inside microfluidic devices. Lab Chip 5:102–107

Ribeiro JC, Minas G, Turmezei P, et al (2005) A SU-8 fluidic microsystem for biological fluids analysis. Sensors Actuators A Phys 123:77–81

Rife JC, Bell MI, Horwitz JS, et al (2000) Miniature valveless ultrasonic pumps and mixers. Sensors Actuators, A Phys 86:135–140. https://doi.org/10.1016/S0924-4247(00)00433-7

Riquelme B, Foresto P, D'Arrigo M, et al (2005) A dynamic and stationary rheological study of erythrocytes incubated in a glucose medium. J Biochem Biophys Methods 62:131–141. https://doi.org/10.1016/j.jbbm.2004.10.004

Robinson BM, Joffe MM, Berns JS, et al (2005) Anemia and mortality in hemodialysis patients: Accounting for morbidity and treatment variables updated over time. Kidney Int 68:2323–2330. https://doi.org/10.1111/j.1523-1755.2005.00693.x

Rodrigue H, Bhandari B, Wang W, Ahn S-H (2015) 3D soft lithography: A fabrication process for thermocurable polymers. J Mater Process Technol 217:302–309. https://doi.org/http://dx.doi.org/10.1016/j.jmatprotec.2014.11.005

Rodrigues R, Faustino V, Pinto E, et al (2013a) Red Blood Cells deformability index assessment in a hyperbolic microchannel: the diamide and glutaraldehyde effect. WebmedCentral Biomed Eng. https://doi.org/10.9754/journal.wmc.2013.004375

Rodrigues RO, Bañobre-López M, Gallo J, et al (2016a) Haemocompatibility of iron oxide nanoparticles synthesized for theranostic applications: a high-sensitivity microfluidic tool. J Nanoparticle Res 18:194. https://doi.org/10.1007/s11051-016-3498-7

Rodrigues RO, Lima R, Gomes HT, Silva AMT (2015a) Polymer microfluidic devices: An overview of fabrication methods. UPorto J Eng 1:67–79. https://doi.org/10.24840/2183-6493_001.001_0007

Rodrigues RO, Lopes R, Pinho D, et al (2016b) In vitro Blood Flow and Cell-Free Layer in Hyperbolic Microchannels: Visualizations and Measurements. BioChip J 10:9–15. https://doi.org/10.1007/s13206-016-0102-2

Rodrigues RO, Pinho D, Faustino V, Lima R (2015b) A simple microfluidic device for the deformability assessment of blood cells in a continuous flow. Biomed Microdevices 17:108. https://doi.org/10.1007/s10544-015-0014-2

Rodrigues RO, Sousa PC, Gaspar J, et al (2020) Organ-on-a-Chip: A Preclinical Microfluidic Platform for the Progress of Nanomedicine. Small 16:1–19. https://doi.org/10.1002/smll.202003517

Rodrigues V, Rodrigues PJ, Pereira AI, Lima R (2013b) Automatic tracking of red blood cells in micro channels using OpenCV. AIP Conf Proc 1558:594–597. https://doi.org/10.1063/1.4825561

Rogers JA, Nuzzo RG (2005) Recent progress in soft lithography. Mater Today 8:50–56. https://doi.org/http://dx.doi.org/10.1016/S1369-7021(05)00702-9

Rogers JA, Paul KE, Jackman RJ, Whitesides GM (1997) Using an elastomeric phase mask for sub-100 nm photolithography in the optical near field. Appl Phys Lett 70:2658–2660

Rosenbluth MJ, Lam WA, Fletcher DA (2008) Analyzing cell mechanics in hematologic diseases with microfluidic biophysical flow cytometry. Lab Chip 8:1062–1070. https://doi.org/10.1039/b802931h

Rubio A, Faustino V, Cabezas MG, et al (2019) Fire-shaped cylindrical glass micronozzles to measure cell deformability. J Micromechanics Microengineering 29:. https://doi.org/10.1088/1361-6439/ab3183

Ruffien-Ciszak A, Baur J, Gros P, et al (2008) Electrochemical microsensors for cutaneous surface analysis: Application to the determination of pH and the antioxidant properties of stratum corneum. IRBM 29:162–170. https://doi.org/http://dx.doi.org/10.1016/j.rbmret.2007.11.020

Saadatmand M, Ishikawa T, Matsuki N, et al (2011) Fluid particle diffusion through high-hematocrit blood flow within a capillary tube. J Biomech 44:170–175. https://doi.org/10.1016/j.jbiomech.2010.09.004

Sabo A, Jakovljević V, Stanulović M, et al (1993) Red blood cell deformability in diabetes mellitus: effect of phytomenadione. Int J Clin Pharmacol Ther Toxicol 31:1–5

Sackmann EK, Fulton AL, Beebe DJ (2014) The present and future role of microfluidics in biomedical research. Nature 507:181–189. https://doi.org/10.1038/nature13118

Sadek SH, Rubio M, Lima R, Vega EJ (2021) Blood Particulate Analogue Fluids: A Review. Materials (Basel) 14:2451. https://doi.org/10.3390/ma14092451

Saha RK, Karmakar S, Roy M (2012) Computational Investigation on the Photoacoustics of Malaria Infected Red Blood Cells. PLoS One 7:e51774

Sajeesh P, Sen AK (2014) Particle separation and sorting in microfluidic devices: A review. Microfluid Nanofluidics 17:1–52. https://doi.org/10.1007/s10404-013-1291-9

Sankar DS, Nagar AK, Kumar A V. (2015) Mathematical analysis of single and two-phase flow of blood in narrow arteries with multiple contrictions. J Appl Fluid Mech 8:871–883. https://doi.org/10.18869/acadpub.jafm.67.223.23336

Schena M, Shalon D, Davis RW, Brown PO (1995) Quantitative monitoring of gene expression patterns with a complementary DNA microarray. Science (80-) 270:467–470

Schonbrun E, Malka R, Di Caprio G, et al (2014) Quantitative absorption cytometry for measuring red blood cell hemoglobin mass and volume. Cytometry A 85:332–338. https://doi.org/10.1002/cyto.a.22450

Sethu P, Sin A, Toner M (2006) Microfluidic diffusive filter for apheresis (leukapheresis). Lab Chip 6:83–89. https://doi.org/10.1039/B512049G

Sharma A, Cornejo C, Mihalic J, et al (2018) Physical characterization and in vivo organ distribution of coated iron oxide nanoparticles. Sci Rep 8:1–12. https://doi.org/10.1038/s41598-018-23317-2

Shelby JP, White J, Ganesan K, et al (2003) A microfluidic model for single-cell capillary obstruction by Plasmodium falciparum-infected erythrocytes. Proc Natl Acad Sci U S A 100:14618–14622. https://doi.org/10.1073/pnas.2433968100

Shevkoplyas SS, Gifford SC, Yoshida T, Bitensky MW (2003) Prototype of an in vitro model of the microcirculation. Microvasc Res 65:132–136. https://doi.org/10.1016/S0026-2862(02)00034-1

Shevkoplyas SS, Yoshida T, Gifford SC, Bitensky MW (2006) Direct measurement of the impact of impaired erythrocyte deformability on microvascular network perfusion in a microfluidic device. Lab Chip 6:914. https://doi.org/10.1039/b601554a

Shevkoplyas SS, Yoshida T, Munn LL, Bitensky MW (2005) Biomimetic autoseparation of leukocytes from whole blood in a microfluidic device. Anal Chem 77:933–7. https://doi.org/10.1021/ac049037i

Shin S, Ku Y-H, Ho J-X, et al (2007) Progressive impairment of erythrocyte deformability as indicator of microangiopathy in type 2 diabetes mellitus. Clin Hemorheol Microcirc 36:253–261

Shin S, Ku Y-H, Suh J-S, Singh M (2008) Rheological characteristics of erythrocytes incubated in glucose media. Clin Hemorheol Microcirc 38:153–161

Silva I, Lima R, Minas G, Catarino SO (2017) Hemozoin and Hemoglobin Characterization by Optical Absorption Towards a Miniaturized Spectrophotometric Malaria Diagnostic System *. In: Proceedings of the 5th IEEE Portuguese BioEngineering Meeting, IEEE-EMBS. Coimbra, Portugal

Singh N, Jenkins GJS, Asadi R, Doak SH (2010) Potential toxicity of superparamagnetic iron oxide nanoparticles (SPION). Nano Rev 1:5358. https://doi.org/10.3402/nano.v1i0.5358

Singhal J, Pinho D, Lopes R, et al (2016) Blood Flow Visualization and Measurements in Microfluidic Devices Fabricated by a Micromilling Technique. Micro Nanosyst 7:148–153. https://doi.org/10.2174/1876402908666160106000332

Sollier E, Cubizolles M Fau - Fouillet Y, Fouillet Y Fau - Achard J-L, Achard JL (2010) Fast and continuous plasma extraction from whole human blood based on expanding cell-free layer devices. Biomed Microdevices TA - Biomed, Microdevices 12:485–497. https://doi.org/10.1007/s10544-010-9405-6

Songjaroen T, Dungchai W, Chailapakul O, et al (2012) Blood separation on microfluidic paper-based analytical devices. Lab Chip 12:3392–3398. https://doi.org/10.1039/c2lc21299d

Sosa JM, Nielsen ND, Vignes SM, et al (2014) The relationship between red blood cell deformability metrics and perfusion of an artificial microvascular network. Clin Hemorheol Microcirc 57:291–305. https://doi.org/10.3233/CH-131719

Sousa PC, Carneiro J, Vaz R, et al (2013) Shear viscosity and nonlinear behavior of whole blood under large amplitude oscillatory shear. Biorheology 50:269–282. https://doi.org/10.3233/BIR-130643

Sousa PC, Pinho FT, Alves MA, Oliveira MSN (2016) A review of hemorheology: Measuring techniques and recent advances. Korea Aust Rheol J 28:1–22. https://doi.org/10.1007/s13367-016-0001-z

Sousa PC, Pinho FT, Oliveira MSN, Alves MA (2011) Extensional flow of blood analog solutions in microfluidic devices. Biomicrofluidics 5:14108. https://doi.org/10.1063/1.3567888

Squires TM, Quake SR (2005) Microfluidics: Fluid physics at the nanoliter scale. Rev Mod Phys 77:977–1026. https://doi.org/10.1103/RevModPhys.77.977

Staples AO, Wong CS, Smith JM, et al (2009) Anemia and risk of hospitalization in pediatric chronic kidney disease. Clin J Am Soc Nephrol 4:48–56. https://doi.org/10.2215/CJN.05301107

Stauber H, Waisman D, Korin N, Sznitman J (2017) Red blood cell dynamics in biomimetic microfluidic networks of pulmonary alveolar capillaries. Biomicrofluidics 11:. https://doi.org/10.1063/1.4973930

Stone HA, Stroock AD, Ajdari A (2004) ENGINEERING FLOWS IN SMALL DEVICES: Microfluidics Toward a Lab-on-a-Chip. Annu Rev Fluid Mech 36:381–411. https://doi.org/doi:10.1146/annurev.fluid.36.050802.122124

Streets AM, Huang Y (2013) Chip in a lab: Microfluidics for next generation life science research. Biomicrofluidics 7:. https://doi.org/10.1063/1.4789751

Sugii Y, Okuda R, Okamoto K, Madarame H (2005) Velocity measurement of both red blood cells and plasma of in vitro blood flow using high-speed micro PIV technique. Meas Sci Technol 16:1126–1130. https://doi.org/10.1088/0957-0233/16/5/011

Suh YK, Kang S (2010) A review on mixing in microfluidics. Micromachines 1:82–111. https://doi.org/10.3390/mi1030082

Suresh S, Spatz J, Mills JP, et al (2005) Connections between single-cell biomechanics and human disease states: gastrointestinal cancer and malaria. Acta Biomater 1:15–30. https://doi.org/10.1016/J.ACTBIO.2004.09.001

Suwanarusk R, Cooke BM, Dondorp AM, et al (2004) The deformability of red blood cells parasitized by Plasmodium falciparum and P. vivax. J Infect Dis 189:190–194. https://doi.org/10.1086/380468

Suzuki Y, Tateishi N, Soutani M, Maeda N (1996) Deformation of Erythrocytes in Microvessels and Glass Capillaries: Effects of Erythrocyte Deformability. Microcirculation 3:49–57.

https://doi.org/10.3109/10739689609146782

Taboada B, Monteiro FC, Lima R (2016) Automatic tracking and deformation measurements of red blood cells flowing through a microchannel with a microstenosis: the keyhole model. Comput Methods Biomech Biomed Eng Imaging Vis 4:229–237. https://doi.org/10.1080/21681163.2014.957868

Tan A, Rodgers K, Murrihy JP, et al (2001) Rapid fabrication of microfluidic devices in poly(dimethylsiloxane) by photocopying. Lab Chip 1:7–9. https://doi.org/10.1039/B102905N

Tanaka T, Ishikawa T, Numayama-Tsuruta K, et al (2012) Separation of cancer cells from a red blood cell suspension using inertial force. Lab Chip 12:4336. https://doi.org/10.1039/c2lc40354d

Taylor AM, Rhee SW, Tu CH, et al (2003) Microfluidic multicompartment device for neuroscience research. Langmuir 19:1551–1556

Terry SC, Jerman JH, Angell JB (1979) A gas chromatographic air analyzer fabricated on a silicon wafer. IEEE Trans on Electron Devices 26:1880–1886

Thadikkaran L, Siegenthaler MA, Crettaz D, et al (2005) Recent advances in blood-related proteomics. Proteomics 5:3019–3034. https://doi.org/10.1002/pmic.200402053

Thielicke W, J. Stamhuis E (2019) PIVlab - Time-Resolved Digital Particle Image Velocimetry Tool for MATLAB

Thielicke W, Stamhuis EJ (2014) PIVlab – Towards User-friendly, Affordable and Accurate Digital Particle Image Velocimetry in MATLAB. J Open Res Softw 2:. https://doi.org/10.5334/jors.bl

Thomas MS, Millare B, Clift JM, et al (2010) Print-and-Peel Fabrication for Microfluidics: What's in it for Biomedical Applications? Ann Biomed Eng 38:21–32. https://doi.org/10.1007/s10439-009-9831-x

Thurston GB (1989) Plasma release-cell layering theory for blood flow. Biorheology 26:199–214

Tomaiuolo G (2014) Biomechanical properties of red blood cells in health and disease towards microfluidics. Biomicrofluidics 8:51501. https://doi.org/10.1063/1.4895755

Tomaiuolo G, Barra M, Preziosi V, et al (2011) Microfluidics analysis of red blood cell membrane viscoelasticity. Lab Chip 11:449–454. https://doi.org/10.1039/c0lc00348d

Toner M, Irimia D (2005) Blood-on-a-chip. Annu Rev Biomed Eng 7:77–103. https://doi.org/10.1146/annurev.bioeng.7.011205.135108

Tripathi S, Kumar YVB, Agrawal A, et al (2016) Microdevice for plasma separation from whole human blood using bio-physical and geometrical effects. Sci Rep 6:26749. https://doi.org/10.1038/srep26749

Tripathi S, Kumar YVBV, Prabhakar A, et al (2015a) Passive blood plasma separation at the microscale: a review of design principles and microdevices. J Micromechanics Microengineering 25:083001. https://doi.org/10.1088/0960-1317/25/8/083001

Tripathi S, Varun Kumar YVB, Prabhakar A, et al (2015b) Performance study of microfluidic devices for blood plasma separation—a designer's perspective. J Micromechanics Microengineering 25:084004. https://doi.org/10.1088/0960-1317/25/8/084004

Tsai CHD, Tanaka J, Kaneko M, et al (2016) An on-chip RBC deformability checker significantly improves velocity-deformation correlation. Micromachines 7:. https://doi.org/10.3390/mi7100176

Tsukada K, Sekizuka E, Oshio C, Minamitani H (2001) Direct Measurement of Erythrocyte Deformability in Diabetes Mellitus with a Transparent Microchannel Capillary Model and High-Speed Video Camera System. Microvasc Res 61:231–239. https://doi.org/http://dx.doi.org/10.1006/mvre.2001.2307

Tsutsui H, Ho C-M, Manuscript A (2009) Cell Separation by Non-Inertial Force Fields in Microfluidic Systems. Mech Res Commun 36:92–103. https://doi.org/10.1016/j.mechrescom.2008.08.006

Tyagi D, Tyminski DE, Proctor LG, Santilli D Monodisperse spherical toner particles containing aliphatic amides or aliphatic acids

Urban GA (2009) Micro-and nanobiosensors—state of the art and trends. Meas Sci Technol 20:12001

VanDelinder V, Groisman A (2006) Separation of Plasma from Whole Human Blood in a Continuous Cross-Flow in a Molded Microfluidic Device. Anal Chem 78:3765–3771. https://doi.org/10.1021/ac060042r

VanDelinder V, Groisman A (2007) Perfusion in Microfluidic Cross-Flow: Separation of White Blood Cells from Whole Blood and Exchange of Medium in a Continuous Flow. Anal Chem 79:2023–2030. https://doi.org/10.1021/ac061659b

Vennemann P, Kiger KT, Lindken R, et al (2006) In vivo micro particle image velocimetry measurements of blood-plasma in the embryonic avian heart. J Biomech 39:1191–1200.

https://doi.org/10.1016/j.jbiomech.2005.03.015

Verma MKS, Majumder A, Ghatak A (2006) Embedded Template-Assisted Fabrication of Complex Microchannels in PDMS and Design of a Microfluidic Adhesive. Langmuir 22:10291–10295. https://doi.org/10.1021/la062516n

Vullev VI, Wan J, Heinrich V, et al (2006) Nonlithographic Fabrication of Microfluidic Devices. J Am Chem Soc 128:16062–16072. https://doi.org/10.1021/ja061776o

Wang L, Kodzius R, Yi X, et al (2012) Prototyping chips in minutes: Direct Laser Plotting (DLP) of functional microfluidic structures. Sensors Actuators B Chem 168:214–222. https://doi.org/http://dx.doi.org/10.1016/j.snb.2012.04.011

Wang X, Hagen JA, Papautsky I (2013) Paper pump for passive and programmable transport. Biomicrofluidics 7:014107. https://doi.org/10.1063/1.4790819

Westin L, Xu X, Miller C, et al (2000) Anchored multiplex amplification on a microelectronic chip array. Nat Biotechnol 18:199–204

Whitesides GM (2006) The origins and the future of microfluidics. Nature 442:368–73. https://doi.org/10.1038/nature05058

Whitesides GM, Ostuni E, Takayama S, et al (2001) Soft lithography in biology and biochemistry. Annu Rev Biomed Eng 3:335–373

WHO (2016) World Malaria Report. Gneva

WHO (2017) Malaria rapid diagnostic test performance: results of WHO product testing of malaira RDTs. World Health Organization, Geneva PP - Geneva

Wilding P, Shoffner MA, Kricka LJ (1994) PCR in a silicon microstructure. Clin Chem 40:1815–1818

Williams SJ, Park C, Wereley ST (2010) Advances and applications on microfluidic velocimetry techniques. Microfluid Nanofluidics 8:709–726. https://doi.org/10.1007/s10404-010-0588-1

Wilson ME, Kota N, Kim Y, et al (2011) Fabrication of circular microfluidic channels by combining mechanical micromilling and soft lithography. Lab Chip 11:1550–1555. https://doi.org/10.1039/C0LC00561D

Wong I, Ho C-M (2009) Surface molecular property modifications for poly (dimethylsiloxane)(PDMS) based microfluidic devices. Microfluid Nanofluidics 7:291–306

Wong KHK, Chan JM, Kamm RD, Tien J (2012) Microfluidic models of vascular functions. Annu Rev Biomed Eng 14:205–230. https://doi.org/10.1146/annurev-bioeng-071811-150052

Wongsrichanalai C, Barcus MJ, Muth S, et al (2007) A review of malaria diagnostic tools: microscopy and rapid diagnostic test (RDT). Am J Trop Med Hyg 77:119–127

Wu H, Odom TW, Chiu DT, Whitesides GM (2003) Fabrication of complex three-dimensional microchannel systems in PDMS. J Am Chem Soc 125:554–559

Wyatt Shields Iv C, Reyes CD, López GP (2015) Microfluidic cell sorting: A review of the advances in the separation of cells from debulking to rare cell isolation. Lab Chip 15:1230–1249. https://doi.org/10.1039/c4lc01246a

Xia Y, McClelland JJ, Gupta R, et al (1997) Replica molding using polymeric materials: A practical step toward nanomanufacturing. Adv Mater 9:147–149

Xia YN, Whitesides GM (1998) Soft lithography. Annu Rev Mater Sci 37:551–575. https://doi.org/10.1146/annurev.matsci.28.1.153

Xu Q, Rioux RM, Dickey MD, Whitesides GM (2008) Nanoskiving: a new method to produce arrays of nanostructures. Acc Chem Res 41:1566–1577

Xue C, Wang J, Zhao Y, et al (2015) Constriction Channel Based Single-Cell Mechanical Property Characterization. Micromachines 6:1794–1804

Yaginuma T, Oliveira MSN, Lima R, et al (2011) Red blood cell deformation in flows through a PDMS hyperbolic microchannel. In: In Proceedings of the Techconnect World 2011—Microtech Conference and Expo. Boston, pp 505–507

Yaginuma T, Oliveira MSN, Lima R, et al (2013) Human red blood cell behavior under homogeneous extensional flow in a hyperbolic-shaped microchannel. Biomicrofluidics 7:54110. https://doi.org/10.1063/1.4820414

YAMAGUCHI T, ISHIKAWA T, TSUBOTA K, et al (2006) Computational Blood Flow Analysis -New Trends and Methods. J Biomech Sci Eng 1:29–50. https://doi.org/10.1299/jbse.1.29

Yan S, Zhang J, Yuan D, Li W (2017) Hybrid microfluidics combined with active and passive approaches for continuous cell separation. Electrophoresis 38:238–249. https://doi.org/10.1002/elps.201600386

Yang C-Y, Kuan C-M, Cheng C-M, Yeh JA (2014) Fabricating small-scale polymeric structures for in-vitro diagnosis via daily-use tools. In: Design, Test, Integration and Packaging of MEMS/MOEMS (DTIP), 2014 Symposium on. IEEE, pp 1–5

Yang S, Ündar A, Zahn JD (2006a) A microfluidic device for continuous, real time blood plasma separation. Lab Chip 6:871–880. https://doi.org/10.1039/B516401J

Yang S, Ündar A, Zahn JD (2006b) A microfluidic device for continuous, real time blood plasma separation. Lab Chip 6:871–880. https://doi.org/10.1039/b516401j

Yang W, Israni RK, Brunelli SM, et al (2007) Hemoglobin variability and mortality in ESRD. J Am Soc Nephrol 18:3164–3170. https://doi.org/10.1681/ASN.2007010058

Yaylali YT, Susam I, Demir E, et al (2013) Increased red blood cell deformability and decreased aggregation as potential adaptive mechanisms in the slow coronary flow phenomenon. Coron Artery Dis 24:11–15. https://doi.org/10.1097/MCA.0b013e32835b0bdf

Yazdani A, Li X, Karniadakis GE (2016) Dynamic and rheological properties of soft biological cell suspensions. Rheol Acta 55:433–449. https://doi.org/10.1007/s00397-015-0869-4

Ye T, Phan-Thien N, Lim CT (2016) Particle-based simulations of red blood cells—A review. J Biomech 49:2255–2266. https://doi.org/10.1016/j.jbiomech.2015.11.050

Yu ZTF, Yong KMA, Fu J (2014) Microfluidic Blood Cell Preparation: Now and Beyond. Small 10:1687–1703. https://doi.org/10.1002/smll.201302907

Zare RN, Kim S (2010) Microfluidic Platforms for Single-Cell Analysis. Annu Rev Biomed Eng 12:187–201. https://doi.org/10.1146/annurev-bioeng-070909-105238

Zeng NF, Mancuso JE, Zivkovic AM, et al (2016) Red Blood Cells from Individuals with Abdominal Obesity or Metabolic Abnormalities Exhibit Less Deformability upon Entering a Constriction. PLoS One 11:. https://doi.org/10.1371/journal.pone.0156070

Zeng NF, Ristenpart WD (2014) Mechanical response of red blood cells entering a constriction. Biomicrofluidics 8:064123. https://doi.org/10.1063/1.4904058

Zhang J, Johnson PC, Popel AS (2009) Effects of erythrocyte deformability and aggregation on the cell free layer and apparent viscosity of microscopic blood flows. Microvasc Res 77:265–272. https://doi.org/10.1016/j.mvr.2009.01.010

Zhang J, Yan S, Yuan D, et al (2016) Fundamentals and applications of inertial microfluidics: A review. Lab Chip 16:10–34. https://doi.org/10.1039/c5lc01159k

Zhang W, Kai K, Soon D, et al (2012) Micro fl uidics separation reveals the stem-cell – like deformability of tumor-initiating cells. 109:18707–18712. https://doi.org/10.1073/pnas.1209893109

Zhao R, Antaki JF, Naik T, et al (2006) Microscopic investigation of erythrocyte deformation dynamics. Biorheology 43:747–765

Zhao R, Marhefka JN, Shu F, et al (2008) Micro-flow visualization of red blood cell-enhanced platelet concentration at sudden expansion. Ann Biomed Eng 36:1130–1141. https://doi.org/10.1007/s10439-008-9494-z

Zhao X, Xia Y, Whitesides GM (1996) Fabrication of three-dimensional micro-structures: Microtransfer molding. Adv Mater 8:837–840

Zheng Y, Nguyen J, Wei Y, Sun Y (2013) Recent advances in microfluidic techniques for single-cell biophysical characterization. Lab Chip 13:2464–2483. https://doi.org/10.1039/C3LC50355K

Zhu D, Long Q, Xu Y, Xing J (2019) Evaluating nanoparticles in preclinical research using microfluidic systems. Micromachines 10:. https://doi.org/10.3390/mi10060414

Ziaie B, Baldi A, Lei M, et al (2004) Hard and soft micromachining for BioMEMS: review of techniques and examples of applications in microfluidics and drug delivery. Adv Drug Deliv Rev 56:145–172

Zografos K, Pimenta F, Alves MA, Oliveira MSN (2016) Microfluidic converging/diverging channels optimised for homogeneous extensional deformation. Biomicrofluidics 10:. https://doi.org/10.1063/1.4954814

Appendix A - List of publications

During the PhD have resulted the following papers in international peer-reviewed journals, papers in international and national conference proceedings and oral presentations.

Book Chapter

Faustino, Vera; Catarino, Susana O.; Pinho, Diana; Minas, Graça; Lima, Rui. ''A Comparative Study of Image Processing Methods for the Assessment of the Red Blood Cells Deformability in a Microfluidic Device''. In Lecture Notes in Computational Vision and Biomechanics, edited by J.M.R.S. Tavares; R.M. Natal Jorge, 923-929. Springer International Publishing, 2017. Doi: 10.1007/978-3-319-68195-5_100

Articles in international journals

Pinho, D.; **Faustino, V.**; Catarino, S. O.; Pereira, A.I.; Minas, G.; Pinho, F. and Lima, R. (2022) ''Label-free multi-step microfluidic device for mechanical and rheological characterization of blood: diabetes type II''. Micro and Nano Eng 16:10049. https://doi.org/https://doi.org/10.1016/j.mne.2022.100149

Faustino, V.; Pinho, D.; Catarino, S.O.; Minas, G. and Lima, R. (2022) ''Geometry effect in multi-step crossflow microfluidic devices for red blood cells separation and deformability assessment''. Biomedical Microdevices 24:20. https://doi.org/10.1007/s10544-022-00616-0

Faustino, V., Rodrigues R.O., Pinho, D., Costa, E., Santos-Silva, A., Miranda, V., Amaral, J.S. and Lima, R. (2019) "A microfluidic deformability assessment of pathological red blood cells flowing in a hyperbolic converging microchannel." Micromachines 10:10. https://doi.org/10.3390/mi10100645

Rubio, A., **Faustino, V.**, Cabezas, M.G., Lima, R.A. and Vega, E.J. (2019) "Fire-shaped cylindrical glass micronozzles to measure cell deformability." J. Micromech. Microeng. 29:105001. https://doi.org/10.1088/1361-6439/ab3183

Faustino, V., Catarino, S.O., Pinho, D., Minas, G., and Lima, R.A. (2018). ''A Passive Microfluidic Device Based on Crossflow Filtration for Cell Separation Measurements: A Spectrophotometric Characterization." Biosensors 8:125. https://doi.org/10.3390/

Bento, D., Rodrigues, R.O., **Faustino, V.**, Pinho, D., Fernandes, C.S., Pereira, A.I., Garcia, V., Miranda, J.M. and Lima, R.A. (2018) "Deformation of red blood cells, air bubbles, and droplets in microfluidic devices: Flow visualizations and measurements." Micromachines 9:151. https://doi.org/10.3390/mi9040151

Boas, L., **Faustino, V.**, Lima, R., Miranda, J., Minas, G., Fernandes, C. and Catarino, S.O. (2018) "Assessment of the Deformability and Velocity of Healthy and Artificially Impaired Red Blood Cells in Narrow Polydimethylsiloxane (PDMS) Microchannels." Micromachines 9:384. https://doi.org/10.3390/mi9080384

Carvalho, D., Rodrigues, A., **Faustino, V**., Pinho, D., Castanheira, E., and Lima, R.A. (2018). "Microfluidic deformability measurements of an innovative blood analogue fluid based on giant unilamellar vesicles". J. Funct biomater., 9(4), 70. https://doi.org/10.3390/jfb9040070

Pinto, E., **Faustino, V**., Pinho, D., Rodrigues, R. O., Lima, R., Pereira, A. I., (2016). "Cell-free layer analysis in a polydimethysiloxane microchannel: a global approach". International Journal of Medical Engineering and Informatics (IJMEI), 8:3. http://dx.doi.org/10.1504/IJMEI.2016.077437

Faustino, V., Catarino, S. O., Lima, R. and Minas, G. (2016). "Biomedical microfluidic devices by using low-cost fabrication techniques: a review". J Biomech 49:2280–2292. https://doi.org/10.1016/j.jbiomech.2015.11.031

Pinho, D., Rodrigues, R. O., **Faustino, V.** and Lima, R. (2016). "Red blood cells radial dispersion in blood flowing through microchannels: the role of temperature". J. Biomech, 49:11, p. 2293–2298. http://doi.org/10.1016/j.jbiomech.2015.11.037

Rodrigues, R. O., Pinho, D., **Faustino, V**. and Lima, R. (2015). "A simple microfluidic device for the deformability assessment of blood cells in a continuous flow". Biomedical microdevices, 17:6, p. 108. https://doi.org/10.1007/s10544-015-0014-2

Publications in proceedings of scientific meetings

Lage, Teresa; **Faustino, Vera**; Rodrigues, Raquel O.; Lima, Rui A.; Minas, Graça. "Haemocompatibility test of simple magnetic nanoparticles using the distribution of deformed RBCs". Paper presented in 6th IEEE Portuguese Meeting on Bioengineering, Lisboa, 2019. Doi: 10.1109/ENBENG.2019.8692543

Madureira, M., **Faustino, V.**, Schütte, H., Pinho, D., Minas, G., Gassmann, S. and Lima, R.A. (2019) "Red Blood Cells Separation in a Curved T-Shaped Microchannel Fabricated by a Micromilling Technique." In: Tavares J., Natal Jorge R. (eds). VipIMAGE 2019. Lecture Notes in Computational Vision and Biomechanics, vol 34. Springer, Cham. https://doi.org/10.1007/978-3-030-32040-9_59

Faustino, V., Catarino, S.O., Pinho, D., Minas, G. and Lima, R.A. (2018). "Chapter 100 - A comparative study of image processing methods for the assessment of the Red Blood Cells

deformability in a microfluidic device", In: J.M.R.S. Tavares and R.M. Natal Jorge (eds.), VipIMAGE 2017, Lecture Notes in Computational Vision and Biomechanics 27, Springer International Publishing AG 2018, https://doi.org/10.1007/978-3-319-68195-5

Faustino, V., Pinho, D., Catarino, S.O., Miranda, J.M., Minas, G., Lima, R.A. (2018). "A passive microfluidic device for cell sorting and deformability measurements", Submitted to the 19th International Symposium on Applications of Laser and Imaging Techniques to Fluid Mechanics, 16/07 – 19/07/2018, Lisbon, Portugal.

Faustino, Vera; Catarino, Susana O.; Pinho, Diana; Minas, Graça; Lima, Rui. "Preliminary evaluation of a microfluidic device for blood separation and deformation assessment". Paper presented in Europeen Advanced Materials Conference, 2017.

Carvalho, D. A. M., Rodrigues, A. R. O., **Faustino, V**., Pinho, D., Lima, R. A., and Castanheira, E. M. S. (2017). "Escoamento em microcanais de fluidos inovadores análogos ao sangue baseados em vesículas unilamelares gigantes". 7° congresso nacional de biomecânica.

Carvalho, Denise A. M.; Rodrigues, Ana Rita Oliveira; **Faustino, Vera**; Ferreira, Olga; Lima, Rui A.; Castanheira, Elisabete M. S.. "Flow behaviour in microchannels of an innovative blood analogue fluid based on giant unilamellar vesicles". Paper presented in XXII Encontro Luso-Galego de Química, 2016.

Oral communications

Vera Faustino, Diana Pinho, Susana O. Catarino, J. M. Miranda, Graça Minas and Rui Lima. "A passive microfluidic device for cell sorting and deformability measurements". Paper presented in 19th International Symposium on the Application of Laser and Imaging Techniques to Fluid Mechanics, Lisbon. July 16 – 19, 2018

Faustino, Vera; Catarino, Susana O.; Pinho, Diana; Minas, Graça; Lima, Rui. "Preliminary evaluation of a microfluidic device for blood separation and deformation assessment". Paper presented in Europeen Advanced Materials Conference, 2017

Faustino, Vera; Catarino, Susana Oliveira; Pinho, Diana; Lima, Rui Alberto Madeira Macedo; Minas, Graça. "A comparative study of image processing methods for the assessment of the red blood cells deformability in a microfluidic device". Paper presented in VII ECCOMAS Thematic Conference VipIMAGE 2017, Porto, 2017

Appendix B

Chapter 12

Haemocompatibility test of simple Magnetic Nanoparticles using the distribution of deformed RBCs[8]

Abstract—Haemocompatibility of nanoparticles is usually evaluated by hemolysis. However, hemolysis assessment does not measure the dysfunctional erythrocytes with pathological changes on the unbroken cellular membrane. This paper presents a microfluidic tool based on a constriction channel with a hyperbolic-shaped contraction capable of evaluating the biocompatibility and toxicity impact of magnetic nanoparticles (MNPs). The aim of this study is to evaluate the deformation index of red blood cells (RBCs) that have different concentrations of MNPs and their distribution on the microchannel. The results showed that MNPs affected the deformability of RBCs, as long as the MNPs concentration increases, however with the increase of the temperature, that dependence between MNP concentration and deformability decreases.

12.1 Introduction

Superparamagnetic iron oxide nanoparticles are being widely used for various biomedical applications, for example, magnetic resonance imaging, targeted delivery of drugs, and in hyperthermia. Although, the potential benefits of iron oxide magnetic nanoparticles are considerable, there is a distinct need to identify any potential cellular damage associated with these nanoparticles (Singh et al. 2010).

---

[8] Lage T, **Faustino V**, Rodrigues RO, et al (2019) Haemocompatibility test of simple Magnetic Nanoparticles using the distribution of deformed RBCs. 6th IEEE Port Meet Bioeng ENBENG 2019 - Proc 2–5. https://doi.org/10.1109/ENBENG.2019.8692543

Red blood cells (RBCs) possess a unique capacity for undergoing cellular deformation to navigate across various human microcirculation vessels, enabling them to pass through capillaries that are smaller than their diameter and to carry out their role as gas carriers between blood and tissues. Since there is growing evidence that RBCs deformability is impaired in some pathological conditions, measurement of RBCs deformability has been the focus of numerous studies over the past decades. Nevertheless, reports on healthy and pathological RBCs are currently limited (Tomaiuolo 2014).

Reports regarding the complex nanoparticle-RBCs membrane interaction are almost unexpected, especially due to the small size of the nanoparticles. Rodrigues et al. (2016a) presents a microfluidic extensional approach, by detecting small increments in the rigidity of the RBCs, when traditional haemotoxicology analysis showed no significant alteration (Rodrigues et al. 2016a). This microfluidic tool based on a constriction channel is capable of evaluating, in mimicked environments, the biocompatibility and toxicity impact in biomedical-oriented MNPs (Rodrigues et al. 2016a).

The aim of this study is to compare the deformation index, DI, (value that indicates the ability of cells to deform) of RBCs with two different concentrations of MNPs in a bath with a controlled temperature, 37 °C during 30 and 60 minutes. The comparison was made with a simple statistical analysis of the average of the cells distribution using a histogram.

12.2 Materials and methods

12.2.1 Materials

Iron (II) chloride tetrahydrate ($FeCl_2.4H_2O$), iron (III) chloride hexahydrate ($FeCl_3.6H_2O$), sodium hydroxide (NaOH), concentrated ammonium solution (NH_4OH) 28%–30%, cetyltrimethylammonium bromide (CTABr), tetraethyl orthosilicate (TEOS), absolute ethanol, potassium hydroxide (KOH) and nitric acid (HNO_3) were purchased from Sigma-Aldrich. Ultrapure and deionized water were prepared in the laboratory. All chemicals and solvents were used as received without further purification.

12.2.2 Synthesis of the iron oxide magnetic nanoparticles

Iron oxide magnetic nanoparticles (MNP) were synthesized adapting the co-precipitation procedure described by Cardoso et al. (2016).

A solution (A) of 4.06 g of FeCl2.4H2O and 7.78 g of FeCl3.6H2O dissolved in 20 ml of deionized water was prepared. In parallel, another solution (B) of 0.04 g of CTABr was dissolved in 3 ml of deionized water under ultrasound stirring and added to 20 ml of NH4OH 28%–30%. The solution (B) was added to the solution (A) under strong mechanical stirring at 1500 rpm and left under agitation for 30 min. Then, the magnetic nanoparticles were cleaned five times with ethanol and deionized water with the help of a magnet.

In order to increase the stability of iron oxide MNs in solution, they were coated with oleic acid (OA). For this, NMs were dispersed in 40 mL of distilled water using the ultrasound bath (Selective Ultrasons). This mixture was immediately placed on mechanical stirring (Heidolph RZR 2020) and heated up to 80 °C. When the temperature was reached, 500 µl of OA was added slowly and the mixture was stirred for 1 hour. After the mixture cool down, it was washed several times with ethanol and deionized water with the help of a magnet and dried in an oven (Memmert) at 60 °C.

12.2.3 Microfluidic geometry and working fluid protocol

The polydimethysiloxane (PDMS) microchannel was fabricated using a soft lithographic technique, previously reported by Pinto et al. (2014b). A schematic view of the dimensions of the microfluidic devices main channel, 20 × 400 µm (height × width), is shown in Figure 60. To perform the deformability assessment, hyperbolic converging microchannels were designed with 370 µm of length, as well as widths of 400 and 20 µm at the wide and narrow sizes, respectively.
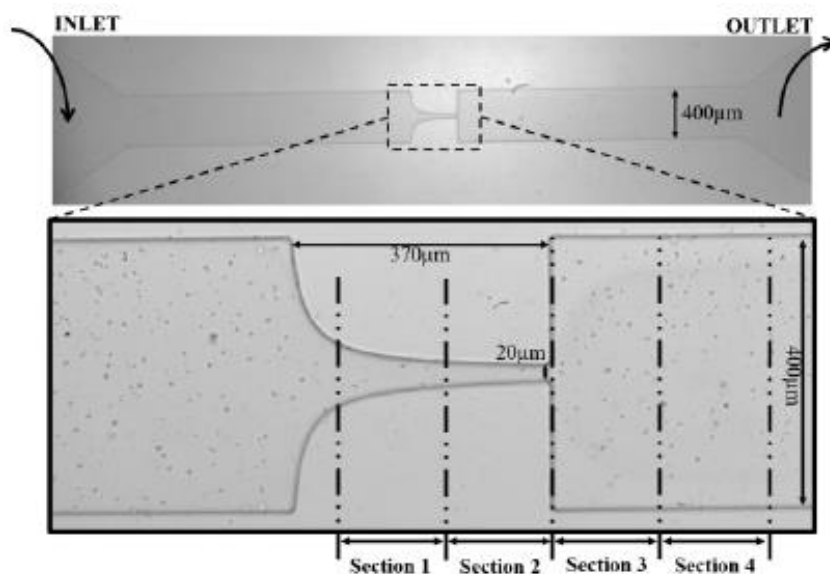

Figure 60. Microfluidic device fabricated in PDMS with a hyperbolic-shaped contraction followed by a sudden expansion, which was subdivided into four sections to assess the DI evolution of the RBCs along the microchannel.

The microscopy system setup used in this work consisted on an inverted microscope (IX71, Olympus) combined with a high-speed camera (Fastcam SA3, Photron, USA). In the inverted microscope, the PDMS microchannel was placed and fixed, and the flow rate of the working fluids was kept constant at 5 µL/min by means of a syringe pump (KD Scientific Inc., Holliston, MA, USA). At the same time, the images of the flowing RBCs, at the established flow rate, were captured by the high-speed camera with a frame rate of 2000 frames/s and a shutter speed ratio of 1/75,000.

There were used 3 solutions. The control solution, which have 2% of hematocrit (Hct) with dextran 40, was used to evaluated the deformation index (DI) of healthy RBCs. The second solution was a 2% Hct with 25 µL of Magnetic Nanoparticles (MNPs) solution with 5mg/mL. The third solution was a 2% Hct with 50 µL of the same MNPs concentration.

12.2.4 Image analysis

The experimental images recorded in each test were transferred to a computer, processed and analyzed by an image handling software, ImageJ (1.46r, NIH, USA). Using this software, the DI of the RBCs was calculated using Eq. (1):

$$DI = L_{major} - L_{minor}/L_{major} + L_{minor} \qquad (1)$$

where L major and L minor are respectively the major and minor axes of an ellipse that represents a RBC (Tomaiuolo 2014; Rodrigues et al. 2016a).

Firstly, the videos were converted to a sequence of images, and a stack of the images' average intensity was processed. The stack image was subtracted to the image sequences, this way it was obtained just the individual cells without the walls and static objects in the image. The brightness and contrast were adjusted and after it was applied a threshold to all the images. Once we have the black and white images a particle analysis was performed measuring the RBCs. This procedure was reported elsewhere (Yaginuma et al. 2013; Faustino et al. 2014b).

12.2.5 Statistical Analysis

The microfluidic results were displayed as mean ± standard deviation using three independent experiments. The statistical analyses were performed using Microsoft Office Excel.

12.3 Results and discussion

The presented results have considered the characterization of the MNPs described in the study of Cardoso et al. (2016). However, in the referred study a haemocompatibility characterization was not performed. The haemocompatibility characterization of the MNPs is crucial, once they will be in contact with cells and they should not present toxicity or influence, in some way, the function of healthy cells.

In this way, it was used a microfluidic tool, to assess the DI of the RBCs. In Table 14, it is shown the number of RBCs (n) that was measured in our study, in each section of the microchannel, for the 5 samples tested.

Table 14. Number of RBCs measured in each section of the microchannel.

Samples/Sections	S1	S2	S3	S4
Control	3198	2688	3839	3657
MNP 25µL, 30min	3277	3235	3260	3278
MNP 25µL, 60min	2344	2850	2585	2210
MNP 50µL, 30min	2998	2875	3376	3390
MNP 50µL, 60min	3067	2986	2851	2972

The number of RBCs is well represented when compared with other similar studies (Pinho et al. 2016), e.g., some of the samples represented in the table I have more than 3000 cells. The large number of RBCs is due to the used method of image analysis (described in the subsection D). This method sets the selection of all RBCs within a calculated area in an established range (between 17 and 100 µm2).

To better understand the deformation index in each section represented in the Figure 60, it was made distribution curves represented the four section of the microfluidic device for the 5 samples used, fig. 2:

- Control RBCs;
- RBCs in contact with MNPs at a final concentration of 25 $\mu g\ (Fe_3\,O_4)/mL$ during 30;
- RBCs in contact with MNPs at a final concentration of 25 $\mu g\ (Fe_3\,O_4)/mL$ during 60 min;
- RBCs in contact with MNPs at a final concentration of 50 $\mu g\ (Fe_3\,O_4)/mL$ during 30 min;
- RBCs in contact with MNPs at a final concentration of 50 $\mu g\ (Fe_3\,O_4)/mL$ during 60 min.

This microfluidic tool allows the deformation of the blood cells along the microchannel, causing the RBC stretching by the larger fluid shear stress providing the most accurate way to determinate the DI of the blood cells in mimic *in vitro* microvascular environment.

The Figure 61 shows 4 histograms that represent the distribution of de DI for the four sections of the microfluidic device. In the section 1 and 2 the DI range is very similar, between 0.65-0.7 and 0.65-0.75, respectively. Although, the similarity, it was verified that the distribution curve of section 1 is wider, with a base much more defined. In this way, section 2 is the section that undergoes the greatest deformation due to a hyperbolic contraction in all the samples tested.
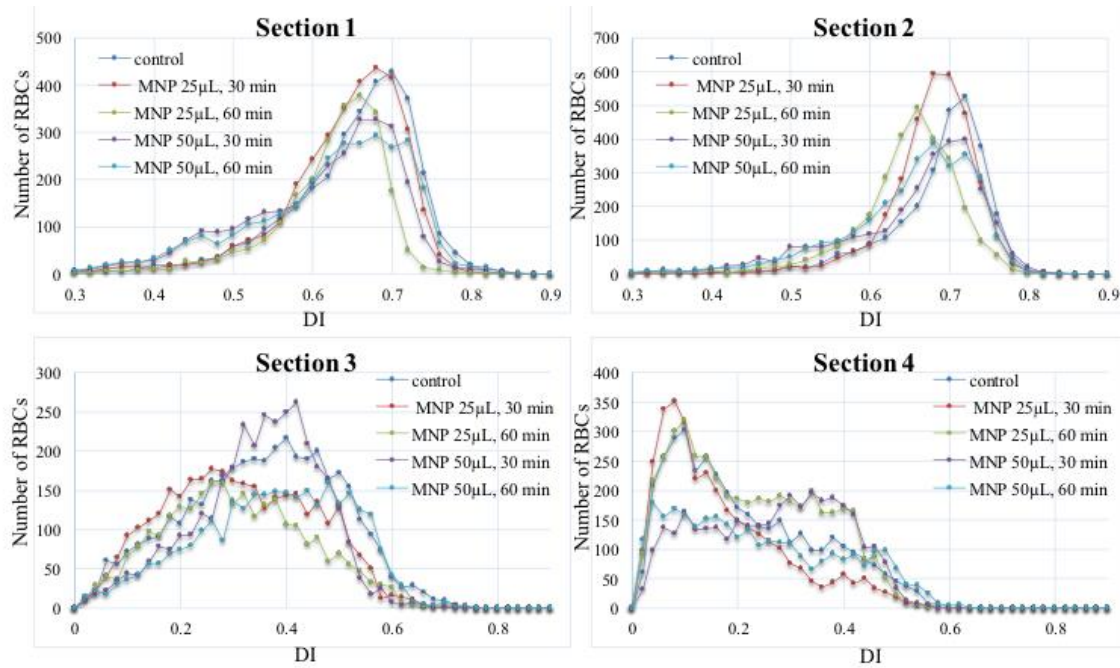

Figure 61. Distribution Curve of each section of the microfluidic device for the 5 samples used: Control RBCs, RBCs in contact with MNPs at a final concentration of 25 µg (Fe3O4) / mL during 30, and 60 min and RBCs in contact with MNPs at a final concentration of 50 µg (Fe3O4) / mL during 30, and 60 min.

The section 3 and section 4, represents the expansion in the microchannel, where the RBCs return to the original round shape. It was found, in the distribution curves, that there is no pattern variation between the control and the RBCs with MNP. Although the inexistent pattern, the DI of the RBCs, between 0.1 and 0.5, are expected, considering that in section 3, due the velocity of the RBCs in the contraction of the hyperbolic, it was expected more deformation of the RBCs than in section 4 (DI between 0.05 and 0.4).

After the evaluation of the RBCs distribution in each section, there were selected the outliers (values that indicate some errors in the measurements techniques) and deleted to improve the accuracy of the DI's average for each section.

As mentioned before, deformability is an important parameter that regulates RBC rheology. Factors regulating deformability at the cellular level are dehydration, membrane protein phosphorylation, cytoskeletal integrity, metabolism and the integrity of hemoglobin. Interaction of these factors makes RBCs more or less deformable. Reduced RBC deformability leads to an

inability of the RBC to pass the splenic circulation and leads to premature removal of RBCs from the blood (Tomaiuolo 2014).

In the literature, there are few studies reporting the haemocompatibility of RBCs with nanoparticles. Although they use different tools from those used in this study, they have the similarity of indicating a DI decrease of RBC with an increasing of nanoparticles concentration (Ran et al. 2015; Pinho et al. 2016; Sharma et al. 2018), which is in agreement with the results obtained in this study.

Figure 62 shows the mean of the obtained DIs with the respective standard deviation for the 5 used samples. It was showed that MNPs affects the deformability of RBCs, as well as the maximum DI obtained, with all tested RBCs samples, was measured in the hyperbolic contraction region – section 2, where the width is minimum. Specifically, in this section (that undergoes higher deformation) the decrease of the DI is verified as long as the rigidity of the RBCs' membrane increases. However, it does not present significant difference when the exposed time increases. In section 3 and 4, and comparing the results obtained between the control sample and the RBCs samples that were placed in contact with the MNPs, it was observed the non-existence of a pattern. The results also showed that MNPs are suitable to performed other biocompatibility tests, once their influence was not very pronounced in this specific deformation test.
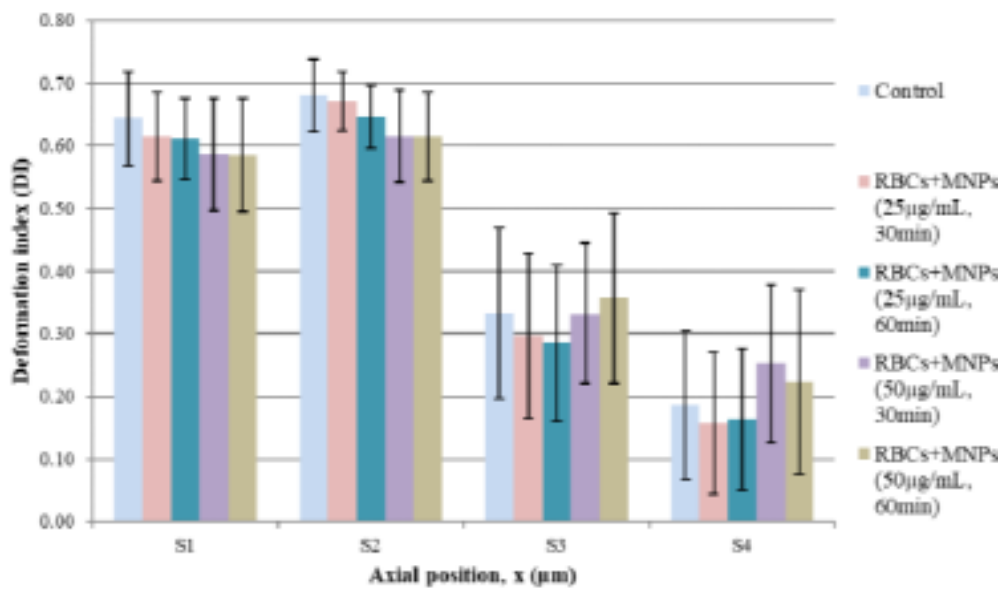

Figure 62. Mean and respective standard deviation of Deformation Index of RBCs along the section 1, 2, 3 and 4 of the hyperbolic microchannel.

12.4 Future directions

The tested microfluidic tool has shown a higher sensitivity to detect small changes in the RBC deformability, which is unreachable using conventional techniques.

In future work, optimization and characterization of magnetic nanoparticles as thermo-responsive drug nanocarriers will be studied. In addition, it will also be studied the Modification of the coating of the MNP, in order to be able to couple the drug and make the MNP more biocompatible. Finally, an evaluation of the biocompatibility and the cytotoxicity of the MNPs, will also be performed.